Alma Mater Studiorum – Università di Bologna

DOTTORATO DI RICERCA

Scienze Chimiche Ciclo XX

Settore scientifico disciplinare di afferenza: CHIM / 03

Titolo della tesi:

Synthesis and characterization of implants for bone substitutions made of biomedical apatites containing silicon

Presentata da: Dott. Simone Sprio

Coordinatore Dottorato

Prof. Vincenzo Balzani

Relatore

Prof. Norberto Roveri

***Co*-Relatori**

Dott.ssa Anna Tampieri
Dott.ssa Elena Landi

Esame finale anno 2008

Motivazione e risultati della ricerca

La presente ricerca si inquadra nell' ambito della risoluzione dei problemi legati alla chirurgia ossea, per la cura e la sostituzione di parti di osso in seguito a fratture, lesioni gravi, malformazioni e patologie quali osteoporosi, tumori, etc…

Vi è un numero elevatissimo di casi nel mondo in cui si rende necessaria la sostituzione di porzioni di tessuto osseo e questo numero è sempre crescente per via del progressivo invecchiamento della popolazione. Questo tipo di intervento è spesso molto invasivo e traumatizzante per il paziente soprattutto nei casi in cui sono coinvolte le ossa principali degli arti o del cranio. Spesso il chirurgo deve intervenire nuovamente a distanza di mesi o di anni, con tutti i traumi legati a simili interventi chirurgici, comportando perciò una sensibile riduzione della qualità della vita del paziente.

Il problema più importante in questo ambito riguarda i materiali in uso per la sostituzione del tessuto osseo. Esiste prova che fin dai tempi più antichi l' uomo ha utilizzato parti sostitutive in metallo mentre successivamente, in tempi più recenti, manufatti in ceramica ne hanno largamente preso il posto per via delle numerose problematiche legate all' introduzione di metalli all' interno dell' organismo. Fin qui, la sostituzione di parti di osso era stata eseguita con il semplice scopo di mantenere la funzione strutturale della parte mancante. Tuttavia, il tessuto osseo è un' entità molto sofisticata, sia da un punto di vista della sua composizione che della sua struttura morfologica, e questo gli conferisce proprietà uniche di adattabilità alle varie sollecitazioni meccaniche, che lo rendono al tempo stesso leggero, resistente ed elastico e soprattutto in grado di autorigenerarsi localmente in seguito a traumi di estensione limitata. Nelle ultime decadi quindi, con l' aumentare dell' aspettativa di vita e dell' accresciuto benessere, è diventato via via più rilevante il ricorso a soluzioni in grado di garantire la massima funzionalità della parte sostituita e quindi di consentire al paziente di tornare in breve tempo ad una vita attiva e soddisfacente. In molti casi, quando è possibile, si ricorre al trapianto di osso *autologo*, che consiste nell' asportazione e nel successivo trapianto di piccole parti di osso dallo stesso individuo, laddove è possibile, spesso dalla cresta iliaca; questa tecnica permette solo il trapianto di piccole parti di osso e comporta tuttavia un notevole disagio poiché il paziente deve sottoporsi a due interventi chirurgici. In alternativa è anche possibile il trapianto di osso *eterologo*, ovvero di porzioni di osso provenienti da altro animale; in questo caso,

tuttavia, non sono pochi i casi di rigetto ed infezione. La soluzione in grado di evitare tutti questi problemi è la realizzazione di un materiale sintetico capace di riprodurre il comportamento dell' osso naturale sia da un punto di vista chimico che strutturale e da ormai quasi cinquanta anni considerevoli sforzi sono in atto da parte della comunità scientifica per ottenere questo risultato.

Il tessuto osseo è costituito per il 70% da una sostanza minerale, l' *idrossiapatite*, a base di calcio, fosforo e piccole quantità di carbonato, magnesio, silicati e altre sostanze in tracce, organizzata in una struttura porosa e complessa, tale da rendere efficiente la distribuzione degli sforzi meccanici; questa struttura minerale è permeata di cellule specializzate, gli osteociti, in grado di regolare l' attività biomeccanica dell' intero osso, grazie alle varie sostanze presenti nella parte minerale. Questa componente minerale nuclea su una matrice proteica a base di collagene, che conferisce all' osso le sue uniche proprietà di elasticità e flessibilità.

Buona parte della comunità scientifica è dunque orientata alla realizzazione di materiali di sintesi *biomimetici*, ovvero in grado di riprodurre la composizione chimica, morfologica e strutturale dell' osso naturale. Da un punto di vista chimico, questo consente di stimolare i processi naturali di rigenerazione del tessuto osseo e nel contempo provoca il riassorbimento dell' impianto di sintesi da parte dell' organismo. Da un punto di vista morfologico-strutturale, l' ottenimento di impianti di morfologia complessa e dall' adeguata resistenza meccanica favorisce l' abitazione e la proliferazione delle cellule e la formazione di nuovo tessuto osseo in grado di sostituire progressivamente l' impalcatura di sintesi impiantata dal chirurgo. La resistenza meccanica è tanto più importante quanto più la porzione di osso sostituito ha funzioni strutturali di sostegno dell' intero scheletro, quali le ossa lunghe delle gambe e delle braccia.

La ricerca scientifica ha finora ottenuto materiali con struttura di idrossiapatite in grado di esibire vari livelli di biomimetismo di tipo chimico, ossia materiali calcio fosfatici contenenti carbonato e/o magnesio e/o silicio in quantità adeguate per l' attività cellulare, mostrando una più intensa attività di ricostituzione e rimodellamento del tessuto osseo in confronto con materiali di composizione chimica differente; tuttavia, una perfetta riproduzione della composizione chimica dell' osso non è ancora stata raggiunta. Analogamente, strutture tridimensionali ceramiche con una distribuzione anisotropa dei pori e delle loro dimensioni sono state altresì ottenute, tuttavia le tecniche di

consolidamento necessarie ad ottenere tali strutture e le limitazioni tecnologiche alla possibilità di ottenere morfologie complesse simili a quelle dell' osso hanno impedito finora di realizzare impalcature per sostituti ossei aventi proprietà analoghe a quelle del tessuto osseo naturale.

Infine, la resistenza meccanica intrinseca dei materiali *bioattivi*, cioè in grado di indurre una risposta biologica positiva nell' organismo, è spesso insufficiente per sopportare gli sforzi e le sollecitazioni biomeccaniche naturali, cosicché si deve ricorrere all' impiego di materiali ceramici inerti che non sono tuttavia in grado di essere riassorbiti dall' organismo.

Per quanto riguarda l' aspetto chimico, il ruolo fondamentale dello ione carbonato nell' apatite biologica è da tempo noto, così come quello del magnesio; in tempi più recenti tuttavia gli studi si sono concentrati sugli effetti positivi del silicio sulla stimolazione dell' attività cellulare e su tecniche in grado di incorporarlo nella struttura dei materiali destinati ad impianto.

Nella presente ricerca il problema dell' ottenimento di sostituti ossei biomimetici è stato affrontato da tre differenti prospettive.

In una prospettiva biochimica, si sono sperimentate ed attuate delle metodologie per ottenere polveri di idrossiapatite calcio-fosfatica contenente simultaneamente i sostituti ionici più rilevanti per la stimolazione dei processi naturali di rigenerazione ossea (carbonato, magnesio e silicio), in quantità ritenute adeguate sulla base di precedenti ricerche sul metabolismo cellulare di queste sostanze.

In prospettiva di applicazioni strutturali sono state anche sperimentate ed attuate tecnologie di consolidamento di miscele di polveri di idrossiapatite con silicati di calcio bioattivi per ottenere materiali ad elevata resistenza meccanica da utilizzare in seguito per la realizzazione di ceramici porosi.

Il problema del biomimetismo della morfologia dell' osso è stato infine affrontato prendendo spunto dalla Natura, in particolare da strutture vegetali come legni e piante che esibiscono naturalmente strutture porose gerarchiche estremamente complesse, grazie alle quali proprietà di resistenza meccanica ed efficiente distribuzione degli sforzi sono coniugate con una elevata leggerezza. In questo modo nel presente lavoro si sono esplorate metodologie del tutto nuove per ottenere strutture ceramiche di idrossiapatite a partire da sostanze naturali, mantenendo la loro medesima morfologia.

I risultati ottenuti nel corso della presente ricerca sono stati positivi ed incoraggianti sotto tutti e tre gli aspetti investigati.

In primo luogo, da un punto di vista chimico, si sono ottenute polveri di idrossiapatite ad accresciuto biomimetismo, come dimostrato dalle varie metodologie di indagine impiegate e dal loro comportamento in ambiente fisiologico e in coltura cellulare. Il procedimento di sintesi ha permesso il controllo del tenore di ioni sostituenti nella struttura dell' idrossiapatite, consentendo di ottenere specifiche composizioni sulla base dell' applicazione desiderata.

In secondo luogo, materiali bioattivi con superiori proprietà meccaniche sono stati ottenuti grazie all' impiego di silicati di calcio come materiali di rinforzo dell' idrossiapatite. L' impiego di tali materiali contenenti silicio ha inoltre aperto la prospettiva di ottenere materiali con accresciuto biomimetismo, oltre che dotati di accresciuta resistenza, grazie ai possibili fenomeni di migrazione di ioni silicio all' interno della struttura dell' idrossiapatite durante i trattamenti termici con cui vengono ottenuti i ceramici finali. Questo fenomeno, se confermato, potrà essere applicato ad una numerosa serie di materiali a base di silicati di calcio contenenti anche altri ioni influenti nel biomimetismo osseo, come il magnesio, consentendo di ottenere allo stesso tempo materiali ad accresciuto biomimetismo e resistenza meccanica.

Infine, specifici processi chimici e termici sono stati applicati ad alcune strutture lignee naturali quali abete, pino e larice, consentendo di trasformarli in idrossiapatite, mantenendo nel contempo l' originaria morfologia porosa e gerarchicamente organizzata. Questo risultato è di assoluta novità, essendo stato applicato in passato solo per l' ottenimento di sostanze dalla composizione più semplice, come il carburo di silicio (che può essere considerato peraltro un materiale bioinerte). Un' idrossiapatite caratterizzata da una struttura gerarchica simile all' osso costituisce potenzialmente la migliore soluzione per una rapida ed efficiente integrazione del nuovo tessuto osseo nell' impianto di sintesi. Allo scopo di migliorare la riassorbibilità di simili impianti, l' idrossiapatite deve presentare differenti sostituzioni ioniche, pertanto le ricerche future in questo campo dovranno essere orientate all' incorporazione di ioni nelle strutture gerarchiche di idrossiapatite derivate da strutture lignee, oltre che alla determinazione delle loro proprietà meccaniche in relazione alla morfologia.

I tre aspetti del biomimetismo affrontati in questo lavoro, chimico, strutturale e morfologico, hanno delineato tre vie maestre che sono orientate a convergere nella realizzazione del sostituto osseo ideale. La ricerca futura dovrà essere rivolta particolarmente alla convergenza dei tre differenti risultati ottenuti, superando le difficoltà che questo comporta. Infatti un accresciuto biomimetismo è associato ad una ridotta stabilità chimica da parte dell' idrossiapatite, analogamente a quanto avviene nell' apatite naturale dell' osso; questa instabilità si verifica soprattutto alle alte temperature, dove hanno luogo i processi di realizzazione di materiali bioattivi strutturalmente resistenti (*sinterizzazione*); da un punto di vista morfologico inoltre, una volta accertata la fattibilità delle trasformazioni chimiche di legni e piante in ceramici porosi a base di idrossiapatite, la ricerca dovrà essere rivolta alla selezione delle strutture legnose più adeguate in base alla loro porosità e resistenza meccanica intrinseca, e all' adeguamento dei processi chimici e termici messi a punto nel presente lavoro allo scopo di migliorarne il biomimetismo chimico e meccanico.

LIST OF CONTENT

Page

LIST OF TABLES……..xi

LIST OF FIGURES……...xiii

1. GENERAL TOPICS……1

1.1 Biology of bone tissue……...1

1.2 Morphology and structure of bone tissue……4

1.2.1 Hierarchical structure of bone……...6

1.2.2 Mechanical properties of bone……..7

1.2.3 Types of bone……8

1.3 Bone remodelling……9

1.4 Need of the development of bone substitutes……12

1.4.1 Current solutions for bone substitutes……14

1.4.2 Synthetic bone substitutes……17

1.4.3 Bioceramics……18

1.5 Calcium phosphates in biologic systems……20

1.5.1 Calcium phosphate dehydrate, Brushite (DCPD)……22

1.5.2 Tricalcium phosphate (TCP)……23

1.5.3 Amorphous calcium phosphates (ACP)……...24

1.6 Bioactivity of calcium phosphates……..24

1.7 Apatites……...26

1.7.1 Hydroxyapatite: structure and chemistry……26

1.7.2 Biological apatites……...28

1.7.3 Effect of carbonate……..29

1.7.4 Effect of magnesium……30

1.7.5 Effect of silicon……30

1.8 Methods for synthesis of HA……32

1.9 Non-stoichiometric and substituted HA……35

1.10 Thermal behaviour of apatites……..41
1.11 Characterization of apatite biomaterials……...43
References……47

2. ANALYTICAL TECHNIQUES…….55
2.1 X-Ray Diffraction (XRD)……...55
2.2 Fourier Transform Infrared Spectroscopy (FTIR)……..61
2.3 Inductively Coupled Plasma Optical Emission Spectroscopy (ICP-OES)……..63
2.4 Scanning Electron Microscopy (SEM)……...64
2.5 Thermogravimetry-Thermoanalysis (TG-DTA)……68
2.6 Powder Analysis…….69
2.6.1 Specific Surface Area…….....69
2.6.2 Electro-acoustic spectroscopy……71

3. DEVELOPMENT OF MULTI-SUBSTITUTED HYDROXYAPATITE…….73
3.1 Synthesis of multi-substituted hydroxyapatite powders…….73
3.2 Characterization of multi-substituted hydroxyapatite powders……..76
3.2.1 Phase analysis by XRD……79
3.2.2 Chemical analysis by ICP……83
3.2.3 Thermal analysis……..86
3.2.4 Chemical analysis by FTIR…….89
3.2.5 Powder analysis…….....93
3.2.6 Solubility tests…….98
3.3 Thermal stability of multi-substituted HA powders…….105
3.4 HA powder substituted with strontium ,carbonate, silicon and magnesium……...110
3.5 *In vitro* tests……..114
3.5.1 Proliferation tests on Si-HA characterized by different silicon content……...114
3.5.2 Cytotoxicity of multi-substituted HA powders……..115

3.6 Conclusions……..116
References……..119

4. DEVELOPMENT OF REINFORCED HA-BASED BIOMATERIALS……...121
4.1 Need of reinforced bone substitutes…….121
4.2 Calcium silicates as biomaterials…….123
4.3 Development of composites HA / silico-carnotite ($Ca_5(PO_4)_2SiO_4$)……...125
4.3.1 Powder synthesis and preparation of mixtures ……..125
4.3.2 Characterization…….126
4.3.3 Cytotoxicity tests……...130
4.4 Development of composites HA / β, γ-Ca_2SiO_4……...131
4.4.1 Structure and phase stability in calcium disilicate system…….131
4.4.2 Synthesis of β and γ-Ca_2SiO_4……132
4.4.3 Preliminary sintering tests…….133
4.5 Development of dense ceramic composites by Fast Hot Pressing (FHP)…….……...134
4.5.1 Sample preparation……135
4.5.2 Sample characterization…….136
4.6 Mechanical characterization of HA and composite ceramics……..140
4.6.1 Sample preparation and mechanical testing……..140
4.6.2 Physical-chemical characterization……...143
4.6.3 Mechanical characterization……..148
4.7 Conclusions……..151
References……..154

5. HIERARCHICALLY ORGANIZED STRUCTURES AS BONE SCAFFOLDS……...159
5.1 Introduction……..159
5.2 Wood structures as templates for bone scaffolds…….160

5.3 Ceramization of native vegetable structures…….162
5.4 The European Project TEM-PLANT……170
5.5 Characterization of the transformed woods……..170
5.6 Conclusions……..179
References……..181

FINAL CONCLUSIONS AND FUTURE PERSPECTIVES……183

ACKNOWLEDGEMENTS……185

LIST OF TABLES

Page

Table 1.I. General properties of different bone grafts……..17
Table 1.II. Present uses of bioceramics……18
Table 1.III. Classification of Bioceramics on the basis of tissue attachment……...19
Table 1.IV. Phosphate minerals present in human tissues..…….22
Table 1.V. Atomic composition of human hard tissues……...29
Table 3.I. Amount of reagents employed in the synthesis of multi-substituted HA powders……...75
Table 3.II. Chemical analysis of the multi-substituted HA powders……..…….84
Table 3.III. Weight fraction of the various elements in the multi-substituted HA powders……..85
Table 3.IV. Percent weight loss in the range 100-400 °C……89
Table 3.V. Particle characteristics in multi-substituted HA…….94
Table 3.VI. Release kinetic data of multi-substituted HA powders in SBF at 37 °C……..104
Table 3.VII. Phase transformation in Si-CHA powders during sintering…….107
Table 3-VIII. Phase transformation in Si-MHA powders during sintering……...109
Table 3.IX. Chemical composition of Sr-Si-MCHA powder…….114
Table 3.X. Weight fraction of the various elements in Sr-Si-MCHA powder……...114
Table 4.I. Main mechanical properties of HA compared to cortical bone…….122
Table 4.II. Mechanical properties of different bioactive calcium silicates in comparison with cortical bone……124
Table 4.III. Comparison between different FHP treatments performed on HA powder……...137
Table 4.IV. Samples to be mechanically tested obtained by FHP…….140
Table 4.V. Results of flexural strength tests performed on HA and composite…….148
Table 4.VI. Results of nanoindentation tests on HA and composite……..149
Table 4.VII. Mechanical behaviour of HA and composite materials under macroscopic investigation……...149

LIST OF FIGURES

Page

Figure 1.1. Schematic drawing of an osteoblast……..……..2
Figure 1.2. Schematic drawing of the cross section of an osteocyte……..3
Figure 1.3. Schematic drawing of an osteoclast…….4
Figure 1.4. Schematic drawing of the bone structure…….5
Figure 1.5. Hierarchical structure of bone……..6
Figure 1.6. Young's modulus of trabecular bone as a function of density of bone……8
Figure 1.7. Different types of bone……9
Figure 1.8. Bone remodelling: effect of reduction (from A to B) and of intensification of strain (from B to A) on bone trabecules…….....10
Figure 1.9. Bone resorption……..10
Figure 1.10. Bone deposition……...11
Figure 1.11. Schematic diagram of the Davy and Hart model for bone remodelling……..12
Figure 1.12. Effect of age on strength and density of bone……..13
Figure 1.13. Comparison of the different chemical activities of different ceramic-based biomaterials……..…20
Figure 1.14. Examples of bioceramic implants for different applications……..…..21
Figure 1.15. Crystal structure of Hydroxyapatite……..…...26
Figure 1.16. Structure of monoclinic hydroxyapatite……..……27
Figure 1.17. View of the two possible arrangement of CO_3 moieties around the PO_4 tetrahedron……37
Figure 2.1. Constructive and destructive interference in Rayleigh scattering of X rays……...…...…56
Figure 2.2. The 14 possible Bravais lattices……58
Figure 2.3. Some examples of Miller planes……59
Figure 2.4. Diffractometer adopting the Bragg-Brentano geometry……61
Figure 2.5. Possible vibrations detected by infrared spectroscopy……..62
Figure 2.6. Scheme of equipment for infrared spectroscopy……...62
Figure 2.7. Signals produced by the interaction of the electron beam with the sample……...64

Figure 2.8. Scheme of a Scanning Electron Microscope…….65
Figure 2.9. Interaction of the electron beam with the electronic cloud……68
Figure 2.10. Schematic of double layer in a liquid at contact with a solid……..71
Figure 2.11. Equipment for electro-acoustic spectroscopy……..72
Figure 3.1. Equipment for the synthesis of HA powder……...74
Figure 3.2. Effect of osteporosis on the bone trabeculae (right)……..76
Figure 3.3. Equipment for solubility tests on multi-substituted HA granulates……...79
Figure 3.4. Comparison between XRD spectra of stoichiometric HA (HA_L) and Si-HA with different content of silicon…….80
Figure 3.5. Comparison between XRD spectra of CHA and Si-CHA with different carbonate content……...81
Figure 3.6. Comparison between the XRD spectra of multi-substituted HA powders containing magnesium, silicon and carbonate……82
Figure 3.7. Crystallization of amorphous Si-CHA-1 (a) and Si-MCHA-1 (b) after treatment at 700 °C……..83
Figure 3.8. Thermogravimetric analysis of multi-substituted HA powders…….87
Figure 3.9. TG-DTA curves of Si-CHA-1 and Si-MCHA-1 powders…….88
Figure 3.10. TG-DSC of pure $CaCO_3$ powder…….88
Figure 3.11. Comparison between TG spectra of Si-CHA-1 and $CaCO_3$……89
Figure 3.12. FTIR spectra of multi-substituted HA powders……...90
Figure 3.13. Effect of silicon on hydroxyl bands in Si-HA powders……...91
Figure 3.14. Water adsorption bands in Si-CHA-1 and Si-MCHA -1 powders……...92
Figure 3.15. Typical morphology of a silicon-substituted HA…….93
Figure 3.16. Self-agglomeration of HA powders…….94
Figure 3.17. Particle size distribution of multi-substituted HA powders.: a) differential; b) cumulative……..96
Figure 3.18. Electrical conductivity of multi-substituted HA powders……...97
Figure 3.19. ζ-potential vs. pH of multi-substituted HA powders……...98
Figure 3.20. Typical morphology of a granulated HA…….99
Figure 3.21. Cumulative release of calcium by multi-substituted HA powders……100
Figure 3.22. Cumulative release of magnesium by multi-substituted HA powders……..101
Figure 3.23. Cumulative release of silicon by multi-substituted HA powders……..102

Figure 3.24. Effect of silicon on the formation of α-TCP after sintering……...106
Figure 3.25. DSC curves of Si-HA powders……..106
Figure 3.26. DSC curves of Si-CHA powders……...108
Figure 3.27. Effect of silicon on MHA powder…….109
Figure 3.28. Effect of silicon on MCHA powder……..110
Figure 3.29. XRD spectrum of Sr-Si-MCHA powder……...111
Figure 3.30. Thermal behaviour of Sr-Si-MCHA powder…….112
Figure 3.31. XRD spectrum of Sr-Si-MCHA fired at 700 °C……112
Figure 3.32. Formation of β-TCP in Sr-Si-MCHA powder……...113
Figure 4.1. XRD spectrum of the calcined gel, precursor of silico-carnotite phase……..126
Figure 4.2. XRD spectrum of the calcined gel after the thermal treatment of transformation in silico-carnotite phase…….127
Figure 4.3. Decomposition of silico-carnotite after firing at different temperatures…….128
Figure 4.4. XRD spectra of mixtures HA-silicocarnotite after sintering at 1250 °C…….129
Figure 4.5. Microstructure of HA pure and doped with different amounts of silico-carnotite: a) 5%; b) 10%, c) 20%; d) 50%.....130
Figure 4.6. Polymorphic transformations of Ca_2SiO_4 [53]……131
Figure 4.7. XRD spectrum of as-synthesized β-Ca_2SiO_4……...132
Figure 4.8. XRD spectrum of as-synthesized γ-Ca_2SiO_4……...133
Figure 4.9. Phase composition of mixture HA-γ-Ca_2SiO_4 after sintering in air at different temperatures…….134
Figure 4.10. Scheme of the equipment for FHP…….135
Figure 4.11. Sample preparation for FHP experiments……..136
Figure 4.12. XRD spectra of stoichiometric HA heat treated by FHP……...137
Figure 4.13. Delamination occurring during FHP of HA under excessive applied pressure……138
Figure 4.14. Different grain growth in external (a) and internal part (b) of a HA sample heated at 1500 °C (100 °C/min)…….139
Figure 4.15. Scheme of the flexural strength test performed on sample bars……141
Figure 4.16. Geometry of a Berkovich indenter tip……...142
Figure 4.17. Example of a load-displacement curve during loading and unloading……..142
Figure 4.18. Comparison between densification curves of HA

at different heating rates……...143
Figure 4.19. XRD spectrum of γ-Ca_2SiO_4 treated at 1500 °C by FHP……..144
Figure 4.20. Morphology of as-obtained γ-Ca_2SiO_4……..145
Figure 4.21. Comparison between XRD of HA and HA / Ca_2SiO_4 composite……..145
Figure 4.22. Microstructures of HA obtained by FHP at different temperatures.
a): 1500 °C; b) 1400 °C; c) 1300 °C……146
Figure 4.23. Microstructures of composites obtained by FHP
at different temperatures. a): 1500 °C; b) 1400 °C; c) 1300 °C……...147
Figure 4.24. EDS analysis performed on several grains of
HA-β-Ca_2SiO_4 composite sintered at 1500 °C by FHP……147
Figure 5.1. Hierarchical structure of wood……161
Figure 5.2. Comparison between mechanical performances of different classes
of materials……...162
Figure 5.3. Reaction pathway to obtain hydroxyapatite scaffolds starting
by native wood…….....164
Figure 5.4. Typical thermal cycle in carburization process……...166
Figure 5.5. Sample arrangement in calcium infiltration. A: liquid phase;
B: gaseous phase……168
Figure 5.6. Morphology of pyrolyzed larch-wood……171
Figure 5.7. XRD spectrum of pyrolyzed wood……..171
Figure 5.8. XRD spectrum of transforming CaC_2 wood-like structure,
when exposed to air……172
Figure 5.9. Formation of calcium carbide into the pores of carbon preform……173
Figure 5.10. Extensive formation of CaC_2 particles into the pore of carbon preform…...173
Figure 5.11. Incomplete carburization in liquid-phase infiltration……174
Figure 5.12. SEM micrographs of pyrolysed wood before and after
the transformation in CaC_2……..174
Figure 5.13. Calcium carbide obtained by initial molar ratio Ca/C >> 1 and
Ca/C = 1……175
Figure 5.14. Comparison between XRD analyses of two different
thermal cycles to obtain CaO……...176
Figure 5.15. SEM micrographs of calcium oxide porous template……176

Figure 5.16. XRD analysis after carbonation process by autoclave (400°C, 22bar P_{CO2}, 24 hours)……...177
Figure 5.17. Carbonation percentage vs time of reaction in kiln (700°C)…….177
Figure 5.18. SEM micrograph calcium carbonate structure……...178
Figure 5.19. XRD analysis after hydrothermal treatment of calcium carbonate in phosphate-saturated atmosphere……..179

CHAPTER 1

GENERAL TOPICS

1.1 Biology of bone tissue

Bones are rigid organs that form part of the endoskeleton of vertebrates. They function to move, support, and protect the various organs of the body, produce red and white blood cells and store minerals. Because bones come in a variety of shapes and have a complex internal and external structure, they are lightweight, yet strong and hard, in addition to fulfilling their many other functions. One of the types of tissues that makes up bone is the mineralized osseous tissue, also called bone tissue, that gives it rigidity and honeycomb-like three-dimensional internal structure. Other types of tissue found in bones include marrow, endosteum and periosteum, nerves, blood vessels and cartilage. There are 206 bones in the adult body and about 300 bones in the infant body.

Bone tissue consists of cells embedded in a fibrous, organic matrix, the **osteoid**, which is primarily constituted by Type I collagen (90%) and 10% amorphous ground substance (primarily glycosaminoglycans and glycoproteins). Osteoid comprises approximately 50% of bone by volume and 25% by weight.

Osteoblasts (from the Greek words for "bone" and "germ" or embryonic) are mono-nucleate cells, descending from osteoprogenitor cells, that are responsible for the secretion of osteoid, and subsequent bone formation through the mineralization of the osteoid matrix.

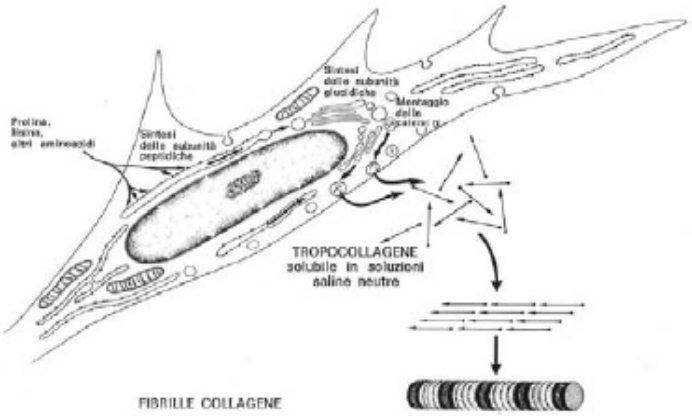

Figure 1.1. Schematic drawing of an osteoblast.

Osteoblasts are located on the surface of osteoid seams and also manufacture hormones, such as prostaglandins, to act on the bone itself (see Fig. 1.1). They robustly produce alkaline phosphatase, an enzyme that has a role in the mineralisation of bone, as well as many matrix proteins. Osteoblasts are the immature bone cells. When osteoblasts are trapped in the bone matrix which they themselves produced they become star-shaped cells named osteocytes, the most abundant cell found in bone.

Osteocytes are mature bone cells, networked to each other via long processes that occupy tiny canals called canaliculi, which are used for exchange of nutrients and waste (see Fig. 1.2). The space that an osteocyte occupies is called a lacuna (Latin for a *pit*). Although osteocytes have reduced synthetic activity and, like osteoblasts are not capable of mitotic division, they are actively involved in the maintenance of bony matrix, through various mechanosensory mechanisms regulating the bone's response to stress.

Bone is a dynamic tissue that is constantly being reshaped by osteoblasts, cells which build bone, and osteoclasts, which resorb bone.

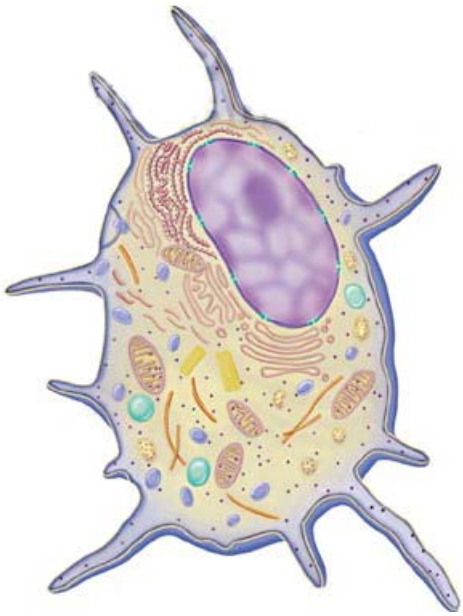

Figure 1.2. Schematic drawing of the cross section of an osteocyte.

Osteoclast (from the Greek words for "bone" and "broken") are multi-nucleated cells responsible for the resorption of bone through the removal of the bone's mineralized matrix (see Fig. 1.3). The removal process begins with the attachment of the osteoclast to the osteon (predominant structures found in compact bone, see later); the osteoclast then induces an infolding of its cell membrane and secretes collagenase and other enzymes important in the resorption process, such as tartrate resistant acid phosphatase, secreted against the mineral substrate. High levels of calcium, magnesium, phosphate and products of collagen will be released into the extracellular fluid as the osteoclasts tunnel into the mineralized bone, also resulting in a transfer of calcium from bone fluid to the blood. During childhood, bone formation exceeds resorption, but as the aging process occurs, resorption exceeds formation.

The characteristic rigidity and strength of bone derives from the presence of mineral salts, that permeate the organic matrix, formed by the osteoid mineralization, due to the secretion of vesicles containing alkaline phosphatase, by the osteoblasts. This cleaves the phosphate groups and acts as the foci for calcium and phosphate deposition. The vesicles then rupture and act as a centre for crystals to grow on. The mineral phase comprises approximately 50% of bone by volume and 75% by weight. The principal constituents of bone mineral are calcium phosphate, mainly carbonated hydroxyapatite, amorphous calcium phosphate and calcium carbonate, with lesser quantities of sodium, magnesium, silicon and fluoride.

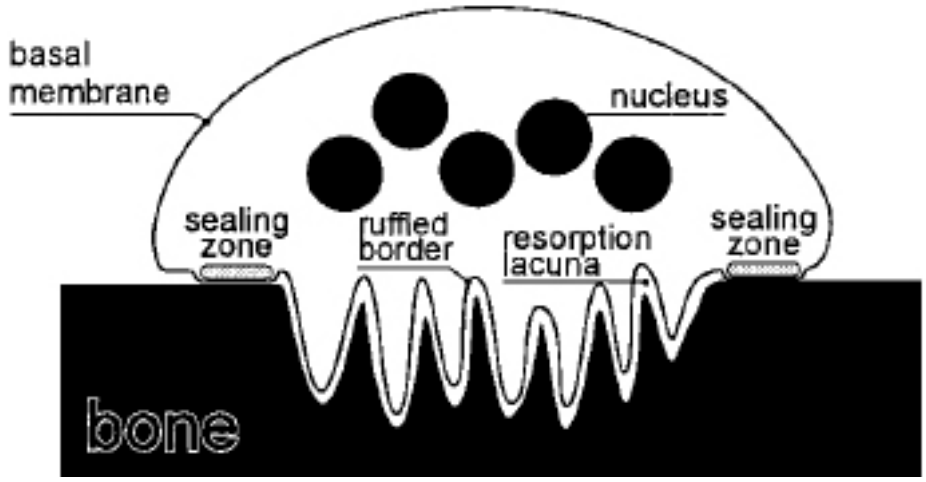

Figure 1.3. Schematic drawing of an osteoclast.

1.2 Morphology and structure of bone tissue

Fig. 1.4 illustrates the structure of bone. Whole bones are composed of two types of bony tissue: cortical and trabecular.

Cortical bone, also known as compact bone, is dense and forms the surface of bones, contributing 80% of the weight of a human skeleton. It is extremely hard, formed of multiple stacked layers with few gaps. Cortical bone comprises the diaphysis of long bones and the thin shell that surrounds the metaphyses.

Cortical haversian bone consists of quasi-cylindrically shaped element called **osteons** or **haversian system**. The individual haversian system themselves are composed of concentric lamellae about 3 to 7 μm thick. These thin lamellae, in turn, are constructed from wrapped collagen fibres impregnated at regularly spaced sites with hydroxyapatite and other mineral crystals about 20 to 40 nm long.

Osteons are typically about 200 μm in diameter, the same thickness as the laminae in laminar bone, and about 10 to 20 mm long. The thickness is the same because bloody supply for the haversian system is a central lumen containing a blood vessel, and thus every point in the haversian system is no more than 100 μm from the bloody supply, as was the case with laminar bone. Haversian bone is organized to accommodate small arteries, arterioles, capillaries, and venues of the microcirculation system.

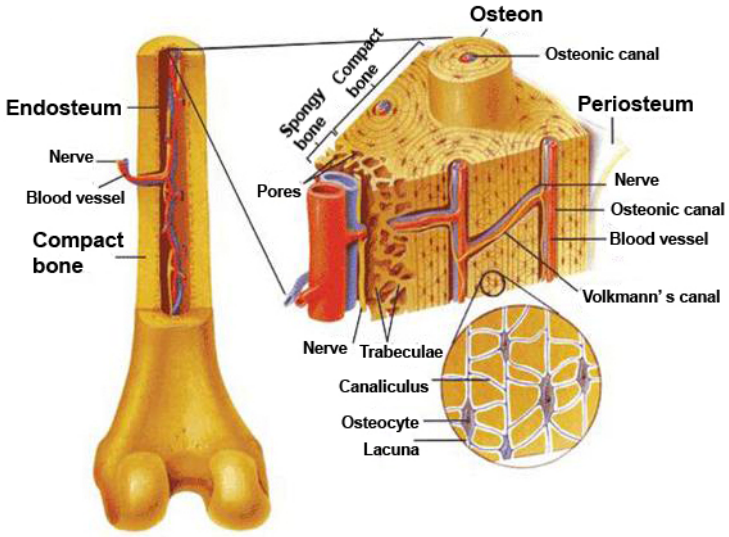

Figure 1.4. Schematic drawing of the bone structure.

The osteons of haversian bone and the laminae of laminar bone are basically just different geometric configurations of the same material. In both geometric configurations no point in the tissue is more than 100 μm away from the bloody supply.

Trabecular bone (also known as **cancellous**, or **spongy**) is a type of osseous tissue with a low density and strength but very high surface area, that fills the inner cavity of long bones, as a three-dimensional, interconnected network of trabecular rods and plates. A network of rods produces low-density, open cells, whereas a network of plates can result in higher density, nearly closed cells. The external layer of cancellous bone contains red bone marrow where the production of blood cellular components (known as hematopoiesis) takes place. Cancellous bone is also where most of the arteries and veins of bone organs are found.

The classification of bone tissue as cortical or trabecular is based on relative density, the ratio of specimen density to that of fully dense cortical bone (usually assumed to have a density of 1.8 $g \cdot cm^{-3}$). The relative density of trabecular bone varies from 0.05 to about 0.7, corresponding to porosities that ranges from about 30 to more than 90%. The relative density of cortical bone ranges from about 0.7 to about 0.95. Obviously, the distinction between low-density cortical bone and high-density cortical bone is somewhat arbitrary.

Bone is first deposited as woven bone, in a disorganized structure with a high proportion of osteocytes in young and in healing injuries. Woven bone is weaker, with a small number of randomly oriented collagen fibres, but forms quickly. It is replaced by lamellar bone,

which is highly organized in concentric arranged laminae with a low proportion of osteocytes. Lamellar bone is stronger and filled with many collagen fibres parallel to other fibres in the same layer. The fibres run in opposite directions in alternating layers, much like plywood, assisting in the bone's ability to resist torsion forces. After a break, woven bone quickly forms and is gradually replaced by slow-growing lamellar bone on pre-existing calcified hyaline cartilage through a process known as bony substitution.
The thickness of the lamina is about 200 μm. Between each lamina and the next there is a net-like system of load vessels. Occasional large radial vessels through lamina connect the net.

1.2.1 Hierarchical structure of bone

The whole architecture of bone is very complex: starting from the smallest constituting elements to the largest scales, the bone is not only organized in an anisotropic manner, but the arrangement of its constituting elements is hierarchical; this means that its structural units are organized at increasing size levels, and this feature confers unique properties to the whole bone structure.

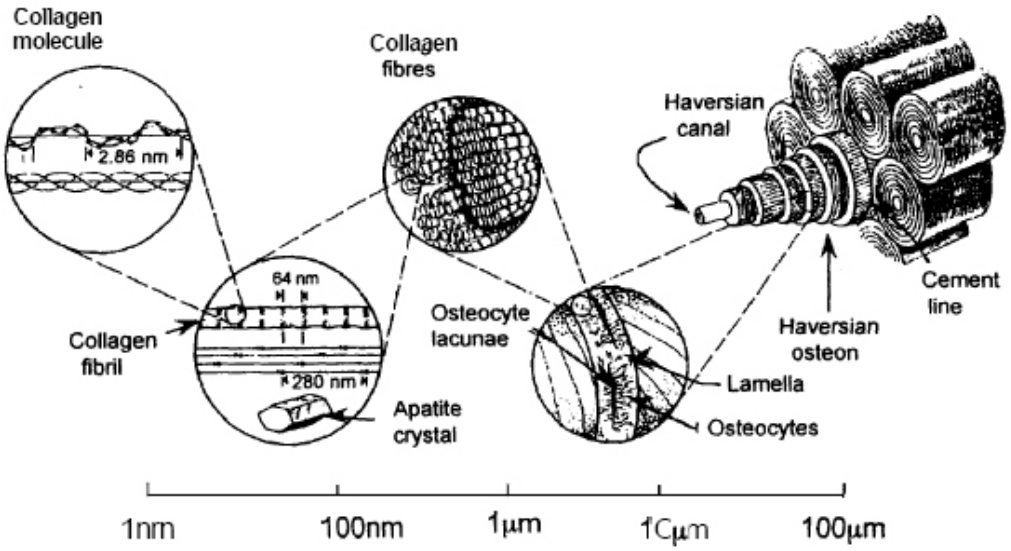

Figure 1.5. Hierarchical structure of bone.

In Fig. 1.5 the hierarchical structure of bone is illustrated, starting from the lowest level, where nanometer-sized crystals of carbonate apatite are embedded in and surround the fibrous protein collagen. At the second lowest level, these mineralized fibres lie bundled together and are attached to each other. At the next level, these fibres come together to

form lamellae at a width of ~2 μm. The lamellae have various patterns; a very common one is a secondary osteon, in which concentric lamellae form cylindrical structures, ~200 μm in diameter, surrounding a central blood vessel. Compact bone, solid to the naked eye, is modified in places to form trabecular bone, which consists of many struts; with the spaces between the struts filled with marrow. As above stated, the struts are not just randomly arranged, but are related to the direction of mechanical loads on the bone. Mechanical and biological properties of the bone depend on the interaction taking place across all levels of organization. A deeper discussion on hierarchy in bone tissue and on the activity devoted to reproduce it by taking advantage of the hierarchic natural structure of woods and plants will be provided in Chapter 5.

1.2.2 Mechanical properties of bone

The different structures of cortical bone and trabecular bone result in different mechanical properties. Bone mechanical properties are highly variable according to species, age, anatomical site, liquid content, etc.

Cortical bone is an *anisotropic* material, meaning that its mechanical properties vary according to the direction of load.

Cortical bone is often considered an *orthotropic* material. Orthotropic materials are a class of anisotropic materials characterized by three different Young's moduli E_1, E_2, E_3 according to the direction of load, three shear moduli G_{12}, G_{13}, G_{23} and six Poisson's ratios ν_{12}, ν_{13}, ν_{23}, ν_{21}, ν_{31}, ν_{32}.

The mechanical characterization of trabecular bone is even more difficult. The mechanical properties of trabecular bone as a whole are due to the mechanical characteristics of single trabecules and to its highly porous structure. Fig. 1.6 shows the dependence of the Young's modulus of trabecular bone from bone density.

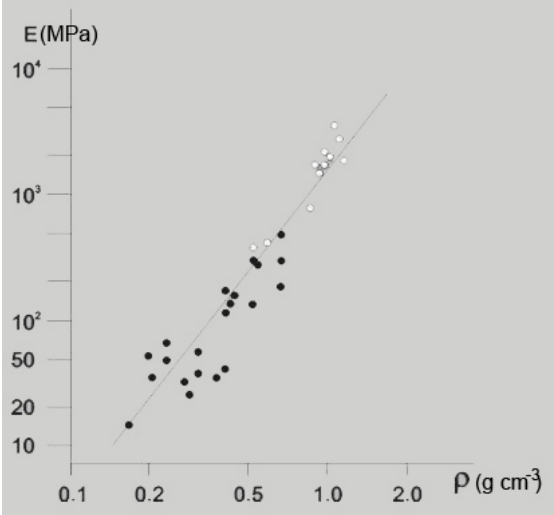

Figure 1.6. Young's modulus of trabecular bone as a function of density of bone.

1.2.3 Types of bone

Bone characterized by different functions in the body are strongly different in shape, so that they exhibit different structures hierarchically organized and, correspondingly, different mechanical properties. Several examples are shown in Fig. 1.7: long bones are found in our extremities (femur, tibia, ulna, radius, humerus, etc..) and provide stability against bending and buckling; they are characterized by a tubular shaft and articular surface at each end. Short bones, which include vertebrae, the head of femur, all of the metacarpals and phalanges in the hands, the metatarsals and phalanges in the feet, and the clavicle (collarbone), provide stability against compression (along the vertical axis, in the case of vertebra). They also have a tubular shaft and articular surfaces but smaller than long bones. Plate-like bones (such as the skull, the scapula, the ribs, and the sternum) are thin and have broad surfaces; their main function is to protect vital organs. Irregular bones are also found in the body; they are irregular in size and shape and are usually quite compact. They include the bones in the vertebral column, the carpal bones in the hands, tarsal bones in the feet, and the patella (kneecap).

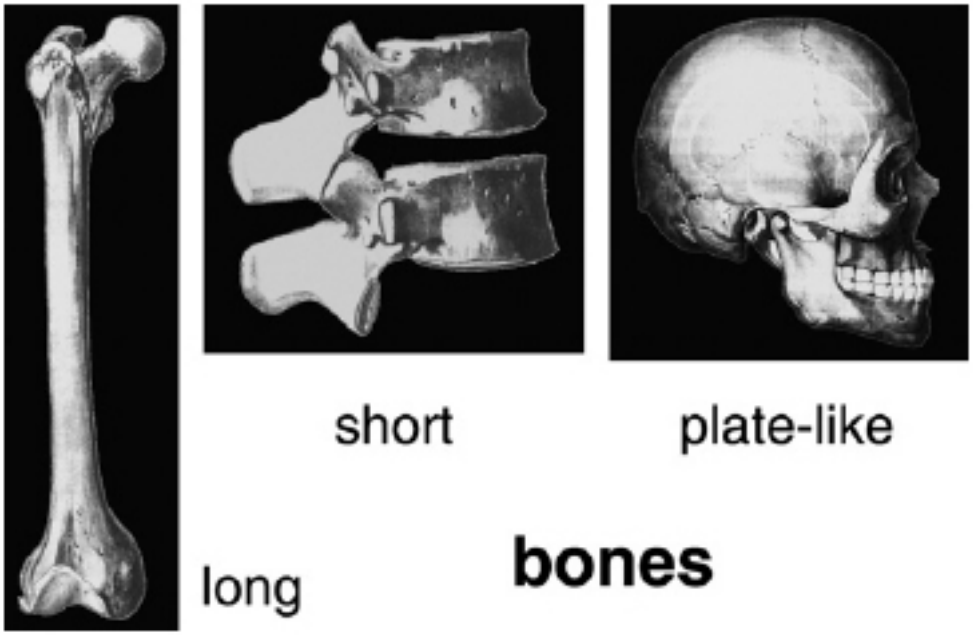

Figure 1.7. Different types of bone.

1.3 Bone remodelling

Bone adapts and remodels in response to the stress applied. Wolff's law[1] states that bones develop a structure most suited to resist the forces acting upon them, adapting both the internal architecture and the external conformation to the change in external loading conditions. This change follows precise mathematical laws.

When a change in loading pattern occurs stress and strain fields in the bone change accordingly. Bone tissue seems to be able to detect the change in strain on a local bases and then adapts accordingly. The internal architecture is adapted in terms of change in density and in disposition of trabecules and osteons and the external conformation in terms of shape and dimensions. When strain is intensified new bone is formed. On a microscopic scale bone density is raised and on a macroscopic scale the bone external dimensions are incremented. When strain is lowered bone resorption takes place. On a microscopic scale bone density is lowered and on a macroscopic scale the bone external dimensions are reduced (Fig. 1.8).

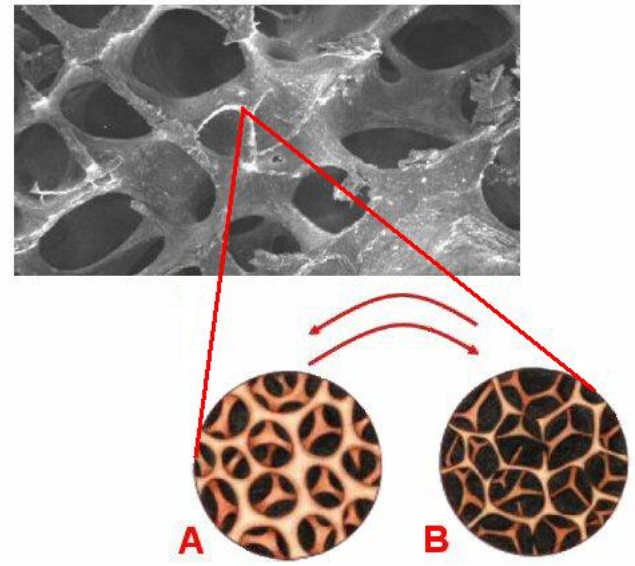

Figure 1.8. Bone remodelling: effect of reduction (from A to B) and of intensification of strain (from B to A) on bone trabecules.

When the change in strain is due to a change in direction of load on a microscopic scale the structure of trabecules and osteons is rearranged and on a macroscopic scale a change in bone shape may occur.

Remodelling is carried out by the cellular component of bone. When resorption takes place osteoclasts reabsorb collagen and mineral phase (Fig. 1.9A) which are then taken into the circulatory system (Fig. 1.9B). During deposition osteoblasts group on the deposition surface and build the collagen network of bone (Fig. 1.10A). Mineralization takes place afterwards (Fig. 1.10B).

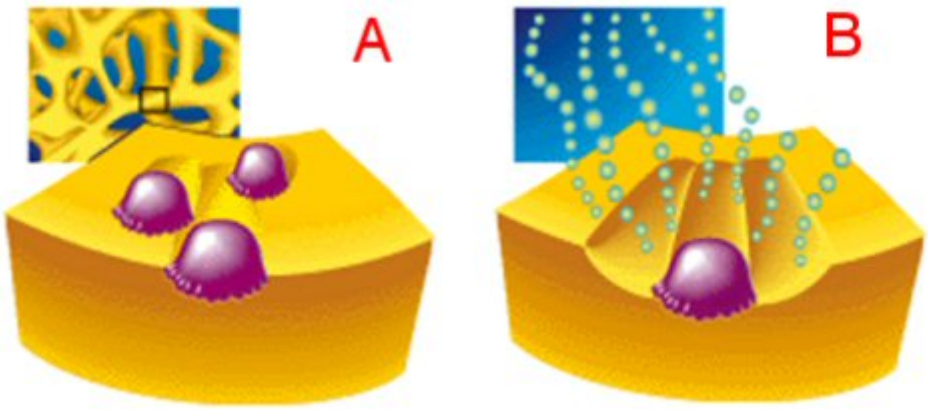

Figure 1.9. Bone resorption.

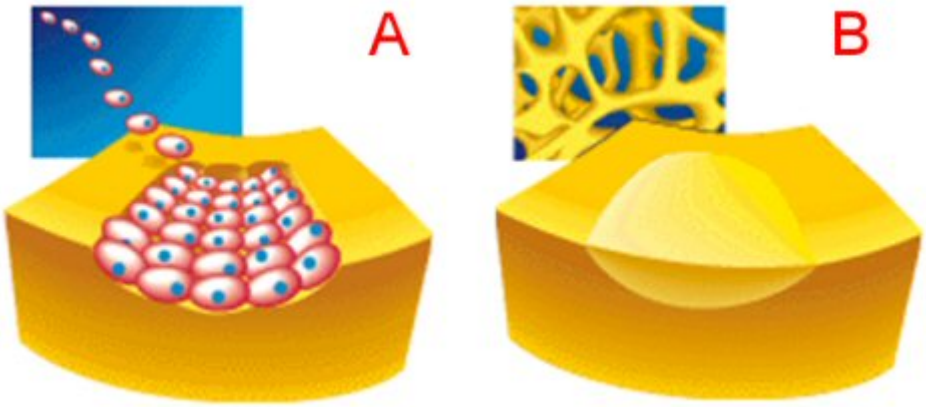

Figure 1.10. Bone deposition.

Bone resorption and bone deposition processes are always active in bone. An equilibrium strain state exists in correspondence to which the two activities are perfectly balanced. When strain intensity is higher than the equilibrium strain deposition activity is more intense than resorption activity and net deposition occurs. When strain intensity is lower than the equilibrium strain deposition activity is less intense than resorption activity and net resorption occurs. Dynamical equilibrium between resorption and deposition is again achieved when the equilibrium strain state is newly established.

The cell-biology based model of Davy and Hart expresses functional dependence of bone remodelling on the strain field, based on cell activity (Fig. 1.11). The load applied to the bone together with geometric and material properties determine the local strain. Strain is detected by a transducer which generates the strain remodelling potential (SRP). This signal is modulated by genetic, hormonal and metabolic factors, generating the remodelling potential which regulates the recruitment rate and the activity of osteoblasts and osteoclasts, stimulating bone formation and bone resorption. The balance between bone deposition and bone resorption determines the net bone remodelling. remodelling modifies bone geometric and material properties through a feedback loop.

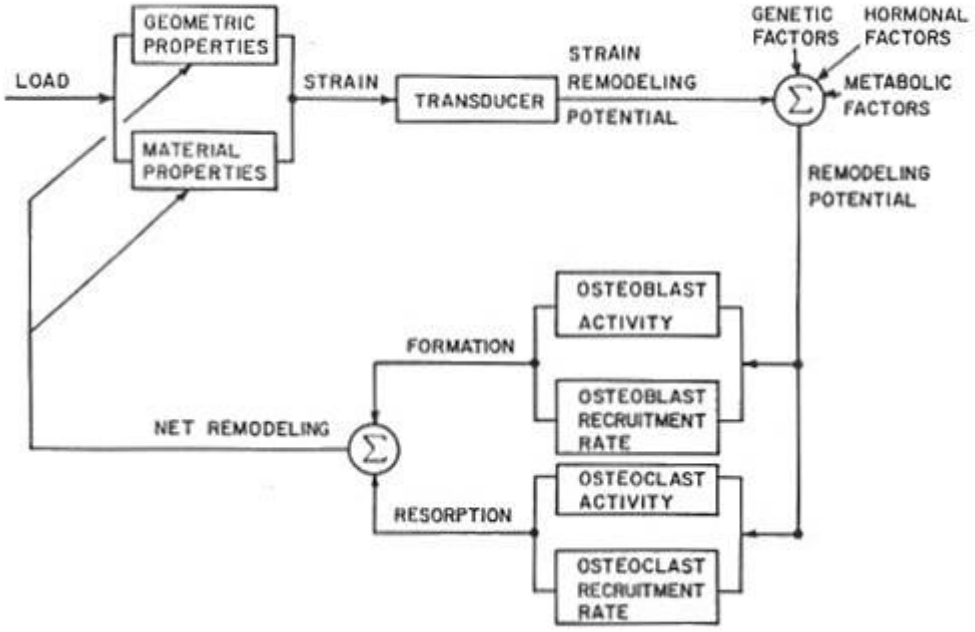

Figure 1.11. Schematic diagram of the Davy and Hart model for bone remodelling.

1.4 Need of the development of bone substitutes

Bone disease is a serious health condition that directly impacts on the quality of life of sufferers, particularly among the aged. In most cases, the treatment of bone defects requires a bone graft, and sometimes in extensive amount[2-7].

Nowadays, more than 2 million bone grafting procedures are happening annually worldwide, with a turn-over of the order of billions of dollars per annum, in order to repair bone defects in orthopaedics, neurosurgery and dentistry[8-9], which include the treatment of posttraumatic skeletal complications, such as delayed unions, non-unions, mal-unions[10]. Bone grafting may be also required for the healing of spinal fusions, filling defects following removal of bone tumours and several congenital diseases.

A major contributor to the need for "spare parts" for the body is the progressive deterioration of tissue with age. Bone is especially vulnerable to fracture in older people because of a loss of bone density and strength with age. Fig. 1.12 summarizes the effect of time on bone strength and density from the age of 30 years onward.

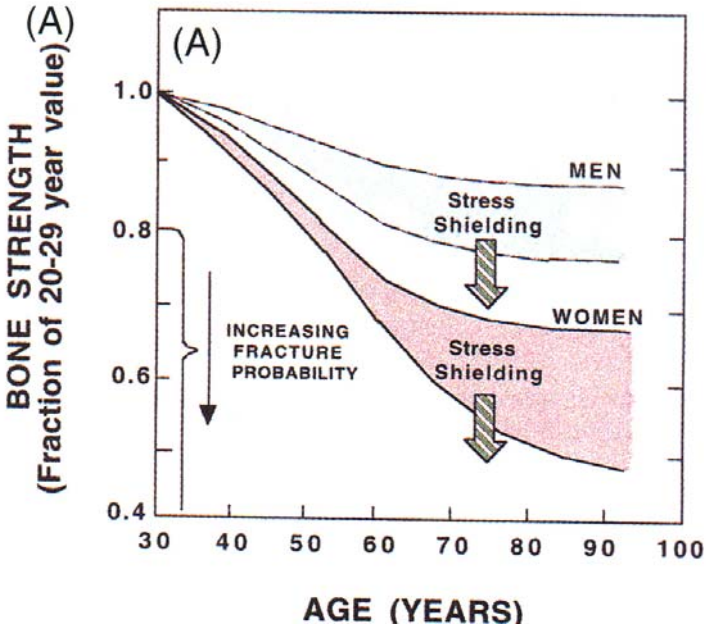

Figure 1.12. Effect of age on strength and density of bone.

The effect is especially severe in women because of hormonal changes associated with menopause. Bone density decreases because bone-growing cells (osteoblasts) become progressively less productive in making new bone and repairing micro-fractures. The lower density greatly deteriorates the strength of the cancellous bone, in the ends of long bones and in vertebrae. An unfortunate consequence is that many old people fracture their hips or have collapsed vertebrae and spinal problems.

In addition, bone composition and properties can vary considerably within a population and are difficult to control. Thus remodelling of the implant can be very different from one person to another and from one implant to another.

The replacement of a bone or a part of must be distinguished from organ grafts (e.g. kidney, heart). In organ grafts, the cells are generally kept alive and the reestablishment of blood supply restores the functions of the whole organ. In bone tissues, however, the blood supply cannot be efficiently restored and the tissue is condemned to die, be reabsorbed, and replaced. In most cases the replacement of bone fragments by foreign bone tissue leads to poor junction, rehabitation, and remodelling problems.

As the average age of the population increases and the patients receiving such implants become younger, the above-mentioned numbers are likely to increase. For these reasons, the field of biomedical materials has grown rapidly over the past 40 years, offering

solutions to repair defects, correct deformities, replace damaged tissue and provide therapy, with a continuously increasing market value. This has contributed to the increase in the average lifetime of individuals in developed countries.

Although current biomaterials provide an effective immediate solution for many patients, concerns have arisen over their short- and long-term clinical success. In the short-term concerns have arisen due to the low bio-reactivity with existing bone. Such properties have highlighted clinical implications for the time required for patient rehabilitation[11]. In longer-term studies, biomaterials degrade with time and this may have adverse effects on interfacial apposition to the implant and its mechanical stability[12-14]. Moreover, it is reported that nearly 20% of the hip replacement surgeries performed in past years were to ‘‘revise’’ the original implants. As a consequence, considerable research interest has focused on investigating mechanisms that contribute to implant-prosthesis failure and on developing new biomaterials with extended lifetimes. One novel design approach towards improved implant performance has involved the use of biomimetic approaches, whereby nano- and micro-scale features and/or chemistry of the implant may be designed to mimic those of living bone tissue.

1.4.1 Current solutions for bone substitutes

Since a very ancient time, diseased bone portions were substituted with parts in metal; in the last century ceramic bodies substituted metal more and more, owing to the problems related to the metal dissolution in the human body and the release of toxic debris. Then, the substitution of bone intended mainly to restore the structural functionality of the missing part, but it was not able to completely restore all its properties; the very complex composition and morphology of the bone tissue are responsible of its unique ability to continuously adapt to the ever changing mechanical solicitations, so to be simultaneously light, tough and elastic and able to locally regenerate after traumas of limited extension.

Thus, with the increasing of the expectance of life and well-being, the development of bone substitutes able to restore the whole functionality of the original tissue was of increasing importance in the last decades; beyond the commercial aspects, the problem has a highly social relevance as the patients can regain a more active and satisfactory life and sooner than in the past.

An ideal bone substitute should be **biomimetic**, i.e. able to perfectly mimic *in vivo* the behaviour of the natural bone. For this reason, not only biocompatibility is required, but

features of bioactivity, osteoinductivity, osteoconductivity and bio-resorbability are also strongly needed.

Biocompatibility is the ability of a material to perform with an appropriate host response in a specific application, without having any toxic or injurious effects on biological systems[15].

The scope of this definition is very wide and many subgroups of applications can be found to make more narrow definitions of biocompatibility. Anyway, for a long-term implantable medical device, like a bone substitute, the biocompatibility refers to the ability of the device to perform its intended function, with the desired degree of incorporation in the host, without eliciting any undesirable local or systemic effects in that host.

Bioactivity is the ability of the implant to bond to bone tissue. The process of bone bonding is the result of multiple, parallel and sequential reactions at the material-tissue interface. These interactions are related to either physicochemical phenomena that occur in the presence or absence of cells, or are related to reactions affected by cellular activity. The events occurring at the bone-implant interface can be summarized as follows:

(1) dissolution from the ceramic[16,17]; (2) precipitation from solution onto the ceramic[18,20]; (3) ion exchange and structural rearrangement at the ceramic-tissue interface[16,18,19,21,22]; (4) inter-diffusion from the surface boundary layer into the ceramic[23]; (5) solution-mediated effects on cellular activity[21,24,25]; (6) deposition of either the mineral phase (a), or the organic phase (b), without integration into the ceramic surface[18,19,22]; (7) deposition with integration into the ceramic[19,21]; (8) chemotaxis to the ceramic surface[21]; (9) cell attachment and proliferation[24-27]; (10) cell differentiation[21]; and (11) extracellular matrix formation[27,28].

Osteoinductivity is the ability of a material to induce cell differentiation oriented to the synthesis of a bone matrix, able to mineralize in bone tissue.

Osteoconductivity is a passive property of the implant consisting in the ability of making easy the formation and diffusion of the new bone both through its chemical (presence of ions and substances able to enhance the cell activity for **osteogenesis**, the process of new bone development) and morphological (hierarchically organized porous structure able to host the growing bone tissue and the vascular system) features.

Bioresorbability is the ability of the implant to be dissolved by the *in vivo* processes of bone remodelling and to be replaced by the new bone tissue.

When the characteristics of bioactivity, osteoinductivity and osteoconductivity are merged together, the implant is rapidly integrated into the growing bone tissue (**osteointegration)** and a direct structural and functional connection between ordered living bone and the implant surface is so established[29].

Several methods of reconstructing bone defects are available namely using autograft, allograft, demineralised bone matrix (DBM), calcium phosphate (in particular hydroxyapatite and tricalcium phosphate), autologous bone marrow aspirates, bone morphogenetic proteins, and several other related growth factors (VEGF, PDGF, etc.).

The gold standard of bone-grafting is harvesting autologous cortical and cancellous bone (**autograft**), which provides optimal osteoinductive, osteoconductive, and osteogenic properties[30]. Iliac crest is the most frequently chosen donor site as it provides easy access to good quality and quantity cancellous autograft. Harvesting autologous bone from the iliac crest has, however, several downsides as it lengthens the overall surgical procedure and is usually complicated by residual pain and cosmetic disadvantages[31,32].

Furthermore, it may fail in clinical practice as most of the cellular (osteogenic) elements do not survive transplant[33]. Other limitations include elderly or paediatric patients and patients with malignant disease[34]. In addition autograft harvesting is associated with a 8.5-20% of complications including haematoma formation, blood loss, nerve injury, hernia formation, infection, arterial injury, urethral injury, fracture, pelvic instability, cosmetic defects, tumour transplantation, and sometimes chronic pain at the donor site[31,35]. Another disadvantage is the elevated levels of resorption during healing[36].

Allograft and **xenografts**, depending whether the bone portion is explanted by other humans or animals, are regarded as the surgeon's second option. Its use has increased 15-fold the past decade and accounts for about one-third of bone grafts performed in the United States[37]. The current increasing availability of allograft tissue has made it possible to manufacture customised types, such as dowels, strips, and chips[33]. Allograft bone has more limitations in the essential bone graft characteristics described earlier and yields more variable clinical results. In addition, allografts carry the risk of transferring viral diseases. The processing of allograft tissue lowers this risk but, that can significantly weaken the biologic and mechanical properties initially present in the bone tissue[38,39]. An overview of the properties of allograft and autograft bone is summarized in Table 1.I.

Table 1.I. General properties of different bone grafts.

Bone graft	Strength	Osteoconduction	Osteoinduction	Osteogenesis
Autograft				
Cancellous	---	+++	+++	+++
Cortical	+++	++	++	++
Allograft				
Cancellous				
Frozen	---	++	+	---
Freeze-Dry	---	++	+	---
Cortical				
Frozen	+++	+	---	---
Freeze-Dry	+	+	---	---

1.4.2 Synthetic bone substitutes

Considerable interest has developed in creating osteoconductive matrices using non-biologic materials. Synthetic products have the advantage to offer controlled composition and properties that can be modified and tailored on the characteristics of the specific patient and optimized for the replacement of specific portions of bone. They can be easily stored, shaped, and sterilized, and do not need the heavy organization of bone organ banks[40].

Degradable polymers, bioactive glasses, and various metals have been studied. Polylactic and Polyglycolic acid polymers have been used extensively as suture materials, and biodegradable fracture fixation implants. These materials have the advantage of being assembled in various forms and can be integrated with growth factors, drugs, and other compounds to create multiphase delivery systems. They provide a porous architecture for the ingrowth of new bone and then fully degrade.

A variety of porous metal surfaces and coatings have been used as surfaces for bone ingrowth intended to fix prosthetic joint replacement components to bone. These include sintered cobalt-chrome beads, titanium alloy fibre metals, and plasma-sprayed surfaces. New metallurgy techniques are creating metallic matrices of much greater porosity. Tantalum can be fabricated as metallic foam-like structure with interconnecting pores, which allows exceptionally rapid and complete ingrowth. Hydroxyapatite coating of metal surfaces enhances ingrowth and direct bonding of bone to porous surface[41].

Essentially, these coatings can be used on implants with relatively simple surface geometry and use excessive high temperatures. This means that it is difficult to coat implants with complex surface geometry (e.g. porous surface) and that no biologically active agents can be added to the coating during the spraying process.

1.4.3 Bioceramics

Since half century, specially designed ceramic materials, called bioceramics, were adopted for the repair, reconstruction, and replacement of diseased and damaged parts of the body, usually the hard tissues of the musculo-skeletal system, such as bones, joints, or teeth[6] (see Table 1.II).

The great challenge facing the use of ceramics in the body is to replace old, deteriorating bone with a material that can function the remaining years of the patients' life (> 20 years). This demanding requirement of survivability is under conditions of use that are especially harsh to ceramic materials: corrosive saline solutions at 37 °C under variable, multiaxial, cyclical mechanical loads.

Table 1.II. Present uses of bioceramics.

Application	Material
Orthopaedic load-bearing applications	Al_2O_3
Coatings for chemical bonding (orthopaedic, dental and maxillary prosthetics)	HA, surface-active glasses and glass-ceramics
Dental implants	Al_2O_3, HA, surface-active glasses
Alveolar ridge augmentations	Al_2O_3, HA, HA-autogenous bone composite, H-PLA composite, surface-active glasses
Otolaryngological applications	Al_2O_3, HA, glasses and glass-ceramics
Artificial tendons and ligaments	PLA-carbon fiber composites
Coatings for tissue ingrowth (cardiovascular, orthopaedic, dental, and maxillofacial prosthetics)	Al_2O_3
Temporary bone space fillers	Trisodium phosphate, calcium and phosphate salts
Periodontal pocket obliteration	HA, HA-PLA composites, trisodium phosphates, calcium and phosphate salts, glasses
Maxillofacial reconstruction	Al_2O_3, HA, HA-PLA composites, glasses
Percutaneous access devices	Bioactive glass-ceramics
Orthopaedic fixation devices	PLA-carbon fiber, PLA-CaP-base glass fibers

Survivability of a bioceramic requires formation of a stable interface with living host tissue. The mechanism of tissue attachment is directly related to the type of tissue response at the implant interface (Table 1.III). No material implanted in living tissues is inert; all materials elicit a response from living tissue. The four types of response allow different

means of achieving attachment of prostheses to the musculo-skeletal system and can be summarized as follows:

If the material is toxic, the surrounding tissue dies
If the material is non-toxic and biologically inactive (almost **inert**), a fibrous tissue of variable thickness forms.
If the material is non-toxic and biologically active (**bioactive**), an interfacial bond forms.
If the material is non-toxic and dissolves, the surrounding tissue replaces it (**bioresorbable**).

Table 1.III. Classification of Bioceramics on the basis of tissue attachment.

Type of attachment	Example
• Dense, non porous, nearly inert ceramics attached by bone growth into surface irregularities by cementing the device into the tissues, or by press fitting into a defect (termed morphological fixation).	• Al_2O_3, Alumina (single crystal and polycrystalline)
• For porous inert implants bone ingrowth occurs, which mechanically attaches the bone to the material (termed biological fixation).	• Porous polycrystalline Al_2O_3 • Hydroxyapatite-coated porous metals.
• Dense, non porous, surface-reactive ceramics, glasses, and glass-ceramics attach directly by chemical bonding with the bone (termed bioactive fixation).	• Bioactive glasses • Bioactive glass-ceramics • Hydroxyapatite
• Dense, non porous or porous resorbable ceramics are designed to be slowly replaced by bone.	• Calcium sulfate (plaster of Paris) • Tricalcium phosphate • Calcium phosphate salts

The reactivity of the surrounding bone tissue to the implant is closely correlated with the rate of formation of an interfacial bond of implants with bone. The relative level of reactivity influences the thickness of the interfacial zone of layer between the material and tissue. The failure of implant materials generally originates from the biomaterial-tissue interface. When biomaterials are almost inert and the interface is not chemically or biologically bonded, there is relative movement, and progressive development of a non-adherent fibrous capsule. Movement at the biomaterial-tissue interface eventually leads to deterioration in function of the implant or of the tissue at the interface or of both. The thickness of the non-adherent capsule varies greatly, depending upon both the material and the extent of the relative motion. It is crucial that inert implants are implanted with a very tight mechanical fit so to maintain a little value of the fibrous tissue thickness, otherwise it can become several hundred micrometers thick, leading to the loosening of the implant and

clinical failure, with fracture of the implant or of the bone adjacent to it. Moreover, the bone at interface with an inert material is very often structurally weak, because of disease, localized death of bone or stress shielding, due to the higher elastic modulus of the implant which prevents the bone from being loaded properly.

Fig. 1,13 shows a comparison of the different chemical activities of different ceramic-based biomaterials.

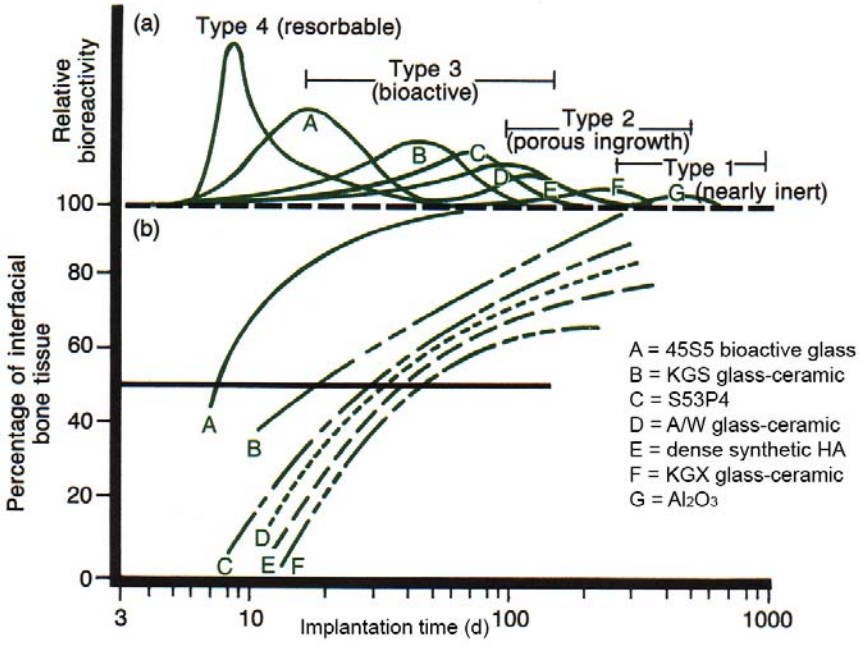

Figure 1.13. Comparison of the different chemical activities of different ceramic-based biomaterials.

1.5 Calcium phosphates in biologic systems

The wide application in the last decades of calcium phosphates as biomaterials is mainly due to the biological properties of these materials, whose composition is very close to the one of bone mineral, which represents about 70% of the mass of dry bone tissue[6,7,42]. The first study dates back to the 1920, reporting an accelerated bone healing in surgically created defects in rabbits[43]. Anyway, specific interest in calcium phosphates for biomedical applications, and specifically in apatites, raised up in the 1960s and initial studies principally involved the synthesis and analysis of hydroxylapatites in an attempt to better

understand the physico-chemical and biological behaviour of natural apatites, which constitute the mineral part of human bones and teeth[42,44,45].

Following these studies, calcium phosphate-based bioceramics have been in use in medicine and dentistry for the last 40 years. Different phases of calcium phosphate ceramics are selected depending upon whether a resorbable or bioactive material is desired. These materials constituted a wide variety of biomaterials like coatings of metal orthopaedic (hip and knee joints) and dental implants (Fig. 1.14), cements, injectable cements, composite materials, and drug carriers (antibiotics, anticancerous drugs, growth factors), three-dimensional dense and porous scaffolds for bone reconstruction or replacement, applied especially in small bones and middle ear bones, powder granulates for the repair of bone defect in maxillofacial surgery, alveolar ridge augmentation, otolaryngology.

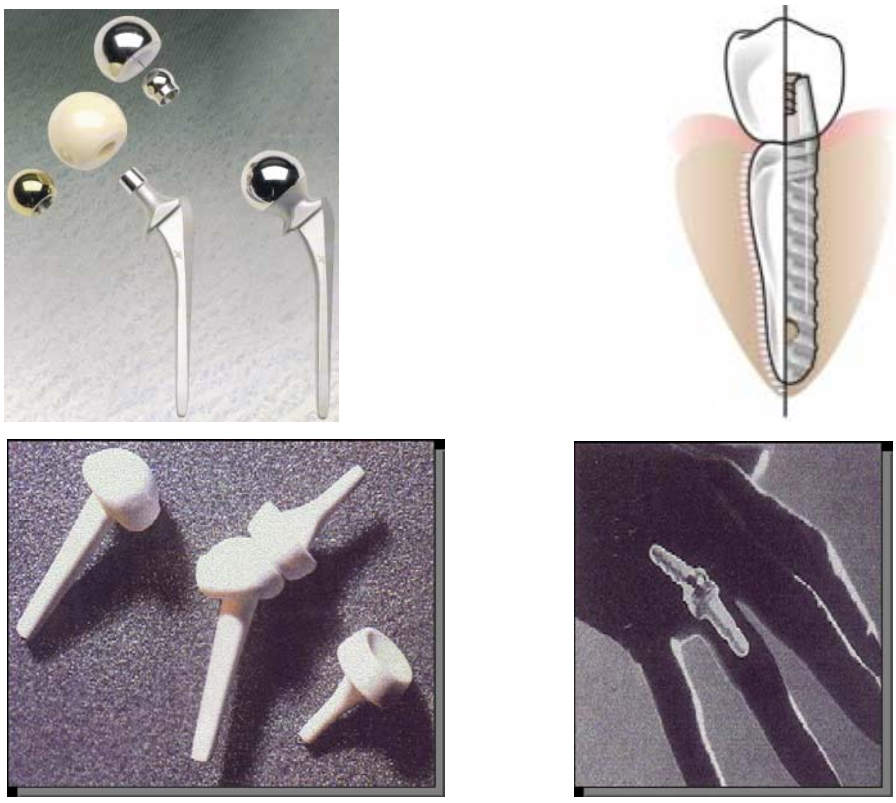

Figure 1.14. Examples of bioceramic implants for different applications.

The stable phases of calcium phosphate ceramics depend considerably upon temperature and the presence of water, either during processing or in the use environment. At body temperature, only two calcium phosphates are stable in contact with aqueous media, such as body fluids: at pH < 4.2, the stable phase is $CaHPO_4 \cdot 2H_2O$ (dicalcium phosphate,

brushite, DCPD), whereas, at pH > 4.2, the stable phase is $Ca_{10}(PO_4)_6(OH)_2$ (Hydroxyapatite, HA). At higher temperatures, other phases, such as $Ca_3(PO_4)_2$ (β-tricalcium phosphate, TCP), and $Ca_4(PO_4)_2O$ (tetracalcium phosphate, TeCP) are present. The unhydrated, high temperature calcium phosphate phases interact with water, or body fluids, at 37 °C to form HA. Thus, the solubility of a TCP surface approaches the solubility of HA and decreases the pH of the solution, which further increases the solubility of TCP and enhances resorption.

Other calcium phosphates have been identified with or without association with apatite; they include: $Ca_8H_2(PO_4)_6{\cdot}5H_2O$ (octacalcium phosphate, OCP); $Ca_2P_2O_7$ (calcium pyrophosphate dehydrate in mono- and triclinic forms, CPP); amorphous calcium phosphate, ACP.

Apatites in normal calcified tissues of teeth and bone have been postulated to form either directly or indirectly by way of precursor calcium phosphates such as ACP, DCPD, OCP or TCP. The general occurrence and co-existence of phosphate minerals in human tissues are summarized in Table 1.IV.

Table 1.IV. Phosphate minerals present in human tissues.

Phosphate minerals	Chemical formula	Occurrences
Apatite or "apatitic" calcium phosphates	$(Ca, NA, Z)_{10}$ $(PO_4, CO_3, Y)_6$ $(OH, X)_2$	Enamel, dentine, bone
Whitlockite, β-TCP	$(Ca, Mg)_9(PO_4)_6$	Salivary stones, dental calculi, tubercular deposits, pulmonary calcifications, calcified cartilage
Octacalcium phosphate	$Ca_8H_2(PO_4)_6{\cdot}5H_2O$	Dental and urinary calculi
Brushite, DCPD, calcium phosphate dehydrate	$CaHPO_4{\cdot}2H_2O$	Dental calculi, concretions in old bones, chondrocalcinosis
Calcium pyrophosphate dehydrate, CPPD, mono and triclinic	$Ca_2P_2O_7{\cdot}2H_2O$	Pseudo-gout deposits, in synovium fluid
Amorphous calcium phosphate (containing Mg^2 and/or $P_2O_7^{4-}$)	Variable composition	Non-visceral calcifications associated with uremia; aortic valves

1.5.1 Calcium phosphate dehydrate, Brushite (DCPD)

The formation of DCPD *in vivo* is observed in dental calculi and in other pathological calcifications. It can forms either by direct precipitation or by dissolution of apatite and reprecipitation of the more stable DCPD crystals under acid conditions. The

presence of trace elements (e.g., F^-, $P_2O_7^{4-}$, Sr^{2+} and Mg^{2+}) is associated with different morphologies of DCPD crystals. DCPD can co-exist with other calcium phosphates, like OCP and apatite, depending on pH.

1.5.2 Tricalcium phosphate (TCP)

Tricalcium phosphate exists under two crystallographic forms: β and α-TCP. The α-form is unstable at low temperature and is obtained by quenching the β-form heated above 1125 °C (transition temperature). The β-form may however be stabilized by several ionic impurities, such as Mg^{2+} ions, frequently associated with Ca salts. α-tricalcium phosphate is more soluble and more reactive than β-TCP, and it can be rapidly hydrolyzed into apatite in aqueous media. Both varieties can be used in Ca-P cement preparations.

The β-form makes an excellent resorbable biomaterial. However, it is not found in biological systems and it cannot be obtained by precipitation.

Biological TCP is always partially magnesium-substituted, giving rise to whitlockite $(Ca, Mg)_9 (PO_4, HPO_4)_6$. It is not detected as constituents of normal tissue calcifications but their presence in several pathological tissue calcifications, in abnormally calcified cartilage and in human dental carious lesions has been reported[46,47].

β-TCP is more soluble than apatite and can be hydrolyzed into apatitic phases; whitlockite on the contrary seems less soluble and has never been shown to convert into apatite[48]. The presence of Mg in β-TCP is thus an important parameter affecting its biological properties, especially its ability to be resorbed.

β-TCP can be obtained by thermal decomposition of a non-stoichiometric apatite with a Ca/P ratio of 1.5 or by solid state reaction at high temperatures (900 °C). The industrial product may sometimes be blended precipitated powders with a correct overall composition but grain heterogeneity. Prolonged heating at 1000 °C is generally sufficient to insure homogenization of the chemical composition.

Although the presence of other trace ions (Mn^{2+}, Fe^{2+}, Co^{2+}, Ni^{2+}) also promotes the formation of β-TCP at the expense of apatite[49], the influence of Mg^{2+} ion is the most significant, so that the Mg/Ca ratio in biological and synthetic systems is the major determining factor in the formation of the whitlockite phase at the expense of apatite[46,50]. However, in presence of CO_3^{2-} or F^- ions, the effect of Mg^{2+} presence is reduced and the formation of apatite phase is favoured.

In order to control the resorbability of Ca-P ceramics, mixtures of β-TCP and HA have been proposed[51,52], showing that the ratio of β-TCP/HA in the final product is related to the resorption rate, *in vivo*. Such mixtures can be obtained either by blending pure powders, or more simply by heating a non-stoichiometric apatite with an adequate Ca/P ratio.

1.5.3 Amorphous Calcium Phosphates (ACP)

Amorphous calcium phosphates is believed to be a constituent of bone mineral[53-55]. The ACP in bone is believed to transform to apatite, thus acting as a transitory precursor of biological apatites just as they are supposed to be in some synthetic preparations[53-56].
Amorphous Ca-P may play an important role in the future because of their high reactivity. Several ways of formation exist: precipitation in highly supersaturated solutions, from alkaline to neutral pH, quenching of fused Ca-P compounds, and non-aqueous precipitations. They may exhibit very different Ca/P ratios, from 1 to 2 or more. All are easily hydrolyzed into apatitic compounds. Amorphous Ca-P begins, generally, to crystallize around 600 °C. Despite different composition, they all appear to be structurally related, independent of the preparation method.
In synthetic systems, the presence of carbonate or magnesium or pyrophosphate promotes the formation of ACP[42]; the simultaneous presence of two or more of these ions are even more effective in promoting the formation of ACP.
The comparative efficiency in promoting the formation of ACP parallels the efficiency in stabilizing the amorphous phase:
$[Mg^{2+} + P_2O_7^{4-}] >> [P_2O_7^{4-}] >> [Mg^{2+} + CO_3^{2-}] >> [Mg^{2+}] >> [CO_3^{2-}]$.
Then, the stability of ACP in human pathological tissue calcifications can be attributed to their magnesium and/or pyrophosphate contents.

1.6 Bioactivity of calcium phosphates

Synthetic bioactive Ca-P materials are not in equilibrium with biological fluids. Thus, several reactions occur on the mineral surface[7]. For apatites, very first reaction is the hydrolysis of the surface PO_4^{3-} groups into HPO_4^{2-} and the uptake of carbonate and sodium ions. Generally the hydrolysis of surface phosphate groups is associated with a decrease of the calcium concentration at the surface[57]. These reactions correspond simply to exchanges between the solution and the first atomic layers of the apatite surface. The extent of these

reactions may vary according to the composition of the mineral and how it was produced. Inflammatory cells in close proximity to the material, may also create an acidic environment. Poorly crystalline apatites with many defects are particularly sensitive to these changes.

As biological fluids are generally supersaturated with respect to apatite, the Ca-P materials also serve as a template for the formation of carbonate-apatite crystals. This event has been shown to be the major factor behind the osteoconductivity of all biomaterials and has been evidenced in different classes of bioactive orthopaedic implants (polymers and bioactive glasses). The crystals formed are very much like bone mineral crystals. They are carbonated apatites and exhibit non-apatitic environments.

The precipitation of the neo-formed crystals can also be boosted by release of calcium, phosphate ions or rise in the pH that may locally increase the supersaturation ratio in the vicinity of the implant surface. This phenomenon can be favoured by hydrolysis reactions of the material constituents. Enlarging the surface area is another way to increase the amount of reactive, neo-formed crystals.

The ability of a biomaterial to generate this layer has been considered as a measure of its biological activity, although such a relationship has not yet been established on a quantitative basis. Despite the analogy of the crystals formed with bone mineral crystals, the processes of formation and organization appear to be rather different. Bone mineral crystals are always formed in an organic collagen matrix with which they are closely associated. Although the layer formed on bioactive biomaterials frequently incorporates bone proteins, there is no organization like that of bone. It appears more like an uncontrolled mineralization.

The functions of the neo-formed layer have not yet been clearly established. This layer creates a very reactive surface with a high specific surface area, which is able to attach bone specific proteins, especially osteopontin and osteocalcin[58]. The neo-formed layer appears, as a support, and the adsorption of proteins to it is necessary to accommodate osteoblast cell attachment and favour their multiplication. Although such proteins might bind directly to the HA surface, the adsorption affinity could be quite different depending on the apatitic substrate. Thus, synthetic apatites rich in labile non-apatitic environments exhibit a high surface reactivity and have a higher affinity for some proteins than stoichiometric HA. Depending on the apatitic substrate and the rate of formation of the

layer, the presence of labile non-apatitic environments and the reactivity of the neo-formed layer may vary.

1.7 Apatites

1.7.1 Hydroxyapatite: structure and chemistry

Apatites are an industrially important group of materials with applications in catalysis, environmental remediation, bone replacement and ceramic membranes amongst others, and constitute a large class of materials with general formula[59] $[M(1)_2][M(2)_3](XO4)_3X$, where:

M represents a bivalent cation;

XO_4 represents a trivalent anion;

Z represents a monovalent anion.

Among all the apatites, calcium hydroxyapatite is the most relevant in biological systems, as it is the major component of bones and teeth; its formula is defined as: $Ca_5(PO_4)_3OH$ or, more often, $Ca_{10}(PO_4)_6(OH)_2$.

M/X ratio commonly defines the stoichiometry of an apatite, in case of HA it corresponds to Ca/P = 1.667.

In ideal HA, calcium, phosphorus and hydroxyl ion are present in the following weight percentage: Ca = 39.84 %; PO_4 = 56.77 %; OH=3.39 %.

The apatite prototype $Ca_5(PO_4)_3F$ structure was first determined by Naray-Szabo in 1930[60] and was confirmed to adopt $P6_3/m$ symmetry (Fig. 1.15).

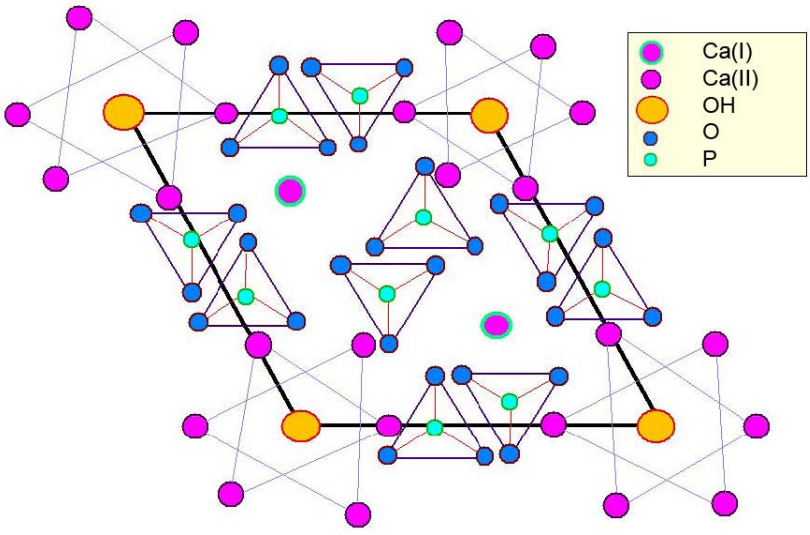

Figure 1.15. Crystal structure of Hydroxyapatite.

The 10 Ca^{2+} ions occupy two crystallographically different symmetry sites, 4f and 6h. Four Ca^{2+} ions (4f) are located in columns along the three-fold axes at 1/3, 2/3, 0 and 2/3, 1/3, 0 separated by approximately one half of the c -axis. These are commonly referred to as Ca1 (or column Ca). Ca1 is coordinated to nine O atoms, with six shorter bonds that define an approximate trigonal prism and three longer bonds capping the prism faces. The Ca-O_9 polyhedra share the trigonal faces to form chains parallel to the c-axis. The remaining six Ca^{2+} ions (6h sites, referred to as Ca2 or triangular Ca) form two triangular sets at z = 1/4 and 3/4 on the mirror planes. The Ca2 ions are seven-coordinated, with six O atoms and one OH^- ion. The six XO_4 tethraedra are PO_4^{3-} groups in a 6h site. OH^- anions occupy the special position 4e at z/c=0.202, that has multiplicity of 4. As in the hexagonal structure the presence of the mirror plane at 1/4 and 3/4 make hydroxyls ions in this position reflected too close to themselves, an occupation factor of 1 would result in an incorrect stoichiometry. Thus, the occupation of the site must be 0.5, and in this case the orientation of the OH^- groups in the lattice cannot be known. A full description of OH^- sites in stoichiometric HA can be achieved by reducing the symmetry of the crystal to the subgroup $P2_1/b$[61]. As the cell contains twice the atoms of the hexagonal one, the correct stoichiometry is retained and the sticking of the hydroxyls is prevented; the resulting unit cell parameters are a = 9.421 Å, b = 18.843 Å, c = 6.881 Å, γ= 120.0°.(Fig. 1.16)

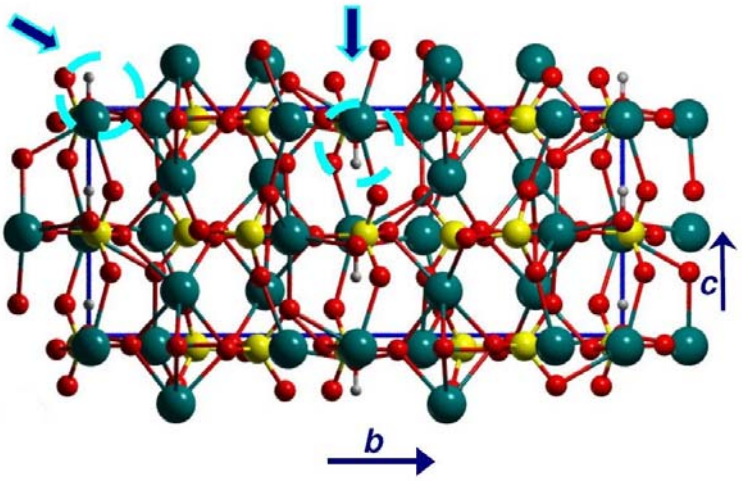

Figure 1.16. Structure of monoclinic hydroxyapatite.

Thus, HA can be described in terms of two interpenetrating lattices: an overall $P6_3/m$ structure, with a local $P2_1/b$ in correspondence of the hydroxyls columns. For this reason and for sake of simplicity, we will always refer to the hexagonal description of HA, as the monoclinic description is required only for explaining the statistical occupation of OH^-

ions and is not influent on the chemico-physical properties of HA related to the biologic behaviour.

1.7.2 Biological Apatites

Although the above-described structure of synthetic HA has been used as a model for the apatite present in the human hard tissues for many years, many differences in composition and in other properties make the biological apatites different from pure calcium hydroxyapatite and from each other and should be more appropriately referred to as calcium-deficient, multi-substituted hydroxyapatite (Tab. 1.V).

The apatite lattice is very tolerant of substitutions, vacancies and solid solutions, for example, X can be replaced by ½CO3 or ½O; Ca by Sr, Ba, Pb, Na or vacancies[62]; and PO_4 by HPO_4, AsO_4, VO_4, SiO_4 or CO_3.

Owing to this ability, biological apatites are capable of variable composition and therefore to be heterogeneous even within each category and even within each calcified tissue (enamel, dentine, bone). Non-stoichiometry (Ca/P of biological apatites ranges from 1.54 to 1.73 compared to 1.67 for pure HA), the presence structural or surface-bound of foreign ions and the co-existence or pre-existence of possible precursors such as DCPD, octacalcium phosphate (OCP), TCP, ACP make an accurate crystallochemical analysis and definition a difficult, if not an impossible undertaking.

Because of these difficulties, many studies on biological apatites have been made indirectly by studying apatites prepared from aqueous and non-aqueous systems. Notwithstanding, the chemico-physical behaviour of the synthetic apatites cannot always be directly extrapolated to biological apatites.

The biological apatites are uniquely similar in that they all contain carbonate in varying amounts as a substitute for phosphate in the apatite structure[63,64]. They differ in crystallite sizes, shapes and other physico-chemical properties such as chemical (susceptibility to acid dissolution) and thermal stabilities[65,66].

Based on observations from *in vitro* systems[63,65,67-70], some of these foreign ions affect the crystallinity (reflecting crystallite size and/or strain), morphology, lattice parameters of the biological apatites[50] and as a consequence, impart stability or instability to the tissues involved. Some of these impurities are associated with the susceptibility or resistance of human tooth enamel to acid dissolution (caries) and of bone resorption processes[50,71,72].

Table 1.V. Atomic composition of human hard tissues.

COMPOSITION	Bone (wt%)	Enamel (wt%)	Dentin (wt%)
Ca^{2+}	**34.8**	**36.5**	**35.1**
PO_4^{3-}	**15.2**	**17.7**	**16.9**
CO_3^{2-}	7.4	3.5	5.6
Mg^{2+}	0.72	0.44	1.23
Na^{+}	0.9	0.5	0.6
Si	0.05	0.14	0.01
Cl^{-}	0.13	0.3	0.1
K^{+}	0.03	0.08	0.05
F^{-}	0.03	0.01	0.06
S	-	0.1	0.2
In traces: Sr^{2+}, Pb^{2+}, Zn^{2+}, Cu^{2+}, Fe^{3+},…			
Total inorganic phase	70.0	97.0	70.0
Total organic phase	23.0	1.5	20.0
Total aqueous phase	7.0	1.5	10.0

Biological apatite is not a stable material, as it is involved in the complex bone metabolism and thus subject to a continuous structural remodelling, due also to its very poor crystallinity degree. One important characteristics of biologic HA is for example, the increase of its crystallinity in the ageing and the increase of Ca/P ratio. This phenomenon reflects in a progressive decrease of the capacity of biologic HA to remodel itself, as the stability and solubility of HA strongly decreases when it approaches to the stoichiometry (Ca/P =1.667).

1.7.3 Effect of carbonate

The presence of carbonate ions in the biological apatites strongly contributes to the variation of Ca/P ratio. As higher its content as higher is the metabolic activity of the tissue: for example, enamel, which is a nearly inert tissue, contains very few carbonate, compared to bone and dentin, which are very active tissues. Carbonate ions are either adsorbed on the surface or incorporated into the HA structure, into two different crystallographic sites, hydroxyl (A-type carbonation) or phosphate (B-type carbonation).
The B-type is the preferential carbonate substitution found in the human bone, in the range 2-8 wt%, depending on the age of individual[73], with the A/B type ratio in the range 0.7-0.9. A higher value of the A/B ratio was observed in old tissue, compared to young tissue[74]. It

has been observed by *in vivo* tests that the decrease of crystallinity in B-carbonated HA yields an increase of solubility[75]. B-type carbonation is related to a higher affinity of apatite for osteoblast cells, compared to A-type carbonation, as it does not alter the surface polarity of HA. This reflects in a higher cellular adhesion and an increase production of collagen[76,77].

1.7.4 Effect of magnesium

Among substituting cations, magnesium is widely studied due to its biological relevance. It has been verified that in calcified tissues, the amount of magnesium associated with the apatite phase is higher (about 5% at.) at the first stages of the bone remodelling process and decreases with increasing calcification and with the ageing of individual[78]. The presence of magnesium increases the nucleation kinetic of HA contemporary retarding that of its crystallization; for this reason magnesium concentration is higher in the cartilage and in young bone and there is growing evidence that it may be an important factor in the qualitative changes of the bone matrix that determines bone fragility. Magnesium depletion adversely affects all stages of skeletal metabolism, causing cessation of bone growth, decrease of osteoblastic and osteoclastic activities and osteopenia.

1.7.5 Effect of silicon

Among the numerous trace elements present in bone mineral, silicon plays an essential role for normal bone and cartilage growth and development[79].

Apart from oxygen, silicon is the most abundant element in the earth's crust. The presence of silicon in mammalian systems is quite variable. Silicon is present at a level of _1 ppm in the serum, 2–10 ppm in the liver, kidney, lung and muscle, 100 ppm in the bone and ligaments and 200–600 ppm in cartilage and other connective tissues[80]. In the examination of a variety of connective tissues using chemical methods, silicon was found in high levels of 200–550 ppm bound to extracellular matrix compounds such as hyaluronic acid, chondroitin sulfate, dermatan sulfate, and heparan sulfate in connective tissues such as cartilage and the umbilical cord[80]. The high concentration of silicon observed in extracellular matrix components implies a role for silicon as a biological cross-linking agent that contributes to the architecture and resilience of connective tissue[80].

The role of silicon as an essential element for higher biological organisms (i.e. other than primitive diatoms, sponges and plants such as bamboo) was discovered in the 1970s through the deficiency studies of Carlisle[81,82], Schwarz[83] and Seaborne[84]. Carlisle performed an initial silicon deficiency study in which silicon was localized in active growth areas, such as the osteoid, of the young bone of mice and rats, and silicon levels up to 0.5 wt% were observed in these areas[81], demonstrating the significant dependence of healthy skeletal development on silicon. Carlisle also reported lower levels of collagen in the cartilage of Si-deficient animals, with no significant difference in the level of non-collagenous proteins[82].

In a similar study, rats raised with a low silicon diet and environment were compared with rats supplemented with sodium metasilicate as a fresh aqueous solution at 50 mg Si/100 g of diet. After, Schwartz and Milne found a 33.8% increase in the growth rate in Si-supplemented animals, compared to the Si-deficient animals[83]. In the Si-deficient animals deformities were observed in the skull and tooth enamel and a lower water content of the bones coincided with a lower glycosoaminoglycan content[83]. On the basis of these studies, it was determined that silicon should be categorized as an essential trace element for metabolic processes associated with development of bone and connective tissues[85,86].

Silicon's primary effect in bone and cartilage appears to be on formation of the organic matrix. Bone and cartilage abnormalities are associated with a reduction in matrix components, resulting in the establishment of a requirement for silicon in collagen and glycosaminoglycan formation. Additional support for silicon's metabolic role in connective tissue is provided by the finding that silicon is a major ion of osteogenic cells, especially high in the metabolically active state of the cell. Further studies also indicate that silicon participates in the biochemistry of subcellular enzyme-containing structures. silicon also forms important relationships with other elements.

A study using cDNA microarray analysis is reported, showing that the rapid release of soluble silicate, phosphate and calcium ions can activate specific genes controlling the cell cycle of osteoblasts for new bone formation and proliferation.

Aqueous silicon in the form of orthosilicic acid ($Si(OH)_4$) has been shown to enhance osteoblasts proliferation, differentiation and collagen production, and to have dose dependent effects on osteoclast cells under *in vitro* conditions, enhancing the alkaline phosphatase and osteocalcin activities, with an associated increase in osteogenesis[87].

A critical step in collagen type I synthesis and its secretion into the extracellular space is the hydroxylation of the proline residues of the collagen chains, a reaction catalyzed by prolyl hydroxylase[88]. Indeed it has previously been reported that optimal activity of prolyl hydroxylase appears to depend on the presence of adequate concentrations of silicon. The increase in prolyl hydroxylase activity observed following the addition of soluble silicon to the diet of Si-deficient animals may reflect the rate of collagen biosynthesis where soluble silicon is generally implicated. Silicon is also known to bind to glycosaminoglycan macromolecules and has been shown to play a role in the formation of cross-links between collagen and proteoglycans[80], thus resulting in the stabilization of bone matrix molecules and preventing their enzymatic degradation.

On the basis of these studies it is clear that silicon plays important and significant roles in the bone and cartilage systems, acting on the physiological system most prominently during the growth and development of the skeletal system of higher organisms. Silicon also influences the cartilage synthesis and the integrity of the extracellular matrix, as well as the biomineralization process and also has dose-dependent effects on the differentiation, proliferation and collagen synthesis of osteoblasts, with a direct influence on the remodeling process and osteoclast development and resorption activities.

The incorporation of foreign ions during the crystallization in solution has inspired researchers to investigate the substitution of chemical groups found naturally in enamel or bone. Application of this knowledge can then be used to adjust properties such as solubility, mechanical behaviour and bone bonding ability. Chemical elements not found in bone can be substituted for different effects. For example, addition of silver has been used for imparting antimicrobial properties[89].

1.8 Methods for synthesis of HA

Many patents, publications and reviews describe the formation of hydroxyapatite[90,91]. Several mechanisms of formation have been explored including precipitation, conversion of other calcium salts, solid state reactions, and sol-gel preparation[4]. Nevertheless, some variability may appear depending on the synthesis method. Precipitation methods are the most widely used since they can produce large amount of HA with good reproducibility.

Precipitation from solution is the most common synthesis route and involves simultaneous addition of a calcium salt and a phosphate compound to water, or drop-wise addition of the phosphate into an aqueous solution of the calcium salt. Examples of calcium salts include calcium nitrate, calcium hydroxide, calcium chloride, or calcium acetate. The salts are reacted with a hydrogen phosphate or the phosphate ions are introduced in solution from di-ammonium hydrogen phosphate or orthophosphoric acid.

The mostly employed reactions involve (i) the neutralization of calcium hydroxide by orthophosphoric acid[92,93], and (ii) the reaction of calcium nitrate with di-ammonium hydrogen phosphate. The precipitation reaction is conducted with pure reactants at a pH greater than 9, with a controlled reactant addition rate, under stirred conditions and a temperature between 25 and 90 °C.

In reactions where ammonium is part of the precursor, dilute ammonium hydroxide is added continuously to restore the pH after a decrease caused by removal of a hydroxide from the solution to precipitate HAP. The slow incorporation of calcium into the apatitic structure must be accompanied by stirring and aging after the reaction. The Ca/P molar ratio of 1.67 is attained in a few hours after the completion of the reaction at 90°C[94]. Post reaction maturation is an important step for ensuring the production of stoichiometric hydroxylapatite[95]. During maturation, the crystal shape is modified and slender crystals become more "blocky" as the Ca/P molar ratio approaches 1.67 [94]. After maturation, the precipitate is washed several times in double distilled water; high water purity is essential at all times because the apatite lattice readily incorporates foreign elements into the structure. The precipitate is finally dried, sieved and in case, calcined.

In the present work, the neutralization method will be employed, to avoid the employment of ammonia ions which could be retained in the HA powder; the neutralization method has the advantage to be carried out in a basic environment (pH ~ 9-12), so that the only stable phase can be hydroxyapatite. The calcium hydroxide suspension is kept under stirring, upon neutralization by the dripping acid solution; as in the previous methodology, the precipitate is washed, and after dried, sieved and in case, calcined.

Crystallinity, a term used to describe the crystal perfection and/or crystallite size, can vary depending upon the synthesis conditions. A high crystallinity is typically desired where an apatite is subjected to elevated processing temperatures for consolidation into dense forms. However, low crystallinity can impart a higher resorbability in applications such as

composites and cements. Synthesis at 90°C produces a purer apatite with a higher degree of crystallinity, than at room temperature. Crystals can be plate-like, acicular or blocky and exhibit a surface area of 30-120 m^2/g[94,96]. Crystal size in the *c*-axis direction can be as small as 50 nm when produced at 25 °C to as large as 700 nm at 90 °C. These crystallites agglomerate into clusters upon drying.

Another method for the preparation of apatite biomaterials is the conversion of a calcium compound in phosphate solution[4]. Calcium hydroxide and calcium carbonate are most often used. These heterogeneous reactions are generally more difficult to control than the simple precipitation, because they involve a dissolution/ reprecipitation phenomenon. The characteristics of the starting material (specific surface area, particle size, porosity) have to be carefully verified to obtain reproducible results. These preparations do however offer some advantages into porous Ca-P ceramics. In addition , the reactants are abundant and inexpensive. The reaction may, in some conditions, be performed at low temperature and do not produce any by-products that have to be disposed of.

Several high temperature solid-solid reactions may lead to hydroxyapatite. These reactions are not generally used to produce large amounts of apatites but they are involved in the direct production of ceramic pieces (reactive sintering).

High-temperature synthesis was the first method of apatite production reported and involved passing phosphorus tri-chloride vapour over red-hot lime. This process involved the reaction of a gaseous and solid phase. Diffusion between two solid calcium phosphates also produces hydroxyapatite, at temperatures in excess of 1000 °C, however, this method does not produce homogeneous apatites and leads to an increase in grain size through growth and reduction in surface area; two aspects that may be important in the further processing and application of calcium phosphates. Other synthesis reactions include hydrothermal techniques, hydrolysis of other calcium phosphates[97] and sol-gel methods[98].

Hydrothermal synthesis is the second most common method and, in comparison to the wet chemical method, is able to produce well-crystallized, compositionally homogeneous apatite[99]. A high crystallinity, carbonate-substituted hydroxyapatite is produced by this method. Calcium phosphates that have been hydrolysed to hydroxyapatite include octacalcium phosphate[100], tricalcium phosphate[101], and brushite[97,102].

1.9 Non-stoichiometric and substituted HA

As pH values decrease, a calcium deficient HA is more likely to be formed[103,104]. During aqueous precipitation, other species may be substituted in the structure or adsorbed onto the surface.

Non-stoichiometric apatites are quite easy to synthesize, as they can be obtained by any precipitation method over a wide range of pH, temperature and concentration. Their composition and crystal characteristics are however more difficult to control. The most interesting of these apatites are HPO_4^{2-} and CO_3^2-containing apatites which are close to bone mineral. Although bone mineral has a variable composition, diverse apatites mimicking the evolution of bone mineral in young and old animals can be prepared. These apatites also show similar crystal shape and dimensions and their composition can be represented by a chemical formula analogous to that of bone mineral.

Addition of more than one substitute element group can lead to a combination of an expansion and contraction of the unit cell[69]. For example, carbonate causes a decrease in the *a*-axis[105] that could be counteracted by an increase from an acid phosphate group[106]. This reaction sequence is complicated by the ability of carbonate to substitute phosphate or hydroxide, the former being the more common[96].

The addition of many of these chemical groups decreases the growth rate at low concentrations. Full substitution of fluoride for the hydroxyl ion removes lattice distortion, produces a more stable apatite and, thus, is able to drive precipitation to completion more easily[107]. Carbonate replaces phosphate in reactions containing fluoride and at high pH[96].

All ionic sites of the apatite structure accept substitutes[42]. It is generally the size of the ionic substitute that determines its incorporation in a given lattice. For Ca-P apatites, the monovalent anionic site substitution of OH^- by F^-, Cl^-, Br^- are known but I^- is not. These sites may also be occupied by carbonate ions, as in enamel and bone. The trivalent anionic phosphate sites may be occupied by bivalent or tetravalent ions like carbonate, HPO_4^{2-}, or silicate SiO_4^{4-} and many other trivalent ions such as vanadate or arsenate. These sites cannot accept vacancies, probably because the trivalent anions are quite large and vacancies would destabilize the lattice[7].

Cationic sites can also be occupied by other divalent cations like Pb^{2+}, Mg^{2+}, Zn^{2+}, Cu^{2+}, Mn^{2+}, and by monovalent ions such as Na^+ and K^+ or trivalent ions like La^{3+}. The cationic site can also accept vacancies: up to maximum of 2 sites out of the 10 existing in

stoichiometric apatites. This property of the apatite structure allows the adaptation of its physical and chemical properties to many different calcified tissues, such as enamel, bone, dentine, and fish scales. However, in the preparation of pure HA, this property is a drawback because many ions from the solution can be incorporated, including toxic ions, or mineral ions with a positive biological activity. Thus the preparation of pure apatite has to take these properties into account.

The pH is an important factor in the precipitation of apatites as it determines the HPO_4^{2-} content of the final product. Stoichiometric apatites are generally obtained at alkaline pH and in boiling solutions. Anyway, stoichiometric hydroxyapatite does not form spontaneously in solution; their formation in highly supersaturated solutions is preceded by the precipitation of an amorphous phase possessing a Ca/P ratio much lower than that of apatite. This first precipitate then transforms into an apatite phase whose Ca/P ratio tends progressively towards that of HA.

Surface properties also play a role in the preparation of apatites. Generally, precipitated apatites have a very high specific surface area (between 50 and 90 m^2/g) that may adsorb many ions or constituents. In fact, adsorbed ions may eventually be incorporated into the lattice during growth or maturation of the crystals. Surface constituents generally slow down the maturation process and the evolution towards stoichiometry. The surface CO_3^{2-} and HPO_4^{2-} ions play a special role as they may alter the global stoichiometry of the solid.

Precipitation has been performed in various conditions. The preparation of HA seems to be better achieved in Ca-rich solutions than in phosphate-rich solutions.

Following, the effect of the most relevant ionic substitutes on the chemico-physical properties of synthetic HA are described in more detail.

Carbonate (CO_3^{2-})

A key target of biomaterials research is the preparation of a synthetic carbonate containing hydroxyapatite (CHA) bone-substitute ceramic, that mimics the chemical composition of the natural hard tissue. The carbonate group can substitute both the hydroxyl and the phosphate ions, giving rise to the A-type and B-type carbonation respectively, so that a CHA substituted in both sites can be described as $Ca_{10-x/2}[(PO_4)_{6-x}(CO_3)_x][(OH)_{2-2y}(CO_3)_y]$. The charge unbalance occurring when $(CO_3)_{2-}$ ions replace $(PO_4)_{3-}$ (B-type CHA) groups is primarily compensated by vacancies in Ca1 sites[107]. The exact position of the carbonate ions in the lattice of the HA has been

elucidated only recently[107,108]. By using full Rietveld refinement of the crystal structure of the synthetic calcium-deficient carbonated apatite two orientations of CO_3 triangles, sharing one of their edges, were found. They occupy randomly the adjacent faces of a PO_4 tetrahedron that are parallel to the c axis. (Fig. 1.17).

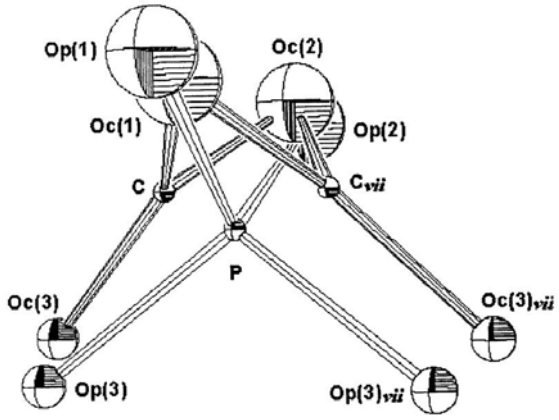

Figure 1.17. View of the two possible arrangement of CO_3 moieties around the PO_4 tetrahedron.

In synthetic non-aqueous (1000 °C) systems, the mode of carbonate incorporation is CO_3 for OH (type A substitution)[109]; in aqueous systems CO_3 for PO_4 (type B substitution); in biological apatites, predominantly CO_3 for PO_4 [42]. The extent of carbonate incorporation is influenced by the presence of other ions such as Na^+, K^+, which favour greater incorporation of carbonate, and Sr^{2+}, which limits the extent of incorporation.

Type B carbonate apatites are obtained when apatites are prepared either by direct precipitation or hydrolysis of ACP, DCPD, DCP or OCP in carbonate-containing solutions. The amount of carbonate incorporated in the apatite is dependent on the CO_3 concentration of the solution, but the maximum incorporation of CO_3 in the apatite is limited to about 22 wt% CO_3, or 3 mol of CO_3. At higher CO_3 concentrations in solution the calcite form of calcium carbonate occurred when precipitations were made at 25 °C and 37 °C; the aragonite form became the preferred phase when precipitation were made at 95-100 °C.

Type B carbonate apatites can be also prepared by conventional synthesis of HA, when carbonate ions are present in the reaction vessel[109].

Carbonate substitution in type B carbonate apatites causes the following effects: a) decrease in *a* axis and increase in *c*-axis dimensions compared to CO_3-free apatites; b) decrease in crystal size as shown by the broadening of the diffraction peaks in the XRD patterns and in TEM; c) increase in crystal strain as shown by the loss of resolution of the

PO_4 absorption bands in the IR spectra; d) change in crystal morphology; e) greater solubility. As carbonation in B site increases the biomimetism of the synthetic apatite, it is advisable to orient the synthesis techniques for the incorporation of suitable amounts of carbonate ions, substituting the phosphate[76,77].

Examination of the CO_3-apatites before and after exposure to acid buffer showed that the apatite after exposure had less carbonate suggesting the dissolution of CO_3-rich apatite and reprecipitation of CO_3-poor apatite. Support for the second alternative was provided by the initial decreases in crystallinity and subsequent increase in crystallinity with time.

The higher solubility of CO_3-containing apatite compared to the CO_3-free apatite could have been predicted on the basis of the carbonate effect on decreasing the crystal size and therefore increasing the surface area as well as its effect on increasing the crystal strain. In addition, the Ca-CO_3 bond is weaker than the Ca-PO_4 bond, thus making a CO_3-containing synthetic and biological apatite more susceptible to acid dissolution than CO_3-free apatite.

Magnesium (Mg^{2+})

As Mg^{2+} is smaller than Ca^{2+} (0.86 Å vs. 1.14 Å), the incorporation of magnesium affect the crystal structure of HA and the substitution cannot occur over the full concentration range. Progressive increase of the amount of incorporated magnesium, in fact, slightly reduces the cell parameters of the crystal and the average crystal radius; above a concentration limit of ~ 0.15 Mg^{2+}/Ca^{2+} the apatite structure likely collapses and the formation of other phases (typically TCP or amorphous calcium magnesium phosphates), that act as segregating phases for this ion, is observed[42]. The incorporation of Mg in synthetic apatites is very limited (maximum of about 4 wt% Mg) unless carbonate or fluoride ions are simultaneously incorporated with Mg. The amount of Mg incorporated in the apatite is proportional to the Mg concentration in the solution. The incorporation of Mg increased by the simultaneous incorporation of F^- or CO_3^{2-}. The limited incorporation of Mg is also observed in apatites prepared at high temperatures (above 900 °C) by solid state reaction.

The presence of Mg in the apatite causes the following effects on its properties: a) decrease in *a*-axis dimension; b) decrease in crystallinity as shown in XRD patterns and IR spectra; c) increase in HPO_4^{2-} incorporation as shown by the higher β-TCP/HA ratio in sintered Mg-containing HA and d) increase in extent of dissolution.

As for B-carbonation, the incorporation of magnesium in synthetic HA is of great interest for the design of biomimetic bone substitutes[110,111].

Silicon (SiO_4^{4+})

The simplest model of incorporation of silicon in the HA structure (Si-HA) is the substitution of SiO_4^{4-} for PO_4^{3-} functional groups[112].

Anyway, to avoid a large cost in energy, local charge neutrality is mandated, and this requires some other defect to be associated with the PO_4^{3-} to compensate for the charge deficit. There are many possible mechanisms for charge compensation and which predominates depends on the thermodynamic conditions during the preparation of the materials. Mechanisms that have been considered include O vacancies and excess Ca, which can each compensate for two Si substitutions. For Si-HA, OH vacancies can also provide compensation[113-117]. Which of the mechanisms dominates depends on the availability of water during the manufacture, and it appears that there is not likely a unique Si-HA material but different types depending on the details of the preparation conditions[118-122].

Further evidence of the importance of silicon on bone formation was found in bioactive silicate containing glass ceramics. As the ionic bond lengths of a P-O bond with tetrahedral coordination (0.157 nm) are comparable to a similarly coordinated Si-O bond (0.166 nm)[123], the X-ray diffraction patterns of Si-HA and stoichiometric HA appear to be identical, anyway refinement of the diffraction data revealed some small structural differences between the two materials. The silicon substitutes the phosphorous in the HA lattice, resulting in a small decrease in the *a* axis and an increase in the *c* axis of the unit cell. This substitution also caused a decrease in the number of hydroxyl (OH) groups in the unit cell, which was expected from the proposed substitution. The incorporation of silicon in the HA lattice resulted in an increase in the distortion of the PO_4 tetrahedra, indicated by an increase in the distortion index[124].

Acid phosphate (HPO_4^{2-})

The non-stoichiometry of biological apatites, especially of human enamel apatite, has been partially attributed to the presence of HPO_4^{2-} ions, either surface-bound, lattice bound (partially substituting for PO_4^{3-}), or as constituent of OCP interlayered with apatite. In biological and in synthetic apatites from aqueous systems, the original presence of

HPO_4^{2-} is deduced from the formation of pyrophosphate upon ignition at temperatures 300 to 500 °C or formation of β-TCP upon ignition at 700 °C to 950 °C.

The incorporation of HPO_4-for-PO_4 in apatite causes an expansion in the *a*-axis and slight contraction in the *c*-axis dimensions. The effect of HPO_4^{2-} incorporation on the properties of apatite has not been directly investigated but can be predicted to cause instability causing the apatite to be more susceptible to acid-dissolution.

The amount of HPO_4^{2-} and CO_3^{2-} in the bone mineral may vary considerably, however the sum of divalent ions is quite constant in most bone tissues. The amount of vacancies in cationic sites and in monovalent anionic sites is always very high and close to the maximum attainable for an apatitic structure.

Pyrophosphate (P_2O_7)

The presence of pyrophosphate in solutions from which apatite forms cause suppression of crystal growth, favouring the formation of ACP. The involvement of $P_2O_7^{4-}$ with the apatite structure, i.e., whether it is lattice- or surface-bound has not been determined. Its presence as a crystal surface poison has been implied.

Strontium (Sr^{2+})

Sr^{2+} substitutes for calcium in synthetic apatites causing an expansion in both *a*- and *c*- axis dimensions. In bone and tooth minerals, strontium is found as one of the minor constituents; its incorporation in bone mineral was correlated with changes in the a-axis dimensions of the bone apatite. In the bone mineral, the presence of strontium was associated with lower solubility, while in enamel, reports on the strontium effect have so far been contradictory.

Lattice H_2O

Pyrolysis below 200 °C of enamel apatites and apatites prepared from aqueous systems causes loss of weight without any significant change in their lattice parameters; pyrolysis at temperatures between 300 and 400 °C causes a contraction in the *a*-axis dimensions concomitant with weight loss. This latter effect has been explained as being due to either loss of "lattice H_2O", or loss of H_2O from reactions between HPO_4^{2-} groups or reactions between HPO_4^{2-} and CO_3^{2-}. Either H_2O-for-OH or HPO_4-for PO_4 substitution in the apatite structure will cause an expansion in the lattice parameters and the loss of H_2O

(from "lattice H_2O or as a reaction product of HPO_4^{2-}) will cause the observed reduction in the a-axis resulting from the reordering of the apatite lattice after pyrolysis.

Multiple substitutions in the apatite structure

The simultaneous or concerted substitutions of different ions in biological apatites cause additive or conflicting effects on the physico-chemical properties of the apatite. Such properties include: lattice parameters, crystallinity (expressing crystallite size and / or strain), chemical and thermal stabilities. In some case, the incorporation of one impurity can suppress the incorporation of another, especially when competing for the same crystallographic site. The effect of multiple substitutions contribute stability or instability to the apatite which is translated in terms of susceptibility to acid dissolution of the teeth and bone mineral. For example, the presence of CO_3^{2-} causes instability, F^- stability, and simultaneously, the stabilizing effect of F^- becomes much more important than the opposite effect of CO_3^{2-}.

1.10 Thermal behaviour of apatites

Apatites are generally sintered in air at 1100-1300 °C[6], following compaction of the powder into a desired shape. Sintering is frequently associated with growth of crystals and a change of their shape.

The phases formed at high temperature depend on temperature and on the partial pressure of water (p_{H2O}) in the sintering atmosphere. When water is present, HA can be formed and is a stable phase up to 1360 °C.. When there is no water, TeCP and TCP are the stable phases. The temperature range of HA stability increases with p_{H2O}, as does the rate of phase transition of TCP or TeCP to HA.

Two ranges of decomposition of apatites and Ca-P compounds can be distinguished[7]: a low-temperature irreversible decomposition (150-1000 °C) and a high-temperature reversible decomposition (above 1000 °C).

The first reaction occurring in Ca-P materials is the condensation of hydrogen-phosphate ion HPO_4^{2-}. The reaction begins at temperatures as low as 150-300 °C in non stoichiometric HA and other HPO_4^{2-} containing compounds:

$2HPO_4^{2-} \rightarrow P_2O_7^{4-} + H_2O$

The P_2O_7 ions are believed to remain in the apatite lattice, in a very distorted form.

Carbonate ions also begin to decompose at low temperature (100-300 °C) especially in HPO_4^{2-} containing apatites, probably because of proton transfer and bicarbonate ion decomposition:

$2HPO_4^{2-} + 2CO_3^{2-} \rightarrow 2PO_4^{3-} + H_2O + 2CO_2$

At higher temperatures (500-1000 °C) carbonate ions begin to decompose by themselves:

$CO_3^{2-} \rightarrow CO_2 + O^{2-}$

The O^{2-} ion, formed in the apatite structure, is generally rapidly hydrolyzed into OH^-. However, when apatites are rich in carbonate ions calcium oxide also forms a separate phase.

At about 700 °C pyrophosphate ions react with OH^- ions to restore PO_4^{3-} ions:

$P_2O_7^{4-} + 2OH \rightarrow 2PO_4^{3-} + H_2O$

All these reactions are irreversible. At around 800 °C massive restructuring of the non-stoichiometric apatite generally occurs depending essentially on the Ca/P ratio of the initial product. When the atomic ratio Ca/P is between 1.5 and 1.667 β-TCP and stoichiometric hydroxyapatite are formed. When the atomic Ca/P ratio is higher than 1.667 then CaO and stoichiometric HA are detected. It is only for a ratio equal to 1.667 that stoichiometric HA is observed a single phase.

This decomposition reaction can represent a very sensitive way to determine the stoichiometry of apatites. However the role of impurities in this decomposition is not clear, especially that of Mg^{2+}, which is the major impurity in Ca-P compounds.

A final reaction may occur at about 850 °C, the decomposition of OH^-:

$2OH^- \rightarrow H_2O + O_2^-$

This reaction depends, of course, on the water partial pressure and is completely reversible. The oxyapatite eventually formed:

$Ca_{10}(PO_4)_6O$, which has been proposed as a potential biomaterial. This compound, very unstable, is however not known in a pure form and only exists as an oxyhydroxyapatite

$Ca_{10}(PO_4)_6OH_xO_{1-x/2}$

At temperatures higher than 1200 °C apatites may begin to decompose in a reversible manner into TCP and tetracalcium phosphate (TeCP). This is attributed to the oxyapatite formed:

$Ca_{10}(PO_4)_6O \rightarrow 2Ca_3(PO_4)_2 + Ca_4(PO_4)_2O$

At higher temperatures (above 1600 °C) a liquid phase forms and CaO is the only solid phase to subsist. Slow cooling in presence of water allows these high temperature phases to react again and restore stoichiometric HA.

1.11 Characterization of apatite biomaterials

The characterization of Ca-P biomaterials covers several aspects[7]. In addition to the traditional physical-chemical and mechanical characterization, implantable materials have to prove their innocuousness and, if possible, their bioactivity. As in many multidisciplinary domains, chemical and physical properties relevant for the use of the biomaterial must also be identified.

Three levels of characterization may be distinguished: a) chemical; b) morphological and c) structural.

The chemical composition of biomaterials can be determined by phase analysis and classical chemical analysis. Phase analysis is commonly performed by X-ray diffraction, representing a fast and powerful tool to assess the type of crystalline compounds formed during apatite synthesis. Calcium phosphates exhibit very similar scattering powers (~0.5 compared to α-Al_2O_3) so that their presence can be easily detected, even in amount ~ 1%; the detection of CaO can even be more sensitive, as its scattering power is 1.3. XRD allows a good identification of well crystallized phases and in some cases may distinguish between different apatite phases, for example in case of strontium-substituted HA, where the higher atomic weight of the substituting atom (Sr for Ca) determines a marked shift of the X-ray diffraction peaks. However the technique is not sensitive enough to identify solid solutions like oxy-hydroxyapatite and in the case of poorly crystalline compounds peak broadening prevents also any precise identification of apatite phases. In addition, it is often difficult to discriminate between closely related structures like octacalcium phosphate and HA. The variation in the cell parameters, when due to multiple substitutions, cannot give information on the presence and type of atom substitutions in anionic and cationic site, so that deeper investigations are needed: infra-red and Raman spectroscopies are usually applied to check the occurrence of carbonation in A or B site, but an accurate determination of the amount of HPO_4^{2-} ions especially in presence of carbonate is not possible.

The classical chemical analysis is finally applied to determine the overall content in atoms in the apatite sample, namely calcium, phosphorus and the substitutes employed for the augmentation of the apatite biomimetism (magnesium, silicon, strontium, fluoride, etc..); anyway no information are provided whether the element is incorporated in the apatite structure or attached to the crystal surface, so that more sophisticated spectroscopic investigations are needed. In fact, the location of the substitute ion greatly influences the chemical properties of apatite in terms of solubility and reactivity with the physiological environment, when present into the cell structure; thus, the substitute itself is released according to the increased solubility of apatite. When attached on the surface, conversely, its release in solution is probably faster and independent on the solubility of HA; anyway the ion release can be mediated by amorphous regions which in low crystallinity HA powders surround the more ordered HA crystals[125]. In this case the kinetic of release depends on the structure, composition and thickness of the amorphous layer. The determination of ion release in substituted apatites is fundamental, as their type and availability strongly influence the activity of osteoblast cells and, in consequence, of the whole process of bone remodelling.

The presence of crystalline and amorphous phases in biological-like HA makes extremely hard its chemical-physical characterization, so that a number of supplementary investigations can be routinely employed for this purpose.

Thermo-gravimetric investigations are employed to determine the thermal behaviour of HA powders, as also described in Section 3.10; thus, it can be estimated the amount of water differently bound to HA, both physically (in the lower temperature region) and chemically (up to 400 °C), the condensation of eventual hydrogen-phosphates and of carbonate. In the region of high temperatures (T > 1000 °C) the weight loss due to OH^- evaporation is detected and can provide information on the OH^- content, more quantitative and complementary with respect to infrared spectroscopy.

Thermo-analytical investigations provide information on the structural changing occurring in HA during heating, due to the variation of latent heat; commonly, the transformation in β-TCP at high temperature can be detected by an exothermic peak, but the rearrangement of the complex structure of a substituted HA (crystallization of the amorphous fraction, carbonate decomposition, grain growth, secondary phase formation at low temperature)

usually yields only continuous variations of latent heat, so that the assignment of a critical temperature for these phenomena is much harder.

The characterization of powder morphology and size is important for further treatment of the apatite powder in preparing three dimensional bodies as bone scaffolds. Ceramic aqueous suspensions are needed for this purpose, which are used for preparation of templates through impregnation by polymeric preforms, freeze-drying techniques and foaming methods. Low crystalline HA is nanosized and exhibit a high surface charge which provokes powder agglomeration and precipitation when suspended in water. A full investigation of powder size and morphology and its surface charge is thus essential for obtaining the optimal conditions to suspend the HA powders, on the basis of their composition. Since the presence of atomic substitutes provokes changing in powder solubility and reactivity, different rheological behaviour are expected and a careful assessment of the powder properties should be performed for each typology of HA.

Solubility tests represent a relatively easy and powerful tool for investigating the behaviour of multi-substituted HA in physiological environment; in fact, when tests are carried out in simulated body fluid (SBF) at 37 °C, the amount and kinetic of the different ion release during a certain lapse of time is representative of the apatite bioactivity, in terms of substances provided to cells in the neighbours of the synthetic implant. This information is indicative of the potential success of the biomaterial, in terms of bone regeneration and scaffold resorption; anyway, the response of cells to the presence of an implant also depend on other features than the chemical ones. First of all, the implant morphology must be adequate for osteoconduction, otherwise the bone formation would occur on the implant surface only; second, the resorption process by osteoclasts must be commensurate to the kinetic of osteoblasts activity, otherwise the scaffold would dissolve prior the complete restoration of the original bone portion; third, in bone remodelling the cell response is stimulated by the biomechanical loads, so that in case of load-bearing implants, the mechanical strain exhibited by the implant and the surrounding bone must be similar, otherwise the stress mismatch can have negative influence on the implant adhesion and on the quality of the newly formed bone.

This last aspect is mainly related to the employment of consolidated 3D scaffolds; in this case the full characterization of the starting HA powder is useful to determine the best conditions for sintering, but a further series of investigations will be needed on the final

ceramic body as its surface properties will be completely different from those of the starting material. Moreover, other properties become fundamental for its success as bone implant, namely the pore size distribution, pore interconnection, solubility, capability of forming an interlayer of carbonated HA when soaked in SBF, which is an important index of bioactivity and finally mechanical strength. The bioactivity assessment is especially important for non-bioresorbable materials, as the surface will establish a permanent contact with living tissues.

Most of the investigated techniques here mentioned will be more extensively illustrated in the next Chapter.

References

1. Wolff J, Hirchwild A. The law of remodelling. Springer-Verlag, Berlin, 1986.

2. Kokubo T, Kim HM, Kawashita M. Novel bioactive materials with different mechanical properties. Biomaterials 2003; 24: 2161–2175.

3. Giannoudis PV, Dinopoulos H, Tsiridis E. Bone substitutes: An update Injury. Int. J. Care Injured 2005; 36S, S20-S27.

4. Gross KA, Berndt CC. Biomedical Application of Apatites. In (Kohn MJ, Rakovan J, Hughes JM, eds): Reviews in mineralogy and geochemistry. 48, 2002: p 631-672.

5. Porter AE. Nanoscale characterization of the interface between bone and hydroxyapatite implants and the effect of silicon on bone apposition. Micron 2006; 37: 681-688.

6. Hench L. Bioceramics. J Am Ceram Soc 1998; 81 (7): 1705-1728.

7. Rey C. Calcium phosphates for medical applications. In (Amjad Z, ed): Calcium phosphates in biological and industrial systems. Kluwer Academic Publishers, Dordrecht, The Netherlands, 1998.

8. Lewandrowski K, Gresser JD, Wise DL, Trantolo DJ. Bioresorbable bone graft substitutes of different osteoconductivities: an istologic evaluation of osteointegration of poly (propylene glycol-co-fumaric acid) based cement implants in rats. Biomaterials 2000; 21(8): 757-764.

9. Muschler GF, Negami S, Hyodo A, et al. Evaluation of collagen ceramic composite graft materials in a spinal fusion model. Clin Orthop 1996; 328: 250-260.

10. Sauer HD, Schoettle H. The stability of osteosyntheses bridging defects. Arch Orthop Trauma Surg 1979; 95: 27-30.

11. Oonishi H. Orthopaedic applications of hydroxyapatite. Biomaterials 1991; 12: 171-178.

12. Bloebaum RD, Becks D, Loor LD, Savory CG, DuPont JA, Hoffmann AA. Complications with hydroxyapatite particulate separation in total hip arthroplasty. Clin. Orthop. 1994; 298: 19-26.

13. Bloebaum RD, Dupont JA. Osteolysis from a press-fit hydroxyapatite-coated implant. A case study. J Arthroplasty 1993; 8(2): 195-202.

14. Baltag I, Watanabe K, Kusakari H, Taguchi N, Miyakawa O, Kobayashi M, Ito N. Long-term changes of hydroxyapatite-coated dental implants. J. Biomed. Mater. Res. (Appl. Biomater.) 2000; 53: 76-85.

15. The Williams dictionary of Biomaterials, DF Williams, 1999, ISBN 0-85323-921-5.

16. Hench L, Splinter R, Greenlee T, Allen W. Bonding mechanisms at the interface of ceramic prosthetic materials. J Biomed Eng 1971; 2: 117-141.

17. Ducheyne P, Radin S, King L. The effect of calcium-phosphate ceramic composition and structure on *in vitro* behavior. I. Dissolution. J Biomed Mater Res 1993; 27: 25-34.

18. de Bruijn JD, Bovell YP, van Blitterswijk CA. Structural arrangements at the interface between plasma sprayed calcium phosphates and bone. Biomaterials 1994; 15: 543-550.
19. Daculsi G, LeGeros RZ, Nery E, Lynch K, Kerebel B. Transformation of biphasic calcium phosphate ceramics *in vivo*: ultrastructural and physicochemical characterization. J Biomed Mater Res 1989; 23: 883-894.
20. Radin SR, Ducheyne P. The effect of calcium phosphate ceramic composition and structure on *in vitro* behavior. II. Precipitation. J Biomed Mater Res 1993; 27: 35-45.
21. Schepers E, Declercq M, Ducheyne P, Kempeneers R. Bioactive glass particulate material as a filler for bone lesions. J Oral Rehab 1991;18: 439-452.
22. Andersson OH, Karlsson KH, Kangasniemi K. Calcium-phosphate formation at the surface of bioactive glass *in vivo*. J Non-Cryst Solids 1990; 119: 290-296.
23. Ducheyne P, Kim CS, Pollack SR. The effect of phase differences on the time-dependent variation of the zeta potential of hydroxyapatite. J Biomed Mater Res 1992; 26: 147-168.
24. Hyakuna K, Yamamuro T, Kotoura Y, Kakutani Y, Kitsugi T, Takagi H, Oka M, Kokubo T. The influence of calcium-phosphate ceramics and glass-ceramics on cultured cells and their surrounding media. J Biomed Mater Res 1989; 23: 1049-1066.
25. Gregoire M, Orly I, Manankau J. The influence of calcium phosphate biomaterials on human bone cell activites. An *in vitro* approach. J Biomed Mater Res 1990; 24: 165-177.
26. Keeting PE, Oursler MJ, Weigand KE, Bonde SK, Spelsberg TC, Riggs BL. Zeolite A increases proliferation, differentiation, and transforming growth factor beta production in normal adult human osteoblast-like cells *in vitro*. J Bone Miner Res 1992; 7: 1281-1289.
27. Matsuda T, Davies JE. The *in vitro* response of osteoblasts to bioactive glass. Biomaterials 1987; 8: 275-284.
28. El-Ghannam A, Ducheyne P, Shapiro IM. Bioactive material template for *in vitro* synthesis of bone. J Biomed Mater Res 1995; 29: 359-370.
29. LeGeros RZ, Craig RG. Strategies to Affect Bone Remodelling: Osteointegration. J Bone Min Res 1993; 8, Suppl. 2: S583-S596.
30. Cypher TJ, Grossman JP. Biological principles of bone graft healing. J Foot Ankle Surg 1996; 35: 413-417.
31. Arrington ED, Smith WJ, Chambers HG, et al. Complications of iliac crest bone graft harvesting. Clin Orthop 1996; 329: 300-309.
32. Dodd CAF, Fergusson CM, Freedman L, et al. Allograft versus autograft bone in scoliosis surgery. J Bone Joint Surg Br 1988; 70: 431-434.
33. Sandhu HS, Grewal HS, Parvataneni H. Bone grafting for spinal fusion. Orthop Clin North Am 1999; 30: 685-698.

34. McCarthy RE, Peek RD, Morrissy RT, Hough Jr AJ. Allograft bone in spinal fusion for paralytic scoliosis. J Bone Joint Surg Am 1986; 68: 370-375.
35. Banwart JC, Asher MA, Hassanein RS. Iliac crest bone graft harvest donor site morbidity: a statistical evaluation. Spine 1995; 20: 1055-1060.
36. Ducheyne P, Qiu Q. Bioactive ceramics: the effect of surface reactivity on bone formation and bone cell function. Biomaterials 1999; 20: 2287-2303.
37. Boyce T, Edwards J, Scarborough N. Allograft bone: the influence of processing on safety and performance. Orthop Clin North Am 1999; 30: 571-581.
38. Damien CJ, Parsons JR. Bone graft and bone graft substitutes: a review of current technology and applications. J Appl Biomater 1991; 2: 187-208.
39. Keating JF, McQueen MM. Substitutes for autologous bone graft in orthopaedic trauma. J Bone Joint Surg Br 2001; 83(1): 3-8.
40. Parikh SN. Bone graft substitutes: past, present, future. Journal of post-graduate medicine 2002; 48(2): 142-148.
41. Soballe K, Hansen ES, Brockstedt-Rasmussen H, Bunger C. Hydroxyapatite coating converts fibrous tissue to bone around loaded implants. J. Bone Joint Surg Br 1993; 75: 270-278.
42. LeGeros RZ, LeGeros JP. Phosphate minerals in human tissues. In (Nriagu JO, Moore PB, eds): Phosphate minerals. Springer-Verlag, New York, 1984.
43. Albee FH, Morrison HF. Studies in bone growth-triple calcium phosphate as a stimulus to osteogenesis. Ann Surg 1920; 71: 32-39.
44. McConnell D. Crystal chemistry of hydroxylapatite. Its relation to bone mineral. Arch Oral Biol 1965; 10: 421-431.
45. Nancollas GH, Mohan MS. The growth of hydroxylapatite crystals. Arch Oral Biol 1970; 15: 731-745.
46. LeGeros RZ. Variations in the crystalline components of human dental calculi. I. Crystallographic and spectroscopic analyses. J Dent Res 1974; 53: 45-50.
47. LeGeros RZ, Shannon IL. The crystalline components of dental calculi: human vs. dog. J Dent Res 1979; 58: 2371-2377.
48. LeGeros RZ, Miravite MA, Klein I. Biological whitlockites, its formation and occurrences. J Dent Res 1974; 53: 117.
49. Nelson D. The influence of carbonate on the atomic structure and reactivity of hydroxyapatite. J Dent Res 1981; 60: 1621-1629.
50. LeGeros RZ. Apatites in biological systems. Prog Crystal Growth Charact 1981; 4: 1-45.

51. Arinzeh TL, Tran T, Mcalary J, Daculsi G. A comparative study of biphasic calcium phosphate ceramics for human mesenchymal stem cell-induced bone formation. Biomaterials 2005; 26: 3631-3638.

52. Okuda T, Ioku K, Yonezawa I, Minagi H, Kawachi G, Gonda Y, Murayama H, Shibata Y, Minami S, Kamihira S, Kurosawa H, Ikeda T. The effect of the microstructure of β-tricalcium phosphate on the metabolism of subsequently formed bone tissue. Biomaterials 2007; 28: 2612-2621.

53. Betts F, Posner AS. An X-ray radial distribution study of the amorphous calcium phosphate. Mater Res Bull 1974; 9: 907-914.

54. Posner AS. Crystal chemistry of bone mineral. Physiol Rev 1969; 49: 760-792.

55. Termin JD. Mineral chemistry and skeletal biology. Clin Orthop 1972; 85: 207-232.

56. Nylen MU, Eanes ED, Termine JD. Molecular and ultrastructural studies of non-crystallne calcium phosphates. Calcif Tissue Res 1972; 9: 95-108.

57. Rey C, Hina A, Amrah-Bouali S, Ranz X. Surface Reactions of Calcium-phosphate Bioceramics, Comparison with Bone Mineral Surface Chemistry. In (Ravaglioli A, ed): Fourth Euro-Ceramics. Symposium Bioceramics. Gruppo Editoriale Faenza Editrice SpA, Faenza, 1995.

58. Kawaguchi H, McKee MD, Okamoto H, Nanci A. Tissue response to hydroxyapatite implanted in an alveolar bone defect: Immunocytochemical and lecitin-gold characterization of the hydroxyapatite-bone interface. Cells and Materials 1993; 3: 337-350.

59. Elliott JC, Wilson RM, Dowker SEP. Apatite Structures In: Advances in X-ray analysis. International Centre for Diffraction Data. 45, 2002, p 172.

60. Naray-Szabo S. The structure of apatite (caf)ca4(po4)3. Z. Kristallogr. Kristallgeom. Kristallphys. Kristallchem. 1930; 75: 387-398.

61. Elliott JC, Mackie PE, Young RA. Monoclinic hydroxyapatite. Science 1973; 180: 1055-1057.

62. Elliot JC. Structure and Chemistry of the Apatites and Other Calcium Ortophosphates. Elsevier. Amsterdam, 1994.

63. LeGeros RZ, LeGeros JP, Trautz OR, Klein E. Two types of carbonate substitution in the apatite structure. Experienta 1969; 24: 5-9.

64. McConnell D. Apatite. Its crystal chemistry, mineralogy, utilization and biologic occurrences. Springer, Vienna New York 1973, p. 68-80.

65. Brown WE, Schroeder LW, Ferris JS. Interlayering of crystalline octacalcium phosphate and hydroxylapatite. J Phys Chem 1979; 83: 1385-1388.

66. Eanes ED. Enamel apatite: chemistry, structure and properties. J Dent Res 1979; 58: 829-834.

67. Elliott JC. The problems of the composition and structure of the mineral components of hard tissues. Clin Orthop 1973; 93: 313-333.

68. LeGeros RZ, Bonel B, LeGeros R. Types of H_2O in human enamel and in precipitated apatites. Calcif. Tiss Intl 1978; 26: 111-118.

69. LeGeros RZ, Miravite MA, Quirolgico GB, Curzon ME. The effect of some trace elements on the lattice parameters of human and synthetic bone. Calc Tiss Res 1977; 22: 362-367.

70. LeGeros RZ, Quirolgico G, LeGeros JP. Incorporation of strontium in apatite: effect of pH and temperature. J Dent Res 1979; A58: 168-169.

71. LeGeros RZ, Kerebel LM, Silverstone L. Comparative properties of fluoridated and non-fluoridated biological apatites. J Dent Res 1980; A59: 523.

72. LeGeros RZ, Tung M. Dissolution properties of CO_3^- containing OH and F-apatites. J Dent Res 1982; 61: 232.

73. Driessens FCM. Bioceramics of Calcium Phosphates. CRC Press, Boca Raton, FL, 1983, p. 1-32.

74. Rey C, Renugopalakrishnan V, Collins B, Glimcher M. Fourier transform infrared spectroscopic study of the carbonate ions in bone mineral during aging. Calcif Tissue Intl 1991; 49: 251-258.

75. Le Geros RZ. Calcium phosphates in oral biology and medicine. In (Myers H, ed): Monographs in oral science, Basel: Karger AG Publishers, 1991, vol 15, p. 82-128.

76. Redey SA, Razzouk S, Rey C, Bernache-Assollant D, Leroy G, Nardin M, Cournot G. Osteoclast adhesion and activity on synthetic hydroxyapatite, carbonated hydroxyapatite and natural calcium carbonate: relationship to surface energies. J Biomed Mater Res 1999; 45: 140-147.

77. Redey SA, Nardin M, Bernache-Assollant D, Rey C, Delannoy P, Sedel L, Marie PJ. Behavior of human osteoblastic cells on stoichiometric hydroxyapatite and type A carbonate apatite: role of surface energy. J Biomed Mater Res 2000; 50: 353-364.

78. Bigi A, Foresti E, Gregoriani R, Ripamonti A, Roveri N, Shah JS. The role of magnesium on the structure of biological apatite. Calcif Tissue Intl 1992; 50: 439-444.

79. Pietak AM, Reid JW, Stott MJ, Sayer M. Silicon substitution in the calcium phosphate bioceramics. Biomaterials 2007; 28: 4023-4032.

80. Schwarz K. A bound form of Si in glycosaminoglycans and polyuronides. Proc Nat Acad Sci USA 1973; 70: 1608-1612.

81. Carlisle EM. Silicon: a possible factor in bone calcification. Science 1970; 167: 279-280.

82. Carlisle EM. Biochemical and morphological changes associated with long bone abnormalities in Si deficiency. J Nutr 1979; 110: 1046-1055.

83. Schwarz K, Milne D. Growth promoting effects of Si in rats. Nature 1972; 239: 333-334.

84. Seaborn C, Nielson F. Si depravation decreases collagen formation in wounds, bone and ornithine transaminase enzyme activity in liver. Biol Trace Elem Res 2002; 89: 251-261.

85. Carlisle EM. The nutritional essentiality of silicon. Nutr Rev 1982; 40: 193-198.

86. Carlisle EM. Silicon as a trace nutrient. Sci Total Environ 1988; 73: 95-106.

87. Xynos ID, Alasdair JE, Buttery LDK, Hench LL, Polak JM. Gene-expression profiling of human osteoblasts following treatment with the ionic products of Bioglass 45S5. J Biomed Mater Res 2001; 55: 151-157.

88. Reffitt DM, Ogston N, Jugdaohsingh R, Cheung HFJ, Evans BAJ, Thompson RPH, Powell JJ, Hampson GN. Orthosilicic acid stimulates collagen type I synthesis and osteoblastic differentiation in human osteoblast-like cells *in vitro*. Bone 2003; 32: 127-135.

89. Kim TN, Feng QL, Kim JO, Wu J, Wang H, Chen GC, Cui FZ. Antimicrobial effects of metal ions (Ag^{+}, Cu^{+}, Zn^{2+}) in hydroxylapatite. J Mater Sci: Mater Med 1998; 9: 129-134.

90. Narasaraju TSB, Phebe DE. Some physico-chemical aspects of hydroxylapatite. J Mater Sci 1996; 31: 1-21.

91. LeGeros RZ, LeGeros JP, Daculsi G, Kijkowska R. Calcium Phosphate Biomaterials: Preparation, Properties and Biodegradation. In (Wise DL, Tarantalo DJ, Altobelli DE, Yaszemski MJ, Gresser JD, Schwartz ER, eds): Encyclopedic handbook of biomaterials and bioengineering. Vol 2, Marcel Dekker 1995, p.1429-1463.

92. Tagai H, Aoki H. Preparation of synthetic hydroxylapatite and sintering of apatite ceramics. In (Mechanical Properties of Biomaterials. Hastings GW, Williams DF, eds): John Wiley and Sons, New York, 1980, p. 477-488.

93. Osaka A, Miura Y, Takeuchi K, Asada M, Takahashi K. Calcium apatite prepared from calcium hydroxide and orthophosphoric acid. J Mater Sci: Mat Med 1991; 2: 51-55.

94. Rodriguez-Lorenzo LM, Vallet-Regi M. Controlled crystallization of calcium phosphate apatites. Chem Mater 2000; 12: 2460-2465.

95. Honda T, Takagi M, Uchida N, Saito K, Uematsu K. Post-composition control of hydroxyapatite in an aqueous medium. J Mater Sci 1990; 1: 114-117.

96. Shimoda S, Aoba T, Moreno EC, Miake Y. Effect of solution composition on morphological and structural features of carbonated calcium apatites. J Dent Res 1990; 69: 1731-1740.

97. Monma H, Kayima T. Preparation of hydroxylapatite by the hydrolysis of brushite. J Mater Sci 1987; 22: 4247-4250.

98. Masuda Y, Matubara K, Sakka S. Syntheis of hydroxylapatite from metal alkoxides through sol-gel technique. J Ceram Soc Japan 1990; 98: 84-95.

99. Yoshimura M, Suda H. Hydrothermal processing of hydroxyapatite: Past, present and future. In (Brown PW, Constantz B, eds): Hydroxylapatite and related materials. CRC Press, Boca Raton, Florida, 1994, p. 45-72.

100. Graham S, Brown PW. Reactions of octacalcium phosphate to form hydroxylapatite. J Crystal Growth 1996; 165: 106-115.
101. Nakahira A, Sakamoto K, Yamaguchi S, Kijima K, Okazaki M. Synthesis of hydroxylapatite by hydrolysis of alpha-TCP. J Ceram Soc Japan 1999; 108: 99-104.
102. Fulmer MT, Brown PW. Hydrolysis of dicalcium phosphate dehydrate to hydroxylapatite. J Mater Sci: Mat Med 1998; 9: 197-202.
103. Silva VV, Lameiras FS, Domingues RZ. Evaluation of stoichiometry of hydroxylapatite powders preprared by coprecipitation method. Key Eng Mater 2001; 189-191: 79-84.
104. Raynaud S, Champion E, Bernache-Assolant D, Thomas P. Calcium phosphate apatites with variable Ca/P atomic ratio. I. Synthesis, characterization and thermal stability of powders. Biomaterials 2002; 23: 1065-1072.
105. LeGeros RZ. Effect of carbonate on the lattice parameters of apatite. Nature 1965; 206: 403-404.
106. Young RA, Holcomb DW. Role of acid phosphate in a hydroxylapatite lattice expansion. Calcif Tiss Intl 1984; 26: 60-63.
107. Ivanova TI, Frank-Kamenetskaya OV, Kol'tsov AB, Ugolkov VL Crystal structure of calcium-deficient carbonated hydroxyapatiteT thermal decomposition. J Solid St Chem 2001; 160: 340–349.
108. Feki HE, Savariault JM, Salah AB, Jemal M. Sodium and carbonate distribution in substituted calcium hydroxyapatite. Solid St Sci 2000; 2: 577–586.
109. Landi E, Tampieri A, Celotti G, Vichi L, Sandri M. Influence of synthesis and sintering parameters on the characteristics of carbonate apatite. Biomaterials 2004; 25: 1763–1770.
110. Percival M. Bone health and osteoporosis. Appl. Nutr. Sci. Rep. 1999; 5: 1-5.
111. Kim SR, Lee JH, Kim YT, Riu DH, Jung SJ, Lee YJ, Chung SC, Kim YH. Synthesis of Si, Mg substituted hydroxyapatites and their sintering behaviours. Biomaterials 2003; 24: 1389-1398.
112. Ruys AJ. Silicon-doped hydroxyapatite. J Aust Ceram Soc 1993; 29: 71–80.
113. Gibson I, Jha L, Santos J, Best S, Bonfield W. Effect of Si content on the chemical and phase composition of novel Si substituted hydroxyapatites. In (LeGeros JP, ed): Bioceramics. 1998, p. 105-108.
114. Gibson I, Best S, Bonfield W. Effect of silicon substitution on the sintering and microstructure of hydroxyapatite. J Am Ceram Soc 2002; 85: 2771-2777.
115. Sayer M, Stratilatov AD, Reid J, Calderin L, Stott MJ, Yin X, MacKenzie M, Smith TJN, Hendry JA, Langstaff SD. Structure and composition of silicon stabilized tricalcium phosphate. Biomaterials 2002; 24: 369-382.

116. Reid J, Pietak A, Sayer M, Dunfield D, Smith T. Phase formation and evolution in the silicon substituted tri-calcium phosphate/apatite system. Biomaterials 2005; 26: 2887-2987.

117. Tuck L, Sayer M, Mackenzie M, Hadermann J, Dunfield D, Pietak A, Reid JW, Stratilatov AD. Composition and crystal structure of resorbable calcium phosphate thin films. J Mater Sci 2006; 41: 4273-4284.

118. Arcos D, Rodriguez-Carvajal J, Vallet-Regi M. Silicon incorporation in hydroxyapatite obtained by controlled crystallization. Chem Mater 2004; 16: 2300-2308.

119. Botelho C, Lopez M, Gibson I, Best S, Santos J. Structural analysis of Si substituted hydroxyapatite: zeta potential and X-ray photoelectron spectroscopy. J Mater Sci: Mater Med 2002; 13: 1123-1127.

120. Leventouri T, Bunaciu C, Perdikatsis V. Neutron powder diffraction studies of silicon-substituted hydroxyapatite. Biomaterials 2003; 24: 4205-4211.

121. Arcos D, Rodriguez-Carvajal J, Vallet-Regi M. The effect of silicon incorporation on hydroxyapatite structure. A neutron diffraction study. Solid State Sci 2004; 6: 987-994.

122. Alberius-Henning P, Aldolfsson E, Grins J, Fitch A. Triclinic oxyhydroxyapatite. J Mater Sci 2001; 36: 663-668.

123. Shannon RD, Prewitt CT. Effective ionic radii in oxides and fluorides. Acta Cryst 1969; B25: 925-946.

124. Gibson IR, Best SM, Bonfield W. Chemical characterization of silicon-substituted hydroxylapatite. J Biomed Mater Res 1999; 44: 422-428.

125. Bertinetti L. Nanomateriali per applicazioni biomediche: sintesi e caratterizzazione delle funzionalità di superficie. PhD thesis, University of Torino.

CHAPTER 2

ANALYTICAL TECHNIQUES

2.1 X Ray Diffraction (XRD)

X-ray diffraction is a non-destructive analytical technique which reveals information about the crystallographic structure, crystallite size, and preferred orientation in polycrystalline or powdered solid samples. This technique is based on observing the scattered intensity of an x-ray beam hitting a sample as a function of incident and scattered angle, polarization, and wavelength or energy.

Powder diffraction is commonly used to identify unknown substances, by comparing diffraction data against a database of Powder Diffraction Files (PDF) maintained by the International Centre for Diffraction Data (ICDD). It may also be used to characterize heterogeneous solid mixtures to determine relative abundance of crystalline compounds and, when coupled with lattice refinement techniques, such as Rietveld refinement, can provide structural information on unknown materials. Powder diffraction is also a common method for determining strains in crystalline materials.

The great advantages of the technique are:

- simplicity of sample preparation
- rapidity of measurement
- the ability to analyze mixed phases

When X-rays hit an atom, they make the electronic cloud move as does any electromagnetic wave. The movement of these charges re-radiates waves with the same frequency (blurred slightly due to a variety of effects); this phenomenon is known as the Rayleigh scattering (or elastic scattering). The scattered waves can themselves be scattered but this secondary scattering is assumed to be negligible. A similar process occurs upon scattering neutron waves from the nuclei or by a coherent spin interaction with an unpaired

electron. These re-emitted wave fields interfere with each other either constructively or destructively (overlapping waves either add together to produce stronger peaks or subtract from each other to some degree), producing a diffraction pattern on a detector or film (Fig. 2.1).

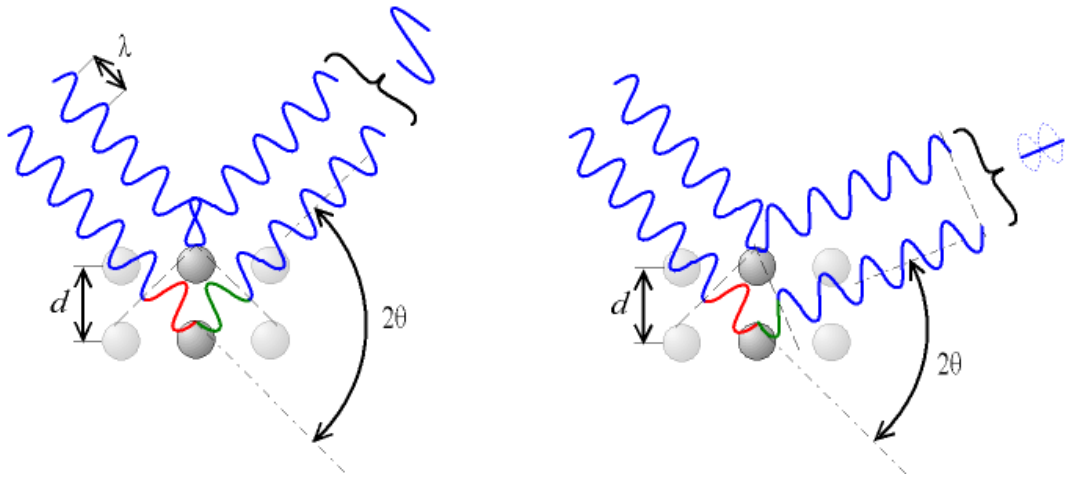

Figure 2.1. Constructive and destructive interference in Rayleigh scattering of X rays.

The resulting wave interference pattern is the basis of diffraction analysis. X-ray wavelength is comparable with inter-atomic distances (~150 pm) and thus is an excellent probe for this length scale.

The interference is constructive when the phase shift is a multiple to 2π; this condition can be expressed by Bragg's law:

$n\lambda = 2d \cdot \sin\theta$,

where:

- *n* is an integer determined by the order of diffraction,
- λ is the wavelength of x-rays,
- *d* is the spacing between the planes in the atomic lattice,
- θ is the angle between the incident ray and the scattering planes

Powder diffraction data are usually presented as a *diffractogram* in which the diffracted intensity I is shown as function either of the scattering angle 2θ.

The most widespread use of powder diffraction is in the identification and characterisation of crystalline solids, each of which produces a distinctive diffraction pattern. Both the positions (corresponding to lattice spacings) and the relative intensity of the lines are indicative of a particular phase and material, providing a "fingerprint" for comparison. A

multi-phase mixture will show more than one pattern superposed, allowing for determination of relative concentration.

Crystal structure

The crystal structure of a material or the arrangement of atoms in a crystal can be described in terms of its unit cell. The unit cell is a tiny box containing the spatial arrangement of atoms. The units cells stacked in three-dimensional space describes the bulk arrangement of atoms of the crystal. The unit cell is given by its lattice parameters, the length of the cell edges and the angles between them, while the positions of the atoms inside the unit cell are described by the set of atomic positions (x_i,y_i,z_i) measured from a lattice point. The symmetry properties of the crystal are embodied in its space group. Crystal structure and symmetry play a role in determining many of its properties, such as cleavage, electronic band structure, and optical properties.

Although there are an infinite number of ways to specify a unit cell, for each crystal structure there is a conventional unit cell, which is chosen to display the full symmetry of the crystal. However, the conventional unit cell is not always the smallest possible choice. A **primitive unit cell** of a particular crystal structure is the smallest possible volume one can construct with the arrangement of atoms in the crystal such that, when stacked, completely fills the space. This primitive unit cell does not always display all the symmetries inherent in the crystal. In a unit cell each atom has an identical environment when stacked in 3 dimensional space. In a primitive cell, each atom may not have the same environment. The crystal structure consists of the same group of atoms, the basis, positioned around each and every lattice point. This group of atoms therefore repeats indefinitely in three dimensions according to the arrangement of one of the 14 Bravais lattices (Fig. 2.2).

The possible lattice centrings are:

- P: Primitive centring, lattice points on the cell corners only;
- I: Body centred, one additional lattice point at the center of the cell;
- F: Face centred, one additional lattice point at centre of each of the faces of the cell;
- A, C: Centred on a single face, one additional lattice point at the centre of one of the cell faces

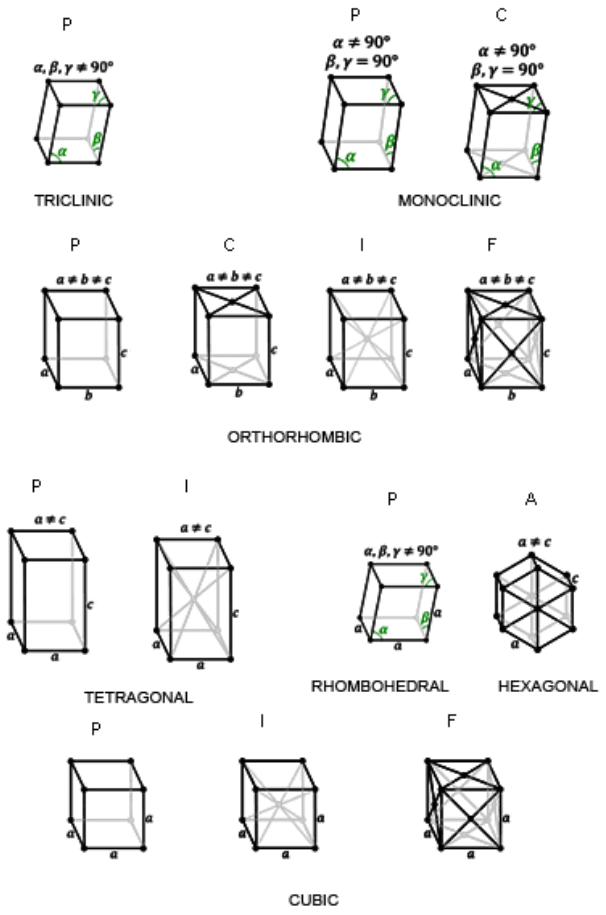

Figure 2.2. The 14 possible Bravais lattices.

There are only seven possible crystal systems that atoms can pack together to produce an infinite 3D space lattice in such a way that each lattice point has an identical environment to that around every other lattice point. The simplest and most symmetric, the cubic (or isometric) system, has the symmetry of a cube. The other six systems, in order of decreasing symmetry, are hexagonal, tetragonal, rhombohedral (also known as trigonal), orthorhombic, monoclinic and triclinic.

When the crystal systems are combined with the various possible lattice centrings, we arrive at the Bravais lattices. They describe the geometric arrangement of the lattice points, and thereby the translational symmetry of the crystal. In three dimensions, there are 14 unique Bravais lattices which are distinct from one another in the translational symmetry they contain.

Miller indices

Miller indices are an useful tool to describe the lattice plans, specifying their orientation with respect to the three axis of the unit cell.

To calculate the Miller indices of a plane one has to determine the reciprocal of its intersections with the three axes in terms of fractions or multiples of the unit cells edges; these numbers are indicated in brackets, e.g. (hkl), which indicates an infinite number of equidistant parallel planes, so that the following expression is satisfied:

h(x/a) + k(y/b) + l(z/c) = n

where n indicates the plane position with respect to the origin.

In Fig. 2.3 some examples of the use of Miller indices is illustrated.

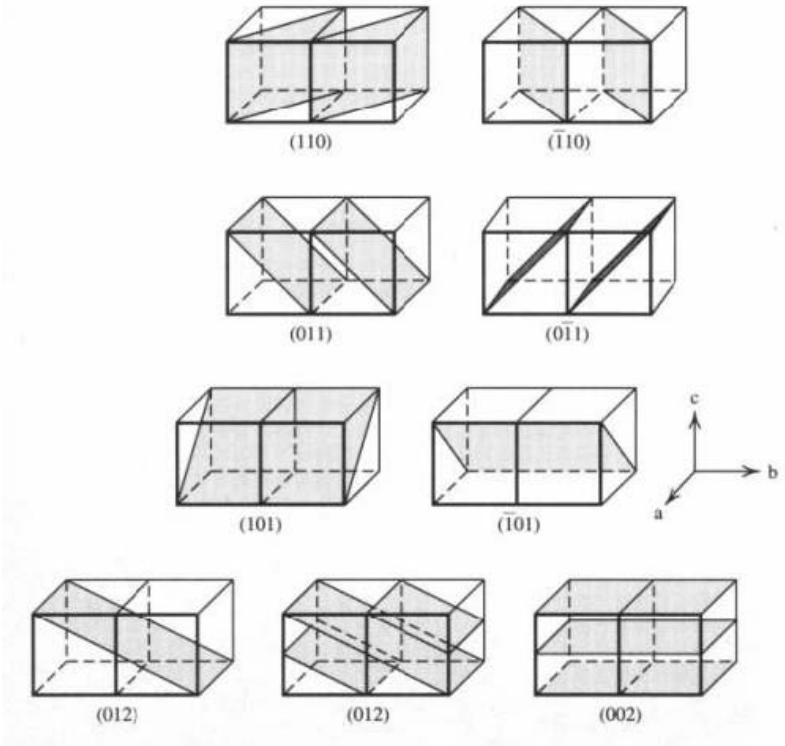

Figure 2.3. Some examples of Miller planes.

Crystallinity

In contrast to a crystalline pattern consisting of a series of sharp peaks, amorphous materials (liquids, glasses etc.) produce a broad background signal. Many polymers, organic molecules or inorganic glasses usually exhibit this kind of pattern, but often also inorganic nanostructured crystalline phases can contain also an amorphous fraction. XRD

can be used to determine the degree of crystallinity by comparing the integrated intensity of the background pattern to that of the sharp peaks.

Size and Strain Broadening

There are many factors that determine the width B of a diffraction peak. These include:

1. instrumental factors
2. the presence of defects to the perfect lattice
3. differences in strain in different grains
4. the size of the crystallites

In powdered samples, the strain can often be neglected, so that a simple formula can be applied to obtain the average size of the diffracting coherent domains, the Scherrer formula:

$$D = \frac{K\lambda}{B\cos\vartheta}$$

where,

D is the crystallite average size

K is a form factor, usually taken as 0.9

λ is the wavelength of the incident radiation

B is the peak width corrected for the instrumental broadening

θ is the diffraction angle

Diffractometers

Diffractometers can be operated both in transmission and in reflection configurations. The reflection one is more common. The powder sample is filled in a small disc-like container and its surface carefully flattened. The disc is put on one axis of the diffractometer and tilted by an angle θ while a detector (scintillation counter) rotates around it on an arm at twice this angle. This configuration is known under the name Bragg-Brentano (Fig. 2.4)

The model of diffractometer employed was a Miniflex (Rigaku, Tokyo, Japan), equipped with a Cu anode, whose characteristic Kα1 wavelength is 0.154056 nm.

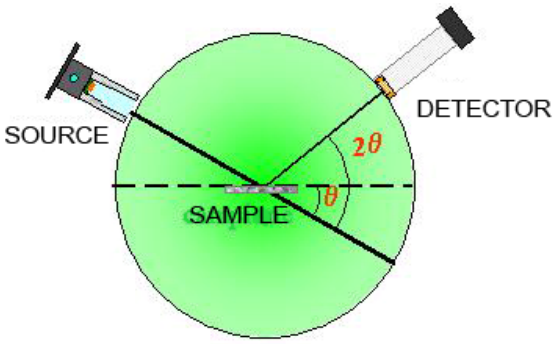

Figure 2.4. Diffractometer adopting the Bragg-Brentano geometry.

2.2 Fourier-Transform Infrared Spectroscopy (FTIR)

Infrared spectroscopy (IR spectroscopy) is the subset of spectroscopy that deals with the infrared region of the electromagnetic spectrum.

The infrared portion of the electromagnetic spectrum is divided into three regions; the near-, mid- and far- infrared, named for their relation to the visible spectrum. The far-infrared, approximately 400-10 cm^{-1} (1000–30 μm), lying adjacent to the microwave region, has low energy and may be used for rotational spectroscopy. The mid-infrared, approximately 4000-400 cm^{-1} (30–1.4 μm) may be used to study the fundamental vibrations and associated rotational-vibrational structure. The higher energy near-IR, approximately 14000-4000 cm^{-1} (1.4–0.8 μm) can excite overtone or harmonic vibrations.

Infrared spectroscopy exploits the fact that molecules have specific frequencies at which they rotate or vibrate corresponding to discrete energy levels (Fig. 2.5). These resonant frequencies are determined by the shape of the molecular potential energy surfaces the masses of the atoms and, by the coupling of vibrational and electronic interactions in the molecule.

Thus, the resonant frequencies can be in a first approach related to the strength of the bond, and the mass of the atoms at either end of it. Thus, the frequency of the vibrations can be associated with a particular bond type and can be used for the characterization of very complex mixtures.

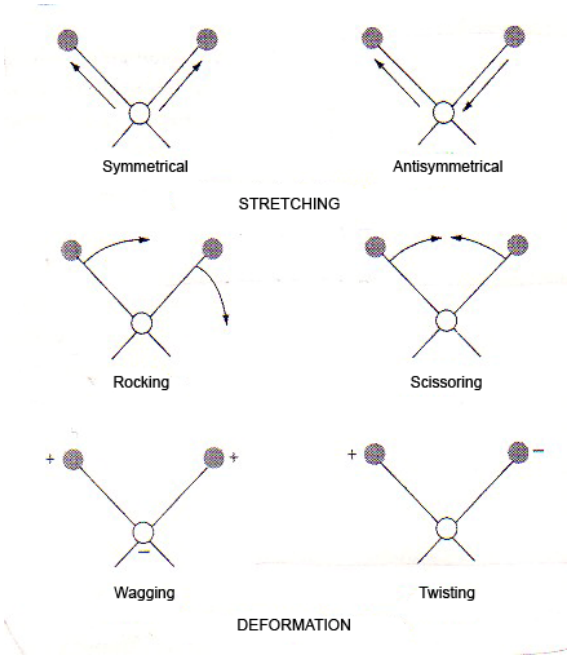

Figure 2.5. Possible vibrations detected by infrared spectroscopy.

The infrared spectra of a sample is collected by passing a beam of infrared light through the sample. Examination of the transmitted light reveals how much energy was absorbed at each wavelength (see Fig. 2.6).

This can be done with a monochromatic beam, which changes in wavelength over time, or by using a Fourier transform instrument to measure all wavelengths at once. From this, a transmittance or absorbance spectrum can be produced, showing at which IR wavelengths the sample absorbs. Analysis of these absorption characteristics reveals details about the molecular structure of the sample.

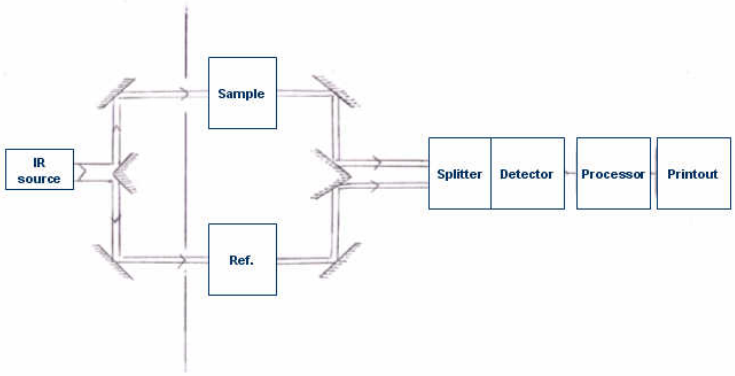

Figure 2.6. Scheme of equipment for infrared spectroscopy

The method employed for sample preparation is to grind a quantity of the sample with potassium bromide finely (to remove scattering effects from large crystals), which is used

also as a reference. This powder mixture is then crushed in a mechanical die press to form a translucent pellet through which the beam of the spectrometer can pass.

A reference is used for two reasons:

- This prevents fluctuations in the output of the source affecting the data;
- This allows the effects of the solvent to be cancelled out (the reference is usually pure solvent).

The equipment employed in the present work was a Thermo Nicolet-Avatar 320 FT-IR.

2.3 Inductively Coupled Plasma Atomic Emission Spectroscopy (ICP-AES)

ICP-AES, also referred to as Inductively Coupled Plasma Optical Emission Spectrometry (ICP-OES), is a type of emission spectroscopy that uses a plasma (e.g. inductively coupled plasma) to produce excited atoms that emit electromagnetic radiation at a wavelength characteristic of a particular element. The intensity of the radiation is proportional to the concentration of the element, which is obtained through a previous calibration obtained with opportune standard solutions.

An inductively coupled plasma (ICP) for spectrometry is sustained in a torch that consists of three concentric tubes, usually made of quartz. The end of this torch is placed inside an induction coil supplied with a radio-frequency electric current. A flow of argon gas is introduced between the two outermost tubes of the torch and an electrical spark is applied for a short time to introduce free electrons into the gas stream. These electrons interact with the radio-frequency magnetic field of the induction coil and are accelerated first in one direction, then the other, as the field changes at high frequency. The accelerated electrons collide with argon atoms, and sometimes a collision causes an argon atom to part with one of its electrons. The released electron is in turn accelerated by the rapidly-changing magnetic field. The process continues until the rate of release of new electrons in collisions is balanced by the rate of recombination of electrons with argon ions (atoms that have lost an electron). This produces a ‘fireball’ that consists mostly of argon atoms with a rather small fraction of free electrons and argon ions.

The samples to be analyzed are firstly solubilized and then introduced into the hot region through an atomizer. The temperature of the plasma is very high, of the order of 10.000 K,

so that the atomization of the sample is nearly complete, improving the accuracy of the analysis. Moreover, the carrier gas is inert (usually argon), so preventing the formation of oxides.

As a droplet of atomized sample enters the central channel of the ICP, it evaporates and any solids that were dissolved in the liquid vaporize and then break down into atoms. At the temperatures prevailing in the plasma a significant proportion of the atoms of many chemical elements are ionized, each atom losing its most loosely-bound electron to form a singly charged ion.

The equipment employed in the present work was a Liberty 200, Varian, Clayton South, Australia.

2.4 Scanning Electron Microscopy (SEM)

The **scanning electron microscope** (**SEM**) is a type of electron microscope that creates various images by focusing a high energy beam of electrons onto the surface of a sample and detecting signals from the interaction of the incident electrons with the sample's surface. The type of signals gathered in a SEM vary and can include secondary electrons, characteristic x-rays, and back scattered electrons (Fig. 2.7). In a SEM, these signals come not only from the primary beam impinging upon the sample, but from other interactions within the sample near the surface.

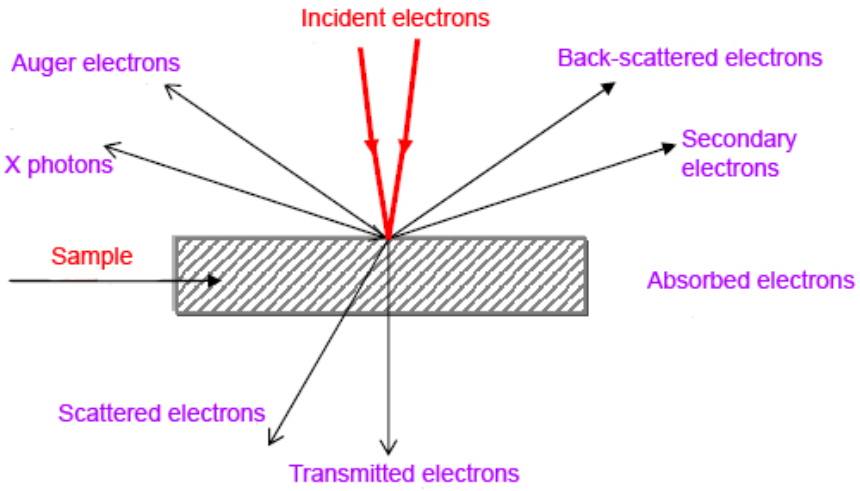

Figure 2.7. Signals produced by the interaction of the electron beam with the sample.

The SEM is capable of producing high-resolution images of a sample surface in its primary use mode, secondary electron imaging. Due to the manner in which this image is created, SEM images have great depth of field yielding a characteristic three-dimensional appearance useful for understanding the surface structure of a sample. This great depth of field and the wide range of magnifications are the most familiar imaging mode for specimens in the SEM. Characteristic x-rays are emitted when the primary beam causes the ejection of inner shell electrons from the sample and are used to tell the elemental composition of the sample. The back-scattered electrons emitted from the sample may be used alone to form an image or in conjunction with the characteristic x-rays as atomic number contrast clues to the elemental composition of the sample.

In a typical SEM, thermo-ionic electrons are emitted from a tungsten cathode and are accelerated towards an anode (Fig. 2.8).

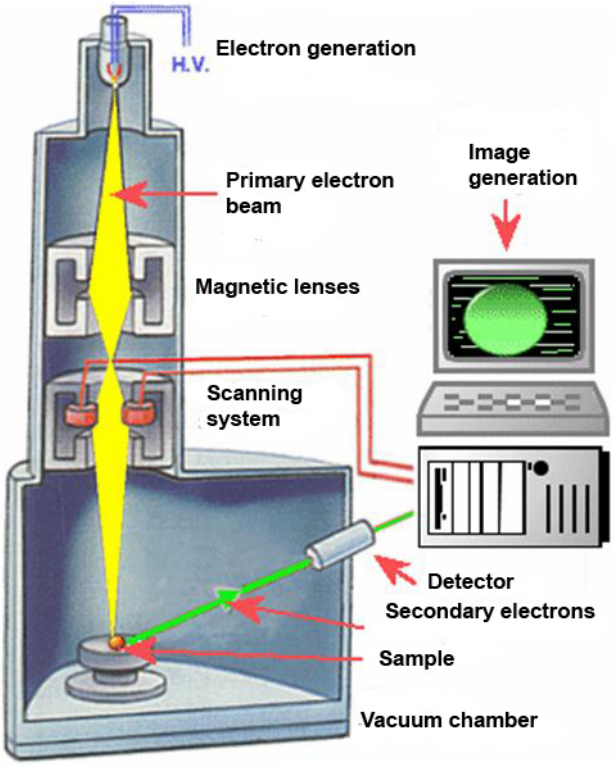

Figure 2.8. Scheme of a Scanning Electron Microscope.

Tungsten is used because it has the highest melting point and lowest vapour pressure of all metals, thereby allowing it to be heated for electron emission. The electron beam, which typically has an energy ranging from a few hundred eV to 100 keV, is focused by one or

two condenser lenses into a beam with a very fine focal spot sized 0.4 nm to 5 nm. The beam passes through pairs of scanning coils or pairs of deflector plates in the electron optical column, typically in the objective lens, which deflect the beam horizontally and vertically so that it scans in a raster fashion over a rectangular area of the sample surface. When the primary electron beam interacts with the sample, the electrons lose energy by repeated scattering and absorption within a teardrop-shaped volume of the specimen known as the interaction volume, which extends from less than 100 nm to around 5 μm into the surface. The size of the interaction volume depends on the electrons' landing energy, the atomic number of the specimen and the specimen's density. The energy exchange between the electron beam and the sample results in the emission of electrons and electromagnetic radiation, which can be detected to produce an image, as described below.

Detection of secondary electrons

The most common imaging mode monitors low energy (<50 eV) secondary electrons. Due to their low energy, these electrons originate within a few nanometers from the surface. The electrons are detected by a scintillator-photomultiplier device and the resulting signal is rendered into a two-dimensional intensity distribution that can be viewed and saved as a digital image. This process relies on a raster-scanned primary beam. The brightness of the signal depends on the number of secondary electrons reaching the detector. If the beam enters the sample perpendicular to the surface, then the activated region is uniform about the axis of the beam and a certain number of electrons "escape" from within the sample. As the angle of incidence increases, the "escape" distance of one side of the beam will decrease, and more secondary electrons will be emitted. Thus steep surfaces and edges tend to be brighter than flat surfaces, which results in images with a well-defined, three-dimensional appearance. Using this technique, resolutions less than 100 nm are possible.

Resolution of the SEM

The spatial resolution of the SEM depends on the size of the electron spot, which in turn depends on both the wavelength of the electrons and the magnetic electron-optical system which produces the scanning beam. The resolution is also limited by the size of the interaction volume, or the extent to which the material interacts with the electron beam.

The spot size and the interaction volume both might be large compared to the distances between atoms, so the resolution of the SEM is not high enough to image individual atoms, as is possible in the shorter wavelength (i.e. higher energy) transmission electron microscope (TEM). The SEM has compensating advantages, though, including the ability to image a comparatively large area of the specimen; the ability to image bulk materials (not just thin films or foils); and the variety of analytical modes available for measuring the composition and nature of the specimen.

The equipment employed in the present work was a Stereoscan 360, Leica, Cambridge, UK.

Energy dispersive X-ray spectroscopy (EDS)

EDS (or EDX) is an analytical technique, coupled with the SEM equipment, used predominantly for the elemental analysis or chemical characterization of a specimen. Being a type of spectroscopy, it relies on the investigation of a sample through interactions between electromagnetic radiation and matter, analyzing X-rays emitted by the matter in this particular case. Its characterization capabilities are due in large part to the fundamental principle that each element of the periodic table has a unique atomic structure allowing x-rays that are characteristic of an element's atomic structure to be uniquely distinguished from each other.

To stimulate the emission of characteristic x-rays from a specimen, an high energy beam of charged particles such as electrons or protons, or a beam of x-rays, is focused into the sample to be characterized. At rest, an atom within the sample contains ground state (or unexcited) electrons situated in discrete energy levels or electron shells bound to the nucleus. The incident beam may excite an electron in an inner shell (Fig. 2.9), prompting its ejection and resulting in the formation of an electron hole within the atom’s electronic structure. An electron from an outer, higher-energy shell then fills the hole, and the difference in energy between the higher-energy shell and the lower energy shell is released in the form of an X-ray. The x-ray released by the electron is then detected and analyzed by the energy dispersive spectrometer. These x-rays are characteristic of the difference in energy between the two shells, and of the atomic structure of the element form which they were emitted.

A detector is used to convert X-ray energy into voltage signals; this information is sent to a pulse processor, which measures the signals and passes them onto an analyzer for data display and analysis.

The equipment employed in the present work was an INCA 300, Oxford Instruments, UK

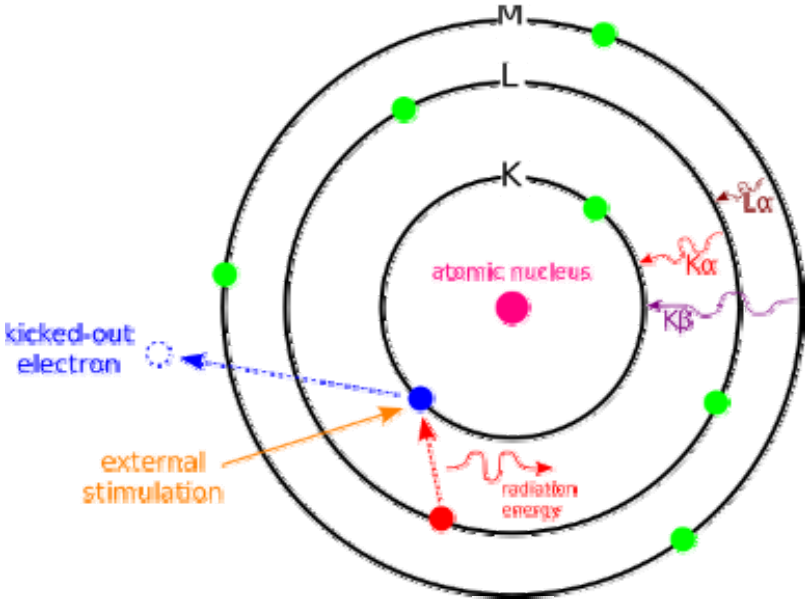

Figure 2.9. Interaction of the electron beam with the electronic cloud.

2.5 Thermogravimetric and Thermoanalytical analyses (TG-DTA)

Thermogravimetric Analysis or **TGA** is a type of testing that is performed on samples to determine changes in weight in relation to change in temperature. Such analysis relies on a high degree of precision in three measurements: weight, temperature, and temperature change. As many weight loss curves look similar, the weight loss curve may require transformation before results may be interpreted. A derivative weight loss curve can be used to tell the point at which weight loss is most apparent.

The analyzer usually consists of a high-precision balance with a pan loaded with the sample. The sample is placed in a small electrically heated oven with a thermocouple to accurately measure the temperature. The atmosphere may be purged with an inert gas to prevent oxidation or other undesired reactions. A computer is used to control the instrument.

Analysis is carried out by raising the temperature gradually and plotting weight against temperature. After the data is obtained, curve smoothing and other operations may be done such as to find the exact points of inflection.

Differential thermal analysis (or **DTA**) is a thermoanalytic technique. In DTA, the material under study and an inert reference (Al_2O_3 in our case) are heated (or cooled) under identical conditions, while recording any temperature difference between sample and reference. This differential temperature is then plotted against time, or against temperature (DTA curve or thermogram). Changes in the sample, either exothermic or endothermic, can be detected relative to the inert reference. Thus, a DTA curve provides data on the transformations that have occurred, such as phase transitions, glass transitions, crystallization, melting and sublimation. The area under a DTA peak can be to the enthalpy change and it is not affected by the heat capacity of the sample.
A DTA apparatus consist of a sample holder comprising thermocouples, sample containers and a ceramic or metallic block; a furnace; a temperature programmer; and a recording system. The key feature is the existence of two thermocouples connected to a voltmeter. One thermocouple is placed in the inert reference material, while the other is placed in a sample of the material under study. As the temperature is increased, there will be a brief deflection of the voltmeter if the sample is undergoing a phase transition. This occurs because the input of heat will raise the temperature of the inert substance, but be incorporated as latent heat in the material changing phase.

The equipment employed in the present work was a Netzsch Gerätebau Jupiter STA (Simultaneous Thermal Analysis) 449C, Selb, Germany.

2.6 Powder Analysis

2.6.1 Specific surface area

Specific surface area is a material property of solids which measures the total surface area per unit of mass, solid or bulk volume, or cross-sectional area.
It is a derived scientific value that can be used to determine the type and properties of a material (e.g. soil). It is defined either by surface area divided by mass (with units of m^2/kg), or surface area divided by the volume (units of m^2/m^3 or m^{-1})
The SSA can be measured by adsorption using the BET isotherm. This has the advantage of measuring the surface of fine structures and deep texture on the particles.
BET theory is a well-known rule for the physical adsorption of gas molecules on a solid surface, that is basis for an important analysis technique for the measurement of the

specific surface area of a material. In 1938, Stephen Brunauer, Paul Hugh Emmett, and Edward Teller published an article about the BET theory in a journal for the first time; "BET" consists of the first initials of their family names.

The concept of the theory is an extension of the Langmuir theory, which is a theory for monolayer molecular adsorption, to multilayer adsorption with the following hypotheses: (a) gas molecules physically adsorb on a solid in layers infinitely; (b) there is no interaction between each adsorption layer; and (c) the Langmuir theory can be applied to each layer. The resulting BET equation is expressed by (1):

$$\frac{1}{v\left[\left(P_0/P\right)-1\right]} = \frac{c-1}{v_m c}\left(\frac{P}{P_0}\right) + \frac{1}{v_m c} \qquad 1);$$

P and P_0 are the equilibrium and the saturation pressure of adsorbates at the temperature of adsorption, v is the adsorbed gas quantity (for example, in volume units), and v_m is the monolayer adsorbed gas quantity. c is the BET constant, which is expressed by (2):

$$c = \exp\left(\frac{E_1 - E_L}{RT}\right) \qquad 2);$$

E_1 is the heat of adsorption for the first layer, and E_L is that for the second and higher layers and is equal to the heat of liquefaction.

Equation (1) is an adsorption isotherm and can be plotted as a straight line with $1 / v[(P_0 / P) - 1]$ on the y-axis and $\varphi = P / P_0$ on the x-axis according to experimental results. This plot is called a **BET plot**. The linear relationship of this equation is maintained only in the range of $0.05 < P / P_0 < 0.35$. The value of the slope A and the y-intercept I of the line are used to calculate the monolayer adsorbed gas quantity v_m and the BET constant c. The following equations can be used:

$$v_m = \frac{1}{A+I} \qquad 3),$$

$$c = 1 + \frac{A}{I} \qquad 4).$$

The BET method is widely used in surface science for the calculation of surface areas of solids by physical adsorption of gas molecules. A total surface area S_{total} and a specific surface area S are evaluated by the following equations:

$$S_{BET,total} = \frac{v_m N s}{V} \qquad 5),$$

$$S_{BET} = \frac{S_{total}}{a} \qquad 6),$$

where N is Avogadro' s number, *s* is the adsorption cross section, *V* is the molar volume of adsorbent gas and *a* is the molar weight of adsorbed species.

The equipment adopted in the present work was a Sorpty 1750, Carlo Erba, Milano, Italy

2.6.2. Electro-acoustic spectroscopy

When an object is immersed in a liquid, a surface electrical charge layer forms, which creates an electrostatic field that then affects the ions in the bulk of the liquid. This electrostatic field, in combination with the thermal motion of the ions, creates a counter charge, and thus screens the electric surface charge. The net electric charge in this screening diffuse layer is equal in magnitude to the net surface charge, but has the opposite polarity. As a result the complete structure is electrically neutral. Some of the counter-ions might specifically adsorb near the surface and build an inner sub-layer, or so-called Stern layer. The outer part of the screening layer is usually called the diffuse layer (Fig. 2.10).

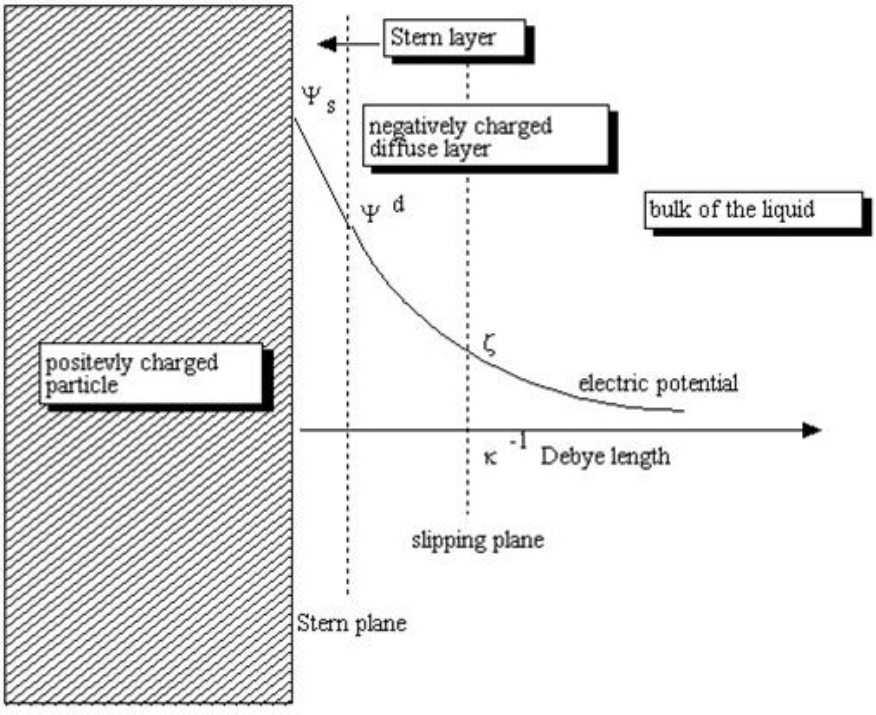

Figure 2.10. Schematic of double layer in a liquid at contact with a solid.

The diffuse layer, or at least part of it, can move under the influence of a tangential stress. There is a conventionally introduced slipping plane that separates mobile fluid from fluid

that remains attached to the surface. Electric potential at this plane is called electrokinetic potential or ζ-potential.

The electric potential on the external boundary of the Stern layer versus the bulk electrolyte is referred to as Stern potential. Electric potential difference between the fluid bulk and the surface is called the electric surface potential. The characteristic thickness of the DL is Debye length κ^{-1}. It is reciprocally proportional to the square root of the ion concentration C. In aqueous solution it is on scale of a few nanometers and the thickness decreases with the concentration of the electrolyte.

Electroacoustic spectroscopy is based on the analysis of the ultrasound waves (ESA) generated by the interaction of externally applied electric fields with charged colloidal particles in liquid medium (Fig. 2.10). The amplitude of ESA depends on the electric charge of the particle, the particle concentration and the amplitude of the electric field; its amplitude is measured through electrodes or transducers transforming the mechanical pressure of the acoustic wave in an electric signal.

The instrument (Acoustosizer, Colloidal Dynamics, Sydney, Australia) is provided with three probes of temperature, pH and electrical conductivity (Fig. 2.11); ζ potential is obtained by automatic titration of the suspension towards acidic and basic values, which also allows to evaluate the size distribution of the particles vs. pH.

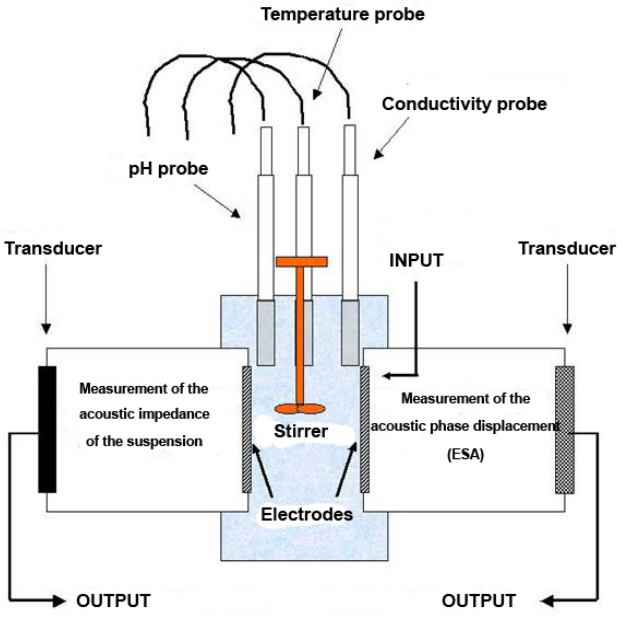

Figure 2.11. Equipment for electro-acoustic spectroscopy.

CHAPTER 3

DEVELOPMENT OF MULTI-SUBSTITUTED HYDROXYAPATITE

3.1 Synthesis of multi-substituted HA powders

The synthesis of multi-substituted HA powders[1] was carried out by employing calcium hydroxide ($Ca(OH)_2$, 95% pure) and orthophosphoric acid (H_3PO_4, 85% pure), with the addition of sodium hydrogen-carbonate ($NaHCO_3$), magnesium chloride hexahydrate ($MgCl_2 \cdot 6H_2O$, 99.5% pure) and silicon tetra-acetate ($(CH_3COO)_4Si$, 98% pure), as sources of carbonate, magnesium and silicon respectively, in aqueous solution; all reactants were provided by Sigma-Aldrich (S. Louis, MO, USA).

The amount of reactants was set up in order to keep the calcium : phosphorus ratio equal to 1.667, so that a competition between Ca^{2+}, PO_4^{3-} and the substituting ions (CO_3^{2-}, Mg^{2+} and SiO_4^{4-}) could be established.

Among the doping elements which can be introduced into the HA structure, magnesium is isoelectronic with calcium and it does not provoke any unbalance of charge in the related crystallographic site; $(CO_3)^{2-}$ ions substituting $(PO_4)^{3-}$ yield a sub-stoichiometry in the calcium site, in order to re-establish the charge neutrality; finally, $(SiO_4)^{4-}$ ions substituting $(PO_4)^{3-}$ yield the loss of OH^- ions[2]. Thus, the approximated general formula for such a multi-substituted HA can be written as follows:

$$Ca_{10-z-x/2}Mg_z(PO_4)_{6-x-y}(CO_3)_x(SiO_4)_y(OH)_{2-y} \quad (1),$$

supposing that no carbonation in A site occurred.

Silicon-substituted hydroxyapatite has been successfully synthesized by using silicon tetra-acetate[2,3] or tetraethyl-orthosilicate[4] as a silicon source**.** The co-substitution of silicon and magnesium in the HA lattice was also performed by Kim *et al.*[5], showing that HA structure can retain both ions in the amount of 2 wt% on the whole.

The extent of substitution in the HA structure will be onwards indicated as X with the symbol of the substituting ion at the subscript, so that X_{Mg}, X_C and X_{Si} indicate the molar ratios Mg : Ca, CO_3 : PO_4, SiO_4 : PO_4 respectively.

Silicon-substituted HA powders (Si-HA) were synthesized with an initial X_{Si} of 0.05 (Si-HA-1), 0.10 (Si-HA-2) and 0.20 (Si-HA-3). Si-HA-1 was prepared by dispersing 20 grams of $Ca(OH)_2$ in 700 ml of distilled H_2O, after the suspension was poured in a glass flask and kept in continuous stirring (Fig. 3.1) at ambient temperature (about 25 °C).

The silicate-containing suspension was prepared by dispersing a suitable amount of $(CH_3COO)_4Si$ (see Table 3.I) in 200 ml of distilled H_2O; after, it was added to the $Ca(OH)_2$ suspension in continuous stirring.

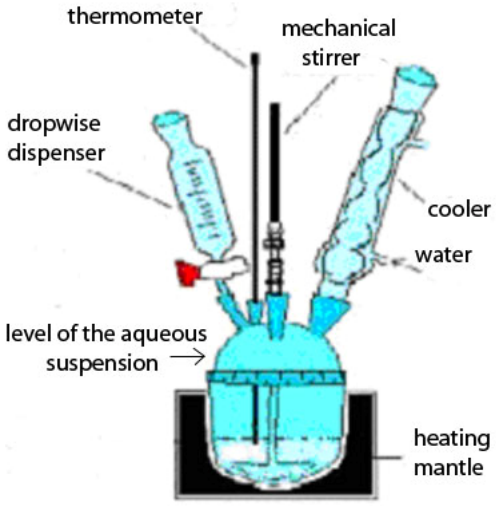

Figure 3.1. Equipment for the synthesis of HA powder.

The phosphate solution was prepared by adding 17.74 g of H_3PO_4 to 400 ml of H_2O and dripped into the suspension containing calcium and silicon. During synthesis, a white precipitate formed; after the dripping of the phosphate solution was completed, the precipitate was left to ripen and decant in the mother liquor for 24 hours, then the supernatant was eliminated and the cake-like product was washed three times in 1 litre of distilled water and centrifuged. The product was dried at low temperature (40 °C), in a ventilated oven in order to preserve the surface state and hydrophilicity of the powder[6], crushed in an agate mortar and sieved under 150 μm.

For the synthesis of silicon substituted carbonated HA (Si-CHA) a reaction vessel equipped with two separated dropwise dispensers, for the phosphate and carbonate-containing solution, was employed. The ion content in the reaction vessel was set up to

have Ca / P = 1.667, as in the synthesis of Si-HA. Powders characterized by different initial carbonate content (X_C) were prepared, while the initial content of silicon was 0.01 or 0.05.

For the synthesis of silicon-magnesium substituted HA powder (Si-MHA), a solution of magnesium chloride hexahydrate was prepared and mixed with the calcium hydroxide suspension at ambient temperature in the reaction vessel. Fixed amounts of silicon (X_{Si} = 0.05) and magnesium (X_{Mg} = 0.15) were selected.

Table 3.I. Amount of reagents employed in the synthesis of multi-substituted HA powders.

	$Ca(OH)_2$	H_3PO_4	$NaHCO_3$	$(CH_3COO)_4Si$	$MgCl_2 \cdot 6H_2O$	X_{Si}	X_{Mg}	X_C
Si-HA-1	20	17.74	---	2.07	---	0.05	---	---
Si-HA-2	20	17.74	---	4.15	---	0.10	---	---
Si-HA-3	20	17.74	---	8.30	---	0.20	---	---
Si-CHA-1	20	17.74	8.66	2.07	---	0.05	---	0.67
Si-CHA-2	20	17.74	1.94	2.07	---	0.05	---	0.15
Si-CHA-3	20	17.74	4.26	2.07	---	0.05	---	0.33
Si-MHA	20	17.74	---	2.07	7.86	0.05	0.15	---
Si-MCHA-1	20	17.74	8.66	2.07	7.86	0.05	0.15	0.67
Si-MCHA-2	20	17.74	1.94	2.07	7.86	0.05	0.15	0.15

The synthesis of silicon-magnesium substituted carbonated hydroxyapatite (Si-MCHA) was performed with fixed amounts of silicon (X_{Si} = 0.05) and magnesium (X_{Mg} = 0.15), while carbonate content (X_C) was 0.67 (Si-MCHA-1) and 0.15 (Si-MCHA-2).

Hydroxyapatite simultaneously substituted with strontium, silicon, magnesium and carbonate in biological–like amounts was synthesized by modifying the procedure above described, employing strontium nitrate ($Sr(NO_3)_2$) as a source of strontium[7]. The synthesis of one powder was performed (Sr-Si-MCHA), with X_{Si} = 0.05, X_{Mg} = 0.15, X_C = 0.15 and X_{Sr} (molar ratio Sr : Ca) set at the value of 0.20.

The employment of strontium in biomaterials has been already reported[8-12] and is of strong interest, as it is expected to increase the implant osteointegration, due to the reduction of bone resorption by osteoclasts and the stimulation of bone formation by osteoblasts[13-15]. Strontium is abundant in natural apatite minerals, but it is present only at ppm levels in the bone tissue, so that in higher amounts strontium can have significantly beneficial effects on bone balance in osteopenic animals[15]; this can also lead to an efficient effect in the

treatment of osteoporosis[15,16]. In Fig. 3.2 it is shown the effect of osteoporosis on bone trabeculae.

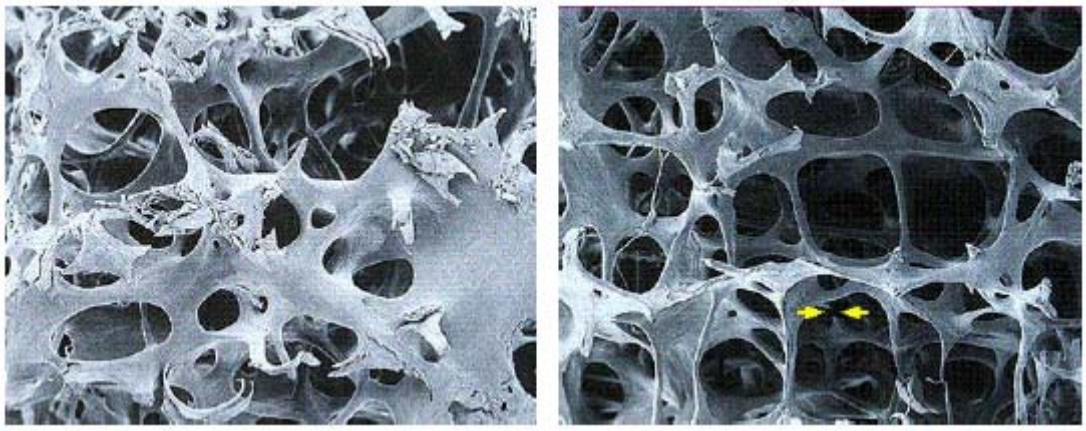

Figure 3.2. Effect of osteporosis on the bone trabeculae (right).

In the present synthesis, a high amount of strontium was tentatively introduced in the HA structure to test the capability of accepting strontium as substitute of calcium, in competition with other elements like magnesium and in presence of anionic substitutes, like carbonate and silicate.

Stoichiometric HA (HA_L), B-carbonated HA (CHA), magnesium-substituted HA (MHA) and HA substituted by both carbonate and magnesium (MCHA), were prepared as references to evaluate the discrepancies in physical-chemical behaviour of multi-substituted HA due to the different atomic substitutions.

The synthesis of these powders was carried out as above described: The Ca/P ratio was set to 1.667 in all powders, with $X_C = 0.15$ in CHA and MCHA, and $X_{Mg} = 0.15$ in MHA and MCHA.

3.2 Characterization of multi-substituted hydroxyapatites

The as-prepared HA powders were characterized by several analytical techniques (see also Chapter.2). X-ray diffraction was employed to evaluate the powder crystallinity and the occurrence and amount of secondary phases. All the spectra were collected with a scan step of 0.04 degrees, with 1s counting time.

The specific surface area (s.s.a.) of the HA powders was evaluated by the Brunauer-Emmett-Teller method. The powder density was measured by helium picnometer (Micromeritics 1305, USA). The particle size distribution was evaluated by electro-

acoustical spectroscopy. Electro-acoustical spectroscopy was also employed for the determination of ζ potential and electrical conductivity of the different HA powders as a function of pH: HNO_3 (1M) and KOH (1M) solutions were used to adjust the pH towards acidic and basic values respectively.

Fourier Transform Infrared Spectroscopy was used to check the occurrence of the typical functional groups present in calcium phosphate phases (phosphate, hydroxyl, water (adsorbed and structural), carbonate); in particular FTIR spectroscopy allowed to assess whether carbonation occurred in phosphate (B) and/or hydroxyl (A) position in the HA powders. All the samples were prepared by carefully mixing 1 mg of HA powder with 100 mg of potassium bromide by pestle and mortar; the obtained pellet was put in a ventilated oven at 130 °C for 2 hours, prior the spectrum acquisition, in order to eliminate the water adsorbed on the powder surface[6]; prior analysis, anyway, the pellet was briefly exposed to air atmosphere. Following this procedure, the water detected by FTIR analysis is more strictly related to the structural water characterizing the specific HA powder, as the contribution of the water adsorbed by potassium bromide is completely eliminated and the H_2O adsorbed by the HA surface is strongly reduced. All the FTIR spectra were obtained by averaging 32 scans collected in the wavelength range 400-4000 cm^{-1}, with a spectral resolution of 4 cm^{-1}.

The thermal behaviour of the powders was analyzed by thermo-gravimetric (TG) and thermo-differential (DTA) analysis: samples of about 10 mg of powder were weighed and put in an alumina crucible of about 180 mg in weight, positioned on one plate of the thermo-balance; an empty alumina crucible of similar weight was also present as a reference. The temperature was raised from ambient temperature up to 1350-1400 °C with a heating rate of 10 °C/min. In the evaluation of the TG curves a reference spectrum was subtracted, yielded by the empty crucible, to account for the buoyancy effects. The extent of the powders carbonation was evaluated by the weight loss in the range 500-1100 °C, due to the decomposition of carbonate groups with evaporation of carbon dioxide, and the corresponding stoichiometric coefficient of CO_3 anion was estimated considering that the highest possible degree of substitution of carbonate ions in the phosphate site (B-carbonation) is ~ 50 mol%, corresponding to ~ 21 wt% CO_3 loss[17].

The chemical composition of the powders was evaluated by inductively coupled plasma-optical emission spectrometry and energy dispersion spectroscopy applied to scanning

electron microscopy system, also employed for the investigation of the powder morphology. The samples for ICP analysis were prepared by dissolving 50 mg of powder, previously dehydrated in ventilated oven at 100 °C for 1 hour, in 10 ml of nitric acid solution (37 wt%); the sample solution was obtained by diluting with deionised water up to 250 ml in volume. A reference solution was prepared by mixing standard solutions containing the investigated atoms at the expected concentrations. An equally diluted solution of nitric acid was also analyzed and the corresponding spectrum subtracted by the experimental one.

EDS analysis was performed by uniaxially compacting the HA powder in a steel die; after, the so-obtained pellet was cold isostatically compacted under a higher pressure (200-300 MPa) to obtain a dense body, which is successively coated with a graphite layer prior to analysis.

An estimation of the chemical composition of the multi-substituted HA powders was performed, starting from the amount of carbonate present in B site (*x* stoichiometric coefficient), as evaluated from TG analysis; following, the molar ratio silicon : phosphorus found by ICP analysis allowed to evaluate the silicate stoichiometric coefficient (*y*):

$$\frac{Si}{P} = \frac{y}{6 - x - y} \qquad (2),$$

and consequently, the phosphorus, namely the quantity 6-*x*-*y*, calcium and magnesium content, obtained by the Ca/P and Mg/Ca molar ratios obtained by ICP analysis. The general equations expressing the chemical compositions of the obtained apatite phases, evaluated by the above-mentioned procedure, can thus be obtained.

Solubility tests were performed on the HA powders, granulated in the range 400-600 μm and immersed in simulated body fluid (SBF, Hanks' balanced salt solution H6648, Sigma Aldrich) thermo-stated at 37 °C. Granulated HA powders were obtained by spreading the loose HA powder on a paper sheet and humidifying with atomized deionised water; this procedure has to be repeated several times, alternating with a gentle mixing of the aggregate. Finally, the soft agglomerate was sieved by mechanical vibration through a 600 μm and 400 μm sieves: the fraction of granulate retained between these two sizes were collected and dried in a ventilated oven at 70 °C, prior its use.

Three grams of granulated powders were put in a beaker with 100 ml of SBF; pure SBF was continuously added by a peristaltic pump with a flow rate of 0.270 ml/min, while the

same amount was simultaneously drawn by the beaker containing the granulated powder, and stored (Fig. 3.3). This liquid medium, containing the products of granules dissolution, was taken away each 24 hours and analysed by ICP.

The duration of all the solubility tests was seven days. For each investigated HA powder the cumulative curves release of the different ions release (calcium, magnesium and silicon), calculated on relative weight over the whole HA (according to its formula, calculated as above explained), were built and the behaviour of the different multi-substituted HA powders were so compared.

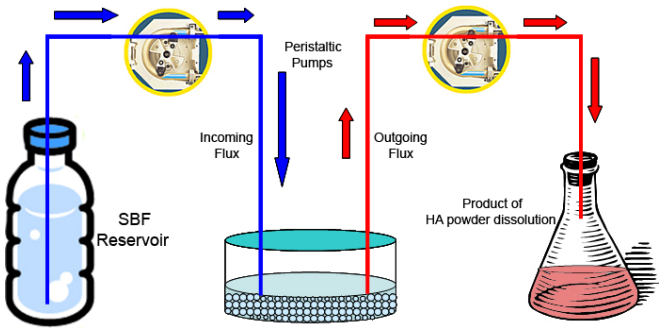

Figure 3.3. Equipment for solubility tests on multi-substituted HA granulates.

3.2.1 Phase analysis by XRD

Figs. 3.4-3.6 show the XRD spectra of the as obtained powders: the only crystalline phase detected is hydroxyapatite, on the basis of the ICDD card n° 09-0432, and no other calcium phosphate or silicate was found.

The XRD spectra of all the HA powders are typical of a low-crystalline phase; this is in agreement with the low temperature employed in the synthesis. The powder crystallinity can be directly estimated by the XRD spectrum following the procedure described in Landi *et al.*[18]

In Fig. 3.4 the comparison between the XRD spectra of HA_L and Si-HA with different silicon content (see also Tab. I) is shown. The powder crystallinity strongly decreased in powder with higher silicon content: in fact, the peaks sharpness in XRD spectra of Si-HA powders is lower and the peaks less resolved. Thus one can infer that the presence of silicon hampered the crystallization of HA phase and this can be due to the substitution of phosphate ions by silicate, and the simultaneous loss of stoichiometry for the elimination of OH^- ions[2].

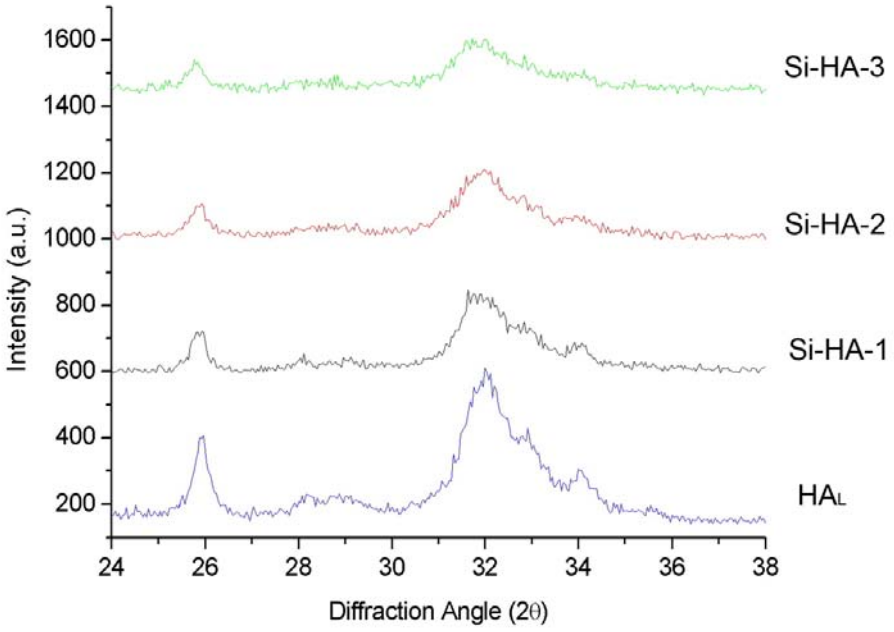

Figure 3.4. Comparison between XRD spectra of stoichiometric HA (HA_L) and Si-HA with different content of silicon.

In Fig. 3.5 the comparison between the XRD spectra of carbonated-hydroxyapatite (CHA) and silicon substituted CHA (Si-CHA) with different carbonate content is shown: a loss of crystallinity from CHA to Si-CHA is evident. The XRD spectra of Si-CHA-2 and Si.CHA-3 are comparable; conversely, the XRD spectrum of Si-CHA-1 is typical of an amorphous phase, with one peak corresponding to the inter-reticular distance of d = 0.303 nm, by applying the Bragg law (see Chapter 2), attributed to calcium carbonate (ICDD n° 05-0586).

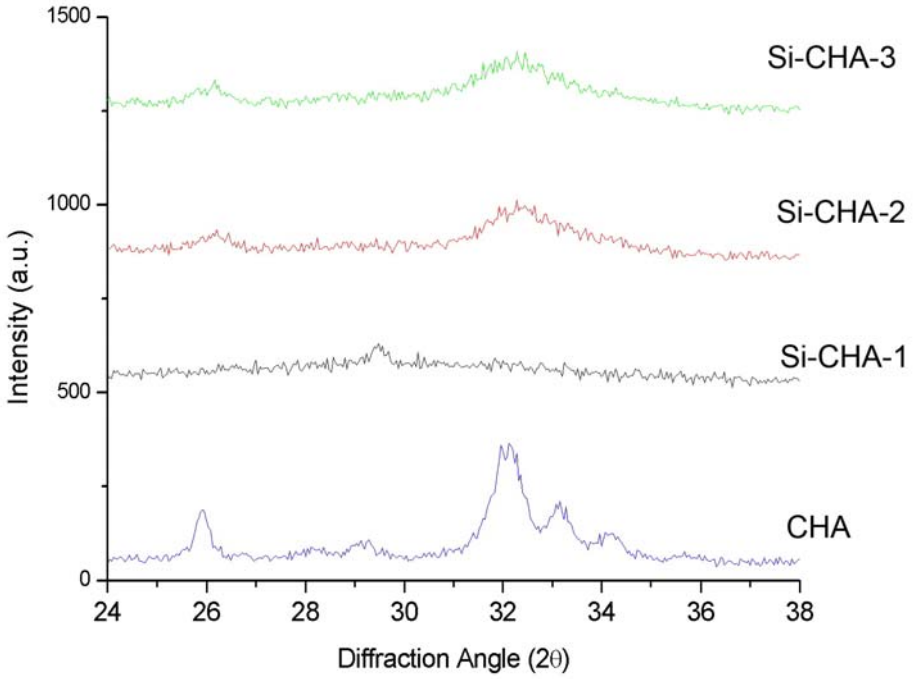

Figure 3.5. Comparison between XRD spectra of CHA and Si-CHA with different carbonate content.

For Si-CHA-1 an initial value of $X_C = 0.67$ was employed, to obtain highly carbonated apatite phase; it is known that the carbonation in B position reduces the stability and crystallinity of hydroxyapatite[19], as vacancies in the calcium site form in order to re-equilibrate the charge neutrality. Anyway, a silicon-free crystalline carbonated hydroxyapatite has been prepared using an initial $X_C = 0.67$ and no formation of calcium carbonate was detected. Thus, the formation of the ACP phase and calcium carbonate in Si-CHA-1 was probably due to the simultaneous substitution of silicon and carbonate in the phosphate site of the hydroxyapatite lattice; as the progressive reduction of the crystallinity leads to a nearly-amorphous phase, there must exist a limit of amount of foreign ions which can substitute phosphate without disrupting the crystal structure of HA; this limit depends on the type and amount of the foreign ions and in Si-CHA-1 it has been overcome. As the starting carbonate content was reduced in Si-CHA-2 and Si-CHA-3 samples, being constant the initial X_{Si}, the crystallization of the apatite phase took place and a fraction of the carbonate ions introduced in the reaction vessel was incorporated in its structure (see also Fig. 3.12).

Fig. 3.6 shows the comparison between the XRD spectra of magnesium-substituted HA (MHA) and MHA containing also carbonate and silicon (MCHA and Si-MCHA). The loss of crystallinity is rather less evident than in Si-CHA and Si-HA; the same behaviour can be observed by comparing the spectra of MCHA and Si-MCHA-2. As well as in Si-CHA-1, the simultaneous presence of different substituting ions yielded the formation of an ACP phase in Si-MCHA-1, synthesized with an initial $X_C = 0.67$ [20], and the crystallization of $CaCO_3$, owing to the carbonate present in the reaction ambient. In this case, anyway, the amount of carbonate formed was rather higher than in Si-CHA-1, as deduced by the higher intensity of the XRD peak of $CaCO_3$, compared with the profile of the amorphous phase. Considering that the initial amounts of silicon and carbonate were the same in the two powders, it is evident that the increase of the $CaCO_3$ content in Si-MCHA-1 is a consequence of the decreased limit of foreign ions which can be present in the reaction ambient without disrupting the crystal structure of HA, due to the simultaneous presence of magnesium also, which is known to reduce the crystallization process of HA[17,21-23].

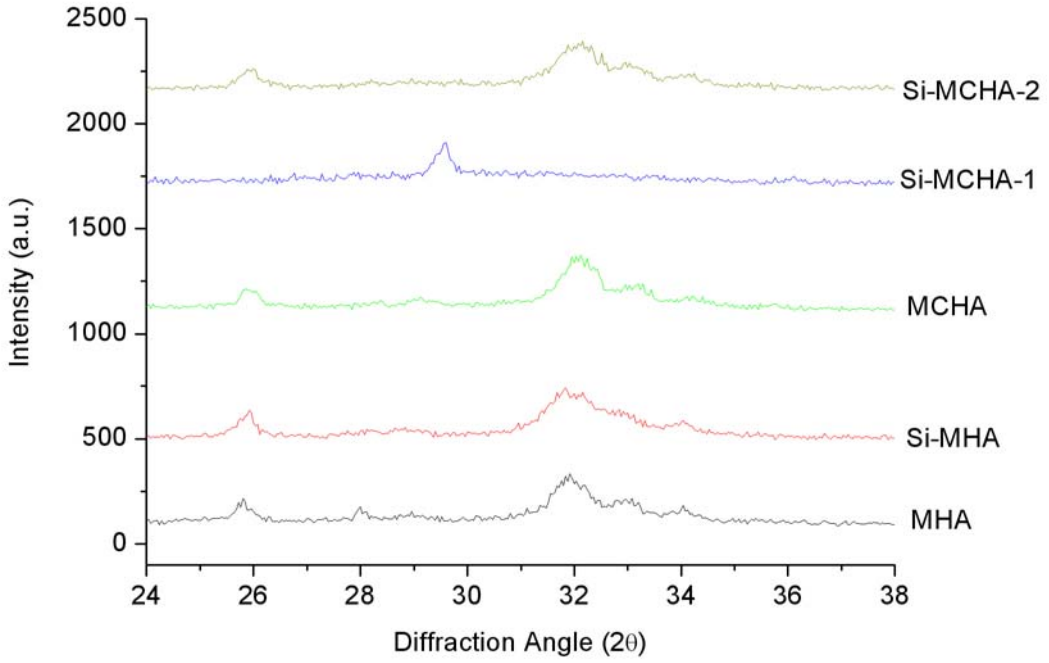

Figure 3.6. Comparison between the XRD spectra of multi-substituted HA powders containing magnesium, silicon and carbonate.

The pyrolysis of ACP at ~700 °C can yield the crystallization of the amorphous phase[20,24]; on this basis, a thermo-analytical spectrum was acquired to assess the actual temperature of

crystallization and, finally, small batches of Si-CHA-1 and Si-MCHA-1 were treated at 700 °C for 1 hour in a conventional furnace. Fig. 3.7 shows the XRD spectra of the powders after the thermal treatment: in Si-CHA-1, the main crystalline phase was HA, but $CaCO_3$ (ICDD card n° 05-0586) and CaO (ICDD card n° 037-1497), already present in the as-obtained powder, were also detected; in Si-MCHA-1 instead, a large formation of β-TCP occurred (ICDD card n° 09-0169), with only a few HA and residual calcite.

On the basis of LeGeros *et al.*[20], it is reasonable that the contemporary presence of carbonate and magnesium promoted the formation of ACP in Si-MCHA-1, and the higher sharpness of the DSC curve, compared to Si-CHA-1, is more similar to the exothermic peak found when thermally treating ACP on purpose synthesized[24]. It is as well confirmed that ACP formed in presence of magnesium exhibits the tendency to resist hydrolysis to apatite: in fact, a large amount of β-TCP formed with only a small amount of HA, although the starting Ca/P ratio was typical of a stoichiometric HA. In fact, the formation of $CaCO_3$ contribute to deplete the calcium reservoir for the formation of HA, so that the reduced Ca/P ratio favoured the formation of β-TCP.

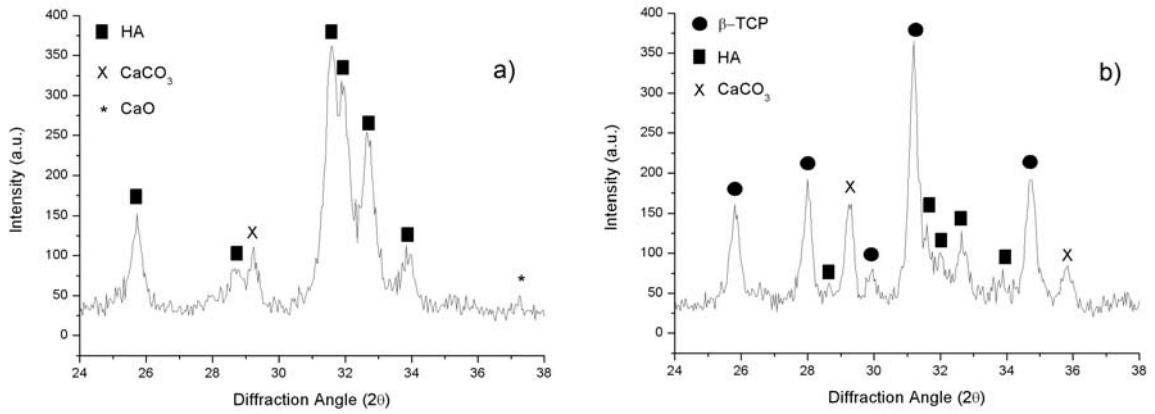

Figure 3.7. Crystallization of amorphous Si-CHA-1 (a) and Si-MCHA-1 (b) after treatment at 700 °C.

3.2.2 Chemical analysis by ICP

Table 3.II shows the results of the chemical analysis of the multi-substituted HA powders examined in this work: at the left side, the starting and the actual degree of atomic substitution in terms of molar ratios are compared; at the right side the related Ca/P molar ratios are reported. X_{Si}, X_C and X_{Mg} respectively indicate the molar ratios Si/P, CO_3/PO_4 and Mg/Ca.

In Table 3.III the weight fractions of each element on the whole HA phase are listed, evaluated on the basis of the chemical and thermo-gravimetric analyses.

Table 3.II. Chemical analysis of the multi-substituted HA powders.

Sample	Starting X_{Si}	Actual X_{Si}	Starting X_C	Actual X_C	Starting X_{Mg}	Actual X_{Mg}	Ca/P
HA_L	---	---	---	0.070	---	---	1.66
Si-HA-1	0.050	0.040	---	0.065	---	---	1.75
Si-HA-2	0.100	0.081	---	0.066	---	---	1.73
Si-HA-3	0.200	0.163	---	0.069	---	---	1.78
CHA	---	---	0.150	0.147	---	---	1.90
Si-CHA-1	0.050	undetected	0.670	---	---	---	---
Si-CHA-2	0.050	0.026	0.150	0.112	---	---	1.72
Si-CHA-3	0.050	0.006	0.330	0.111	---	---	1.79
MHA	---	---	---	0.054	0.150	0.053	1.61
Si-MHA	0.050	0.045	---	0.069	0.150	0.040	1.73
MCHA	---	---	0.150	0.150	0.150	0.045	1.82
Si-MCHA-1	0.050	undetected	0.670	---	0.150	0.135	---
Si-MCHA-2	0.050	0.028	0.150	0.135	0.150	0.046	1.81

The chemical analysis performed on the as-obtained HA powders confirms the presence of the doping atoms, namely silicon and magnesium; while the use of sodium hydrogen-carbonate allowed the entering of carbonate ions in the apatite structure: sodium was not detected in the powders, therefore it was eliminated during washing procedures.

Table 3.II shows that in Si-HA powders the silicon concentration approached the starting nominal Si values in term of X_{Si}: the efficiency of silicon substitution, i.e. the ratio between the actual and the initial X_{Si} was about 80%. In Si-MHA powder the substitution efficiency was even higher, while in Si-CHA samples it was related to X_C and more precisely it decreased by raising X_C, keeping X_{Si} constant.

A value of X_C=0.15 (Si-CHA-2) yielded a carbonate substitution of 75% of the initial amount, and simultaneously, ~50% of the silicon introduced; conversely, starting from X_C=0.33 (Si-CHA-3), the silicon present in the powder decreased up to ~10% of the initial amount and, correspondingly, the carbonate substitution was limited to ~35%. Finally, when X_C=0.67 (Si-CHA-1), as already described above, the crystalline apatite phase

structure collapsed: the silicon was completely eliminated during powder washing and no more detectable by ICP analysis.

Table 3.III. Weight fraction of the various elements in the multi-substituted HA powders

Sample	wt% of the elements on the apatite phase				
	Ca	P	Si	CO_3	Mg
HA_L	38.7	18.0	---	2.75	---
Si-HA-1	39.3	17.4	0.63	2.5	---
Si-HA-2	38.3	17.1	1.26	2.4	---
Si-HA-3	37.6	16.3	2.41	2.35	---
CHA	40.8	16.6	---	5.4	---
Si-CHA-2	38.5	17.3	0.41	4.1	---
Si-CHA-3	39.8	17.2	0.09	4.2	---
MHA	37.8	18.1	---	2.1	1.24
Si-MHA	38.6	17.2	0.70	2.6	0.96
MCHA	39.3	16.7	---	5.5	1.04
Si-MCHA-2	38.9	16.6	0.42	4.9	1.08

The behaviour exhibited by the Si-CHA samples revealed that a competition arose between the silicon and carbonate ion to occupy the phosphate site. The substitution efficiency of silicate to enter into the phosphate site even in non-artificially carbonated samples resulted <100%; this can be due to the presence of the above-mentioned spontaneous carbonation.

It is interesting the stabilizing effect of magnesium towards the other foreign ions: in presence of magnesium higher amounts of silicon (comparing Si-MHA with Si-HA-1) and carbonate (comparing Si-MCHA-2 with Si-CHA-2) were retained in the HA structure. Conversely, in presence of silicate and/or carbonate, a lower amount of magnesium could enter in the HA structure (compare Si-MHA with MHA and MHA with Si-MHA and Si-MCHA-2); in this case, carbonate seemed more influent than silicon in allowing the incorporation of magnesium. In Si-MCHA-1, containing ACP phase, a very high amount of magnesium was found; as $CaCO_3$ does not contain any magnesium, one can infer that almost all the magnesium introduced was incorporated in the ACP phase, as also described above.

3.2.3 Thermal analysis

Fig. 3.8 shows the thermo-gravimetric (TG) spectra of the multi-substituted HA powders. All powders show a similar behaviour: the carbonated HA powders (CHA and Si-CHA-2) exhibit a higher weight loss in the region 500-1100 °C, where the decomposition of carbonate takes place. All the powders without carbonate added, however, experience a weight loss of ~2,5 wt% (see Table 3.III), confirming the spontaneous carbonation revealed by FTIR analysis (see later, Fig. 3.12).

The strong weight loss occurring in Si-CHA-1 and Si-MCHA-1 in the region 500-1100 °C is evident (Fig. 3.9); however, most of the CO_3 decomposition occurred in the restricted region 650-750 °C. In fact, these powders are composed by an ACP phase and crystalline $CaCO_3$ in different amounts; a TG-DTA spectrum of pure $CaCO_3$ was acquired, revealing that CO_2 is exhaled in the restricted range 650-800 °C (Fig.3.10).

The DSC spectra exhibit inflections around ~700 °C, in particular in Si-CHA-1 the inflections are at ~620-630 °C and at ~715 °C, while in Si-MCHA-1, they were more net-shaped and at ~670 and 705 °C. On the basis of a previous study[24], the first inflection was attributed to the crystallization of ACP, while the second one, corresponding to the net weight loss occurring in both powders, was attributed to the decomposition of $CaCO_3$ and the evaporation of CO_2, on the basis of a TG-DSC of pure $CaCO_3$ acquired in the same range of temperature (Fig. 3.11).

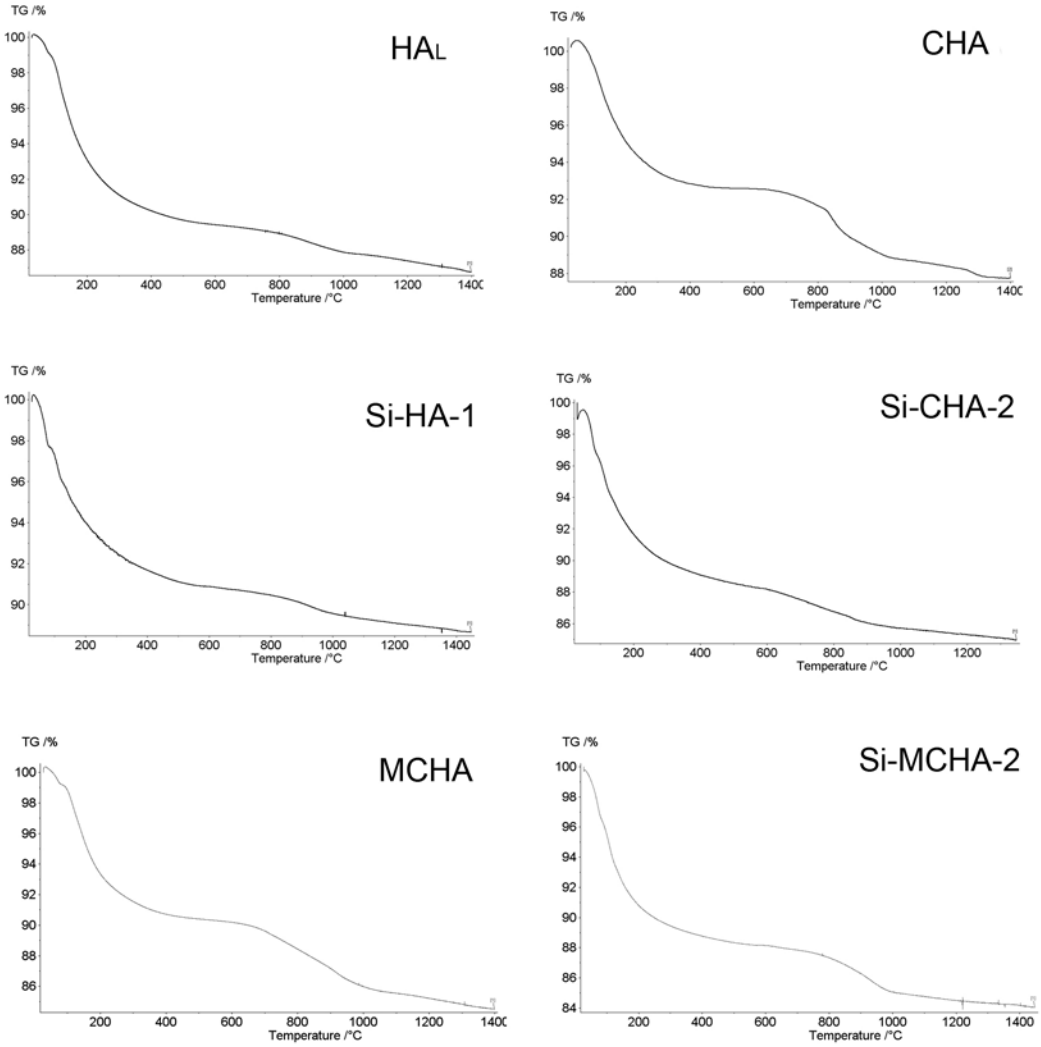

Figure 3.8. Thermogravimetric analysis of multi-substituted HA powders.

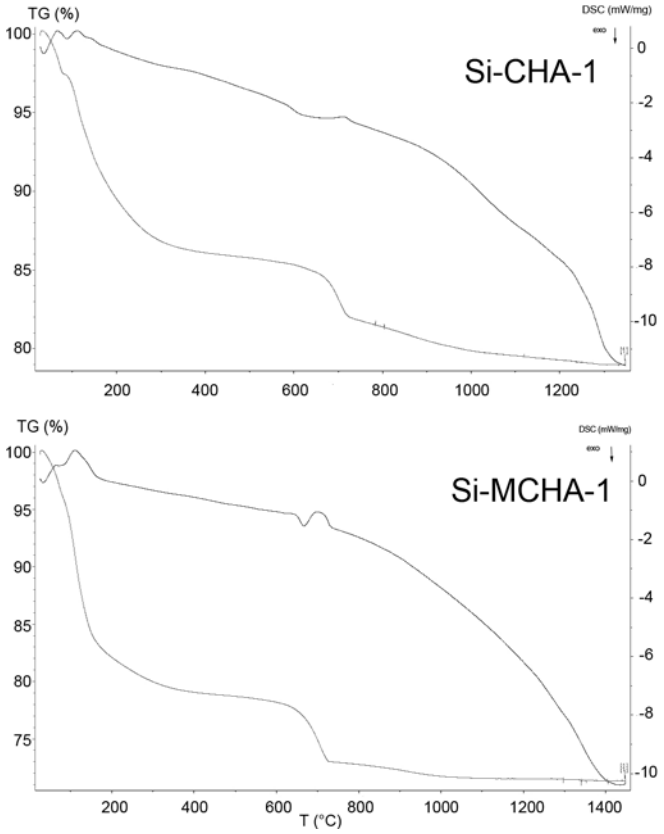

Figure 3.9. TG-DTA curves of Si-CHA-1 and Si-MCHA-1 powders.

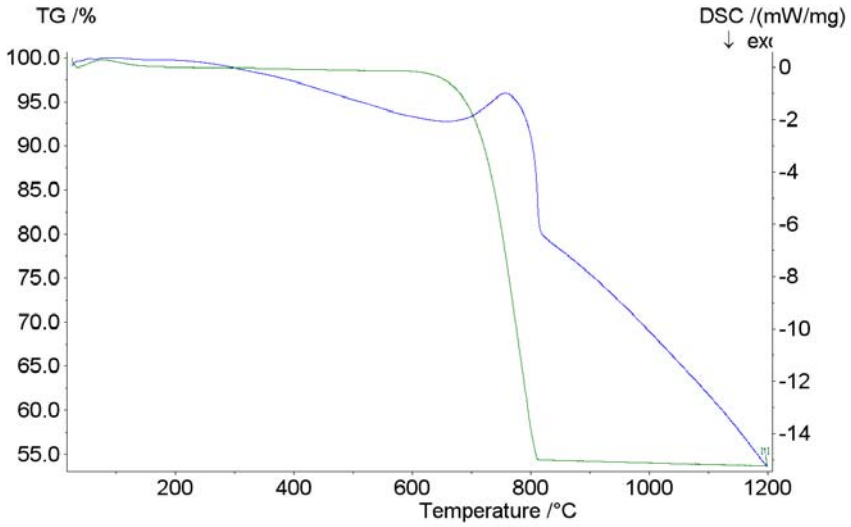

Figure 3.10. TG-DSC of pure $CaCO_3$ powder.

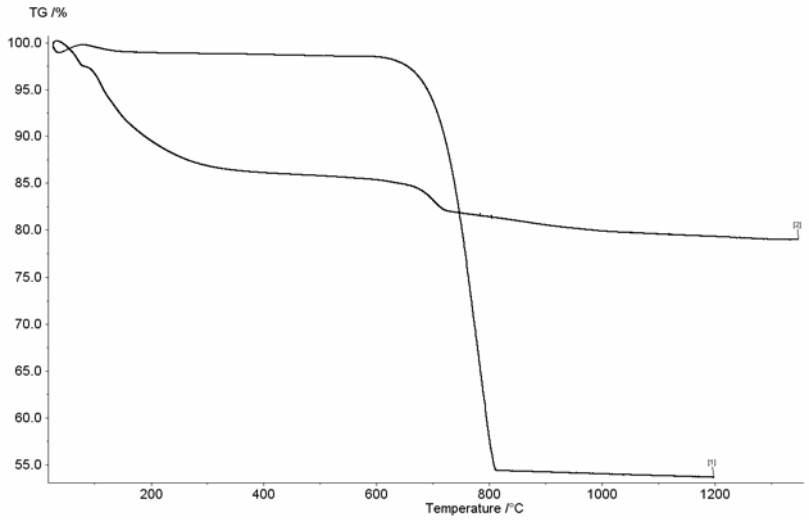

Figure 3.11. Comparison between TG spectra of Si-CHA-1 and $CaCO_3$.

It is interesting also to note the weight loss in the low temperature range between 100 and 400 °C (Tab. 3.IV); here, most of the adsorbed water is already eliminated, thus the weight loss is supposed to be due to the evaporation of the water more structurally bonded to the HA structure[25]. Again, Si-CHA-1 and, even more, Si-MCHA-1 exhibit a much higher weight loss in this temperature range, so that this phenomenon can be related to the incorporation of a higher amount of water in the ACP structure, released during the firing up to 400 °C.

Table 3.IV. Percent weight loss in the range 100-400 °C.

	HA_L	**Si-HA-1**	**Si-HA-2**	**Si-HA-3**
wt%	8.33	5.66	5.62	6.17
	CHA	**CHA_Si_1**	**CHA_Si_2**	**CHA_Si_3**
wt%	5.27	10.57	7.23	6.15
	MHA	**Si-MHA**	**Si-MCHA-1**	**Si-MCHA-2**
wt%	5.18	6.21	14.62	6.75

3.2.4 Chemical analysis by FTIR

The IR spectra of the investigated HA powders (Fig. 3.12) show the typical absorption bands related to the modes of phosphate (ν_2 bending, ~470 cm^{-1}; ν_4 bending, ~565 cm^{-1}; ν_1 sym stretch, ~960 cm^{-1}; ν_3 asym stretch, ~1035 cm^{-1}), hydroxyl (stretch,

~3570 cm^{-1}), water (bending, ~1635 cm^{-1}; sym+asym stretch, ~3410 cm^{-1}) and carbonate in B position (ν_3 bending, ~875 cm^{-1}; ν_3 stretching, 1417, 1455 cm^{-1}).

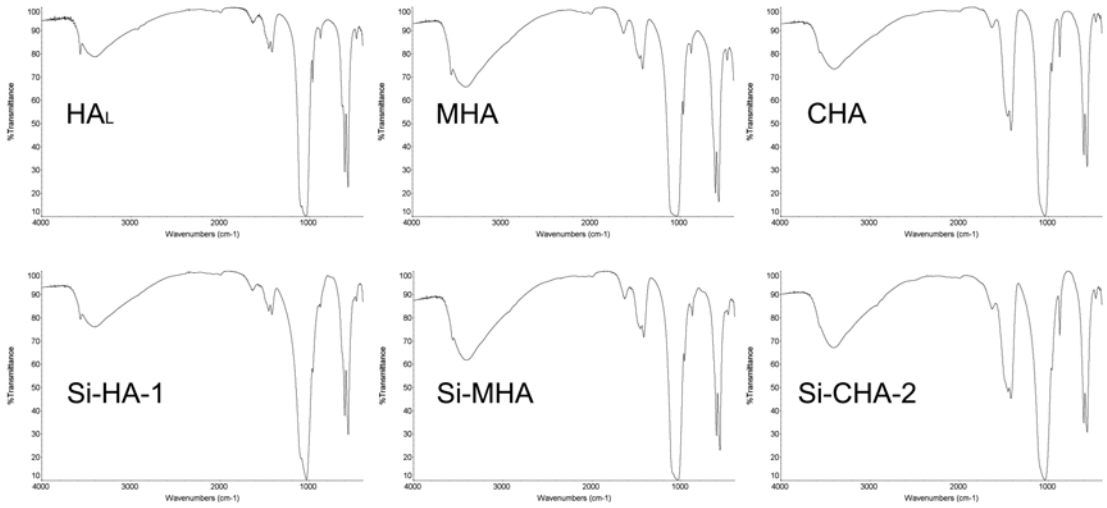

Figure 3.12. FTIR spectra of multi-substituted HA powders.

The $NaHCO_3$ as a reactant resulted efficient in yielding a high degree of carbonation of the apatite phase in B position. The typical bands related to B carbonation are also exhibited by HA powders obtained in absence of added carbonate, due to impurities present in the reactant calcium hydroxide, or to carbon dioxide present in the atmosphere and dissolved into the mother solution during powder synthesis.

A careful inspection of the IR spectra shows that a very small amount of carbonation in the hydroxyl site (A-carbonation) is present in all the investigated powders (see the shoulder at ~1540 cm^{-1}, which together with the signal at 1455 cm^{-1} corresponds to ν_3 stretching); notwithstanding, these powders can rightly be considered mainly B-carbonated. The carbonation in A site and the silicon substitution in the phosphate position provoke a reduction in hydroxyl content[2], as can be noted in Fig. 3.12 as the OH stretching band (~3570 cm^{-1}) is reduced in multi-substituted HA powders compared to the reference HA. The same effect is put in evidence in Fig. 3.13, where the IR spectrum of HA_L is compared with those of Si-HA powders characterized by an increasing silicon content (see also Table I).

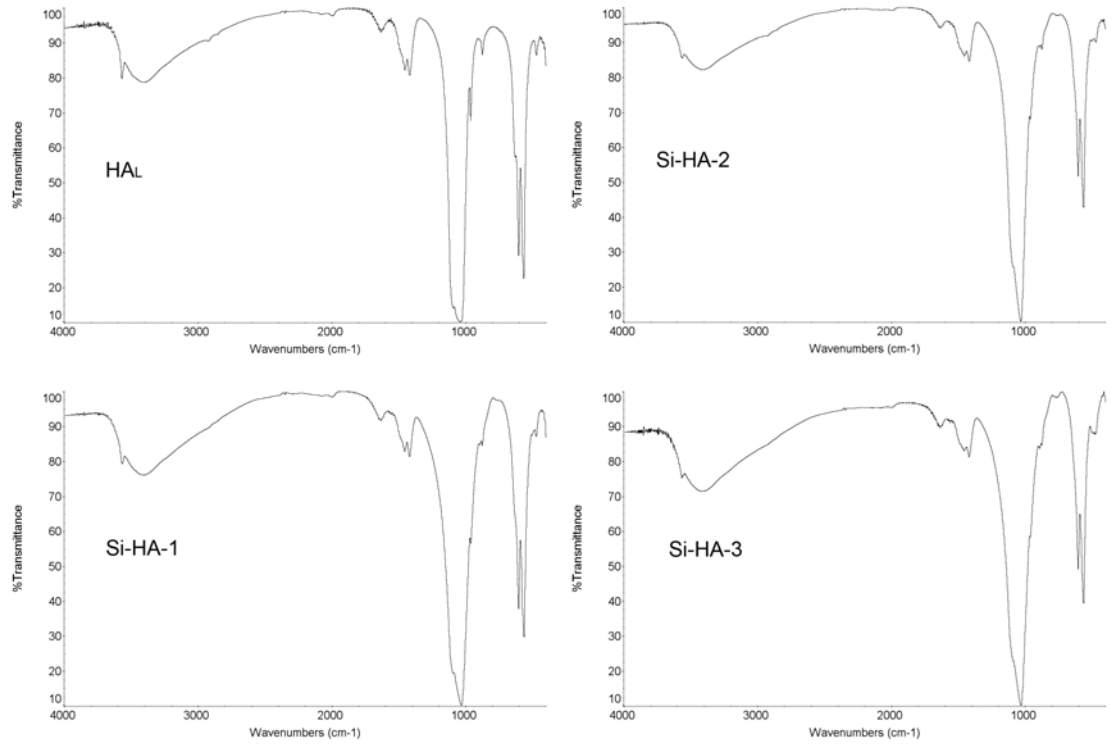

Figure 3.13. Effect of silicon on hydroxyl bands in Si-HA powders.

Fig. 3.12 also puts in evidence the different intensities of the FTIR adsorption bands of water at ~3410 cm^{-1}. It is observed that the IR bands of water exhibited by the HA powders containing magnesium are much more intense than in Mg-free HA powders.

Another interesting features can be noted by inspecting the FTIR curves of Si-CHA-1 and Si-MCHA-1 (Fig. 3.14): the adsorption band related to the stretching of water molecule at ~3410 cm^{-1}, especially for Si-MCHA-1, is much more broaden and intense, compared to the other multi-substituted HA. The band is also doubled, while for the other HA powders it appeared more like one single band. As TG analysis showed an increased weight loss in the 130-400 °C range, in HA powders containing ACP phase, it is confirmed that the amount of structurally bound water is increased in the presence of ACP; the double band appearing in the related FTIR spectra can reveal the presence of water molecules differently bound, with chemical bonds of different energies. The sample containing magnesium again exhibited a higher water content; these findings confirm the higher strength with which Mg-HA surface binds water molecules and consequently coordinates a higher number of water layers, compared to magnesium-free HA[25]. As concerns the silicon-substituted HA powders, there is no evidence of an analogous effect of silicon on

their surface properties, anyway further investigations are needed for extensively discussing this point.

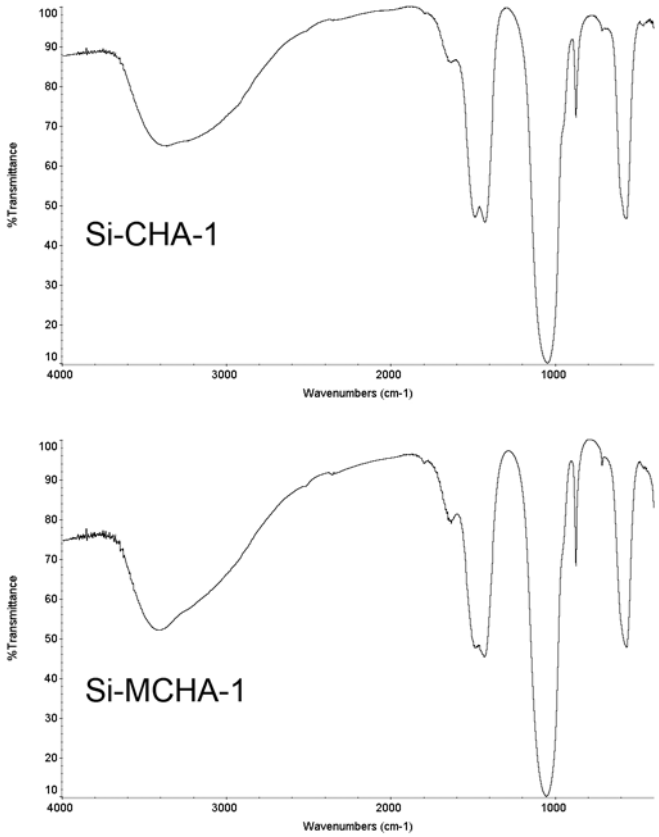

Figure 3.14. Water adsorption bands in Si-CHA-1 and Si-MCHA -1 powders.

Finally, two additional IR bands are also visible in the IR spectra of Si-substituted HA powders, situated in the range 490-505 and 890-895 cm^{-1}, respectively. Fig. 3.13 shows that the peaks intensities increase by raising the silicon content, thus their occurrence should be ascribed to modifications of the apatite structure induced by the presence of silicon. It is hard to assign such bands without further analysis, we can suggest however the existence of a bond between silicon and some impurities present in the reactants, like chloride and fluoride; such bonds give rise to strong peaks in the spectral regions where our additional peaks are located, as obtained by a computer simulation through the software IR Mentor Pro 6.5, by Bio-Rad Laboratories, Sadtler Division.

3.2.5 Powder analysis

The typical morphology of multi-substituted HA powders is reported in Fig. 3.15. The primary particles are well visible, they appear as elongated grains of about 30x70 nm and form a small agglomerate of ~300 nm in size.

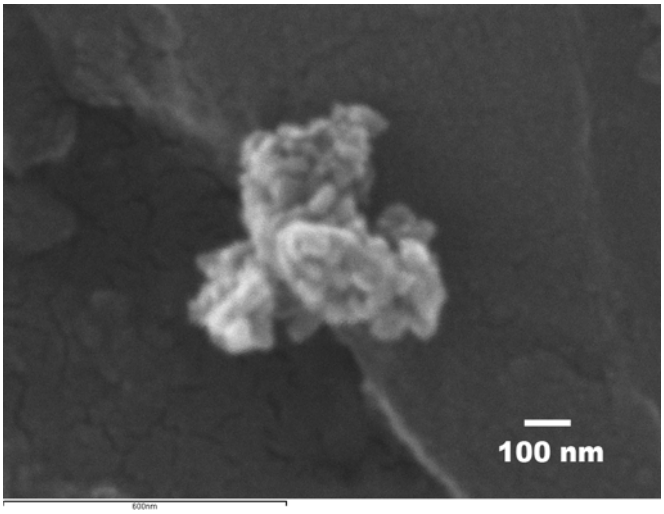

Figure 3.15. Typical morphology of a silicon-substituted HA.

Table…reports the results of particle size analysis in terms of specific surface area, obtained by BET (see Section 2.6.1) and powder density measurement, obtained by helium picnometry. Both measurements were carried out after a thermal treatment to eliminate the adsorbed water: for BET the heating was carried out in vacuum up to 200 °C, while for density measurement, the powder was previously treated at 130 °C for 1 hour in a ventilated oven.

An estimation of the particle size can be obtained, if we suppose that all the particles have the same sphericity, that is highly reasonable, by the following expression:

$$d = \frac{6}{\rho \cdot SSA} \qquad (3).$$

Table 3.V shows that the incorporation of ionic substitutes raised the specific surface area, contemporary decreasing the density of the powder. The mild heating did not eliminate all the water present in the powder, but only the one physically adsorbed on the powder surface, so the density value can be affected by the presence of lattice H_2O, differently formed between the HA crystalline domains.

Silicon-carbonated apatites exhibit the highest value of s.s.a. and, correspondingly, the smallest particle size; anyway the average particle size of the different HA powders resulted ~30 nm, irrespective of the chemical composition (Table 3.V), thus no conclusions can be derived on the effect of atomic substitutes on particle size and morphology. Anyway, the here detected particle size is in close agreement with the SEM investigations and the results found by Bertinetti[6], on the basis of TEM observations on HA powders characterized by different crystallinity.

Table 3.V. Particle characteristics in multi-substituted HA.

Material	Specific surface area (m^2/g)	Powder density (g/cm^3)	Estimated particle size (nm)
HAL	70.43	3.068	27.8
Si-HA-1	75.03	2.804	28.5
Si-HA-2	83.73	2.700	26.5
Si-HA-3	80.91	2.748	27.0
CHA	83.11	2.856	25.3
Si-CHA-2	182.86	2.573	12.7
Si-CHA-3	214.64	1.940	14.4
MCHA	89.54	2.789	24.0
Si-MHA	84.73	2.718	26.0
Si-MCHA-2	78.54	2.645	28.9

As-synthesized HA powders are typically very sensitive to moisture, thus they tend to easily form agglomerates (Fig. 3.16) as larger as the particle size is decreased, owing to the increase of the surface charge[18].

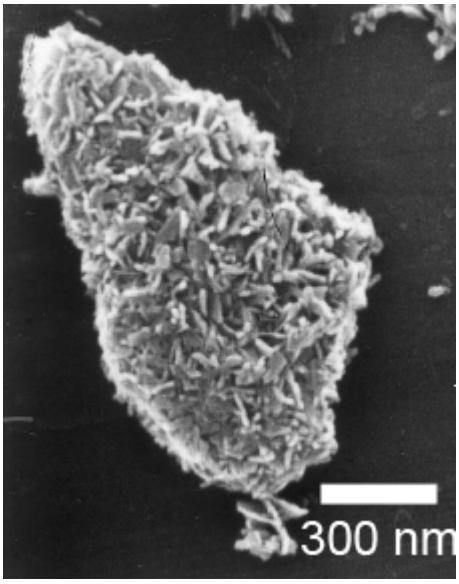

Figure 3.16. Self-agglomeration of HA powders.

A control of the degree of agglomeration of HA powders is crucial: in fact, highly stable powder suspensions in water are often needed to produce green dense or porous bodies to be subsequently sintered in three-dimensional devices, destined to be implanted. An excess of agglomeration soon provokes powder decantation and no stable suspensions can be obtained.

Electroacoustical spectroscopy is a powerful tool to investigate the state of powder surfaces (see Section 2.6.2); in the present work, the electrical conductivity and the particle size distributions of multi-substituted HA powders in aqueous solutions were evaluated.

Particle size distributions are described both in terms of differential (Fig. 3.17a) and cumulative fractions (Fig. 3.17b). The solutions containing the HA powders were analyzed after ultrasonic treatment.

In Fig. 3.17a, displaying the occurrence of a certain particle size in each HA powder, it can be seen that, except Si-CHA, all powders containing silicon are characterized by a particle size distribution described by a continuously decreasing curve. Conversely, the remaining powders exhibit agglomerates statistically distributed around a typical mean value; for all powders this value is below 300 nm, in particular HA is centred around 150 nm, Si-CHA at 200 nm, while CHA and MCHA have agglomerate centred at ~40 nm. On the basis of the previous data on effective particle size (Tab. 3.V), it can be deduced that powders seem to have undergone different extents of agglomeration. There is no clear relationship between the specific surface areas and the degree of agglomeration occurred in HA powders; anyway silicon-substituted HA showed a reduced tendency towards aggregation, as a large number of particles in their original size is still present.

In Fig. 3.17b the cumulative size distribution allows a better evaluation of the degree of agglomeration: HA, and even more Si-CHA confirmed to be highly agglomerated, with few particles below 100-150 nm. Among the remaining powders, silicon-containing HA confirmed their very reduced agglomeration: 80% of powder was below 30 nm, so virtually not agglomerated, and 90% was below 70 nm, which is the size of a group of 3-4 primary particles.

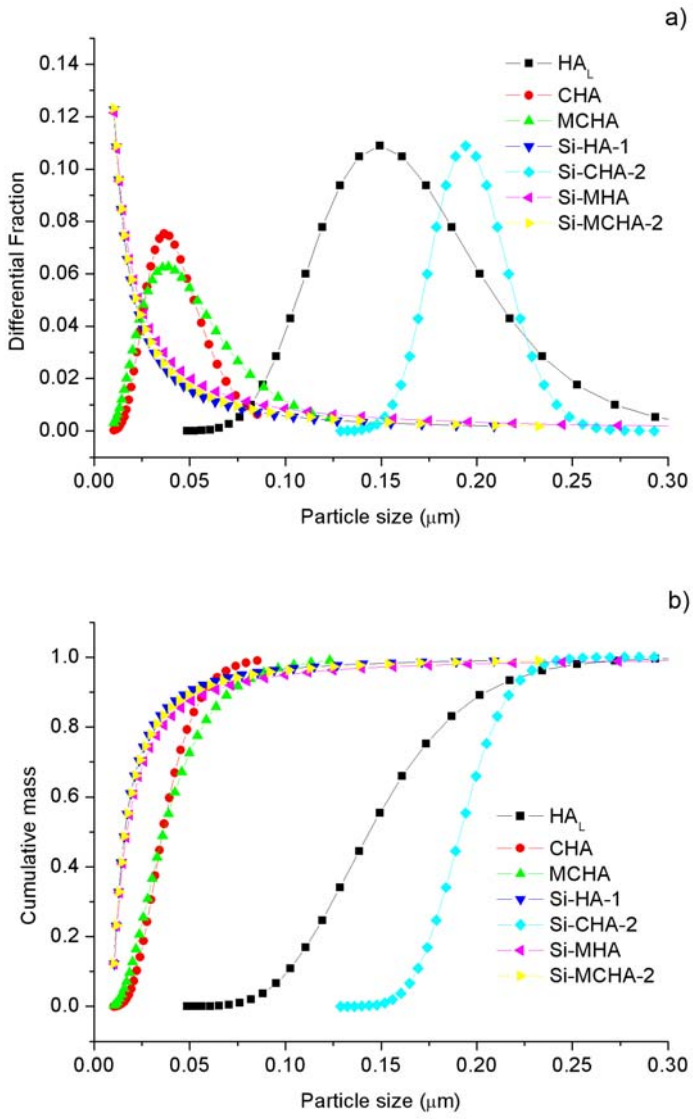

Figure 3.17. Particle size distribution of multi-substituted HA powders.: a) differential; b) cumulative.

Conductivity measurements were performed to evaluate the behaviour of powder under an applied electric field in liquid medium. pH was continuously varied during the analysis, towards both acidic and basic conditions.

It is of particular interest the region around neutral pH, as it is more similar to the physiologic conditions; towards acidic environment, at pH < 5, HA tends to dissolve and brushite ($CaHPO_4 \cdot 2H_2O$) is the most stable phase; in consequence of the HA dissolution, the increase of ions present in solution determined the enhancement of the conductivity.

Fig. 3.18 shows that all the investigated powders displayed similar conductivities. The powder containing the highest amount and type of substitutes, Si-MCHA-2, exhibited the highest conductivity values in the pH region 5 – 8, as also highlighted in the detail; this behaviour suggests an increased instability and solubility of this powder, especially at lower pH values. At physiological pH 7.4, anyway, this behaviour can reflect in a higher reactivity *in vivo*, i.e. higher resorption and release of biologically active ions which can yield a faster and more effective new bone formation with improved amount and quality of the new bone.

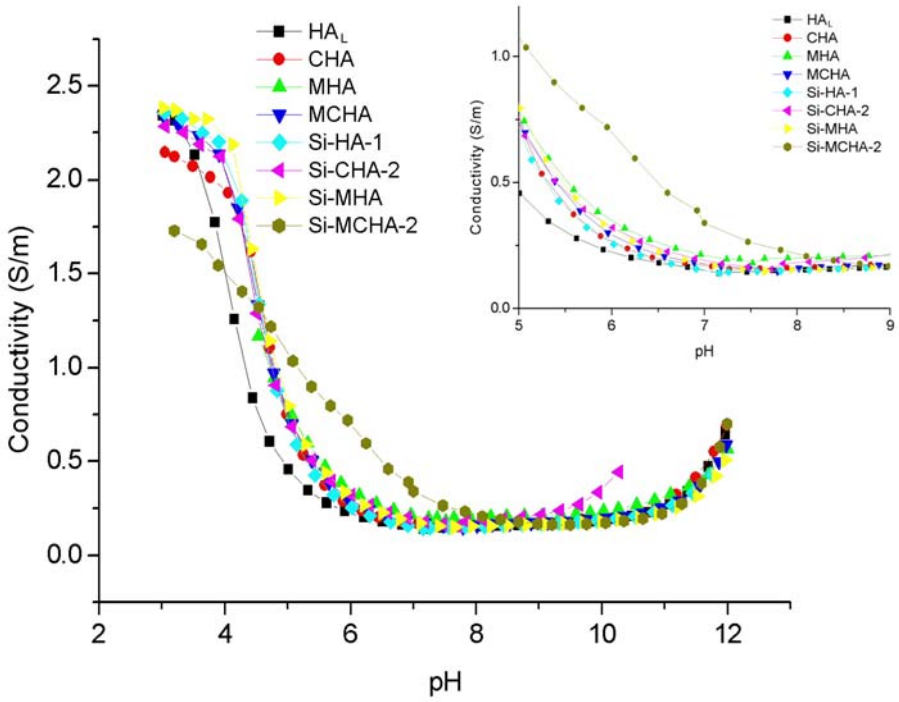

Figure 3.18. Electrical conductivity of multi-substituted HA powders.

In the detail, it is more evident the similar behaviour of multi-substituted HA powders in the region of neutral pH; the general increase of the conductivity in the region of acidic pH is reduced in the case of stoichiometric HA, which confirmed to be the most stable HA powder.

The characterization of the surface state of HA powders included also the determination of ζ potential.

The determination of the ζ potential is determinant in the set up of the optimal conditions to prepare powder aqueous suspensions, particularly the determination of iso-electric point,

corresponding to the point of zero charge, where no potential exists between particles and flocculation occurs.

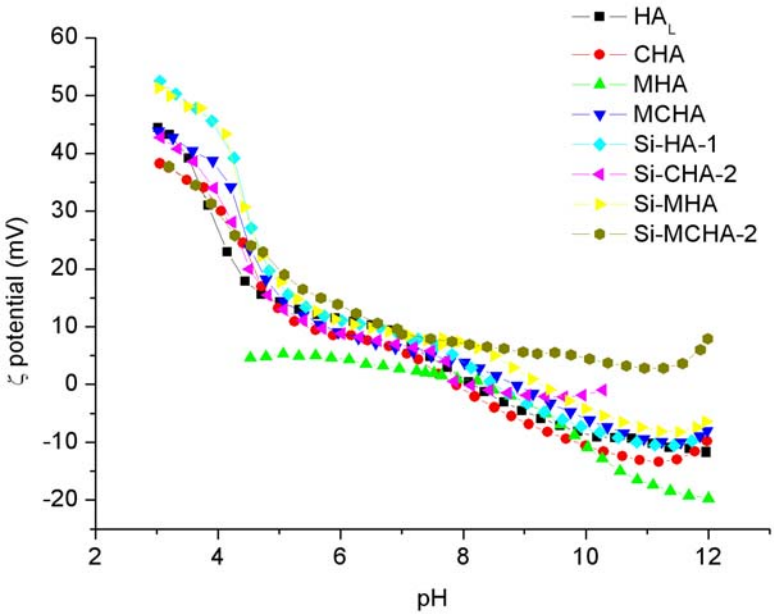

Figure 3.19. ζ-potential vs. pH of multi-substituted HA powders.

All HA powders exhibit a very small ζ potential in the neutral region (pH=7.4), becoming close to zero around pH ~8 (Fig. 3.19). The tendency to agglomeration is very high and decreases towards basic pH values, when ζ potential assumes negative values. The only exception is Si-MCHA-2, the powder with the highest doping, whose ζ potential never goes to zero. Towards acidic pH values, ζ potential slightly increases and becomes very high at pH< 4.5, in correspondence of the dissolution of HA in brushite. Commonly, specific deflocculating agents are employed for decreasing the ζ potential up to -30 ÷ -40 mV, so to have well dispersed powder suspensions, characterized by a high solid : liquid ratio. In this stage, electroacoustic spectroscopy is one of the most powerful tool for the setting up of the optimal conditions.

3.2.6 Solubility tests

Si-HA-1, Si-CHA-2, Si-MHA and Si-MCHA-2 powders, containing silicon in biological-like amounts (see Tab. II), were selected for solubility tests and compared with the corresponding silicon-free HA samples: HA_L, CHA, MHA and MCHA.

The amount of ions released by the selected granulated HA powders (granules size range: 0.4-0.6 mm, see Fig. 3.20) in SBF bath thermo-stated at 37 °C during seven days, are shown in Figs. 3.21-3.23: the plots display the ion dissolution with respect to the starting ion content.

In Fig. 3.21 the calcium release is shown: HA_L exhibits a limited calcium dissolution which saturates after less than 100 hours, accordingly with the very low solubility product of stoichiometric hydroxyapatite. MHA exhibits a slightly increased calcium release in the long term. Among the remaining powders, the release data address to a continuous powder dissolution characterized by an approximately linear trend. The HA powders containing silicon exhibit a more abundant calcium release with respect to the silicon free HA powders (Si-HA-1 vs. HA_L; Si-CHA-2 vs. CHA and Si-MHA vs. MHA).

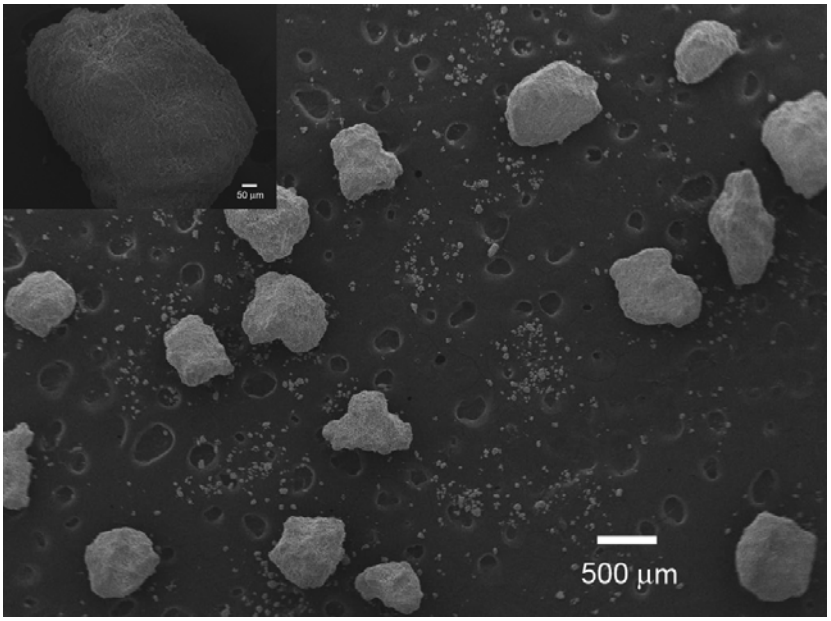

Figure 3.20. Typical morphology of a granulated HA.

The HA powders containing carbonate (CHA, Si-CHA and Si-MCHA-2) released a larger relative amount of calcium ions and the rate of release is more than doubled, compared to the carbonate-free HA (Si-HA and Si-MHA, see Tab. III). Finally, in MCHA, the presence of magnesium limits the release of calcium, compared with the other carbonate containing HA, but it is much higher than the carbonate-free HA.

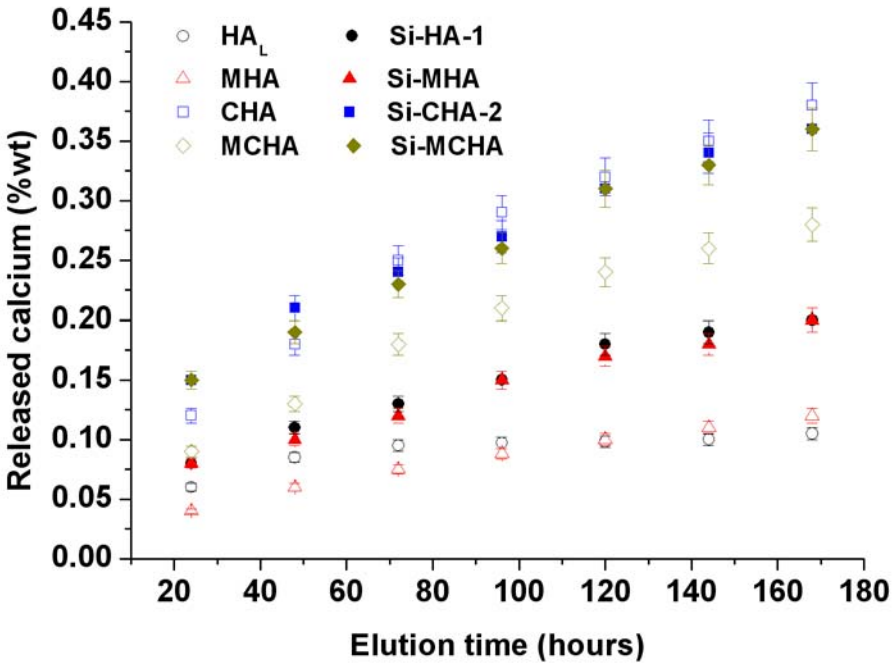

Figure 3.21. Cumulative release of calcium by multi-substituted HA powders.

The cumulative release of magnesium also followed a linear trend (Fig. 3.22), with a similar release rate (Tab. 3.VI); in this case, it is interesting to note that the magnesium-substituted apatite containing also silicon (Si-MHA) exhibited a strongly reduced magnesium release, even compared with the silicon-free powder (MHA). This feature suggests that in absence of carbonate, which strongly increases the solubility of the HA structure, the presence of silicon stabilized magnesium in the HA structure.

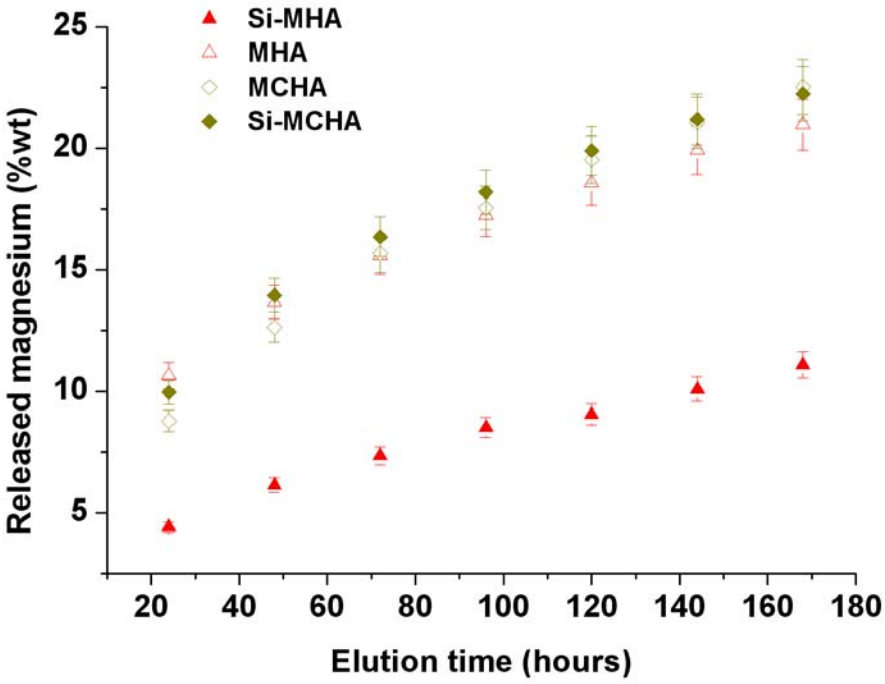

Figure 3.22. Cumulative release of magnesium by multi-substituted HA powders.

The same behaviour can be observed in Fig. 3.23, displaying the silicon release in multi-substituted HA powders: as expected, carbonate-containing HA powders exhibited the highest silicon release; moreover, with or without carbonate, the presence of magnesium stabilized silicon into the HA structure.

The mutual limitation of ion solubility involving silicon and magnesium suggests the formation of complexes containing these two ions, more strongly bound to the HA crystal structure or to its amorphous surface.

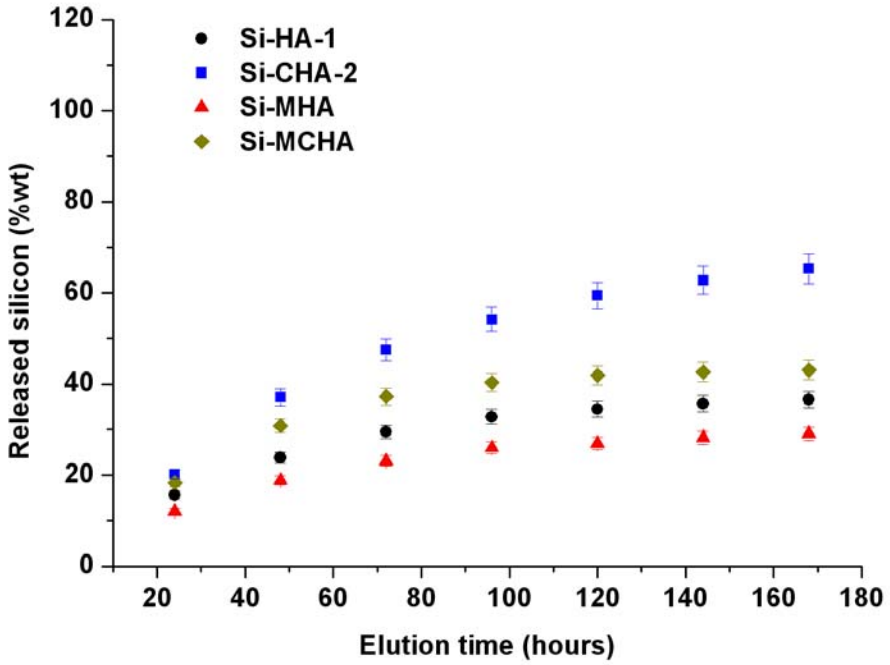

Figure 3.23. Cumulative release of silicon by multi-substituted HA powders.

Fig. 3.21 reports that in HA_L, the release of calcium was observed up to 96h (a) time range, see Table 3.VI) after immersion in SBF, while in the single and multi-substituted powders it prolonged continuously over the whole investigated period, with different release rates, on the basis of the curve slopes. In HA_L the early exhaustion of the calcium release confirms the low solubility product of stoichiometric hydroxyapatite,

The determination of the ion release kinetic in physiological-like environment is important for predicting the *in vitro* and *in vivo* behaviour of the biomaterial. In most cases, it was possible to interpolate the values of ion release with a straight line, so indicating the existence of a single mechanism of ion release in equilibrium with the SBF solution, kept continuously renewed.

The fit with a straight line was more efficient in case of calcium and magnesium release; calcium dissolved only in very small amounts, substituted HA exhibited up to 4 times the calcium dissolution than stoichiometric HA (Fig. 3.21); magnesium is released up to 25 % in a week (Fig. 3.22), in this case it was interesting the stabilizing effect of silicon, in absence of carbonate, but no significant enhancement of magnesium dissolution was found, although the release of Si-MCHA-2 was likely to be increasing for times longer than a week (Fig. 3.22).

The incongruent dissolution of calcium and magnesium in multi-substituted HA, compared to their composition, suggests that magnesium could be more likely present in the amorphous part of the HA particles, rather than replacing Ca; it is reasonable in fact that the amorphous layer surrounding the apatite grains dissolved within the first period of immersion in SBF leaving a more stable and less soluble core. Concerning HA_L, it can be supposed that the whole amorphous layer is dissolved within the first 100 hours; in substituted HA, characterized by a decreased crystallinity (see Figs. 3.4-3.6), the amorphous shell can be thicker and contain part of the substitute ions, yielding a more intense and prolonged release in SBF.

Alternatively, since magnesium has a higher affinity with water than calcium[25], its tendency to migrate outside the cationic site of HA can be enhanced in aqueous environment, so that atomic vacancies could be created in the HA structure. The increase of vacancies in the HA crystal structure could favour its phase decomposition above 1000 °C in β-TCP containing magnesium.

Silicon also was released in a much higher extent, compared to calcium and magnesium (see Figs. 3.21-3.23); as found for Mg-substituted HA[6], it is possible that part of silicon is situated in the amorphous layer, anyway deeper investigations are needed to confirm this assertion.

The release curves of silicon are not linear in the whole investigated time range, so indicating two different mechanism of release; they were considered in two different lapses of time: a) range 0-96 h and b) range 96-168 h; in this way, two approximate straight lines for the two time ranges were obtained.

Table 3.VI shows the solubility data in terms of release rate, measured by the slope of the straight line interpolating the experimental data; the accuracy of the interpolation is high, as the coefficient of correlation R^2 is very close to 1.

As expected, HA powders containing carbonate exhibit the highest release rates, it is also evident that the presence of other substitutes (magnesium, silicon) partially stabilized the release of calcium. Among the non-carbonated HA powders, a higher calcium release is detected in presence of silicon, rather than magnesium.

The release of magnesium is not enhanced in presence of silicon, comparing MHA and Si-MHA. Conversely, in presence of carbonate, the stabilizing effect of silicon towards magnesium is more evident; this is in agreement with the results found by the plots of ion

release, where the stabilization of magnesium by silicon in term of ion amount was evident.

The release rate of silicon is very high, compared to calcium and magnesium also, especially in the first stage (t<96 h). The highest rates of silicon release were detected in carbonated HA (Si-CHA-2 and Si-MCHA-2); again the mutual stabilization of magnesium and silicon was confirmed, as the release rate of Si-MHA is the lowest.

In the second stage, after four days, there is a strong decrease of silicon release rate; in this case, the highest effect was in Si-MCHA-2, while Si-CHA-2 exhibited again the highest value, although reduced at one third.

Even though there is still a lack of information about the surface and crystal states of multi-substituted HA powders, it is reasonable to guess that their different release kinetics are related both to the intrinsic solubility of HA, presenting several ion substitutes in its cell, and the characteristics of the amorphous shell around the crystallized apatite, in terms of thickness and composition, which can mediate the ion release from itself and the HA crystal.

Table 3.VI. Release kinetic data of multi-substituted HA powders in SBF at 37 °C.

Sample	Ca release		Mg release		Si release		
	Release rate ($wt\%\cdot h^{-1}$) $\cdot 10^{-3}$	R^2	Release rate ($wt\%\cdot h^{-1}$) $\cdot 10^{-3}$	R^2	Release rate ($wt\%\cdot h^{-1}$) $\cdot 10^{-3}$		R^2
CHA	1.8	0.97	---	---	---		---
MHA	0.6	0.99	69	0.97	---		---
MCHA	1.3	0.97	92	0.97	---		---
Si-HA-1	0.8	0.98	---	---	238(a)	52(b)	0.97
Si-CHA-2	1.4	0.98	---	---	469(a)	153(b)	0.97
Si-MHA	0.8	0.99	68	0.98	192(a)	44(b)	0.97
Si-MCHA-2	1.5	0.99	82	0.95	301(a)	24(b)	0.95

(a) and (b) indicate the first and second branch of the release curves of silicon, respectively.

The solubility behaviour of the multi-substituted HA powders is such that it is predictable that ion release can occur over a long period of time; this is an important finding in the viewpoint of *in vivo* application, as these materials, at physiological conditions, are able to continuously supply elements which are essential for osteoblast activity and new bone tissue formation and development. The simultaneous presence of many of such elements

can further enhance the cell activity; *in vitro* and *in vivo* investigations will be performed to corroborate this hypothesis.

3.3 Thermal stability of multi-substituted HA powders

HA powder can be used as-synthesized, in form of granulate, which can be implanted *in vivo* as a bone filler, and according to its bioactivity and bioresorbability, it can yield the development of new bone tissue. Many applications of bone healing need instead three-dimensional bodies, to be implanted *in vivo* as porous scaffolds, able to induce the proliferation of osteoblasts, with growing and osteointegration of new bone tissue. The general procedure to achieve consolidated ceramics is the pre-forming of a green body, subsequently consolidated through a thermal treatment of sintering. Since substituted HA phases usually exhibit a reduced stability to both chemical and thermal treatments, preliminary tests were carried out by sintering the multi-substituted HA at different temperatures between 1000 and 1400 °C and analyzed by XRD to assess phase decomposition, in comparison with stoichiometric HA.

In Si-HA powders an increasing fraction of α-TCP formed (ICDD card n° 29-0359), with the increase of the initial silicon content; at high silicon content, the decomposition starts already at 1000 °C (Fig. 3.24).

On the basis of Sayer *et al.*[26], the presence of silicon induces the formation of α-TCP at lower temperatures, compared with stoichiometric HA; moreover silicon partially substitutes phosphorus in the α-TCP structure; in the samples investigated in this work this tendency is confirmed, and the amount of α-TCP formed increased with higher contents of silicon.

Fig. 3.25 displays the increasing reactivity of Si-HA powders during thermal treatments; starting by the low temperature, the latent heat is well higher in Si-HA-3, a small inflection is visible at ~700 °C, in the region in which ACP usually crystallizes. Thus, it can be hypothesized that a certain amount of amorphous phase is present in silicon-substituted apatites, increasing with the silicon content. Above 1000 °C, the difference between the three curves is much more evident, due to the different extent of HA decomposition (Fig. 3.24).

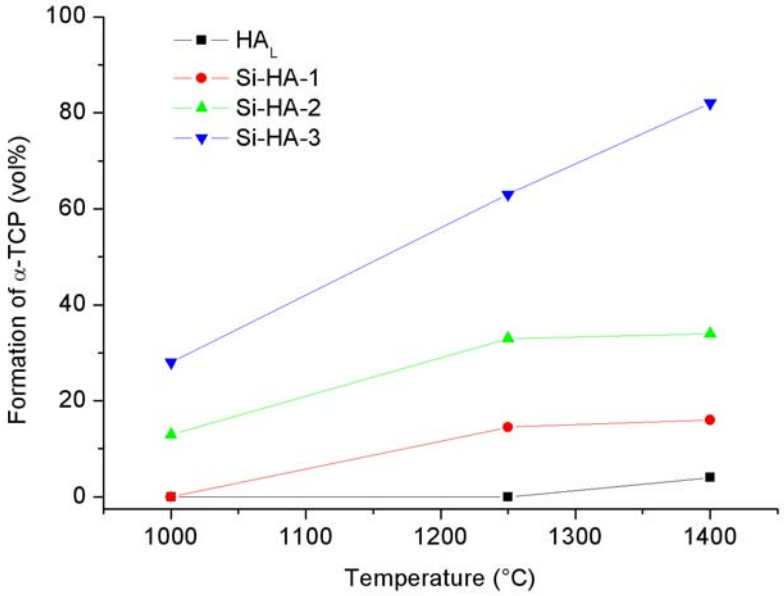

Figure 3.24. Effect of silicon on the formation of α-TCP after sintering.

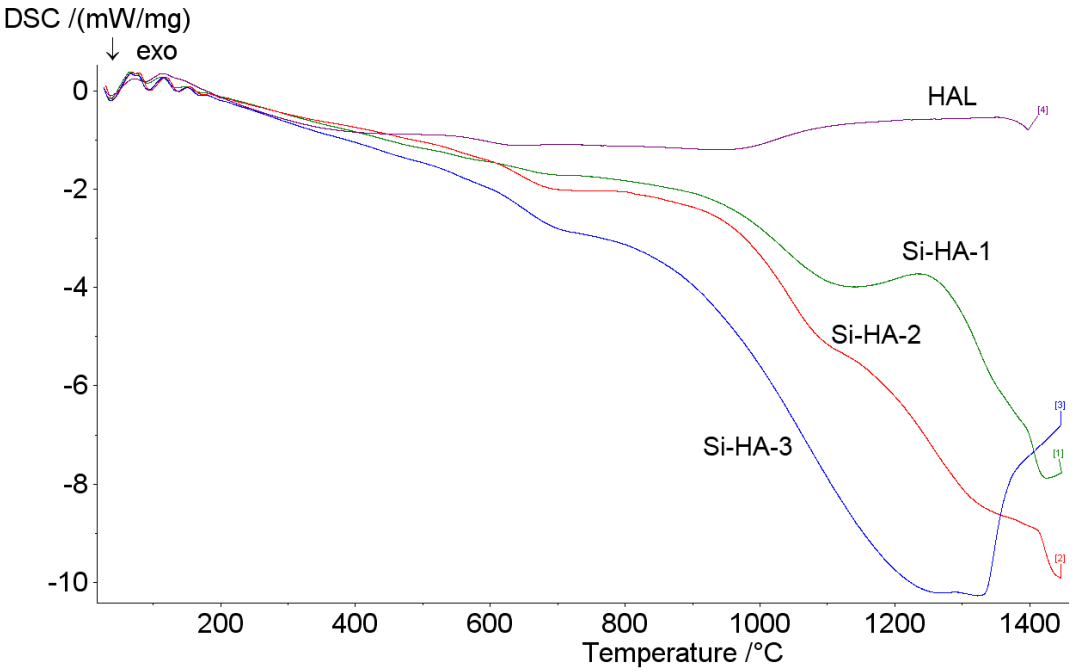

Figure 3.25. DSC curves of Si-HA powders.

The presence of carbonate stabilized the HA structure during the thermal treatments, even in presence of silicon (Tab. 3.VII). It was detected the formation of a limited amount of β-TCP, CaO and $CaCO_3$: in the initially amorphous powder (Si-CHA-1), the crystallization

of HA took place at ~700 °C; at higher temperatures, the residual $CaCO_3$ started to decompose, giving rise to a residual amount of CaO. The powders with less initial carbonate showed a high stability, with some residual calcium oxide and traces of β-TCP.

Table 3.VII. Phase transformation in Si-CHA powders during sintering.

	β-TCP	CaO	$CaCO_3$	Remarks
CHA				
1000 °C		<1		
1250 °C		1.5		
1400 °C	4	1.5		
Si-CHA-1				Amorphous
700 °C		2.5	5	
1000 °C		3.5	1.5	
1250 °C		5		
1400 °C		5		
Si-CHA-2				
1000 °C				
1250 °C	1.7	1.8		
Si-CHA-3				
1000 °C				
1250 °C	1.7	4.0	0.4	

Similar differences in the DSC curves are observed also in Si-CHA powders. The initially amorphous calcium phosphate (Si-CHA-1) crystallized at around 700 °C, as revealed by the inflection in DSC curve (Fig. 3.26). Such inflection is not visible in the other Si-CHA powders, but a wide endothermic phenomenon, extending up to 1000-1100 °C, and probably related to the decomposition of carbonate. The different behaviour revealed by the DSC curves cannot be related to the carbonate content as it is nearly the same in both powders; the most remarkable difference in the chemical composition of the two powders is their content in silicon (0.09 vs. 0.41 wt%), so that a variation in the kinetic of carbonate decomposition related to the presence of silicon could be hypothesized.

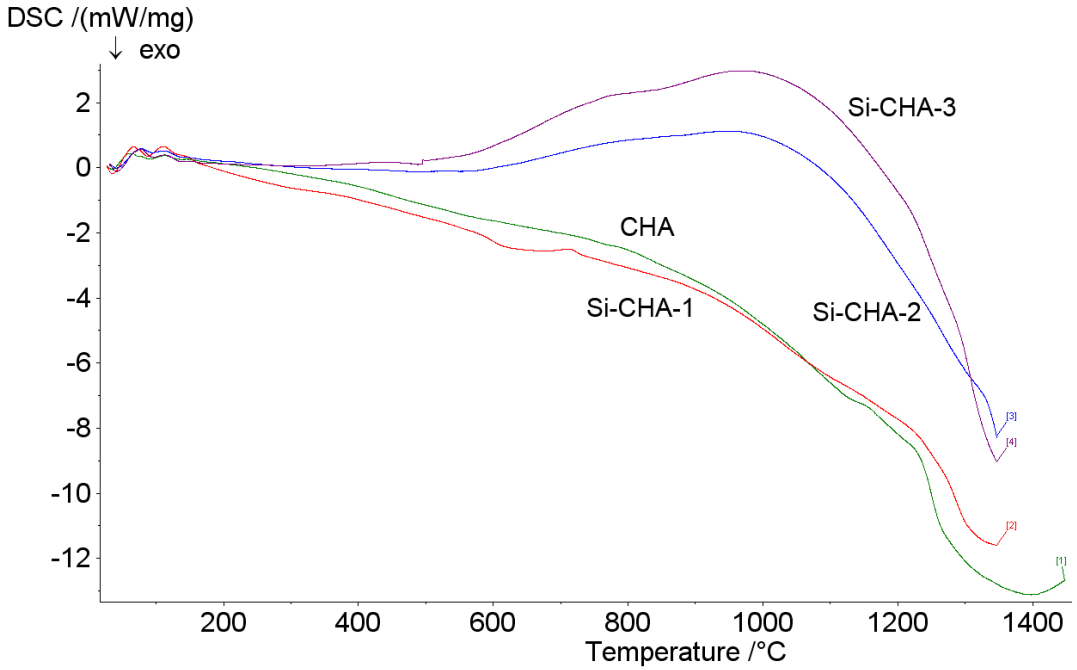

Figure 3.26. DSC curves of Si-CHA powders.

The presence of magnesium influenced the formation of secondary phases (Tab. 3.VIII). α-TCP formed only in small amounts at 1400 °C in Si-MCHA-2; instead, a large amount of β-TCP formed, induced by the presence of magnesium in Si-MHA[17]. In Si-MCHA-1, constituted by ACP and $CaCO_3$, a large amount of TCP formed already at 700 °C (see also above), strongly decreasing at the highest temperatures, when HA content simultaneously increased up to 96 % after sintering at 1400 °C. Few calcium oxide (< 3 vol%) was also detected. In Si-MCHA-2, the overall amount of secondary phase is very limited, so that the mutual stabilization of HA structure by the doping ions is evident.

The presence of silicon influences the reactivity of MHA powders, especially above 1000 °C (Fig. 3.27), where the formation of high amounts of β-TCP, probably containing the magnesium originally present in the HA structure, took place. DSC analysis confirms the higher thermal stability compared with MHA (Fig. 3.28); Si-MCHA-1 shows the inflection at ~700 °C, in correspondence with the crystallization of ACP. This powder, in comparison with Si-MCHA-2, exhibited very different behaviour during heating, on the basis of XRD analysis, but their DSC curves are very similar, suggesting that part of phenomena of β-TCP crystallization observed in Si-MCHA-1, took place during cooling.

Table 3-VIII. Phase transformation in Si-MHA powders during sintering.

	β-TCP	α-TCP	CaO	$CaCO_3$	Remarks
MHA					
1000 °C	22				
1250 °C	22				
1400 °C	18	14			
Si-MHA					
1000 °C	6				
1250 °C	29				
1400 °C	26				
MCHA					
1000 °C			0.5-1		
1250 °C			0.5-1		
1400 °C			0.5-1		
Si-MCHA-1					Amorphous
700 °C	74			7	
1000 °C	44			2	
1250 °C	11		3		
1400 °C	3		1		
Si-MCHA-2					
1000 °C					
1250 °C	9				
1400 °C	5.5	2.5			

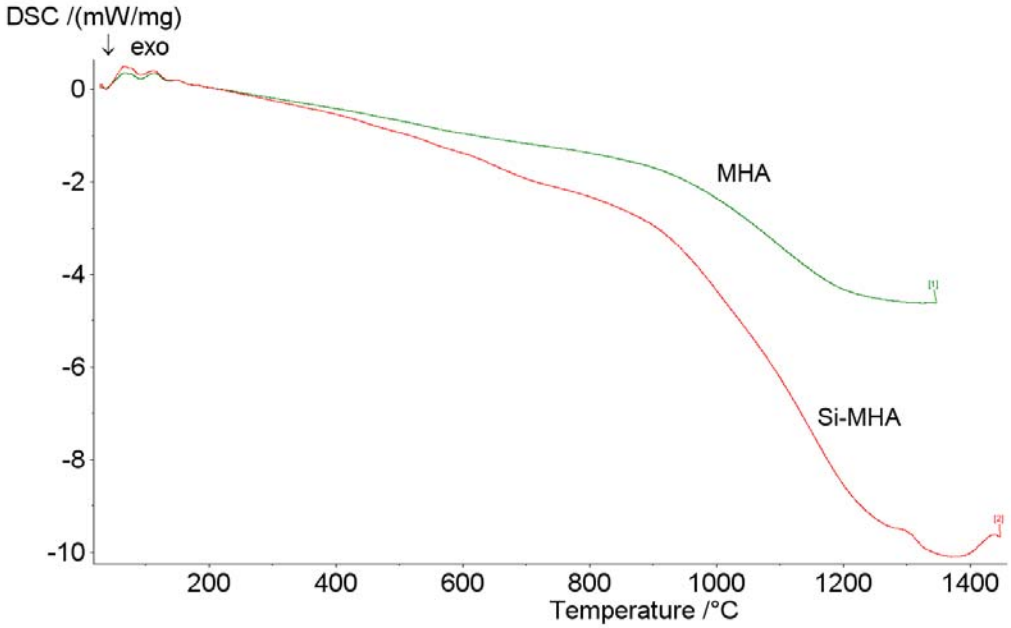

Figure 3.27. Effect of silicon on MHA powder.

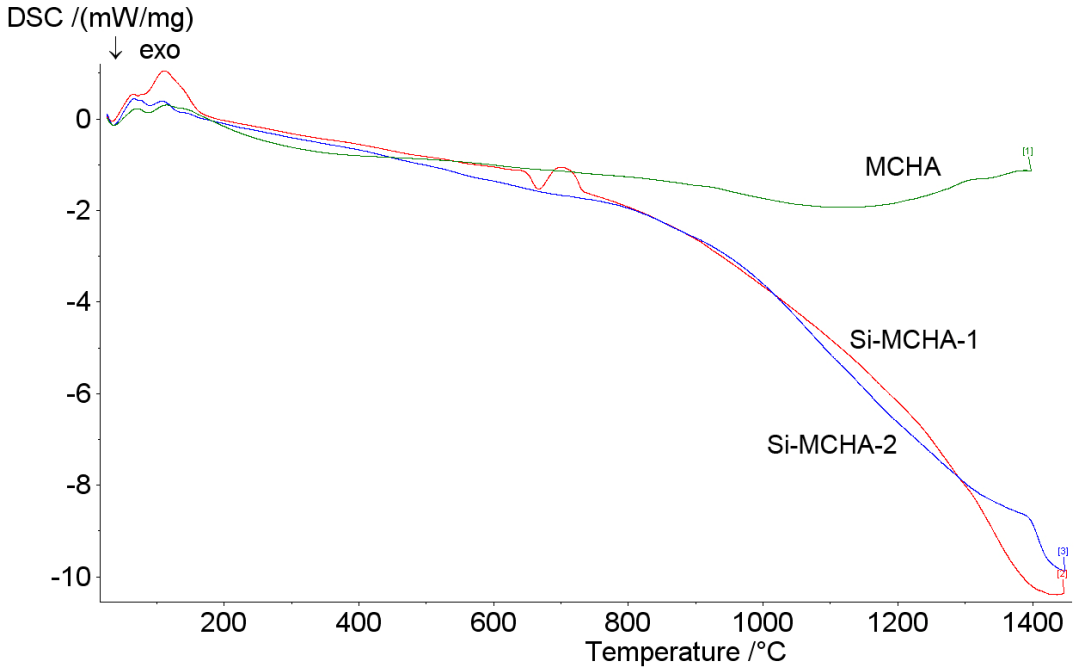

Figure 3.28. Effect of silicon on MCHA powder.

3.4 HA powder substituted with strontium, carbonate, silicon and magnesium

Chemical-physical characterization was performed by XRD, FTIR and ICP to assess the phase composition and purity after synthesis and the extent of phase decomposition after sintering at different temperatures.

The presence of four different ionic substitutes in anionic and cationic sites provoked the formation of ACP phase, as also occurred in other multi-substituted HA powders, characterized by an excess of carbonate (X_C=0.67, see above, Figs. 3.5, 3.6).

In these HA powders the excess of carbonate, coupled with the simultaneous presence of several ionic substitutes, was responsible of the lack of HA formation, yielding instead the formation of crystalline calcium carbonate also; in fact, the same typology of powders, successively synthesized with a reduced amount of carbonate (X_C=0.15), allowed the crystallization of HA, although its crystallinity was very low (see above, Figs. 3.5, 3.6).

In the present synthesis instead, ACP phase formed even in presence of reduced carbonate (Fig. 3.29) and neither $CaCO_3$ nor other crystalline phases were present. A number of mineral apatite phases containing a high number of foreign ions, including strontium, exist

in nature in a crystalline form; in this case, anyway, the high number of anionic substitutes, which strongly destabilize the apatite structure, coupled with three different atomic species in cationic sites, precluded the crystallization of HA.

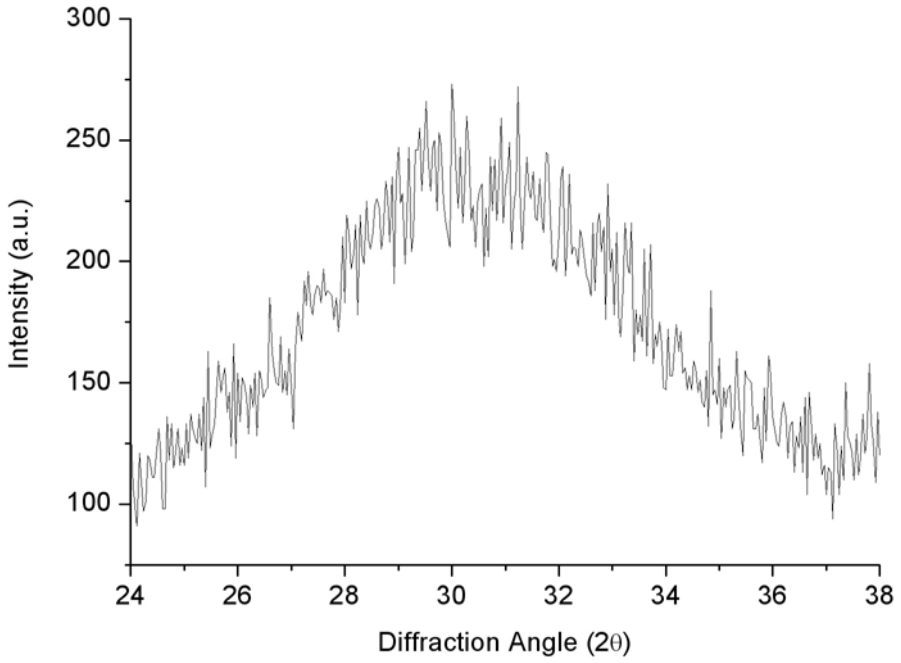

Figure 3.29. XRD spectrum of Sr-Si-MCHA powder.

The thermal analysis of the Sr-Si-MCHA powder confirmed the occurrence of the inflection at ~ 700 °C (Fig. 3.30), which should indicate the temperature of ACP crystallization, in agreement with the results described above.

For this reason, thermal treatments were performed on the as-prepared powder, at 700 °C or 1 hour, to investigate the phase formed after crystallization of ACP, and at 1000, 1250 and 1400 °C, to investigate the sintering behaviour at similar conditions as the above investigated powders.

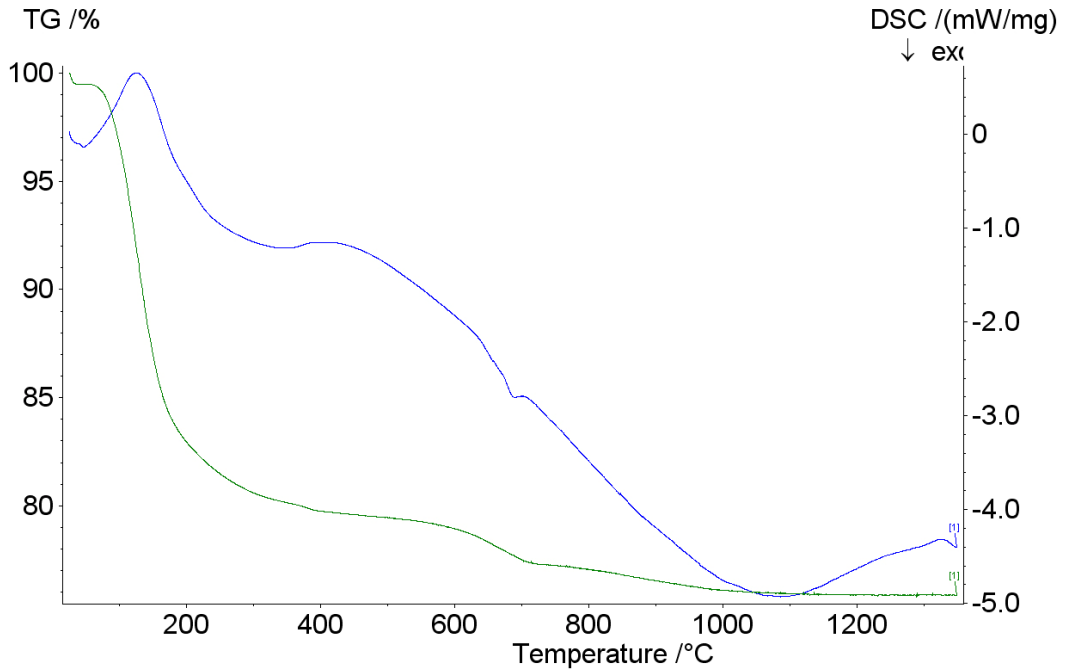

Figure 3.30. Thermal behaviour of Sr-Si-MCHA powder.

After firing at 700 °C, HA phase crystallized and no calcium carbonate (Fig. 3.31), nor other calcium phosphates or compound of magnesium and/or strontium were found.

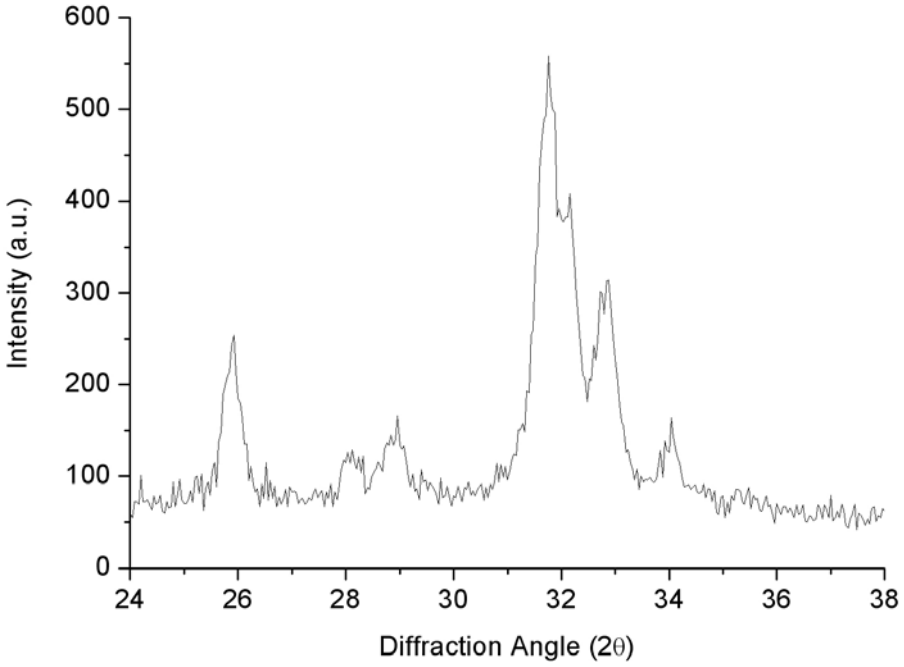

Figure 3.31. XRD spectrum of Sr-Si-MCHA fired at 700 °C.

β-TCP was detected after sintering at 1000 °C (~ 30%), slightly increasing up to 1400 °C (Fig. 3.32).

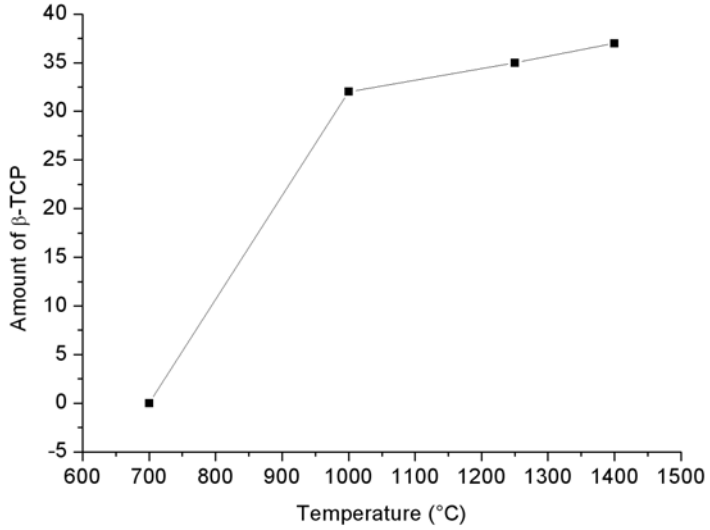

Figure 3.32. Formation of β-TCP in Sr-Si-MCHA powder.

The absence of any secondary phases in the as-crystallized HA, containing also silicon, carbonate, magnesium and strontium suggests that the composition of initial ACP must be the one of the apatite formed after firing at 700 °C; at this temperature only few of the carbonate present in the apatite is lost. For this reason the determination of the approximate composition of the powder by chemical analysis was justified, as performed with the other substituted HA.

Tables 3.IX and 3.X report the results of ICP analysis in comparison with powder with similar initial composition, so to evaluate the influence of strontium on the entering of the other substitutes.

The presence of strontium strongly limited the entering of silicon in HA structure, compared with any other HA powder here investigated; similarly, carbonate uptake was reduced, so that the general tendency of an increased carbonate uptake, in presence of cationic substitutes (see also Tab. 3.II) was not confirmed, in this case the presence of multiple cationic substitutions reduces the effect in the carbonate uptake, in comparison with single ion exchange.

Compared with Si-MHA and Si-MCHA, the presence of strontium enabled the uptake of a higher amount of magnesium, even compared to powder containing only magnesium, counterbalancing the negative effects of the anionic substitutes, silicate and carbonate.
Strontium itself is limited in entering into the HA structure, comparing with HA containing only strontium as substitute[11,12], only 40% of the introduced strontium was retained.

Table 3.IX. Chemical composition of Sr-Si-MCHA powder.

Sample	Starting X_{Si}	Actual X_{Si}	Starting X_C	Actual X_C
Sr-Si-MCHA	0.050	0.014	0.150	0.100
Si-MCHA-2	0.050	0.028	0.150	0.135
Si-CHA-2	0.050	0.026	0.150	0.112
Si-MHA	0.050	0.045	---	---
Si-HA-1	0.050	0.040	---	---
Sample	**Starting X_{Mg}**	**Actual X_{Mg}**	**Starting X_{Sr}**	**Actual X_{Sr}**
Sr-Si-MCHA	0.150	0.090	0.20	0.08
Si-MCHA-2	0.150	0.046	---	---
Si-MHA	0.150	0.040	---	---

Table 3.X. Weight fraction of the various elements in Sr-Si-MCHA powder.

Sample	wt% of the elements on the apatite phase					
	Ca	**P**	**Si**	**CO_3**	**Mg**	**Sr**
Sr-Si-MCHA	35.9	15.9	0.20	3.70	2.03	6.6
Si-MCHA-2	38.9	16.6	0.42	4.9	1.08	---

3.5 *In vitro* tests

3.5.1 Proliferation tests on Si-HA characterized by different silicon content

The evaluation of the effect of silicon on the cell proliferation in vitro using normal human osteoblasts as cellular model, was performed in collaboration with University of Parma, Department of Experimental Medicine, Histology Section.
The SiHA has been studied in the form of as-synthesised powders to choose the most critical conditions for the test (highest specific surface area of the material, thus highest reactivity conditions and ion release). The effect on the cells proliferation of different level

of silicon in Si-HA powders has been explored; in particular powders containing a biological amount (Si_bHA, like Si-HA-1) and the half value of the biological amount ($Si_{b/2}$HA) have been considered. The effect of the modification of the surface hydration consequent to the sintering process has also been investigated. Preliminary results showed that the as-synthesised HA powder substituted with the higher amount of Si and the sintered Si-HA were both toxic: the viability test (MTT) showed value lower than 20% compared to the control (100%) after 7 days. Cells observed at SEM showed high levels of sufferance. This is apparently in contrast to the results obtained by Botelho *et al.*[27], but in that study HA substituted with biological amount of Si in the form of dense pellet was analysed; thus, the reactivity and the biomaterial-cell interactive surface was highly lower and the test conditions less critical than in our case. $Si_{b/2}$HA showed a viability of about 75% , indicating a reduction of the proliferation compared to the control. However this was not due to toxicity but to involvement of cells in production activities. The ALP (alkaline phosphatase) test indicative of the osteoblast activity in the bone formation and regeneration, gave lower value compared to the control but high proteins levels, proportional to the number of cells have been detected. Thus the lower proliferation value can be related to the positive effect of $Si_{b/2}$-HA on the proteins of the matrix. Further investigation are in progress to assess what is the protein specifically involved (collagen?) and if new apatite nuclei will be synthesized by cells.

3.5.2 Cytotoxicity of multi-substituted HA powders

HA powders characterized by different simultaneous biomimetic substitution, i.e. carbonate, magnesium and silicon, can rightly be considered as very interesting and promising biomaterials for resorbable bone substitutes. Once assessed the biomimetic chemistry of the synthetic apatites, a subsequent step is the investigation of the cellular response, when in contact with surface of HA powder. Granulates of MHA and MCHA have been previously tested *in vitro* and *in vivo* and their improved performance compared to stoichiometric HA[28,29], induced by Mg and even more by co-substitution of Mg and CO_3, well assessed.

Si-MCHA-2 was selected as optimum material to be investigated by means of cytotoxicity test. The test was performed on the as-obtained material, after granulation between 400 and 600 μm, in similar way as in solubility tests; the reason for this choice is that granulated powder is currently employed as a bone filler, characterized by a high specific surface, i.e.

reactivity, thus the present test is a natural prologue to the *in vivo* experiments on animals. The tests were performed by the certified company BioLab SpA[1].

4 g of granulate was soaked into 20 ml of a culture medium, containing NCTC L929 fibroblast cells, in order to have a weight / volume ratio of 0.2 g/ml. The sample was incubated for 72 hours at 37 ±1 °C. After centrifugation, 2 ml of the extract were put in contact with the cultivated cells for 48 hours at 37±1 °C, in CO_2-containing air. After 24 and 48 hours, the cultivated cells were examined by optical microscopy to assess the cell activity.

After 24 and 48 hours of incubation, a low cellular activity was detected, corresponding to less than 20% of cells not presenting intracytoplasmatic granulations. In consequence of this, the investigated powder can be considered as slightly cytotoxic.

The results of cytotoxicity tests show that the granulate is bio-tolerated, as the cell reactivity was weak; the powder under investigation was characterized by optimal amount of magnesium, carbonate and silicon, and the results of this test suggests that the overall amount of released doping ions can be in excess compared to the needs of the cell culture. Anyway the behaviour of the biomaterial can be very different after *in vivo* implantation and the granulate can express good bioactivity and bone regeneration. This assumption has been verified in other cases, i.e. a material giving cell iperstimulation *in vitro* corresponded to very good behaviour *in vivo*; this is reasonable, as *in vitro* systems are static while the *in vivo* environment is dynamic, experiencing continuous flow and renewal of fluids.

Thus, further investigation shall be devoted to *in vivo* implantation of multi-substituted HA-based granulates for assessing the increased bioactivity and bio-resorbability.

3.6 Conclusions

Multi-substituted hydroxyapatite powders exhibiting very different chemical composition were successfully synthesized. The synthesis technique here employed was not difficult, not expensive and allowed to produce large amounts of powder; the substituting ions were introduced as soluble salts, while counter-ions eliminated (Cl^-, Na^+, NO_3^-, etc…) during powder washing and not incorporated in the HA structure.

In almost all cases, HA formed as the only crystalline phase, and the substituting ions were detected in biologic amounts or more abundant, so that the contemporary presence of many

[1] BioLab SpA, Via B. Buozzi, 2 20090 Vimodrone, Milano, Italy

foreign ions in the range of biomimetic composition is achievable. The comparison between the introduced and the actually found substituting ions in the different HA powders revealed their competition in occupying the same crystallographic site of calcium and phosphorus. The actual presence of the foreign ions in the HA structure was also demonstrated by their different solubility behaviour: carbonate confirmed to be the most important ion for the increase of HA dissolution in SBF; silicon and magnesium were continuously released over a long period of time, so that their presence in the extracellular matrix can provide enhancement of the new bone formation and adhesion. Silicon and magnesium showed to mutually stabilize in the HA structure; the reason for this behaviour is still not investigated, but it can be supposed that complexes containing these two ions can form as amorphous moieties on the HA surface. The influence of the different ions on the kinetic of their release in physiological environment is as well an important phenomenon to investigate, as the kinetic of ion release can influence the cellular response *in vivo*; a careful study of the surface state of HA powders is thus needed, for this purpose.
Finally, cytotoxicity tests, carried out *in vitro* on silicon-magnesium-carbonated HA, demonstrated that these materials are feasible for the development of bone fillers or materials for drug dispensers, even though a careful set-up of the overall phase composition of the powder can be needed, in order to avoid an excess of ions in contact with the extracellular matrix, with respect to the cell needs.
Three-dimensional ceramic bodies are needed to substitute whole portions of bone, including the ones subject to mechanical loads; for this reason, the thermal behaviour of multi-substituted HA powder was investigated, evidencing some limitations to the employment of these materials in high temperature treatments. Nevertheless, the stabilization of the HA structure, due to the mutual effect of different doping ions, opens the way to a possible achievement of sintered HA, characterized by the presence of different substituting ions in its structure.
In alternative, it is possible in principle to obtain consolidated bodies made with substituted HA by solid state reaction at high temperature between stoichiometric HA and a ceramic phase containing biomimetic ions. The development of such composite materials will be possible if no secondary calcium phosphates will form during the sintering of the mixture, altering the phase composition and bioactive properties in an unpredictable manner. The resulting material should exhibit good biomimetic properties, to ensure a proper activation

of the bone remodelling processes, so that the secondary phase added to HA should also exhibit bioactive properties.

Thus, following the development of biomimetic HA powders to be used as-prepared in bone filling surgery, the future research in this field will be mainly addressed in the obtainment of sintered HA, characterized by an adequate level of doping and a minimal formation of secondary phases.

In the next Chapter the development of bioactive composites made by HA and calcium silicates will be discussed, taking advantage of the bioactive properties of calcium silicates and their higher mechanical strength compared with HA, so to be promising for the development of load-bearing bioactive / bioresorbable bone implants.

References

1. Sprio S, Tampieri A, Landi E, Sandri M, Martorana S, Celotti G, Logroscino G. Physico-chemical properties and solubilità behaviour of multi-substituted hydroxyapatite powders containing silicon. Mat Sci Eng C 2008; 28: 179-187.

2. Gibson IR, Best SM, Bonfield W. Chemical characterization of silicon-substituted hydroxyapatite. J Biomed Mater Res 1999; 44: 422-428.

3. Ruys AJ. Silicon-doped hydroxyapatite. J Aust Ceram Soc 1993; 29: 71-80.

4. Kim SR, Riu DH, Lee YJ, Kim YH. Synthesis and characterization of silicon substituted hydroxyapatite. Key Eng Mater 2002; 218-220: 85-88.

5. Kim SR, Lee JH, Kim YT, Riu DH, Jung SJ, Lee YJ, Chung SC, Kim YH. Synthesis of Si, Mg substituted hydroxyapatites and their sintering behaviours. Biomaterials 2003; 24: 1389-1398.

6. Bertinetti L. Nanomateriali per applicazioni biomediche: sintesi e caratterizzazione delle funzionalità di superficie. PhD thesis, University of Torino.

7. Landi E, Tampieri A, Celotti G, Sprio S, Pressato D, De Luca C. A plurisubstituted hydroxyapatite and the composite thereof with a natural and/or synthetic polymer, their preparation and uses thereof. International Patent, Application N° PCT/IB2006/002844, 12/10/2006.

8. Guo D, Xu K, Zhao X, Han Y. Development of a strontium-containing hydroxyapatite bone cement. Biomaterials 2005; 26: 4073-4083.

9. Zhao F, Lu WW, Luk KDK, Cheung KMC, Wong CT, Leong JCY, Yao KD. Surface Treatment of Injectable Strontium-Containing Bioactive Bone Cement for Vetebroplasty. J Biomed Mater Res-Part B Appl Biomater 2004; 69: 79-86.

10. Leroux L, Frèche M, Lacout JL. Calcium phosphate cement to prepare Sr-containing biomaterials. Key Eng Mater 2001; 192-195: 235-238.

11. Landi E, Tampieri A, Celotti G, Sprio S, Sandri M, Logroscino G. Sr-subtituted hydroxyapatites for osteoporotic bone replacement. Acta Biomater 2007; 3: 961-969.

12. Landi E, Sprio S, Sandri M, Celotti G, Tampieri A. Development of Sr and CO_3 co-substituted hydroxyapatites for biomedical applications. Acta Biomater 2007 DOI:10.1016/j.actbio.2007.10.010.

13. Grynpas MD, Hamilton E, Cheung R, Tsouderos Y, Deloffre P, Hott M, Marie PJ. Strontium increases vertebral bone volume in rats at a low dose that does not induce detectable mineralization defect. Bone 1996; 18: 253-259.

14. Christoffersen J, Christoffersen MR, Kolthoff N, Bärenholdt O. Effects of strontium ions on growth and dissolution of hydroxyapatite and on bone mineral detection. Bone 1997; 20: 47-54.

15. Marie PJ, Ammann P, Boivin G, Rey C. Mechanisms of action and therapeutic potential of strontium in bone. Calcif Tissue Intl 2001; 69: 121-129.

16. Marie PJ, Hott M, Modrowski D, de Pollak C, Guillemain J, Deloffre P, Tsouderos Y. An uncoupling agent containng strontium prevents bone loss by depressing bone resorption and maintaining bone formation in estrogen-deficient rats. J Bone Miner Res 1993; 8: 607-615.

17. LeGeros RZ. In: Myers KH, editor. Calcium phosphates in oral biology and medicine, Monographs in oral science. Vol. 15. Basel, Switzerland: AG Publishers, 1991, 82-107.

18. Landi E, Tampieri A, Celotti G, Sprio S. Densification behaviour and mechanisms of synthetic hydroxyapatite. J Eu Ceram Soc 2000; 20: 2377-2387.

19. Landi E, Celotti G, Logroscino G, Tampieri A. Carbonated hydroxyapatite as bone substitute. J Eu Cer Soc 2003; 23: 2931-2937.

20. Legeros RZ, LeGeros JP. Phosphate minerals in human tissues. In: Nriagu JO, Moore PB (eds): Phosphate Minerals, Springer-Verlag, New York 1984.

21. Driessens FCM. Bioceramics of Calcium Phosphates. In: De Groot K (ed.). CRC Press, Boca Raton, USA 1983, p. 1-32.

22. Bigi A, Falini G, Foresti E, Gazzano M, Ripamonti A, Roveri N. Magnesium influence of hydroxyapatite crystallization. J Inorg Biochem 1993; 49: 69-78.

23. Tenhuisen KS, Brown PJ. Effects of magnesium on the formation of calcium-deficient hydroxyapatite from $CaHPO_4 \cdot 2H_2O$ and $Ca_4(PO_4)_2O$. J Biomed Mater Res 1997; 36: 306-314.

24. Celotti G, Tampieri A, Sprio S, Landi E, Bertinetti L, Martra G, Ducati C. Crystallinity in apatites: what is the disordered fraction made of?. J Mater Sci: Mater Med 2006; 17: 1079-1087.

25. Bertinetti L, Tampieri A, Landi E, Martra G, Coluccia S. Punctual investigation of surface sites of HA and magnesium-HA. J Eu Ceram Soc 2006; 26: 987-991.

26. Sayer M, Stratilatov AD, Reid J, Calderin L, Stott MJ, Yin X, MacKenzie M, Smith TJN, Hendry JA, Langstaff SD. Structure and composition of silicon-substituted tricalcium phosphate. Biomaterials 2003; 24: 369-382.

27. Botelho CM, Brooks RA, Best SM, Lopes MA, Santos JD, Rushton N, Bonfield W. Human osteoblasts response to silicon-substituted hydroxyapatite. J Biomed Mater Res A 2006; 79A: 723-730.

28. Landi E, Tampieri A, Mattioli-Belmonte M, Celotti G, Sandri M, Gigante A, Fava P, Bigini G. Biomimetic Mg- and Mg,CO_3- substituted Hydroxyapatites: Synthesis, Characterization and in Vitro Behaviour. J Eur Ceram Soc 2006; 26: 2593-2601.

29. Landi E, Logroscino G, Proietti L, Tampieri A, Sandri M, Bertinetti L, Sprio S. Biomimetic Mg- substituted Hydroxyapatite: from synthesis to in vivo behaviour. J Mater Sci: Mater Med 2007, DOI 10.1007/s10856-006-0032-y.

CHAPTER 4

DEVELOPMENT OF REINFORCED HA-BASED BIOMATERIALS

4.1 Need of reinforced bone substitutes

In Chapter 3, it has been shown that multi-substituted HA powders exhibit a reduced structural stability, leading to a higher extent of ion dissolution in SBF and phase decomposition during thermal treatments. Although these features are positive for the biomimetic behaviour of the multi-substituted HA, their employment to produce consolidated 3D bone scaffolds is more difficult, due to secondary phase formation.

The development of a porous bone scaffold exhibiting a high degree of biomimetism is nowadays strongly required for the replacement of diseased portions of bone. Biomimetism should be exhibited through different perspectives, i.e. biochemical, morpho-structural and mechanical.

Chemically, a bone scaffold must be bioactive, so to stimulate the remodelling processes at the interface with the physiological environment, and bioreabsorbable, so that during the osteoblasts activity of new bone formation, the scaffold should be progressively reabsorbed by the osteoclasts and completely integrated into the newly grown bone.

Moreover, a scaffold must be also osteoconductive and cells have to proliferate inside the pores and habit the whole scaffold volume; this feature is mainly controlled by the morphological architecture of the scaffold, which is to be designed in an accurate way, to ensure its full habitation by cells.

The morphological features also influence the mechanical performances of the scaffold, when subject to the biomechanical loads; in fact, bone structure is hierarchically organized (see Fig. 1.5) and this feature allows to distribute the mechanical stresses along a huge number of small trabeculae, which can be more easily replaced after their breaking. The

mechanical behaviour of a scaffold is thus very dependent on its morphology, but also on the intrinsic mechanical resistance of the material, constituting the scaffold itself.

This concept is of importance, especially in case of development of dense materials, for which a high number of clinical applications is addressed (endomedullar nails for long bones).

Dense HA is characterized by a fracture toughness slightly below the lower limit of cortical bone (see Table 4.I); Conversely, Young modulus is typically higher[1] and the flexural strength is limited to ~80 MPa[2-6], unless the samples are well polished before mechanical testing[7-9], so not useful for load-bearing applications, involving long bones like femur.

Table 4.I. Main mechanical properties of HA compared to cortical bone.

	Fracture toughness ($MPa \cdot m^{½}$)	Bending strength (MPa)	Young modulus (GPa)	Compressive strength (MPa)
Cortical bone	2-12	50-150	7-25	100-230
HA	~ 1.0	≤ 100	80-110	500-1000

Many attempts have been performed to develop composite materials for applications as bone scaffolds, characterized by improved mechanical behaviour; ceramic composites for bone scaffolds were obtained in a series of different compositions, e.g. bioglasses[1,10], HA + ZrO_2[11-13], HA + Al_2O_3 and other highly resistant ceramics[14-17].

The problems arising when developing such materials mainly concern phase decomposition, due to the chemical interactions between HA and the reinforcing phases at high temperatures; in these cases, HA largely decomposes in β- and α-TCP and, although in many cases the presence of zirconia raises the mechanical resistance of the composite, secondary phases form and alters the degree of bioactivity and bioreabsorbability of HA, as they are characterized by a higher solubility behaviour; moreover, the formation of α-TCP yields a volume increase in the ceramic body, compared with HA, and it can induce micro-cracks in the final scaffold.

The ceramic materials exhibiting high mechanical strength usually sinter at higher temperatures compared to HA, thus to achieve a complete sintering of the material, temperature must be raised well above 1200-1300 °C, usually up to 1500 °C. At these temperatures the extent of HA decomposition is huge, with formation of phases stable at

high temperatures like α-TCP and tetracalcium phosphate (TeCP), and in some cases an incongruent melting of HA can be observed.

Another inconvenient arising with ceramic composites is that in most of the cases the higher thermal stability of the reinforcing phases is also coupled with a higher chemical stability, so that the reinforcement behaves as a bioinert body, which in some cases can also be bioactive, as it can induce the formation of a HA layer on its surface[18-20], but it can not be reabsorbed by osteoclasts neither in the long term.

The main limitations to the development of an ideal 3D bone scaffold are so due to the difficulty to obtain a material exhibiting bioactivity, bioreabsorbability and mechanical resistance in the meantime.

HA is considered the election material for bone scaffolds, but the incorporation of biomimetic foreign ions in its structure is needed, although it determines a higher instability, and the mechanical performances have to be increased by the presence of a reinforcing phase, which should be bioactive at least.

4.2 Calcium silicates as biomaterials

Calcium silicates were studied as biomaterials for hard tissue repair and replacement since the early 1970s, when Hench and co-workers discovered Bioglass®[21]. Various types of silicate glasses and glass-ceramics such as bioactive glasses[22-25], and wollastonite-based glass-ceramics[26-30], have been investigated; the results showed that biomaterials containing $CaO–SiO_2$ appeared to have excellent bioactivity and were found to bond to living bone and soft tissue, through the development of a biologic HA layer on their surface. Another study illustrates the analogies between the hydration behaviour of calcium silicates and calcium phosphates[31], when forming the calcium silicate hydrated ($xCaO{\cdot}SiO_2{\cdot}nH_2O$, $0.833<x<z1.7$) and HA phase respectively. The analogies in the hydration behaviour are significant, as the very early modifications of the implant surface, when *in vivo* it is in contact with the physiological environment, are determinant for the development of the HA layer, and the adhesion of proteins and other growing factors.

Recent studies showed that some calcium silicate ceramics such as wollastonite and pseudowollastonite[32-39] also have excellent bioactivity and are potential candidates of new biomaterials for hard tissue repair. Furthermore, Lamy[40] and Liu[41] have shown that

dicalcium silicate (Ca_2SiO_4) as plasma sprayed coating on titanium alloys substrates exhibited very good bioactivity.

Further studies have shown that pure $CaSiO_3$ powders and 3D ceramics were highly bioactive and induced formation of a hydroxyapatite layer on their surface after soaking in simulated body fluid (SBF)[32,39,42,43] or in human saliva[33].

Tricalcium silicate Ca_3SiO_5, the main raw material used to elaborate paste in Portland cement (the most common in house building), was found to possess ability of HA formation and consolidation with spontaneous development of strength (spontaneous consolidation) towards water, so that it might be used as a self-setting bioactive cement[44].

Amorphous calcium silicates were also investigated, showing an increased solubility compared to crystalline calcium silicates[45].

All these materials were investigated for their intrinsic mechanical properties also[46-48]; Long[48] obtained samples by using a high-speed sintering technique, characterized by high density and a bending strength of nearly 300 MPa. Table 4.II shows a comparison between the main mechanical features of some investigated calcium silicates, HA and cortical bone.

Table 4.II. Mechanical properties of different bioactive calcium silicates in comparison with cortical bone.

Material	K_{IC} (MPa $m^{1/2}$)	E (GPa)	σ_b (MPa)
Ca_3SiO_5 [44]	~2	~40	~100
Ca_2SiO_4 [47]	~2	~40	~200
$CaSiO_3$ [48]	~2	~40-50	~300
$Ca_7MgSi_4O_{16}$ [49]	~1.6	~40-50	~150
$CaMgSi_2O_6$ [50]	3.5	170	~300
Cortical bone[51]	~ 2 - 12	7-30	50-150

All these materials exhibit different levels of mechanical strength and similar values of fracture toughness; among them, calcium disilicate (Ca_2SiO_4) was finally selected as a reinforcing phase for composites with HA.

Silico-carnotite, a silico-phosphate phase of composition similar to that of HA ($Ca_5(PO_4)_2SiO_4$) was also selected as a potential material to be mixed with stoichiometric HA. In fact, as multi-substituted HAs are not optimal for sintering in standard conditions, stoichiometric HA must be used for this purpose; anyway, stoichiometric HA has a limited

bioactivity *in vivo*, but the overall biomimetism of the composite could be improved, even after sintering, by the presence of a phase exhibiting similar composition as HA and containing some of ions considered influent in the new bone formation and remodelling processes (Mg, Si, CO_3).

Thus, the employment of bioactive calcium silicates in composite with HA has two different potential advantages: 1) the possible increase of the mechanical performance of HA-based implants; 2) the increase of the biomimetism of stoichiometric HA by doping its structure during sintering.

4.3 Development of composites HA / silico-carnotite ($Ca_5(PO_4)_2SiO_4$)

4.3.1 Powder synthesis and preparation of mixtures

The crystal structure of silico-carnotite is well known and the related ICDD file also contains the procedure for synthesising the pure phase (ICDD card n° 40-393).

Thus, following the synthesis procedure there indicated, 300 g of $Ca(NO_3)_2 \cdot 4H_2O$ were put in a beaker with 300 ml of deionized H_2O, after 15.11 g of amorphous silica were added, under continuous stirring. A solution was prepared by dissolving 58.01 g of ortophosphoric acid (in aqueous solution 85 %) in 150 ml of deionized water and dripped into the calcium-silicate suspension (all reactants were provided by Sigma-Aldrich (S. Louis, MO, USA).

The suspension was kept under stirring and the temperature was raised to 95 °C, until, after few hours, water completely evaporated and a gel formed. The gel was calcined at 700 °C for 2 hours, obtaining a fine precursor powder; the precursor powder was finally treated at 1600 °C for 30 minutes, followed by a step at 1420 °C for 9 hours and finally quenched in air; the quenching of samples was achieved by using a expressly devoted elevator furnace.

As silico-carnotite is a material devoted to improve the mechanical strength of HA-based bioactive composites, the sintering behaviour of silico-carnotite was investigated by thermal treatments in the range 900-1400 °C for 1 hour in air.

After, mixtures of stoichiometric HA and silico-carnotite in different proportions (5-50 wt%) were prepared, by using polyethylene jars filled with the powders, in water and using zirconia grinding media. The mixing was prolonged for 24 hours and after water was eliminated by centrifugation and the final powder was dried at 80 °C in a ventilated oven and sieved under 150 μm.

The powder mixtures were pressed in pellets and sintered at 1250 °C for 1 hour, following the typical sintering cycle employed for HA; the resulting samples were analyzed by XRD and the microstructure examined by SEM-EDS. For this purpose, the sintered pellets were cut and polished up to a grain size of 0.25 μm; after a chemical etching of HCl 1M for 5 seconds was applied to selectively attack the grains boundaries and make them visible under SEM observation.

4.3.2 Characterization

Fig. 4.1 shows the XRD spectrum of the powder precursor of silico-carnotite phase, obtained after calcinations of the gel at 700 °C. The crystalline phases present in the powder were identified as mainly HA and a calcium silicate identified as $Ca_5(SiO_4)_2(OH)_2$ (mineral name: Reinhardbraunsite, ICDD n° 29-0380); a small amount of calcium oxide (ICDD n° 37-1497) was also detected.

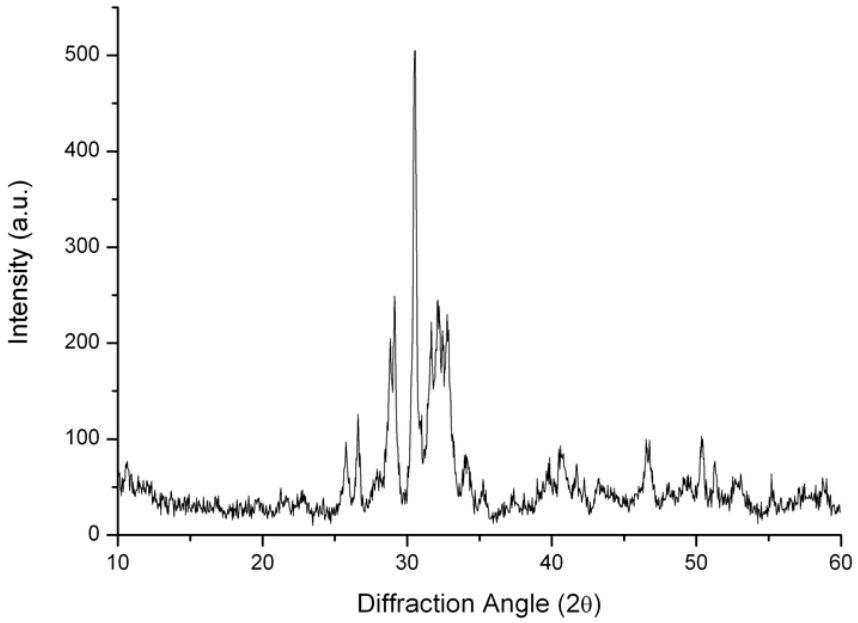

Figure 4.1. XRD spectrum of the calcined gel, precursor of silico-carnotite phase.

After the thermal treatment at high temperature and rapid quenching, the obtained powder is nearly pure silico-carnotite (Fig. 4.2), with some impurities identified as $Ca_3Si_3O_8(OH)_2$, a mineral known as Rosenhahnite (ICDD n° 29-0378).

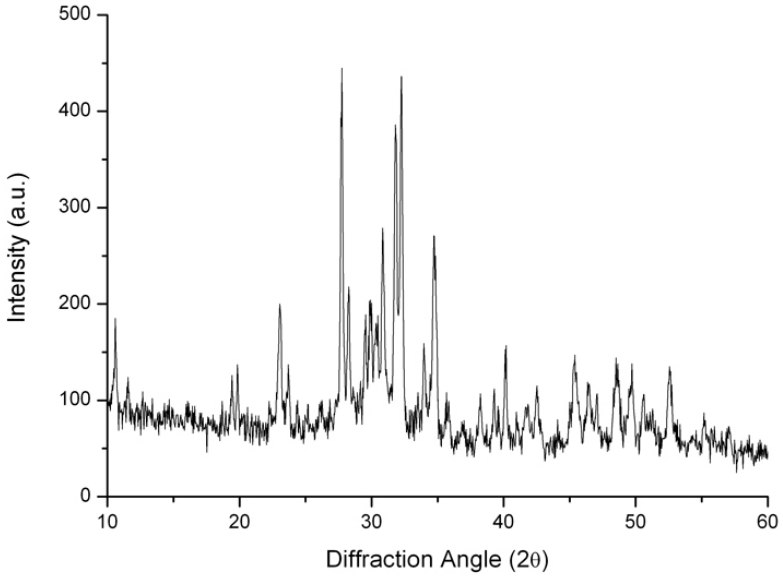

Figure 4.2. XRD spectrum of the calcined gel after the thermal treatment of transformation in silico-carnotite phase.

The phase composition of the powder after firing in the range 900-1400 °C was obtained by XRD analysis and showed in Fig. 4.3. The semiquantitative analysis of the amount of the phases formed during the thermal cycles was evaluated on the basis of the intensity of XRD peaks, normalized on the basis of the scattering power of each phase. It was found that silico-carnotite is stable in air only up to 900 °C; at 1000 °C about 30 % of TCP formed, which increased up to ~60% at 1200 °C, and also HA phase formed. At 1400 °C, silico-carnotite completely disappeared and β-$CaSiO_3$ (wollastonite) formed.

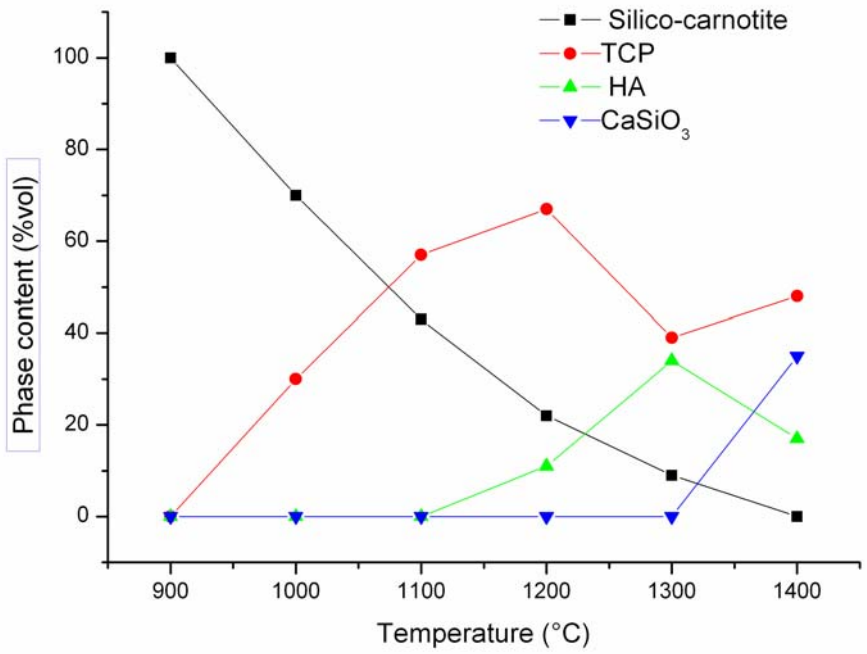

Figure 4.3. Decomposition of silico-carnotite after firing at different temperatures.

Thus, although silico-carnotite was synthesized by thermal treatment at a very high temperature, reaching 1600 °C, further heating, even at only 1000 °C, provoked phase decomposition in a large extent. This behaviour can be explained, as the synthesis of silico-carnotite phase occurred after rapid quenching in air from 1420 °C; thus, it is reasonable to conclude that the slow cooling of the silico-carnotite sample in air allowed the recrystallization of secondary phases, like HA and TCP.

Fig. 4.4 shows the phase composition of mixtures HA / silico-carnotite after sintering at 1250 °C for 1 hour, obtained by XRD analysis. In concentration up to 10%, only HA phase was recognized and very small amount of β-TCP formed. In higher concentrations β-TCP increased and silico-carnotite started to form; in concentrations of 50 % the peaks of silico-carnotite were well visible and also α-TCP formed, so that HA became a minor phase.

The absence of the characteristic XRD peaks of silico-carnotite drives to the conclusion that a reaction between the two phases can have occurred, as following: $(1-x)Ca_{10}(PO_4)_6(OH)_2 + xCa_{10}(PO_4)_4(SiO_4)_2 \rightarrow Ca_{10}(PO_4)_{6-2x}(SiO_4)_{2x}(OH)_{(2-2x)}$,

giving rise to a silicon-substituted HA.

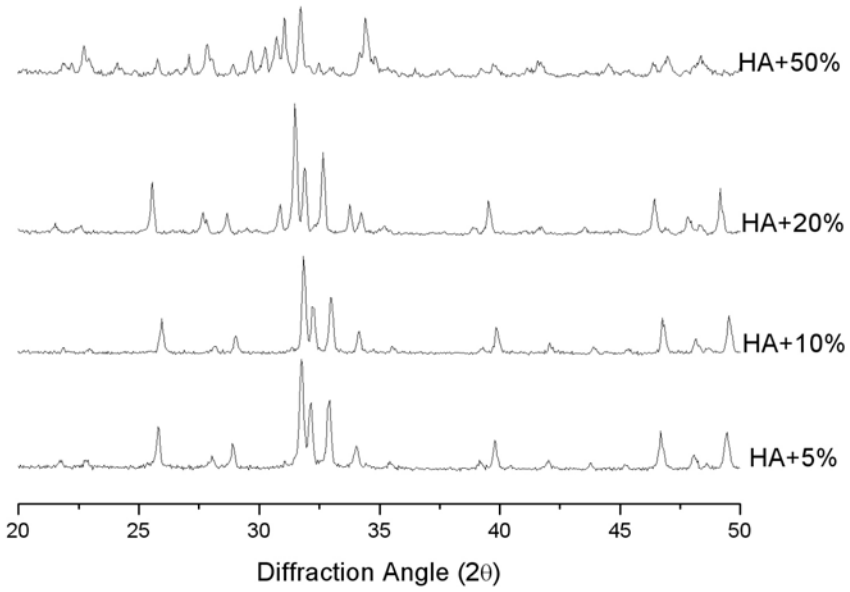

Figure 4.4. XRD spectra of mixtures HA-silicocarnotite after sintering at 1250 °C.

In this case, the maximum amount of silico-carnotite able to dissolve into the HA matrix corresponds to a *x* value of ≈ 0.2.

The formation of β-TCP after sintering can be induced by the presence of silico-carnotite; this finding is confirmed by the increase of β-TCP by raising the content in silico-carnotite. The analysis by SEM confirmed this assumption. Fig. 4.5 show the SEM micrographs of the polished and etched surfaces: EDS analysis was performed on a high number of grains, revealing the overall presence of silicon with similar concentrations, in particular in the sample containing 10% of silico-carnotite the amount of silicon is 0.46 wt% (0.39 at%).

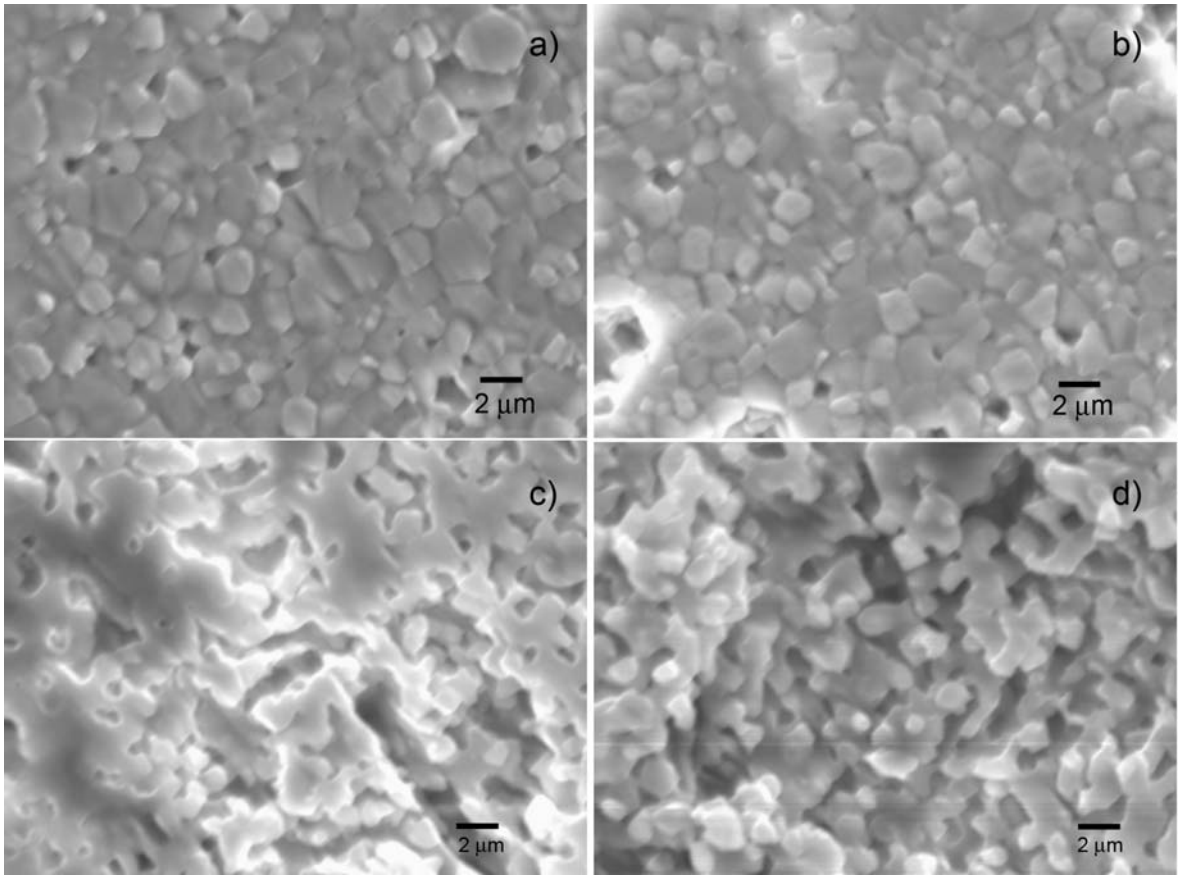

Figure 4.5. Microstructure of HA pure and doped with different amounts of silico-carnotite: a) 5%; b) 10%, c) 20%; d) 50%.

4.3.3 Cytotoxicity tests

As shown in the previous section, the mixture HA / silico-carnotite (20 wt%), sintered at 1250 °C for 1 hour yielded a material made by HA characterized by the presence of silicon in physiological amounts, and no residual silico-carnotite was detected. This material, exhibiting improved biomimetic behaviour, is promising for application as a bone substitute and thus, a toxicological test was performed to assess its biocompatibility / cytotoxicity. The cytotoxicity test was performed on the sintered material, dusted below 150 µm: 1 g of powder was soaked into 5 ml of a culture medium, containing NCTC L929 fibroblast cells, in order to have a weight / volume ratio of 0.2 g/ml. The sample was incubated for 72 hours at 37 ± 1 °C. After centrifugation, 2 ml of the extract were put in contact with the cultivated cells for 48 hours at 37 ± 1 °C, in CO_2-containing air. After 24 and 48 hours, the cultivated cells were examined by optical microscopy to assess the cell activity. The tests were performed by the company BioLab SpA*.

After 24 and 48 hours, no cellular reactivity was detected; in particular, some small intra-cytoplasmatic granulations were observed and no cellular lysis occurred. In consequence of the substantially absence of cellular reactivity, the powder under investigation can be considered as not cytotoxic.

4.4 Development of composites HA / β, γ-Ca_2SiO_4

4.4.1 Structure and phase stability in calcium disilicate system

Dicalcium silicate (Ca_2SiO_4) can exist in five polymorphic forms under ambient conditions[52]. Fig. 4.6 shows the transformation temperatures and the related volume changes; the most notable feature in this scheme is the transition β→γ, occurring during cooling from high temperatures. Thus, following a thermal treatment, a three-dimensional ceramic body made by γ-Ca_2SiO_4 would undergo to a complete cracking during cooling, due to the huge volume cell variation (~12 %); this feature may hamper the development of composite materials including γ-Ca_2SiO_4 phase.

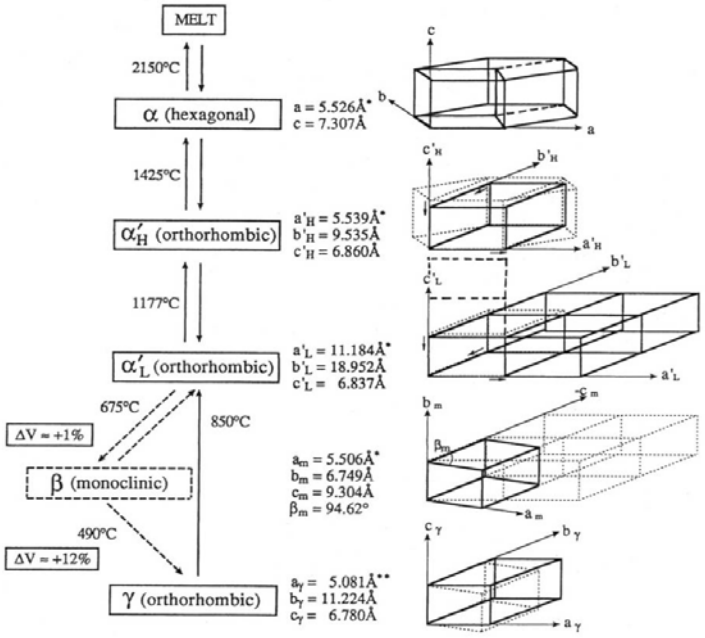

Figure 4.6. Polymorphic transformations of Ca_2SiO_4 [53].

Anyway, previous studies show that some physical-chemical effects can stabilize the monoclinic β-polymorph after cooling[53]; these phenomena include particle size effect and matrix effect. In the first case, a reduced particle size, less than a critical value, would stabilize γ-polymorph after cooling from high temperatures; the second case is related to

the presence of a matrix which stabilizes γ-phase, due to the physical constrain exerted by the matrix itself, which hamper the volume expansion occurring in the β→γ transformation. The critical size of the γ-Ca_2SiO_4 for the retaining of β-polymorph after cooling is disputed: Chan[53] reported a value of ~ 10 μm, while Hong[54] found a critical value of <~2 μm.

4.4.2 Synthesis of β and γ-Ca_2SiO_4

The synthesis of Ca_2SiO_4 phases was performed as following: β-Ca_2SiO_4 was synthesized by mixing 100 g of $Ca(OH)_2$ and 38.5 g of amorphous silica in 400 ml of deionized H_2O; the temperature was raised at 95 °C under vigorous stirring for 6 hours. After the process, the water was eliminated by centrifuging and the powder was dried at 80 °C in a ventilated oven; then put in a platinum crucible and fired at 1500 °C for 2 hours, prior quenching in air.

XRD analysis (Fig. 4.7) confirmed that pure β-Ca_2SiO_4 phase was obtained (ICDD card n° 49-1673).

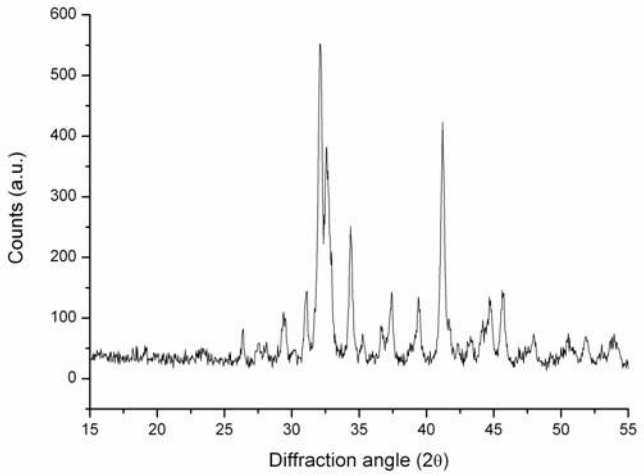

Figure 4.7. XRD spectrum of as-synthesized β-Ca_2SiO_4.

γ-Ca_2SiO_4 was synthesized by following the procedure described in Gou *et al.*[55], so employing microcrystalline quartz as a silicon source. In detail, 100 g of $Ca(OH)_2$ were put in 1 litre of deionized H_2O and stirred while temperature increased up to 95 °C; then, quartz was introduced in the reaction flask and stirred for 4 hours; finally, centrifugation, drying and sintering at 1450 °C for 2 hours with slow cooling in air. XRD analysis

confirmed that pure γ-Ca_2SiO_4 phase was obtained (Fig. 4.8), exhibiting some crystallographic orientations (ICDD card n° 49-1672).

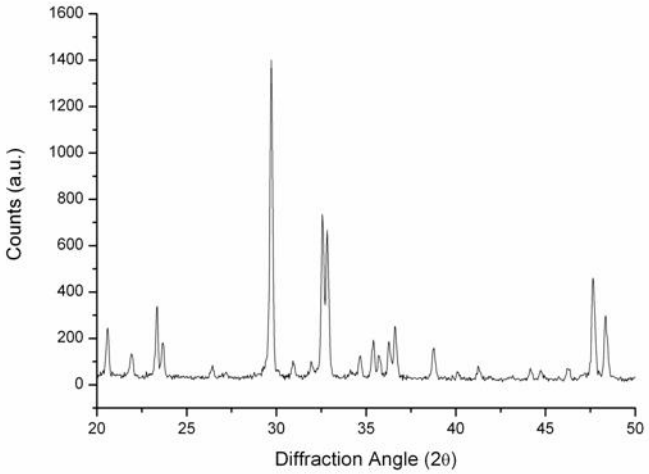

Figure 4.8. XRD spectrum of as-synthesized γ-Ca_2SiO_4.

4.4.3 Preliminary sintering tests

In view of the densification of composite ceramics with HA, preliminary sintering tests were carried out in air, in the range 1200-1500 °C. HA powder was mixed with γ-Ca_2SiO_4 in proportion 80:20 in weight and small pellets were formed by uniaxial pressing of the powder mixture; the dwell time at the final temperature was set at 30 minutes, with the purpose of investigating the reactivity of HA at high temperatures when mixed with γ-Ca_2SiO_4. Finally, samples spontaneously cooled into the furnace.

The resulting samples were investigated by XRD (Fig. 4.9): after sintering at 1200 °C, the crystalline phases detected were HA, silico-carnotite and β-Ca_2SiO_4. It is remarkable that no TCP, nor TeCP formed after sintering at so high temperatures; the XRD peaks belonging to HA are narrow up to 1300 °C and start to broaden at higher temperatures, this indicates a lose in HA crystallinity, due to the increasing instability of the HA structure above 1400 °C.

Silico-carnotite started to form at 1300 °C, while γ-Ca_2SiO_4 completely disappeared already at 1200 °C; the main evidence of the disappearance of γ-Ca_2SiO_4 is in the absence of the strong reflection at d=3.013 nm, corresponding to a diffraction angle of 29.624

degrees in 2θ. There are some evidence of formation of β-Ca_2SiO_4, which can be due to phenomena of phase stabilization occurred during cooling, as stated above.
Anyway, silico-carnotite formed in increasing amount as higher the sintering temperature, and after sintering above 1200 °C, calcium disilicate is no more detected by XRD.

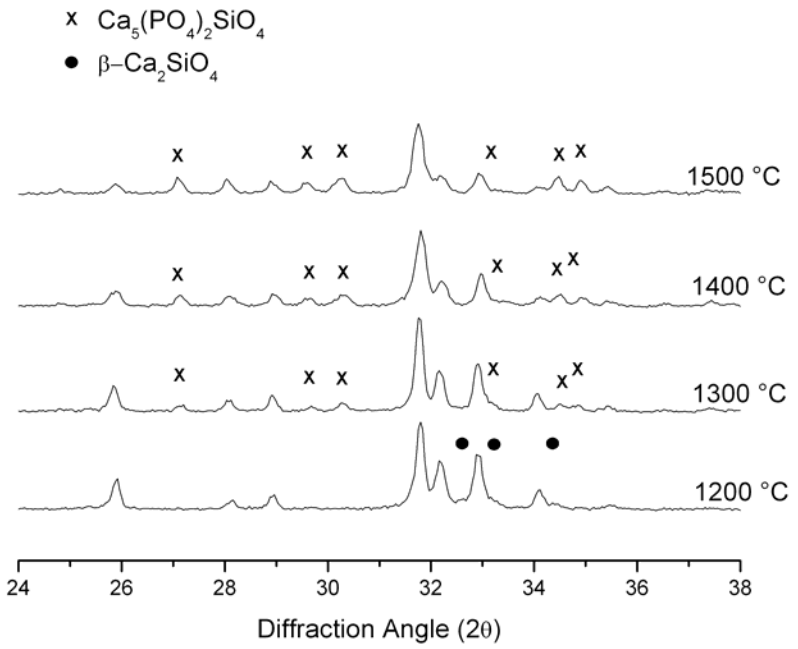

Figure 4.9. Phase composition of mixture HA-γ-Ca_2SiO_4 after sintering in air at different temperatures.

4.5 Development of dense ceramic composites by Fast Hot Pressing (FHP)

The sintering of ceramic composites HA-calcium silicates proved to be feasible even at temperatures high as 1500 °C: HA phase did not decompose in undesired secondary phases like TCP and although a phase transformation of the calcium silicate actually occurs above 1300 °C, the newly formed silico-phosphate (silico-carnotite) is interesting for its similarity to HA in composition; moreover, it proved to be not cytotoxic, after reaction with HA, and also showed the capability to dissolve in solution with HA, giving a silicon-substituted HA phase.
Alternative procedures to obtain dense ceramic bodies were attempted by employing a sintering technique characterized by high heating rates and short dwell times. This

technique consisted in the employment of a furnace where heating was produced by a high frequency current induced in a coil (see Fig. 4.10). The coil surrounds a graphite matrix, which consists in a hollow cylinder filled with the ceramic powder, at the two sides two graphite punches can exert a pressure up to 30 MPa (Fast Hot Pressing, FHP). The raise of the temperature was controlled by varying the electric field at the basis of the currents induced in the graphite matrix, which provoked the heating of the sample; the sample temperature was monitored by a pyrometer, and the punches were connected to a transducer so that the shrinkage of the sample during heating could be recorded.

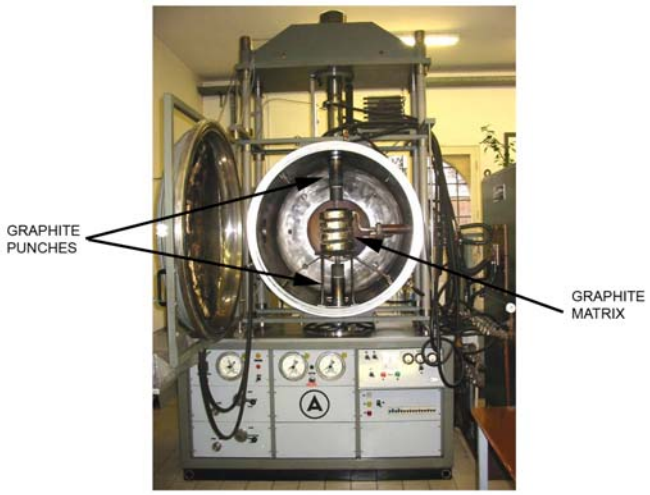

Figure 4.10. Scheme of the equipment for FHP.

The adoption of an applied pressure and the short dwell times can contribute to a higher extent of sample densification and a reduction of grain growth occurring at high temperatures; both these features can contribute to raise the final mechanical resistance. Thus, a series of experiments were performed both with pure stoichiometric HA powder and a powder mixture HA-γ-Ca_2SiO_4, to investigate whether the presence of a reinforcing phase can actually raise the mechanical strength of the final ceramic body.

4.5.1 Sample preparation

The FHP experiments were carried out by filling the graphite matrix (see the scheme in Fig. 4.11) with ceramic powders in different amounts (25-60 g); the chamber was closed, evacuated by rotary pump (base pressure ≈ 1 Pa) and temperature was raised at different heating rates (between 30 and 100 °C/min) and applying different applied pressure (1-30 MPa), up to final temperatures ranging between 1250 and 1500 °C. The recording of the sample shrinkage allowed to in situ assess the progress of the densification

process, so the dwell times at the final sintering temperature were set up accordingly, generally in the range of few minutes.

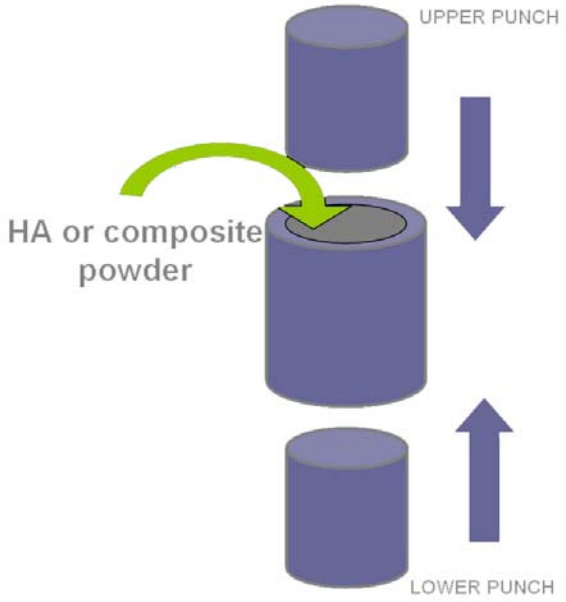

Figure 4.11. Sample preparation for FHP experiments.

After cooling, the sintered piece was extracted and cut by a low-speed saw.
XRD analysis was performed on the surface of the sectioned sample, Archimede' s method was also employed for measuring the sample density. The density was referred to the theoretical density of HA which can be calculated by the volume cell and the weight of the atoms therein present, which is ≈3.16 $g \cdot cm^{-3}$. SEM observations were performed on the internal surfaces of the samples after polishing at 0.25 μm and chemical etching to put in evidence the grain boundaries.

4.5.2 Sample characterization

HA powder was treated by FHP at temperatures up to 1500 °C; the XRD analysis of the obtained samples put in evidence a very important result: even after sintering at 1500 °C, HA phase was found as the only crystalline phase and no other calcium phosphates were present (Fig. 4.12). The crystallinity of the sample strongly decreased at temperatures higher than 1300 °C, as evident by the peak broadening and the reduction of the intensity; it is possible that the high speed of the sintering process and the vacuum have retarded the decomposition of HA, and this proves that FHP process was suitable to produce HA bodies sintered at 1500 °C without phase decomposition.

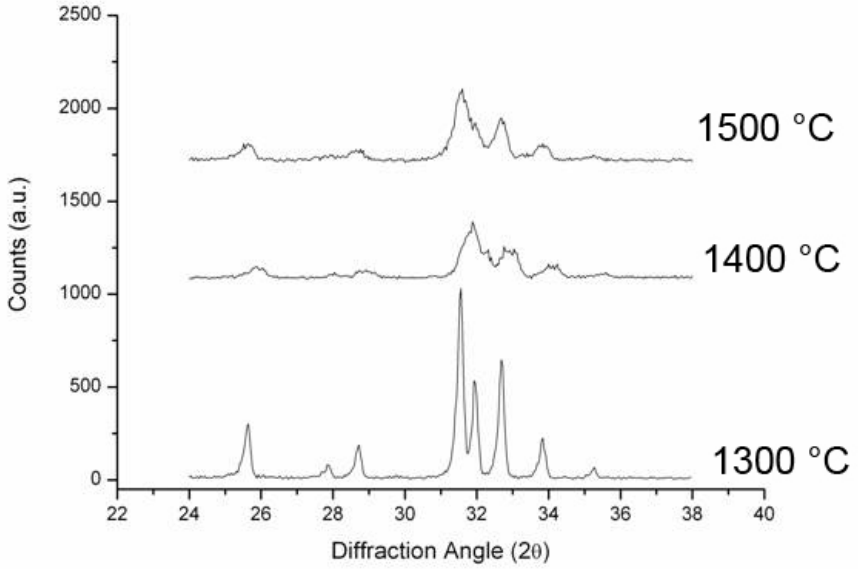

Figure 4.12. XRD spectra of stoichiometric HA heat treated by FHP.

Experiments performed with different amounts of powder (30-60 g), heating rates, applied pressure and final temperatures (Table 4.III) gave rise to similar results, in terms of HA stability, thus all the investigated samples did not exhibit any phase decomposition, according to Fig. 4.12.

Table 4.III. Comparison between different FHP treatments performed on HA powder.

Experiment	Applied pressure (MPa)	Thermal cycle	Heating rate (°C·min^{-1})	Density (g·cm^{-3})
F1	30	1500 °C x 1’	100	2.60
F2	10	1500 °C x 1’	50	2.69
F3	5	1500 °C x 3’	50	2.96
F4	1.5	1500 °C x 12’	100	2.95
F5	1.5	1500 °C x 12’	50	2.83
F6	1.5	1500 °C x 1’	30	2.93
F7	30	1400 °C x 1’	100	2.78
F8	1.5	1400 °C x 15’	100	2.92
F9	1.5	1400 °C x 18’	50	2.98
F10	1.5	1400 °C x 18’	30	2.94
F11	1.5	1300 °C x 46’	100	2.79
F12	1.5	1300 °C x 40’	50	2.76
F13	1.5	1300 °C x 40’	30	2.70
F14	1.5	1200 °C x 50’	50	2.43

The experiments carried out at 1500 °C (F1-F6) under different applied pressures show that a higher density is achieved as the applied pressure decreased. Moreover, an extended delamination occurred in the macro-structure of the sintered bodies under high pressure applied, also confirmed by SEM investigations (Fig. 4.13), so that a minimal pressure is recommended to achieve homogeneous sintered HA bodies. A pressure of ~1.5 MPa was finally selected, as it allowed to obtain structurally homogeneous products and the shrinkage behaviour could be recorded so to stop the heating when the densification was completed.

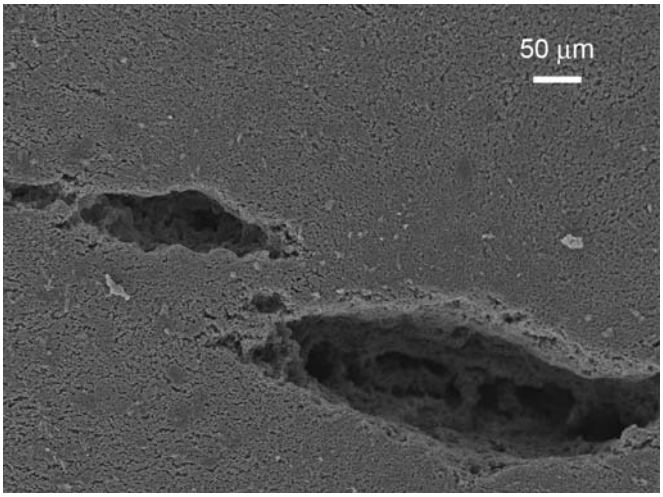

Figure 4.13. Delamination occurring during FHP of HA under excessive applied pressure.

The investigation of the final density values in comparison with the heating rates (Tab. 4.III**)** reveals that a higher density can be achieved through a slower heating of the sample; in this condition, the heat gradient inside the HA powder is less pronounced and the microstructure of the final body is more uniform. In fact, in the sintering process, as the temperature is raised, HA particles start to coalesce and subsequently grow, filling the voids and leading to a volume reduction of the sample. After the densification is complete, the large HA grains start to grow at the expenses of the smallest ones; this process is accelerated at higher temperatures and prolonged permanence, leading to a decrease of the mechanical strength. In Fig. 4.14 the microstructure of different areas of the same sample is showed, exhibiting a different grain size, due to an excessive heating rate (100 °C/min). The external part exhibited a much higher grain size compared to the internal part, due to the heat flux from the graphite matrix inwardly, leading to a strong anisotropy in the heating of the whole body: the low thermal conductivity of the ceramic did not allow an uniform heating of the powder in a short time and thus, the employment of too high

heating rates and short dwell times revealed not adequate for the sintering of a high mass of powder.

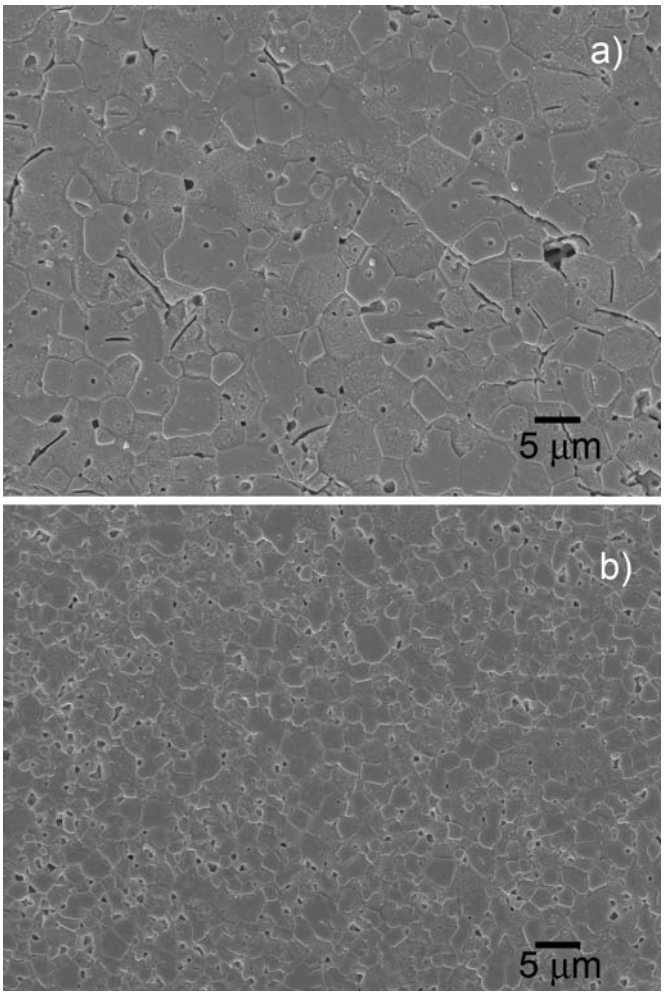

Figure 4.14. Different grain growth in external (a) and internal part (b) of a HA sample heated at 1500 °C (100 °C/min).

Moreover, the same effect was obtained, by increasing the amount of powder employed in the experiment, so increasing the sample mass with a reduced heating rate; a similar anisotropy was detected, confirming that a careful control of the heat flow inside the sample is strongly required to achieve homogeneous materials.

The best results in term of sample homogeneity and density were achieved by limiting the heating rate at ≈30 °C/min and the mass of HA powder to about 25-30 g; these parameters were applied in a series of experiments devoted to obtain dense HA and composite samples for the test of their mechanical properties.

4.6 Mechanical characterization of HA and composite ceramics

4.6.1 Sample preparation and mechanical testing

The main purposes for obtaining ceramic composites is the improvement of the mechanical behaviour of the bioceramics, compared to HA, and the maintenance of a phase composition with a high degree of bioactivity / bioreabsorbability; for this reason, a series of HA pellets were obtained by sintering at 1300-1500 °C.

Composite bodies were also prepared, starting with γ-Ca_2SiO_4 as reinforcement; γ-Ca_2SiO_4 was synthesized following the above described procedure and mixed with HA powder; an initial concentration of 20 wt% was chosen for the first experiments. The specific surface area of the two powders was measured by BET method, and they resulted comparable (HA: 3.93; γ-Ca_2SiO_4: 3.62 m^2/g). The two powders were mixed in a polyethylene jar with water and zirconia grinding media for 24 hours; the water was eliminated by freeze drying and the final powder dried and sieved under 150 μm.

Batches of 25-30 g of powder mixture were sintered through FHP at the same conditions as HA, the only difference was in the dwell times at the final temperature (Table 4.IV), as this parameter depended only on the end of the sample shrinkage, obtained by the continuously recording of the shrinkage curve. The presence of the reinforcing phase induced differences in the shrinkage kinetics of HA. A reference sample was also prepared, by sintering pure γ-Ca_2SiO_4 powder at 1500 °C. Apart from this latter sample, hot-pressed at 30 MPa, all samples were obtained under a pressure of ~1.5 MPa.

Table 4.IV. Samples to be mechanically tested obtained by FHP.

Material	T (°C)	Dwell(min)	Density($g \cdot cm^{-3}$)	Rel. Density
HA	1300 °C	40	2.76	0.87
HA	1400 °C	18	2.98	0.94
HA	1500 °C	3	2.93	0.93
γ-Ca_2SiO_4	1500 °C	2	3.17	0.96
HA+ γ-Ca_2SiO_4	1300 °C	39	2.30	0.72
HA+ γ-Ca_2SiO_4	1400 °C	33	2.83	0.89
HA+ γ-Ca_2SiO_4	1500 °C	12	3.03	0.95

After sintering, the samples were characterized by XRD, density measurement and SEM observations; a mechanical characterization was also performed, in order to assess whether

the presence of the reinforcing phase was effective. The main property investigated was the material resistance to the flexure: this measurement was carried out by obtaining rectified bar in a defined size (in our case, they were 25 x 2 x 2.5 mm) from the sintered samples; the bars were subjected to flexure under an increasing pressure up to rupture (see Fig. 4.15**)** and the recorded stress-deformation profile can give information on the elastic properties of the material.

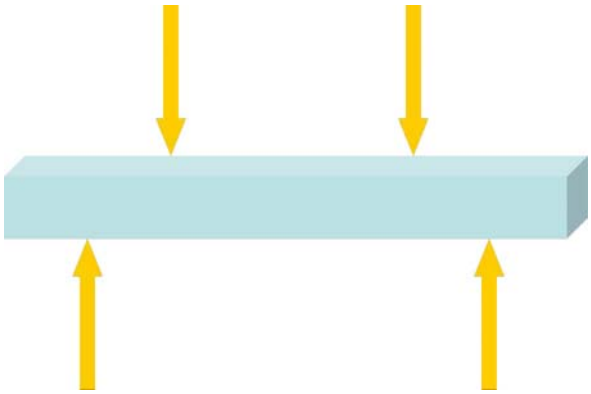

Figure 4.15. Scheme of the flexural strength test performed on sample bars.

The actual point of rupture gives information on the flexural strength of the material. This property is not only related to the intrinsic microstructural features of the sample, as the starting point of the rupture is always a crack occurring at a defect size (pore, flaw, etc…), thus a careful preparation of the samples is of great importance. Anyway, the assessment of flexural strength is of great relevance in view of the possible clinical applications: in order to implant a bone substitute in a load-bearing site without any external fixation (which has to be removed in a second, painful, surgical intervention), the scaffold must bear the biomechanical loads which *in vivo* normally occur in ***that*** site [**Ritchie**]. A wider mechanical characterization was performed, by analysing some selected materials by nanoindentation methods. In these measurements, a nanosized Berkovich indenter (see Fig. 4.16) exerted a pressure of 50 mN on several points of the polished sample surface.

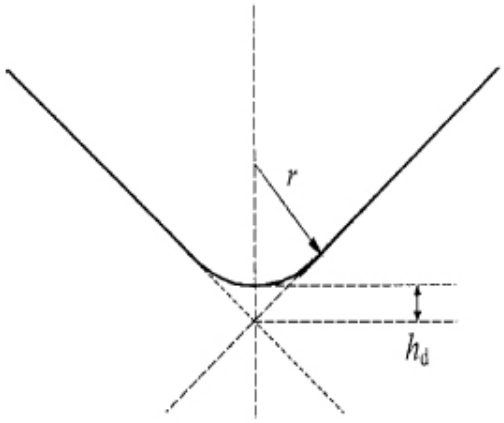

Figure 4.16. Geometry of a Berkovich indenter tip.

The load-displacement curves (Fig. 4.17) were built during load and unload and analyzed for the achievement of the elastic modulus of the material.

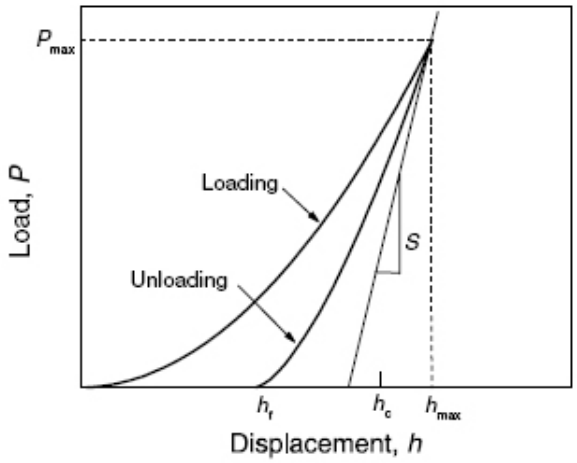

Figure 4.17. Example of a load-displacement curve during loading and unloading.

The elastic modulus found by the analysis of the load-displacement curves in the flexural strength tests is related to the behaviour of the overall sample; in fact the response of the bar to the mechanical solicitation is influenced by the microstructure of the whole sample, included pores and flaws. Conversely, the elastic modulus found by nanoindentation tests is related to the investigation of very smaller volume (few μm^3), so that the response is independent on the macroscopic defects of the sample but it is more related to the intrinsic behaviour of the material investigated.

4.6.2 Physical-chemical characterization

The analysis of the densification curves of HA during heating at 1500 °C reveals that heating rate influenced the densification path; moreover the onset of the densification was at higher temperatures, increasing the heating rate: 1220 °C, 1320 °C and 1500 °C, respectively. At 100 °C /min, the final temperature is reached before the starting of the shrinkage; in consequence, the first part of the related curve is approximately a unique straight line (Fig. 4.18), so characteristic of a single sintering mechanism[57,58]. In the remaining curves, the slope changed with time, as different temperatures are related to different sintering kinetics.

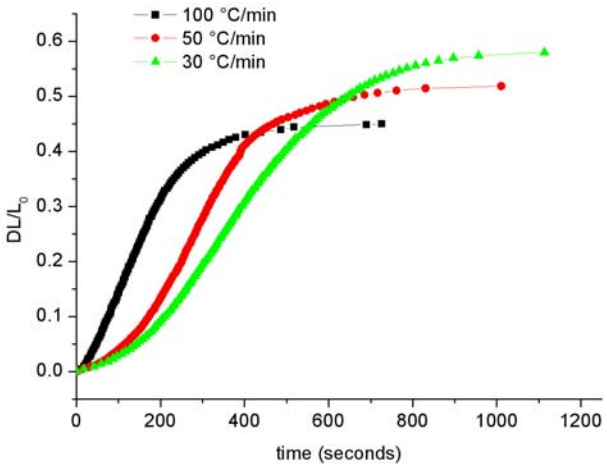

Figure 4.18. Comparison between densification curves of HA at different heating rates.

As a consequence, the permanence at the final temperature is higher at the lowest heating rates (see also Table 4.III, Experiments F4-F6); finally, on the basis of the microstructural features also, 30 °C/min was selected as the most suitable heating rate.

The XRD analysis of the pure γ-Ca_2SiO_4 sintered at 1500 °C is showed in Fig. 4.19: γ-polymorph completely transformed in the β-form of Ca_2SiO_4, due to the characteristics of the starting γ powder, which prevented the recrystallization of γ-Ca_2SiO_4.

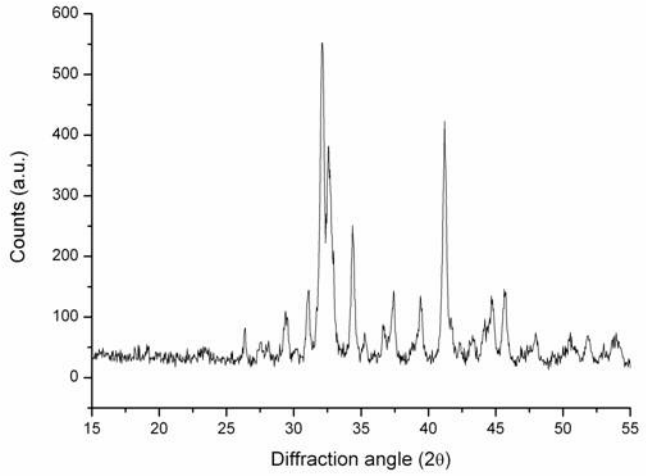

Figure 4.19. XRD spectrum of γ-Ca_2SiO_4 treated at 1500 °C by FHP.

In fact, as its specific surface was 3.62 m^2/g, obtained by BET measurement, it was possible to estimate the average grain size as ~0.6 μm, supposing that particles have the same shape (see also Chapter 2): thus, on the basis of the researches of Chan[53] and Hong[54], this reduced grain size can have yielded the stability of the β-polymorph during cooling, as also stated above. This finding seems in contrast with the SEM image of the as-synthesized γ-Ca_2SiO_4 (Fig. 4.20), in which the average grain size appears larger than 10 μm, recognized as the limit size for β-polymorph stabilization. Anyway, the irregular grains of γ-Ca_2SiO_4 are often made by smaller lath-like units, weakly bounded to form larger particles[53]; in this case, the physical effect responsible of the β-Ca_2SiO_4 stabilization applies to these smaller sub-particles.

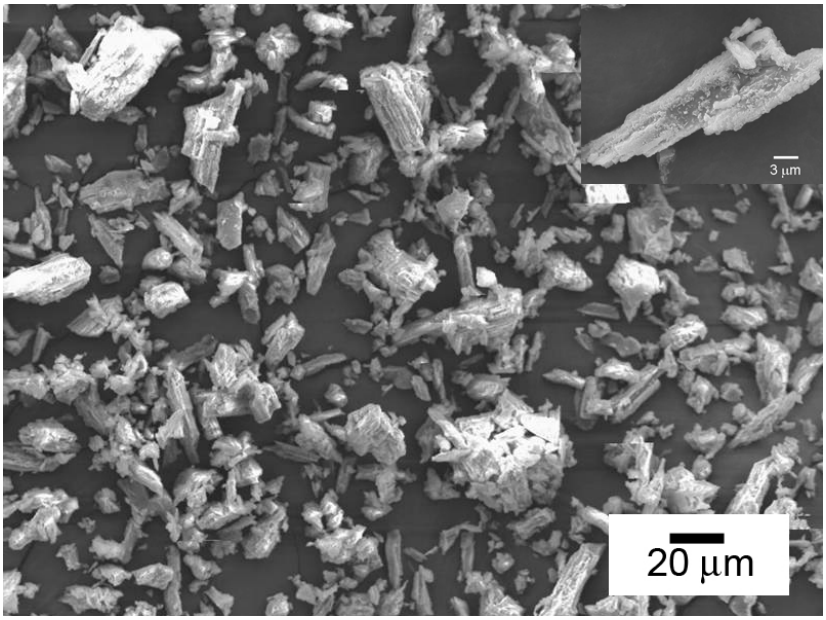

Figure 4.20. Morphology of as-obtained γ-Ca_2SiO_4.

In composite samples, fired in the range 1300-1500 °C, HA remained stable even at 1500 °C and no other silicate phase were present, apart from HA and Ca_2SiO_4 (Fig. 4.21): the only modification was, as in the pure Ca_2SiO_4 sample, the changing in the β- polymorph and its stabilization at room temperature.

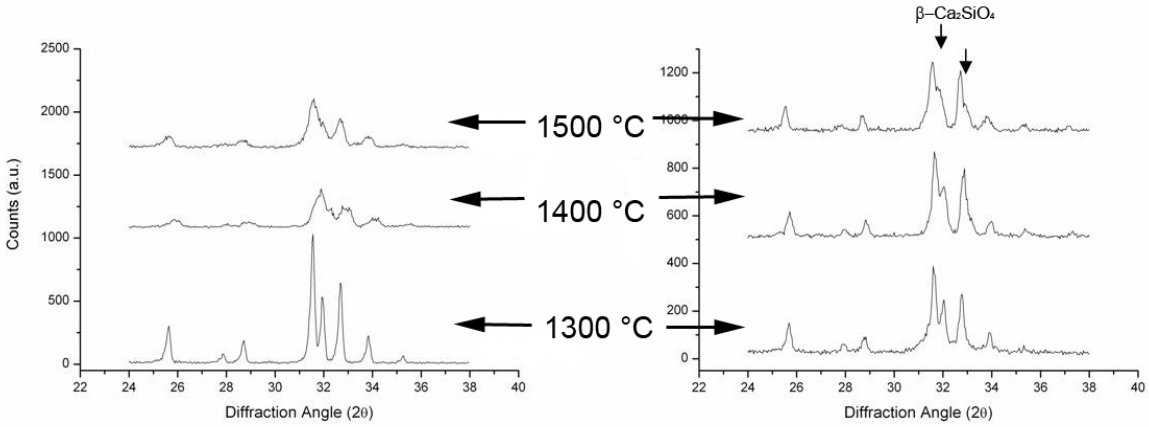

Figure 4.21. Comparison between XRD of HA and HA / Ca_2SiO_4 composite.

The analysis of sample morphology and local composition was performed by SEM-EDS, after polishing and chemical etching of the surface. Figs. 4.22 and 4.23 show the microstructure of HA and composite samples after FHP sintering at different temperatures. HA samples exhibited increasing grain sizes as higher the sintering temperature (Fig. 4.22); anyway, the grain size is limited up to 1400 °C, so that it can be considered the limit

temperature for HA-based materials, in view of load-bearing applications. In fact a reduced grain size yields reduced defect size also so that mechanical properties can improve.

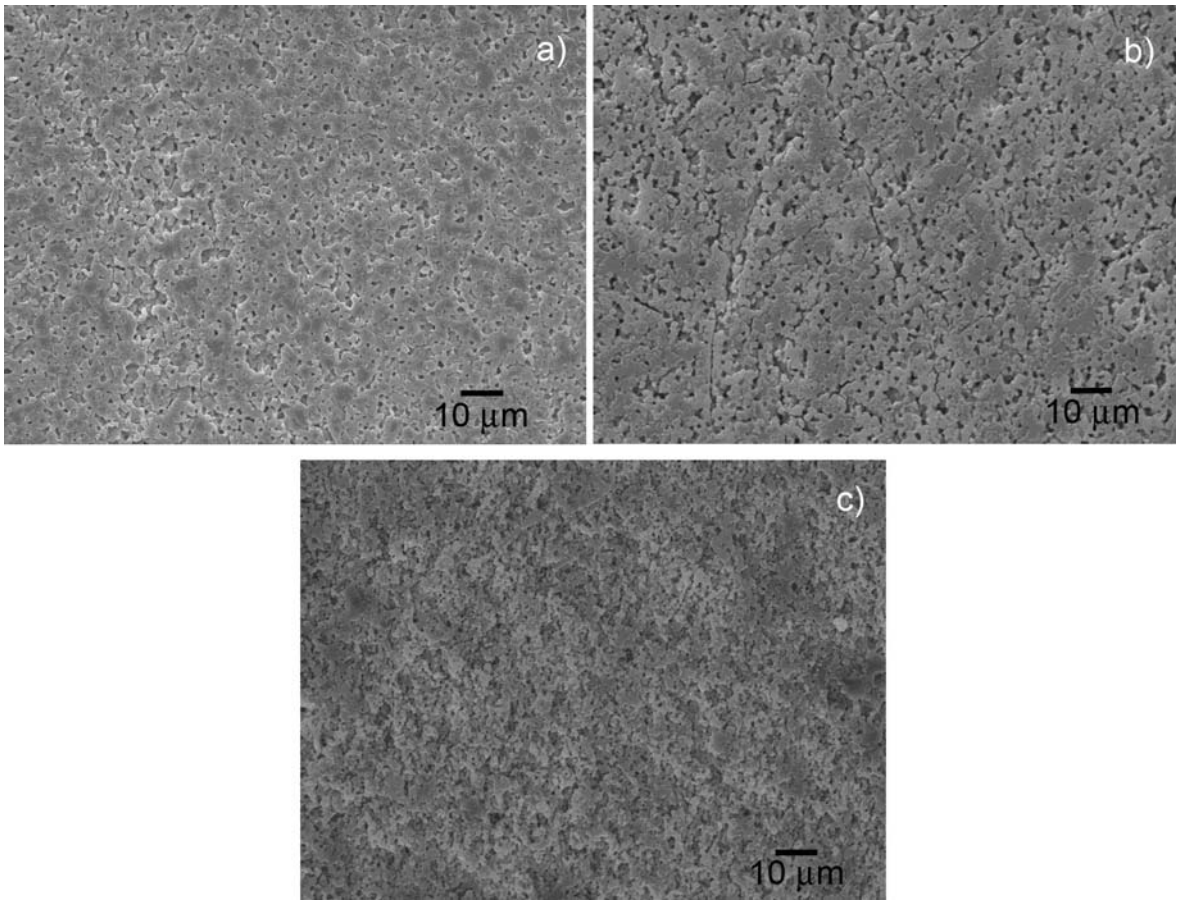

Figure 4.22. Microstructures of HA obtained by FHP at different temperatures. a): 1500 °C; b) 1400 °C; c) 1300 °C.

The composites reveal a higher pore fraction compared to HA (Fig. 4.23), anyway it is evident that a denser microstructure is achieved when sintering at 1500 °C, otherwise a too much extended porosity is found in the sample, also confirmed by the density measurements (see Tab. 4.IV), with consequent depletion of the mechanical resistance (see later, Table 4.V).

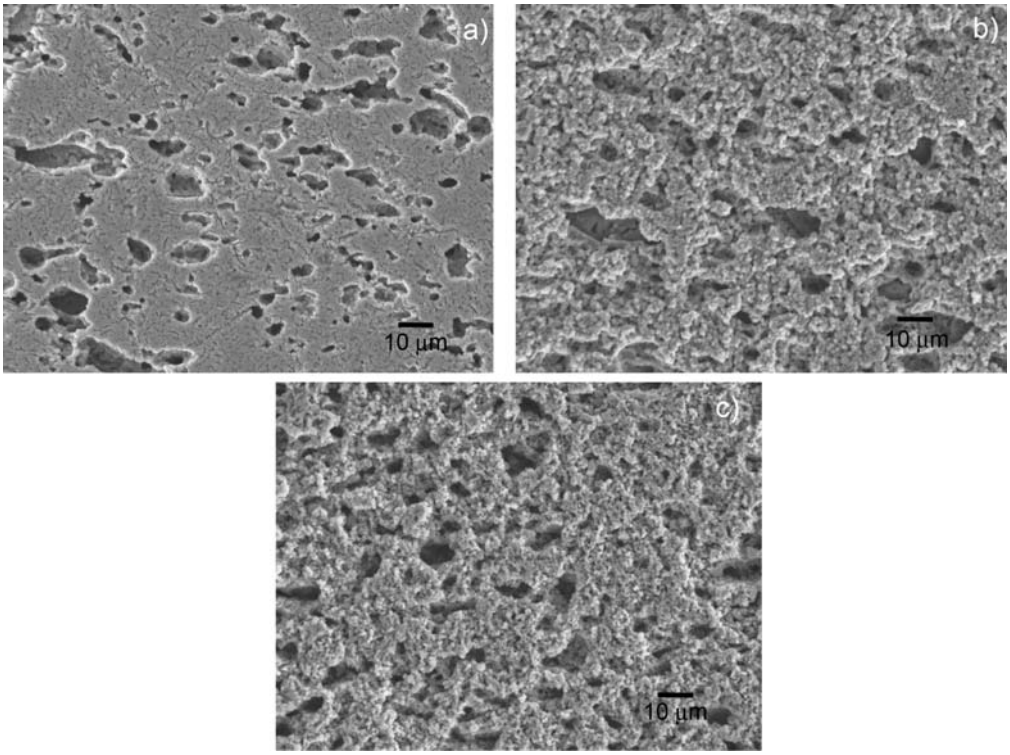

Figure 4.23. Microstructures of composites obtained by FHP at different temperatures. a): 1500 °C; b) 1400 °C; c) 1300 °C.

EDS analyses confirm that silicon was present in the whole composite in concentrations ~1.6 at% (see Fig. 4.24) and ~1.8 wt%. The average Ca/P molar ratio is ~1.70 and Si/P ratio is ~0.10.

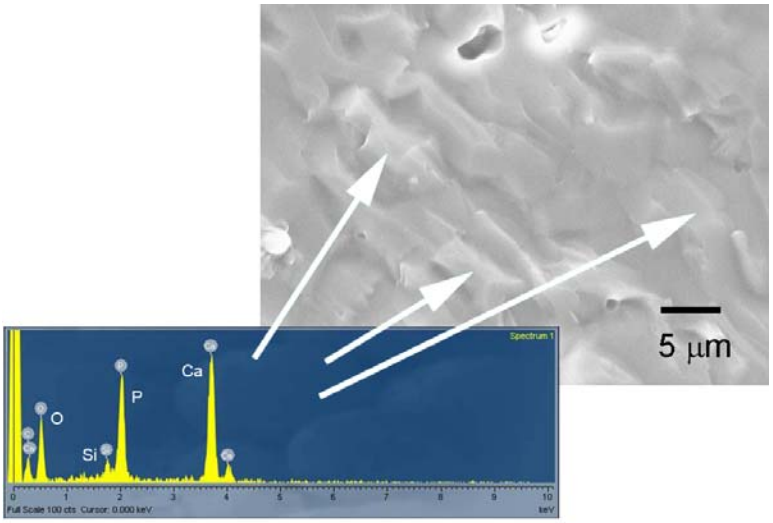

Figure 4.24. EDS analysis performed on several grains of HA-β-Ca_2SiO_4 composite sintered at 1500 °C by FHP.

Thus, although it was hard to identify the HA and silicate grains by their morphology, it was found that the FHP sintering technique can yield dense materials characterized by a chemical homogeneity, and a silicon content related to the amount of Ca_2SiO_4 in the initial mixture, so that a complete control of the final phase composition is achievable.

4.6.3 Mechanical characterization

Mechanical tests were performed on the sintered HA and composite samples, Table 4.V shows the results in terms of flexural strength.

Table 4.V. Results of flexural strength tests performed on HA and composite.

Material	Temperature (°C)	Relative density (%)	σ_{bend} (MPa)
HA	**1300**	0.87	34 ± 2
HA	**1400**	0.94	47 ± 2
HA	**1500**	0.93	42 ± 7
β-Ca_2SiO_4	**1500**	0.96	171 ± 4
HA \ β-Ca_2SiO_4	**1300**	0.72	36 ± 5
HA \ β-Ca_2SiO_4	**1400**	0.89	57 ± 8
HA \ β-Ca_2SiO_4	**1500**	0.95	70 ± 7

Both relative density and σ_b values of HA are the highest in the sample sintered at 1400 °C. HA sintered at 1500 °C shows similar σ_b values but the uncertainty in the measurement is higher. This finding is in agreement with the grain growth observed in this sample, much higher than in HA sintered at lower temperatures, and with the increasing instability of HA at 1500 °C, confirmed by its poorly resolved XRD spectrum (Fig. 4.21).

The effect of the reinforcing phase, γ-Ca_2SiO_4 transformed in the β-polymorph, was positive for flexural strength: the σ_b values exhibited by the composite are higher than those of HA at all temperatures; the highest resistance is exhibited by the composite sintered at 1500 °C, confirming that a so high temperature is needed to achieve the consolidation of both phases. Anyway, the optimal temperature could be slightly below 1500 °C to find a compromise between the starting of HA phase degradation and the maximum level of strength exhibited by the reinforcing phase.

Table 4.VI shows the results of nanoindentation analysis for some selected samples: the procedure for obtaining the final data is described elsewhere[59].

Table 4.VI. Results of nanoindentation tests on HA and composite.

Material	Relative density	Young modulus (GPa)	Nano-hardness (GPa)
HA 1500 °C	0.93	113 ± 3	4.7 ± 0.3
HA 1400 °C	0.94	113 ± 3	5.0 ± 0.3
HA+ β-CS 1500 °C	0.95	121 ± 12	5.7 ± 1.4
β-CS 1500 °C	0.96	124 ± 6	5.1 ± 1.1

The elastic properties and hardness of HA are not significantly affected by the sintering temperature; the presence of the reinforcement slightly increases both Young modulus and hardness, even if the dispersion of data is higher, as an effect of the increased number of defects in the sample microstructure, due to the coexistence of two different phases.

The elastic properties obtained by the load-displacement behaviour of HA and the composite during the flexural strength test gave quite different results, compared to nanoindentation (Table 4.VII): elastic modulus is strongly reduced, as well as the hardness.

Table 4.VII. Mechanical behaviour of HA and composite materials under macroscopic investigation.

Material	Relative density	Young modulus (GPa)	K_{IC} ($MPa \cdot m^{1/2}$)	Hardness (GPa)
HA 1500 °C	0.93	70 ± 5	0.75 ± 0.05	3.3 ± 0.1
HA 1400 °C	0.94	64 ± 5	0.87 ± 0.22	3.2 ± 0.1
HA+ β-CS 1500 °C	0.95	73 ± 5	0.71 ± 0.09	4.1 ± 0.1
β-CS 1500 °C	0.96	69 ± 3	2.92 ± 0.36	4.4 ± 0.9

The reduction of rigidity and hardness is due to the different volume of material investigated: the nanoindenter penetrates few tenths of nanometers, sensing a volume of some μm^3, so that it can be considered free of defects and nearly free of pores; the breaking of a bar of macroscopic size involves the whole sample instead, including pores and defects.

Thus, it can be assumed that porosity is responsible for the loss of rigidity. The fracture toughness, indicated by K_{IC}, was obtained by the Chevron notch method[60]. K_C expresses the resistance of a material against different deformations under loading; in particular K_{IC}

is the resistance to a tensile-opening loading[56] and it is one of the possible loading which naturally occurs *in vivo*.

The mechanical properties exhibited by the composites are in the range of cortical bone, concerning the fracture toughness and Young modulus, especially considering that in porous materials the elastic behaviour can be enhanced; the fracture toughness should be slightly raised, especially for some specific bone portions to be substituted (see also Ritchie *et al.* [56]).

The reason for matching the stiffness of the implant material to bone is that in this condition stress transfer is allowed from the implant to the surrounding bone in loading conditions. Known as Wolff's law[61], this effect stimulates the surrounding bone for continued bone remodelling, a part of which includes bone deposition onto the biomaterial surface.

Flexural strength values are still insufficient for many load-bearing applications. Anyway, HA alone can exhibit much higher values, previous suitable treatment of calcinations and agglomeration[2,9,62]; the sinterability of HA powders is in fact strictly related to their morphology and chemical composition. The presence of volatile moieties, as water and carbonate, which decompose and evaporate at high temperatures, are an obstacle to powder densification and it can provoke cracks after the residual porosity is too tight to allow their evaporation. For this reason HA powder is usually calcined at intermediate temperatures (600-1000 °C) to eliminate these volatile species. Moreover, the fine grain size of as-prepared HA makes this powder very hydrophilic and large agglomerates of particle easily form; in this condition the achievement of an homogeneous mixture with other powders is more difficult. Thus, following the treatment of calcination, the powder surface also modifies: its hydrophilicity decreases up to 300 °C, where water is prevented from being re-asdsorbed on the surface[63]; above 600 °C the HA particles start to grow through a superficial transport mechanism without an actual densification[64]; the true densification starts at ~850 °C, where larger particles grow at the expenses of the smallest ones. HA used in the present work was calcined at 1000 °C, in order to make its specific surface area similar to that of γ-Ca_2SiO_4 and allow a better powder mixture; anyway the calcining at 1000 °C does not favour mechanical properties after sintering at conventional temperatures (1250 °C), while it could favour the sintering at higher temperatures, as reported by previous studies on kinetics of HA sintering[58,62].

Anyway, at 1000 °C grain coalescence starts to be evident in HA; grains form hard agglomerates, which do not easily break under the cold compaction in pellet, so to be not suitable for the achievement of optimal green bodies. As the green body is not sufficiently dense and compact, the final sintered body will exhibit a higher number of defects, like residual pores, affecting the final mechanical properties. Thus, a lower temperature of calcination is likely to be more effective in yielding more resistant HA ceramics[62], in consequence, the composite also will exhibit a higher strength.

For these first tests, a concentration of 20 wt% of the reinforcement was selected; this choice was purely arbitrary, to investigate the feasibility of research in this field. The results in term of chemical-physical and mechanical properties are promising to investigate the biologic behaviour of these materials; on the basis of the *in vitro* / *in vivo* investigations, the optimal concentrations of the reinforcing phase, determining the bioactive properties of the final material, will be set up.

4.7 Conclusions

It was demonstrated that calcium silicates are a promising class of materials for the development of bioactive ceramic composites with HA, characterized by improved mechanical strength so to represent a potential biomaterial for load-bearing applications. Moreover, there was some evidence of silicon incorporation in HA structure, in biological-like amounts, following the thermal treatments of consolidation. A more detailed observation of the sample morphology and investigation of the local phase composition is needed to confirm this finding; the increased bioactivity, due to the increased solubility of substituted HA, has to be ascertained through solubility tests performed on sintered solids and by tests of cell cultures *in vitro* and cell response *in vivo*.

The positive result of the cytotoxicity tests encourages the development of materials based on HA / silico-carnotite mixtures. Chemically, the material can exhibit an increased bioactivity and reabsorbability compared to stoichiometric HA, due to the presence of silicon; the control of the phase stoichiometry is allowed by the virtual absence of any secondary phases, so that substituted HA characterized by tailored amount of silicon can be achieved.

Sintered bodies are destined to be employed as three-dimensional bone substitutes; thus, the future activity will be devoted to the development of dense and porous bodies to be

implanted in animals; the amount and quality of the formed bone will be analyzed, as well as the kinetic of its formation on the surface and inside the pores of the bioceramic. For this reason, the architecture of the bone substitute will be accurately designed and suitable technological procedures should be optimized and applied for this purpose.

The enhancement of the mechanical properties is fundamental in this field; a proper osteointegration is achieved when the biomechanical loads are well distributed in the synthetic scaffold and the surrounding bone. If an increased bioactivity of the composites HA / calcium silicates will be assessed, they will represent a new wide field of investigation for the development of HA-based high-resistant materials with a variety of compositions. In fact, many different second phases, beyond the ones investigated in this work and belonging to the calcium silicate system, can be investigated: a number of these materials have shown a good bioactivity *in vitro* and *in vivo*; these materials also contain magnesium (bredigite, diospide, etc..), so they can express a potentially superior bioactivity, in terms of quality of cell response; their mechanical properties are similar but the solid state interactions occurring when mixed with HA at high temperatures are still unpredicted. For each material, a wide range of investigation has to be carried out:

1) The assessment of the reactivity between HA and the second phase at different temperatures and atmospheric conditions. This implies a full chemical-physical investigation of the ceramic powders employed, in terms of chemical composition, thermal behaviour, grain morphology and size, and of the final materials, in the bulk and on the surface.

2) The assessment of the mechanical strength and its relationship with the microstructure, which strongly depends on the sintering treatment itself. Thus, the sintering cycle must be set up according to an optimized microstructure, in terms of density and grain size, with a minimal formation of defects. For this purpose thermo-analytical and microscopic investigations will be carried out on powders and sintered materials, in feed-back with a complete assessment of the mechanical properties, on a micro- and a macro-scale.

3) The assessment of the bioactivity and resorbability of the composite and its relationship with the chemical composition at the implant surface. For this purpose, solubility tests in SBF will be performed; a deeper investigation will involve cell

culture on the surface of powders and consolidated bodies and when particularly promising, small animals (rabbits, goats, sheep) will be employed for scaffold implantation and subsequent analysis of the newly formed tissues, in term of bone mineral qualification and quantification; scaffolds can also be previously cultivated with stem cells and / or growth factors to enhance the osteointegration.

4) The *in vivo* behaviour of 3D scaffolds, especially concerning osteointegration, strongly depends on the scaffold morphology, in particular pore size and interconnectivity. Thus, suitable technologies will be developed for porous bodies manufacturing; for this purpose, a full characterization of the powders will be needed, in term of morphology, size, and surface charge, to be achieved through techniques like BET, electro-acoustic spectroscopy and sedimentography. On this basis, the different technological procedures (foaming, impregnation, freeze-drying, biomimetic syntheses, etc..) will be optimized for the achievement of ceramic bodies characterized by suitable porosities and pore interconnection; the employment of a composite implies the presence of at least two powders, which can have different morphological and surface properties; for this purpose preliminary treatments of homogenization can include spray-drying techniques to obtain spherical granulates prior forming and sintering. It has been shown, in the case of silico-carnotite and also in part with dicalcium silicate, that sintering can make react HA and the second phase, giving rise to a powder with more uniform characteristics; in this case, the set-up of ceramic suspensions is made easier.

The picture deriving by the interactions at high temperature of HA with bioactive calcium silicates is thus rather complex, as it includes a wide number of materials characterized by similar properties but exhibiting very different effects when heated in mixture with HA. The inter-relationship between physico-chemical, mechanical and biological properties, makes necessary a careful investigation of the properties of the raw materials and the effects on their interaction at high temperature at a chemical, microstructural and mechanical level; these three effects strongly reflect in a complicated manner on the biologic performances, which are the ultimate reason for the development of these composite materials.

References

1. Hench L. Bioceramics. J Am Cer Soc 1998; 81 (7): 1705-1728.

2. Thangamani N, Chinnakali K. Gnanam FD. The effect of powder processing on densification, microstructure and mechanical properties of hydroxyapatite. Ceram Inter 2002; 28: 355-362.

3. Kothapalli C, Wei M, Shaw MT. Influence of temperature and concentration on the sintering behaviour and mechanical properties of hydroxyapatite. Acta mater 2004; 52: 5655-5663.

4. Juang HY, Hon MH. Effect of calcinations on sintering of hydroxyapatite. Biomaterials 1996; 17: 2059-2064.

5. Pattanayak DK, Dah R, Prasad RC, Rao BT, Rama Mohan TR. Synthesis and sintered properties evaluation of calcium phosphate ceramics. Mat Sci Eng C 2007; 27: 684-690.

6. Kobayashi S, Kawai W, Wakayama S. The effect of pressure during sintering on the strength and the fracture toughness of hydroxyapatite ceramics. J Mater Sci: Mater Med 2006; 17: 1089-1093.

7. Jarcho M, Bolen CH, Thomas MB, Bobick J, Kay JF, Doremus RH. Hydroxylapatite synthesis and characterization in dense polycrystalline form. J Mater Sci 1976; 1: 2027-2035.

8. Halouani R, Bernache-Assolant D, Champion E, Ababou A. Microstructure and related mechanical properties of hot pressed hydroxyapatite ceramics. J Mater Sci: Mater Med 1994; 5: 563-568.

9. Tampieri A, Celotti G, Szontagh F, Landi E. Sintering and characterization of HA and TCP bioceramics with control of their strength and phase purity. J Mater Sci: Mater Med 1997; 8: 29-37.

10. Chen OZ, Thompson ID, Boccaccini AR. 45S5 Bioglass®-derived glass–ceramic scaffolds for bone tissue engineering. Biomaterials 2006; 27 (11): 2414-2425.

11. Sung YM, Shin YK, Ryu JJ. Preparation of hydroxyapatite/zirconia bioceramic nanocomposites for orthopaedic and dental prosthesis applications. Nanotechnology 2007; 18 (6): 065602-065607.

12. Abdelrazek KK. Won KS, Yong KH. Consolidation and mechanical properties of nanostructured hydroxyapatite–(ZrO_2 + 3 mol% Y_2O_3) bioceramics by high-frequency induction heat sintering. Mater Sci Eng A 2007; 456 (1-2): 368-372.

13. Singh D, de la Cinta Lorenzo-Martin M, Gutiérrez-Mora F, Routbort JL, Case ED. Self-joining of zirconia/hydroxyapatite composites using plastic deformation process. Acta Biomater 2006; 2 (6): 669-675.

14. Wiswanath B, Ravishankar N. Interfacial reactions in hydroxyapatite/alumina nanocomposites. Scr Mater 2006; 55 (10): 863-866.

15. Chiba A, Kimura S, Raghukandan K, Morizono Y. Effect of alumina addition on hydroxyapatite biocomposites fabricated by underwater-shock compaction. Mater Sci Eng A 2003; 350 (1-2): 179-183.

16. Choi JW, Kong YM, Kim HE. Reinforcement of hydroxyapatite by addition of Ni_3Al and Al_2O_3. J Am Ceram Soc 1998; 81 (7): 1743-1748.

17. Shi LS, Pan W, Fang MH, Fang ZY. Reinforcement of hydroxyapatite bioceramic by addition of Ti_3SiC_2. J Am Ceram Soc 2006; 89 (2): 743-745.

18. Uchida M, Kim HM, Kokubo T, Miyaji F, Nakamura T. Bonelike Apatite Formation Induced on Zirconia Gel in a Simulated Body Fluid and Its Modified Solutions. J Am Ceram Soc 2001; 84: 2041-2044.

19. Uchida M, Kim HM, Kokubo T, Fujibayashi S, Nakamura T. Structural dependence of apatite formation on titania gels in a simulated body fluid. J Biomed Mater Res 2003; 64: 164-170.

20. Shirkhanzadeh M, Sims S. Immobilization of calcium phosphate nano-clusters into alkoxy-derived porous TiO2 coatings. J Mater Sci: Mater Med 1997; 8: 595-601.

21. Hench LL, Splinter RJ, Allen WC, Greenlee TK. Bonding mechanisms at the interface of ceramic prosthetic materials. J Biomed Mater Res Symp 1971; 36: 117.

22. Örjan HA, Kaj HK. On the bioactivity of silicate glass. J Non-Cryst Solids 1991; 129: 145.

23. Yan HW, Zhang K, Blanford CF, Francis LF, Stein A. *In vitro* hydroxycarbonate apatite mineralization of $CaO\text{-}SiO_2$ sol-gel glasses with a three-dimensionally ordered macroporous structure. Chem Mater 2001; 13: 1374.

24. Branda F, Arcobello-Varlese F, Costantini A, Luciani G. Effect of the substitution of M_2O_3 (M=La, Y, In, Ga, Al) for CaO on the bioactivity of $2.5CaO.2SiO_2$ glass. Biomaterials 2002; 23: 711.

25. Izquierdo-Barba I, Sanlinas AJ, Vallet-Regi M. *In vitro* calcium phosphate formation on sol-gel glasses of the $CaO\text{-}SiO_2$ system. J Biomed Mater Res 1999; 47: 243.

26. Kokubo T. A/W Glass-ceramics: Processing and properties. In: Hench LL, Wilson J (eds). An Introduction to Bioceramics. World Scientific, USA, 1993, p. 75.

27. Ono K, Yamamuro T, Nakamura T, Kakutani Y, Kitsugi T. Apatite-wollastonite containing glass–ceramic–fibrin mixture as a bone defect filler. J Biomed Mater Res 1988; 22: 869.

28. Kokubo T. Surface chemistry of bioactive glass-ceramics. J Non-Cryst Solids 1990; 120: 138.

29. Kokubo T, Kushitani H, Saka S, Kitsgi T, Kitsugi T, Yamamuro T. Solutions able to reproduce *in vivo* surface structure changes in bioactive glass-ceramic A-W. J Biomed Mater Res 1990; 24: 721.

30. Cho SB, Miyaji F, Kokubo T, Nakamura T. Induction of bioactivity of a non-bioactive glass-ceramic by a chemical treatment. Biomaterials 1997; 18: 1479.

31. Brown PW. Hydration behavior of calcium phosphates is analogous to hydration behavior of calcium silicates. Cem Concr Res 1999; 29: 1167–1171.

32. De Aza PN, Guitian F, De Aza S. Bioactivity of wollastonite ceramics: *in vivo* evaluation. Scr Metal Mater 1994; 31: 1001.

33. De Aza PN, Luklinska ZB, Anseau MR, Guitian F, De Aza S. Bioactivity of pseudo-wollastonite in human saliva. J Dent Res. 1999; 27: 107.

34. De Aza PN, Luklinska ZB, Anseau MR, Hector M. Reactivity of a wollastonite- tricalcium phosphate Bioeutectic® ceramic in human parotid saliva. Biomaterials 2001; 21: 1735.

35. De Aza PN, Guitian F, De Aza S. Eutectic structures that mimic porous bone. In: Tomsia AP, Glaeser A (eds). Ceramic Microstructure Control at the Atomic Level. Plenum Press, New York, 1999, p. 741.

36. Liu XY, Ding CX, Wang ZY. Apatite formed on the surface of plasma-sprayed wollastonite coating immersed in simulated body fluid. Biomaterials 2001; 22: 2007.

37. De Aza PN, Guitian F, De Aza S. Bioeutectic: a new ceramic material for human bone replacement. Biomaterials 1997; 18: 1285.

38. Liu XY, Ding CX. Charaterization of plasma sprayed wollastonite powders and coatings. Surf Coat Tech 2002; 153: 173.

39. Siriphannon P, Hayashi S, Yasumori A, Okada K. Preparation and sintering of $CaSiO_3$ from coprecipitated powder using NaOH as precipitant and its apatite formation in simulated body fluid solution. J Mater Res Soc 1999; 14: 529.

40. Lamy D, Pierrc AC, Heimann RB. Hydroxyapatite coatings with a bond coating of biomedical implants by plasma projection. J Mater Res 1996; 11: 680.

41. Liu XY, Tao SY, Ding CX. Bioactivity of plasma sprayed dicalcium silicate coatings. Biomaterials 2002; 23: 963.

42. Siriphannon P, Kameshima Y, Yasumori A, Okada K, Hayashi S. Influence of preparation conditions on the microstructure and bioactivity of α-$CaSiO_3$ ceramics: formation of hydroxyapatite in simulated body fluid. J. Biomed. Mater. Res. 2000; 52: 30-39.

43. Siriphannon P, Kameshima Y, Yasumori A, Okada K, Hayashi S. Formation of hydroxyapatite on $CaSiO_3$ powders in simulated body fluid. J Eu Ceram Soc 2002; 22: 511.

44. Zhao W, Chang J. Sol–gel synthesis and *in vitro* bioactivity of tricalcium silicate powders. Materials Letters 2004; 58: 2350– 2353.

45. Wan X, Chang C, Mao D, Jiang L, Li M. Preparation and *in vitro* bioactivities of calcium silicate nanophase materials. Mat Sci Eng C 2005; 25: 455–461.

46. Lin K, Zhai W, Ni S, Chang J, Zeng Y, Qian W. Study of the mechanical property and *in vitro* biocompatibility of CaSiO3 ceramics. Ceram Int 2005; 31: 323–326.

47. Gou Z, Chang J, Zhai W. Preparation and characterization of novel bioactive dicalcium silicate ceramics. J Eu Cer Soc 2005; 25: 1507–1514.

48. Long LH, Chen LD, Bai SQ, Chang J, Lin KL. Preparation of dense β-CaSiO3 ceramic with high mechanical strength and HAp formation ability in simulated body fluid. J Eu Cer Soc 2006; 26: 1701–1706.

49. Wu C, Chang J, Wang J, Ni S, Zhai W. Preparation and characteristics of a calcium magnesium silicate (bredigite) bioactive ceramic. Biomaterials 2005; 26: 2925-2931.

50. Nonami T, Tsutsumi S. Study of diopside ceramics for biomaterials. J Mater Sci. Mater Med 1999; 10: 475-479.

51. Hench LL. Bioceramics: From concept to clinic. J Am Ceram Soc 1991; 74 (7): 1487-1510.

52. Ghosh SN, Rao PB, Paul AK, Raina K. The chemistry of dicalcium silicate minerals. J Mater Sci 1979; 14: 1554-1556.

53. Chan CJ, Kriven WM, Young JF. Physical stabilization of the β→γ transformation in dicalcium silicate. J Am Ceram Soc 1992; 75(6) 1621-1627.

54. Hong SH, Young JF. Hydration kinetics and phase stability of dicalcium silicate synthesized by the Pechini process. J Am Ceram Soc 1999; 82 (7): 1681-1686.

55. Gou Z, Chang J. Synthesis and *in vitro* bioactivity of dicalcium silicate powders. J Eu Ce Soc 2004; 24: 93–99.

56. Ritchie RO, Kinney JH, Kruzic JJ, Nalla RK. Cortical bone fracture. In: Akay M (ed), Wiley Encyclopedia of Biomedical Engineering, New York, 2006.

57. Tampieri A, Celotti G, Sprio S, Caciuffo R, Rinaldi D. Study of the sintering behaviour of MgB_2 superconductor during hot-pressing. Phys C 2004; 400: 97-104.

58. Landi E, Tampieri A, Celotti G, Sprio S. Densification behaviour and mechanisms of synthetic hydroxyapatites. J Eu Ceram Soc 2000; 20: 2377-2387.

59. Oliver WC, Pharr GM. Measurement of hardness and elastic modulus by instrumented indentation: Advances in understanding and refinements to methodology. J Mater Res 2004; 19 (1): 3-20.

60. Munz DG, Shannon JL, Bubsey RT. Fracture toughness calculation from maximum load in 4 point bend tests of chevron notch specimens. Intl J Frac 1980; 16 (3): R137-R141.

61. Wolff J, Hirchwild A. The law of remodelling. Springer-Verlag, Berlin, 1986.

62. Juang HY, Hon MH. Effect of calcinations on sintering of hydroxyapatite. Biomaterials 1996; 17: 2059-2064.

63. Bertinetti L. Nanomateriali per applicazioni biomediche: sintesi e caratterizzazione delle funzionalità di superficie. PhD thesis, University of Torino.

64. Bernache Assollant D, Ababou A, Champion E, Heughebaert M. Sintering of calcium phosphate hydroxyapatite $Ca_{10}(PO_4)_6(OH)_2$ I. Calcination and particle growth. J Eu. Ceram Soc 2003; 23 (2): 229-241.

CHAPTER 5

HIERARCHICALLY ORGANIZED STRUCTURES AS BONE SCAFFOLDS

5.1 Introduction

As already discussed in the previous Chapters, the morphology of 3D bone scaffolds, in term of pores size distribution and pores interconnectivity is fundamental for an efficient osteoconduction, i.e. cell habitation and proliferation even in the inner part of the scaffold.

In a different perspective, the scaffold morphology should approach to the complex morphology of natural bone, which also allows an efficient distribution of the mechanical loads to the smallest trabeculae, where the strain-sensing mechanism exhibited by the osteocytes can take place and activate the permanent bone remodelling process (see also Chapter 1). This mechanism allows the continuous re-arrangement of the bone tissue in presence of biophysical stimuli from the environment, so that the local damage is minimized and the functionality of the bone as a whole is optimized.

Thus, only a scaffold exhibiting a structure with a high degree of hierarchy can be able to yield the optimal biophysical response, after implantation *in vivo*; such a solution is particularly required in the healing of long bone disease, where the biomechanical loads are more complex and intense, so that the development of hierarchically organized bone scaffolds would represent a breakthrough in the knowledge in this field, surpassing the current solutions in the field of synthetic bone substitutes.

In fact, during the last few decades, a variety of scaffolds characterized by complex structures have been developed and launched on the market, reaching a good compromise in term of mimicking the micro and macro-porosity of natural bone. Indeed, open-pore geometries with highly porous surface and microstructure allowing cell in-growth and

reorganization and providing the necessary space for neovascularization have been obtained.

Regrettably, the current production processes do not allow to generate an organised hierarchical structure, owing to limitations in the currently available processing technology. Therefore, surgeons are now forced to use cadaver bones from tissue banks, just because it can be loaded as soon as they are implanted. In general, acceptable clinical results have been obtained so far, but no suitable solution have been found yet for regenerating long and load-bearing bone segments.

One of the most advanced 3D processing technologies is Rapid Prototyping (e.g stereolithography, laser sintering etc), which allows to generate porous structures with designed geometry out of virtually any material. Porous scaffolds designed in hydroxyapatite with a strut thickness of a few hundred micrometers have been obtained. However the rapid prototyping techniques so far developed have not enough spatial resolution to reproduce the complex hierarchical structure of bone and the resulting scaffolds have very poor bio-mechanical properties.

Natural bio-structures usually have properties that in most of the cases significantly surpass those of analogous synthetically manufactured materials with similar phase compositions. Most of the structural materials used by Nature are polymers or composites of polymers and ceramic particles. Such materials would not be the first choice of an engineer who intends to build very stiff and long-lived mechanical structures. Nevertheless, Nature makes the best out of the limitations in the chemical environment, adverse temperatures and uses polymers and composites to build trees and skeletons[1]. Thus, the solutions developed by Nature can serve as a source of inspiration[2] for manufacturing synthetic hierarchical structures with superior functional properties.

5.2 Wood structures as templates for bone scaffolds

The vegetable kingdom includes a great variety of hierarchical tissue structures with impressive biomechanical properties; for example, some tree branches can support the weight of an entire house, and others can be bent and stretched into any shape.

At the macroscopic level, spruce wood can be considered as a cellular solid, mainly composed of parallel hollow tubes, the wood cells. As an example, the hierarchical structure of spruce wood is shown in Fig. 5.1. The wood cells are clearly visible and they

have a thicker cell wall in latewood than in earlywood, within each annual ring. The cell wall is a fibre composite made of cellulose microfibrils embedded into a matrix of hemicelluloses and lignin[3].

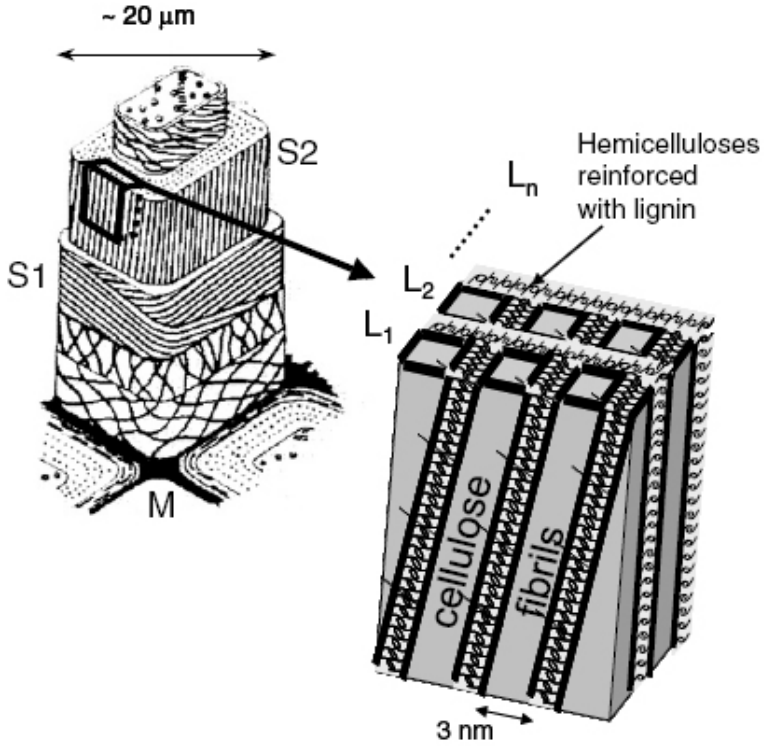

Figure 5.1. Hierarchical structure of wood.

Typically, the cell-wall consists of several layers (S1, S2, . . .), where the S2 is by far the thickest. While the cellulose microfibrils in the S1-layer run at almost 90° to the cell axis[3], the cellulose microfibrils in the S2 layer are more parallel to it, with microfibril angles ranging from 0° to about 45°.

In summary, wood can be regarded as a cellular material at the scale of hundred micrometers to centimetres. Parameters which can be varied at this hierarchical level (and, therefore, used for adaptation to biological and mechanical needs) are the diameter and shape of the cell cross-section, as well as the thickness of the cell wall. In particular, the ratio of cell-wall thickness to cell diameter is directly related to the apparent density of wood which, in turn is an important determinant of the performance of light weight structures. The stem is further organized in annual rings with alternating layers of thin- and thick-walled cells. This creates a fairly complex structure with layers of alternating density. At the lower hierarchical level, the complexity increases even further since the wall of individual cells is a fibre composite. The orientation of the cellulose fibril direction with

respect to the cell axis has a major influence on the mechanical properties of the tissue as a whole, and – depending on the (biological or mechanical) needs – the microfibril angle can be adjusted locally.

In this respect, native or semi-processed wood and plant habits may be successfully used as templates for generating ceramic materials through transformation processes, involving pyrolysis and chemical reactions (with solid, liquid or gaseous phases); this materials, which might be called "lignocers**",** can exhibit a hierarchic structure very close to the one of the original wood.

The mechanical properties of wood itself are remarkable: in the Ashby diagram reported in Fig. 5.2, wood exhibits improved performances compared to the polymeric materials currently used in engineering, although wood itself is a polymeric material, also due to its very low density.

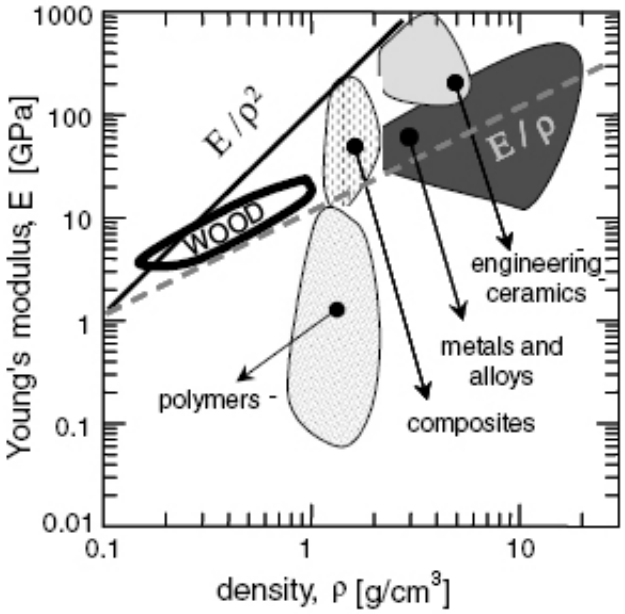

Figure 5.2. Comparison between mechanical performances of different classes of materials.

5.3 Ceramization of native vegetable structures

Preliminary investigation on ceramization processes of native wood structures has led to the development of porous bodies in silicon carbide[4-9] by wood pyrolysis and subsequent infiltration with melted silicon; BioSiC® technology was also developed[10-12] with similar technology, to manufacture porous biocompatible ceramic bodies,

characterized by very good mechanical performances and morphology very well resembling the cortical human bone.

The pyrolysis of wood is commonly carried out in inert atmosphere and temperature varying from 800 to 2000 °C, so to decompose all the organic components; thus, it is accompanied by the thermal degradation of cellulose, hemicellulose and lignin as its main components of the wood and a subsequent conversion into a carbon structure. The mechanism of cellulose thermal decomposition was suggested as follows:

- Desorption of adsorbed water (< 150 °C)
- Dehydration of the cellulose crystal water (150 - 240 °C)
- Chain scissions, breaking C-O and C-C bonds (240 - 400 °C)
- Aromatization (> 400 °C)

The resulting product is a carbon preform, maintaining the morphological arrangement of the native wood. Starting by the carbon preform, through a sequence of infiltration and/or electrochemical processes, ceramic materials showing uniform as well as non-uniform (hierarchical) pore structures can be obtained.

Moreover, on the basis of the structure of the native vegetable, different morphologies can be obtained by setting up the different steps of the ceramization process, so to develop scaffolds for bone substitution with a suitable structure-morphology to reach improved biomechanical performance. Finally, by developing material synthesis and assembly processes able to mimic biological principles and hierarchic morphology, it is possible to pave the way for realizing prosthetic devices which could get closer to the extraordinary performance of human bones.

In order to achieve bone scaffolds merging the biomimetic, mechanical and morphological features of the bone tissue, the idea was to obtain apatite-based materials, starting by pyrolyzed wood structure through a series of reaction with calcium- and phosphate-containing reactants: The reactions are carried out at high and ambient temperatures leading to increasingly complex materials, approaching apatite phase by following the pathway displayed in Fig. 5.3.

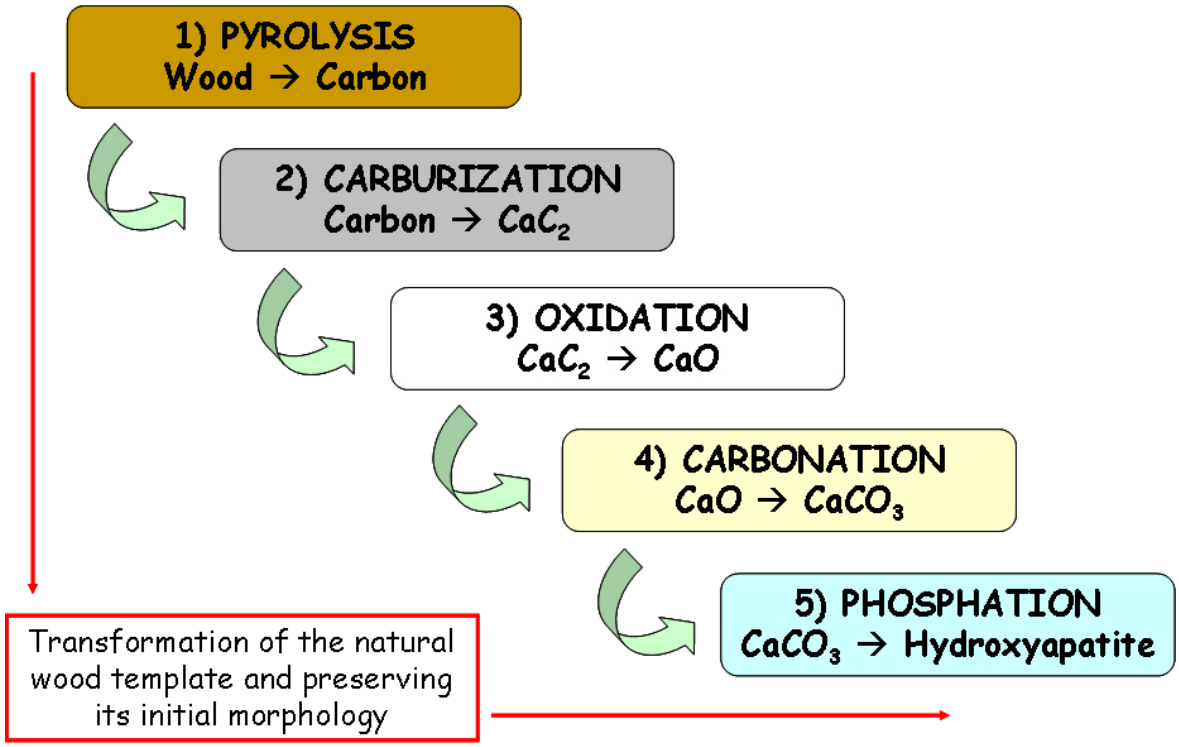

Figure 5.3. Reaction pathway to obtain hydroxyapatite scaffolds starting by native wood.

In detail, starting from vegetal raw materials, selected on the basis of their structure (pine-wood and larch-wood for initial experimentations), a treatment of pyrolysis yielded carbon templates, which were subsequently infiltrated by vapour or liquid phase calcium to produce calcium carbide (carburization); after, porous calcium oxide was obtained by a further process of oxidation and subsequently transformed in calcium carbonate by reaction with carbon dioxide. All these steps were carried out by thermal and hydrothermal reactions in controlled environment; finally the final step was reached through a phosphation treatment in which porous calcium carbonate was transformed in hydroxyapatite. The set up of the transformation of the carbon preform was carried out by using commercial raw materials: calcium carbide powder for testing the oxidation and carbonation processes and calcium carbonate powder for testing the phosphation process.

The phase composition and morphology of raw, intermediate and final materials, as well as the correspondence between the initial and final microstructure for each step were investigated by X-ray diffraction (XRD: CuKα radiation, Miniflex Rigaku) and scanning electron microscopy (SEM: Stereoscan 360, Leica, Cambridge) with energy dispersion spectroscopy (EDS: INCA 300, Oxford Instruments).

Pyrolysis

Native woods (mainly larch-wood and pine-wood) of different pore size distribution and composition were used, in form of parallelepiped specimens (about 1 cm^3 in volume). The pyrolysis process was performed on woods in their native form, after preliminary drying at at 80°C in ventilated oven. The selected temperature for pyrolysis was 1000°C in Argon atmosphere; during the pyrolysis process, in order to prevent the cracking of the carbon template due to the release of volatile moieties (H_2O, CO and CO_2), a slow heating rate of 1 °C/min was applied up to the final temperature; the specimens were hold at the final temperature for 1 hour, and after cooled at -2°C/h.

Anisotropic shrinkage in axial, tangential and radial directions was associated with the pyrolysis process, according to the starting pore arrangement. Despite the large weight loss during pyrolysis, the carbon template reflected the microstructure and morphology of the native specimen.

Carburization

Spherical metallic calcium particles (in small spheres, ~2 mm diameter size) or calcium hydride powder (CaH_2) were employed as a calcium source for carburization process on the carbon preforms.

The carburization was carried out by infiltration of liquid or vapour calcium into the porous carbon template, involving a suitable heating treatment where the calcium reacted with the carbon surface and diffused into the core of its structure. Different thermal cycles were investigated to achieve selectively liquid or vapour phase infiltration, as well as the arrangement of samples and reactants inside the furnace chamber. A furnace equipped with graphite heating elements was employed for carburization process, performed in argon flux, similarly as in the pyrolysis process

The chemical reaction involving the carbon template and liquid or gaseous calcium to form calcium carbide ceramics is:

$$2C + Ca \rightarrow CaC_2 \qquad 1).$$

In the liquid phase method, spontaneous infiltration was achieved by immersing the carbon preform into the calcium source, so that melted calcium penetrated into the pores and canals by capillarity; in the vapour phase method, the carbon preform and calcium are separated and the reaction occur only by solid-gas interaction. The thermal cycle was set up to allow the slow the melting and subsequent evaporation of the calcium (Fig. 5.4).

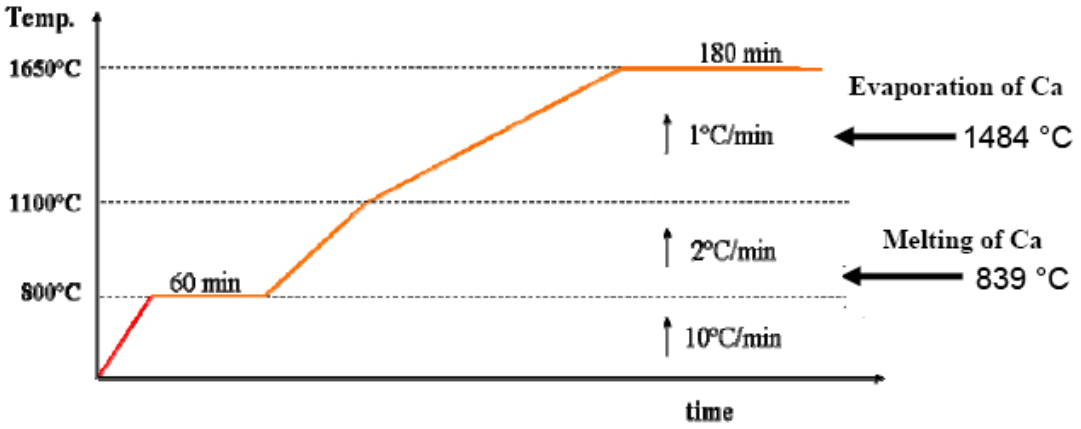

Figure 5.4. Typical thermal cycle in carburization process.

In these processes, the most influent parameters on the formation of the products and the final sample structure were found to be the local carbon morphology, the calcium / carbon ratio, the furnace final temperature and dwell time.

To check whether complete reaction occurred, small pieces of samples were plunged in water: calcium carbide strongly reacts with water, forming white calcium hydroxide and acetylene gas, so the absence of any residual black un-reacted carbon indicate the complete conversion of carbon in calcium carbide.

After the process, the final calcium carbide structure exhibited an improved toughness compared to the carbon preform, but it is easily degraded by moisture following the reaction:

$$CaC_2 + 2H_2O \rightarrow Ca(OH)_2 + C_2H_2 \qquad 2),$$

so that, once extracted by the furnace, the pieces must be preserved in inert gas environment or vacuum conditions.

In **liquid phase infiltration**, the porous carbon preform was put in a graphite crucible and covered by the calcium source (Fig. 5.5A). The crucible was closed and positioned inside the furnace chamber. Some graphite felt was put around the crucible in order to avoid the corrosion of the graphite heating elements by the evaporating calcium.

The thermal cycle was set up in order to achieve the melting of calcium (melting point of Ca: 839 °C) and its spontaneous infiltration in the porous carbon preform along different orientations (axial and radial). Firstly, the temperature was rapidly raised up to 800 °C, while the subsequent step was carried out at a reduced heating rate to allow the slow

melting of calcium: in fact, as the calcium source is often surrounded by a thin layer of calcium oxide, due to the exposure to atmosphere, the melted core has to overcome this layer, so that an excessively rapid decrease of the metal viscosity provokes the violent expulsion of the metal from the core, resulting detrimental for a careful control of the carburization process.

The final steps of the thermal cycle of carburization were set up in the range of 1550-1850 °C (higher than boiling point of calcium, 1484 °C), with the purpose of eliminating the excess of calcium by evaporation.

The final temperature was reached after gradually raising at 1 °C/min; the dwell time was 1 hour to allow the complete reaction of calcium with the carbon structure and the evaporation of the not reacted calcium. All the processes occurred under Argon atmosphere, preserving the calcium source by oxidation, the ignition of pyrolysed wood and the hydration of the formed calcium carbide.

Thermal shock may cause collapse of the carbon network when penetration of liquid calcium is too rapid. The un-reacted calcium partly remained into the pore channels so that $Ca(OH)_2$ phase, formed after exposure to the moisture, was observed. The residual calcium content depends on the total porosity, the pore channel diameter distribution and the deviation of calcium amount from the stoichiometry (eq.1).

In **vapour phase reaction**, the carbon preform was placed above the calcium source. The thermal cycle was set up in order to achieve the evaporation of calcium (above 1484 °C), with final temperatures in the same range of the liquid phase process, 1550-1850 °C.

The ideal temperature was found to be 1650 °C: below this temperature the reaction is not complete and part of the starting carbon remain un-reacted, while too high temperatures can provoke the deformation of the calcium carbide network.

A typical experiment was set up as follows: a graphite cylindrical crucible was filled with calcium granules; another crucible was prepared as follows: its lateral walls were drilled right through, in the same way a piece of pyrolysed wood was also drilled. A supporting wire (thickness: 0.9 mm) was used, passing through the wood and the crucible; the crucible so prepared was overturned and positioned upon the crucible filled with calcium. A reaction chamber was so created, forming a closed environment where calcium is at the

bottom part and the pyrolysed wood suspended at the top by the supporting wire (Fig. 5.5 B).

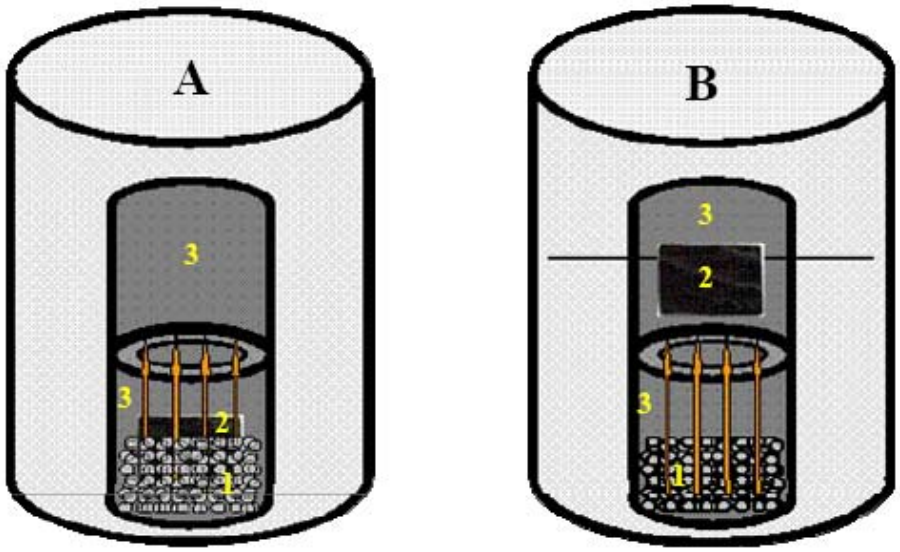

Figure 5.5. Sample arrangement in calcium infiltration. A: liquid phase; B: gaseous phase.

Oxidation

Preliminary experiments to transform calcium carbide in calcium oxide were performed, using commercial CaC_2 powder.

The oxidation process allows the conversion of calcium carbide to calcium oxide in moist air after suitable thermal cycle in furnace chamber.

It is assumable that the involving mechanisms are two: hydration of calcium carbide by water in air and, at the same time, the de-hydration of the new formed calcium hydroxide above its decomposition temperature (about 480 °C).

The hypothesized chemical reactions involved in the oxidation process are indicated below:

$CaC_2 + 2H_2O \rightarrow Ca(OH)_2 + C_2H_2$ 3),

$Ca(OH)_2 \rightarrow CaO + H_2O$ 4).

Total reaction: $CaC_2 + H_2O \rightarrow CaO + C_2H_2$ 5).

The steps were performed via thermal cycles according to the characteristics of the reactions:

- fast heating up to 500 °C (10 °C/min) to reduce the hydration of the CaC_2 on the basis of the reaction 1) and to minimize the formation of $Ca(OH)_2$, which is detrimental for the maintenance of the original preform structure.

- once the formation of $Ca(OH)_2$ is hampered by the high temperature (> 480 °C), a slow heating from 500 to 1000 °C (2 °C/min) was performed: in this step the reaction 2) is favoured and the formation of CaO is extensive. The slow heating rate reduced the structural deformation of the original CaC_2 porous ceramic.

Carbonation

Porous calcium carbonate structures were obtained from calcium oxide via either the flux of gaseous CO_2 inside the furnace chamber or via the addition of compressed CO_2 into a high-pressure closed autoclave. The chemical reaction involved in both the processes was the following:

$CaO + CO_2 \rightarrow CaCO_3$

In the experiment carried out in furnace, a gas flow of CO_2 (1 l/min) is put in contact with CaO porous ceramic at temperatures between 500 and 700°C and the carbonation reaction takes place to form $CaCO_3$. This temperature range is ideal to avoid the hydration of CaO (below 480 °C) and the decomposition of $CaCO_3$ (above 750-800 °C).

In autoclave, the full conversion of CaO in $CaCO_3$ was obtained by high pressure treatments in autoclave. The employment of high pressure values allowed the penetration of CO_2 across the layer of the new formed $CaCO_3$ up to the core of the CaO structure, also increasing the rate of carbonation.
Typical conditions for carbonation by autoclave were 300-400 °C for temperature and 10-20 bar for pressure.

Phosphation

Initial tests to transform calcium carbonate to calcium phosphate-based ceramics were performed using KH_2PO_4 as a phosphate source; both $CaCO_3$ commercial powder and $CaCO_3$ templates coming from the ceramization process described above were used, following the reaction:

$10CaCO_3 + 6KH_2PO_4 \rightarrow Ca_{10}(PO_4)_6(OH)_2 + ...$

The $CaCO_3$ piece was put inside KH_2PO_4 solution (CO_3/PO_4 molar ratio 1:3) and the reactions were carried out in autoclave, at 200 °C and 12 bar in water vapour (hydrothermal conditions).

5.4 The European Project TEM-PLANT

The topics and activities described in this Chapter are one of the main subject of a STRP European Project (NMP4-CT-2006-033277), entitled **New Bio-ceramization processes applied to vegetable hierarchical structures -TEM-PLANT** and coordinated by ISTEC-CNR (Faenza, Italy).

Started on 1st October 2006, with a foreseen duration of four years, the purpose of TEM-PLANT is to develop bone and ligament substitutes, taking advantage of the hierarchical architecture exhibited by native structures like wood, plants, lianas, etc. The starting materials will be converted in rigid bone scaffolds through treatments of ceramization and in elastic ligament-like composites by controlled fibration of biopolymers like collagen and cellulose. The project involve nine partners from European countries, including ISTEC-CNR, which are experts in wood science, material science, organic and inorganic bio-composites; moreover expertises in cytotoxicity tests as well as orthopaedics are also present to guarantee a suitable assessment of the *in vitro* and *in vivo* performances of the obtained materials.

5.5 Characterization of the transformed woods

Pyrolysis

After the pyrolysis treatment, black pieces were obtained, strongly reduced in volume. SEM observations revealed a porous microstructure reproducing the features of the original wood (Fig. 5.6). XRD analysis confirmed that the only phase present was amorphous carbon (Fig. 5.7).

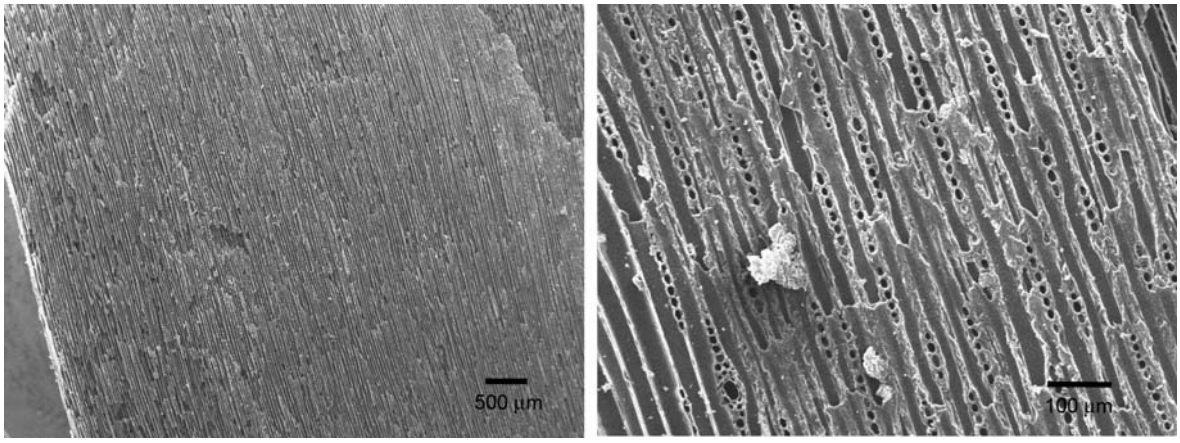

Figure 5.6. Morphology of pyrolyzed larch-wood.

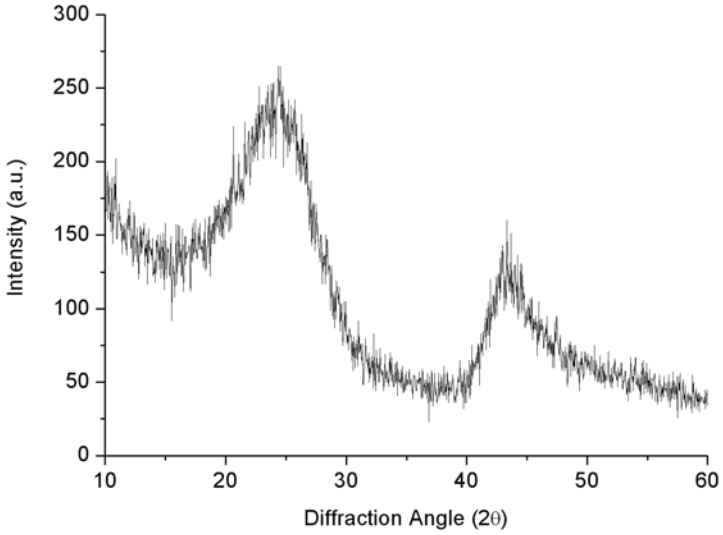

Figure 5.7. XRD spectrum of pyrolyzed wood.

Carburization

Local phase analysis was performed on the sample struts by EDS, and the presence of calcium was confirmed in the regions characterized by an altered morphology. XRD performed on samples as extracted by furnace (Fig. 5.8) revealed the presence of peaks belonging to two different polymorphs of calcium carbide (ICDD cards n° 51-1167 and 1-962).

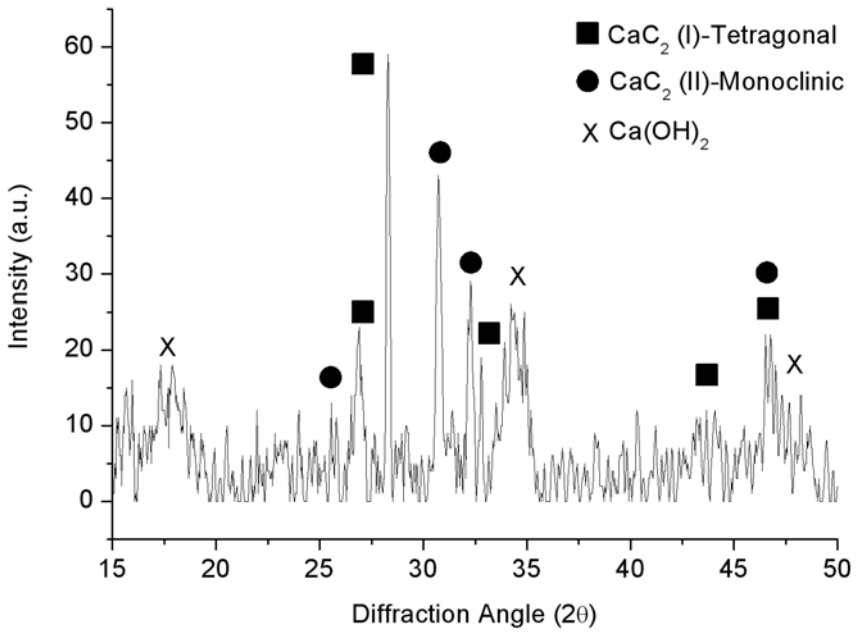

Figure 5.8. XRD spectrum of transforming CaC_2 wood-like structure, when exposed to air.

Anyway, in few minutes of exposure to the environment, from the extraction by the furnace to the complete analysis of the sample, calcium carbide started to oxidise, partially transforming in calcium hydroxide. Contrary to the sharp peaks of CaC_2 phase, $Ca(OH)_2$ exhibited broaden XRD reflections, confirming that this phase was in course of formation by hydration of CaC_2 due to the presence of water vapour in the environment.

The process of liquid infiltration provoked the formation of elongated CaC_2 crystals on the surface of the internal wall of pores (Fig.5.9), as confirmed by XRD and local elemental analysis by SEM-EDS.

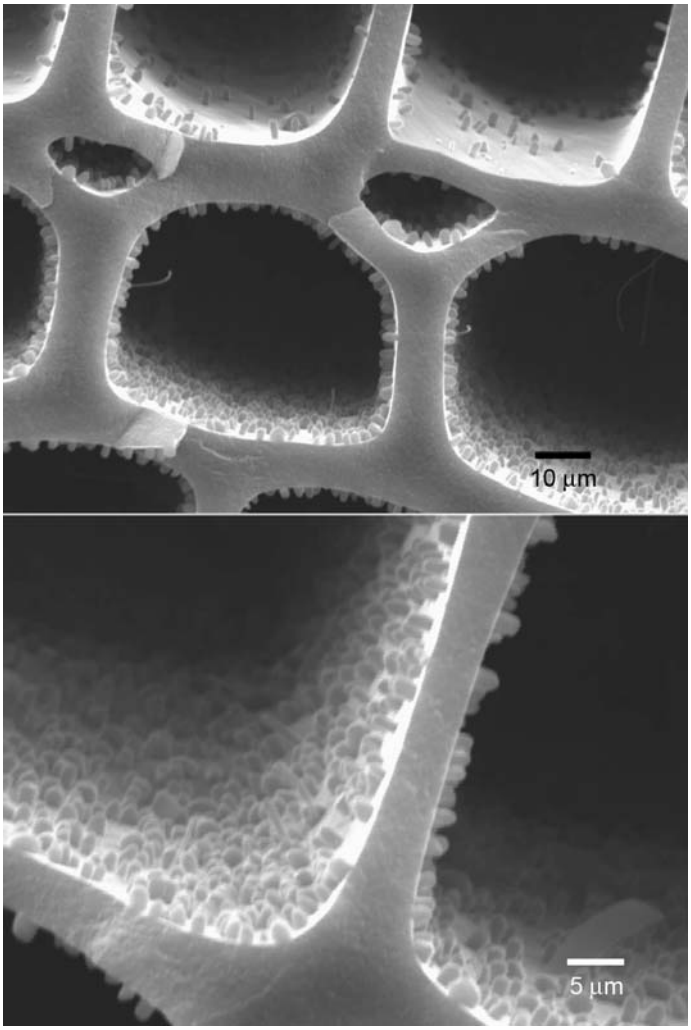

Figure 5.9. Formation of calcium carbide into the pores of carbon preform.

Nevertheless, the transformation process was not uniform, thus some regions exhibited an extensive formation of CaC_2 (Fig. 5.10), and others showed only a limited carburization, leaving wide non-reacted areas in the inner part of the sample (Fig. 5.11).

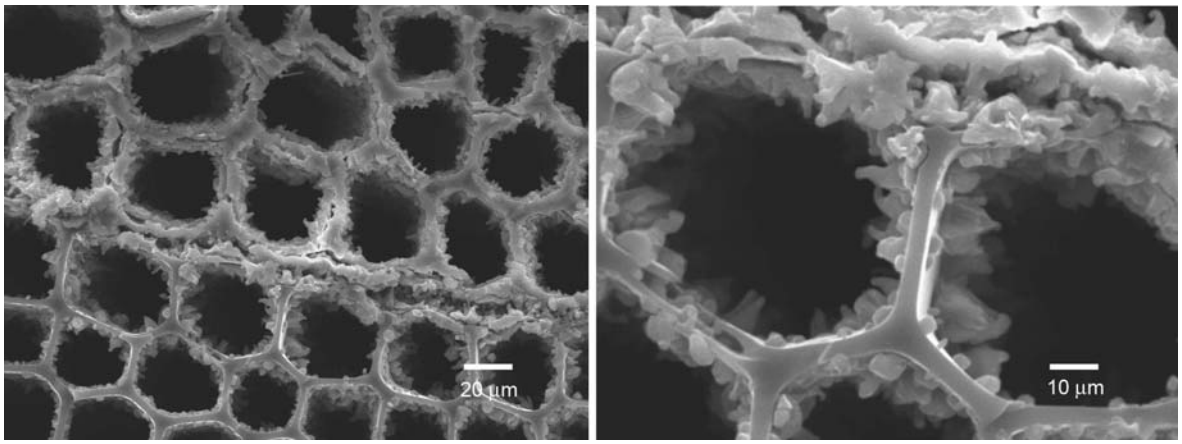

Figure 5.10. Extensive formation of CaC_2 particles into the pore of carbon preform.

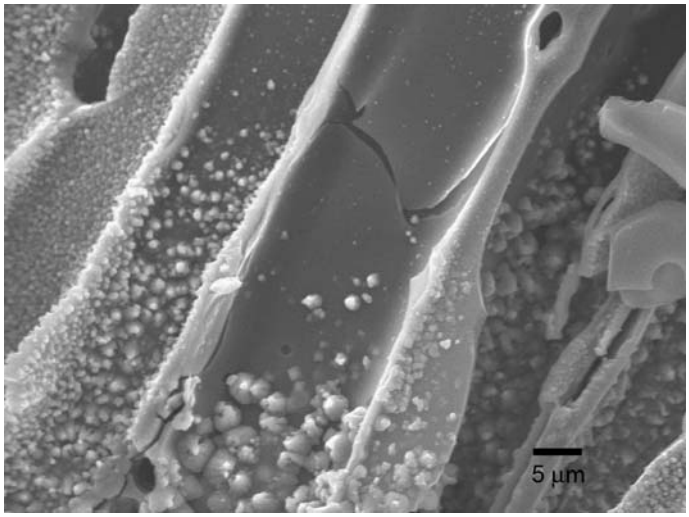

Figure 5.11. Incomplete carburization in liquid-phase infiltration.

The process of reaction with gaseous calcium yielded better results, compared with liquid phase infiltration. In fact, the microstructure of the resulting sample was more similar to the original carbon preform (Fig. 5.12), even though the strut thickness increased, due to the volume expansion following the transformation $C \rightarrow CaC_2$.

As well as the samples obtained by liquid infiltration, the moisture provoked the fast transformation of calcium carbide into calcium hydroxide, so that the pieces had to be immediately stored under inert gas, after extraction by the furnace.

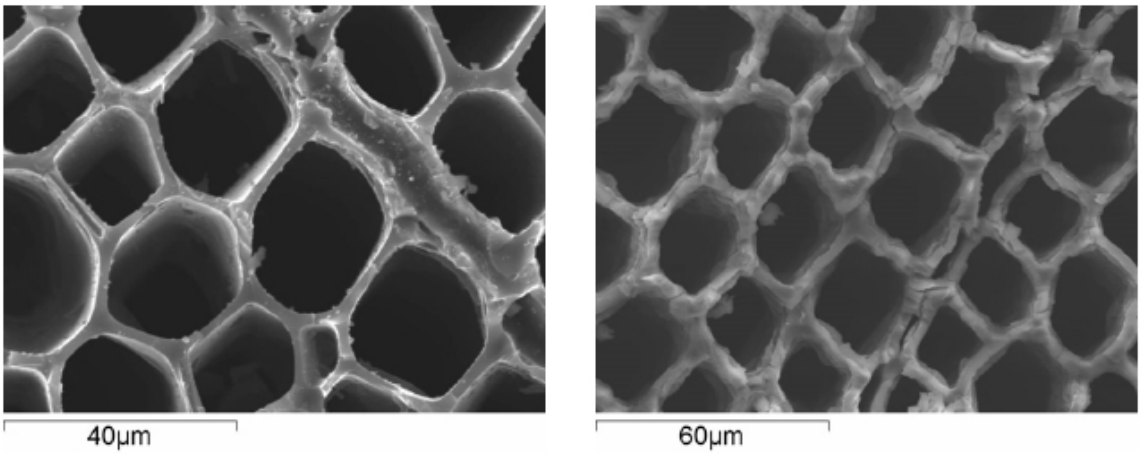

Figure 5.12. SEM micrographs of pyrolysed wood before and after the transformation in CaC_2.

The increase of the struts thickness between pores was found to be related to the amount of calcium used for the carburization reaction. A molar ratio Ca/C = 1 has given the best results in terms of similar thickness between carbon and calcium carbide final structure (Fig. 5.13).

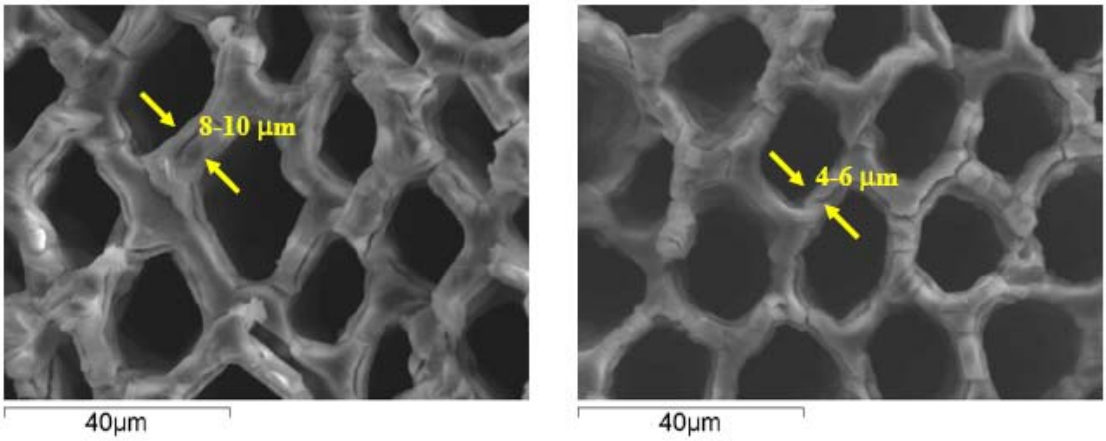

Figure 5.13. Calcium carbide obtained by initial molar ratio Ca/C >> 1 and Ca/C = 1.

XRD and SEM-EDS analyses confirmed the extensive formation of calcium carbide phase in the wood structure and on the struts, contrary to what occurred in the case of liquid phase reaction. After the Ca-vapour infiltration and reaction process, the CaC_2 material reproduced the cellular morphology of native wood.

The nucleation and growth of CaC_2 yielded the formation of a continuous CaC_2 layer in both liquid and vapour phase processes. Anyway, following the liquid phase process, some areas contained calcium or calcium-oxide filling the pores and cavities of the initial wood structure and isolated regions of amorphous, residual carbon, covered by the grains of the re-condensed calcium. The reaction by vapour phase yielded more homogeneous samples: in fact, as the carbon preform was in contact with gaseous calcium only, the filling of pores was strongly reduced and all calcium could react with carbon to give CaC_2. The calcium not reacting with carbon was captured by the graphite felt surrounding the crucible and did not accumulate inside the preform.

Oxidation

The comparison of the X-ray diffraction spectra of CaC_2 after two different heating treatments (1000 °C for 2 hours and 700 °C for 24 hours) showed that the reaction to form CaO was completed in the first case, while after treatment at 700 °C impurities of $Ca(OH)_2$ were still present even after 24 hours of treatment (Fig. 5.14).

No calcium carbide nor any unreacted carbon during carburization process remained in the core of the material synthesized through reactions described in equations 3) and 4) (see Section 5.2): the total reaction (5) was completed and the residual carbon burned out during heat treatment at 700-1000 °C in air.

Other final temperatures were tested, in the range 600-1000 °C in step of 100 °C; anyway, complete oxidation reactions occurred only after 12 hours of treatment at 800 °C.

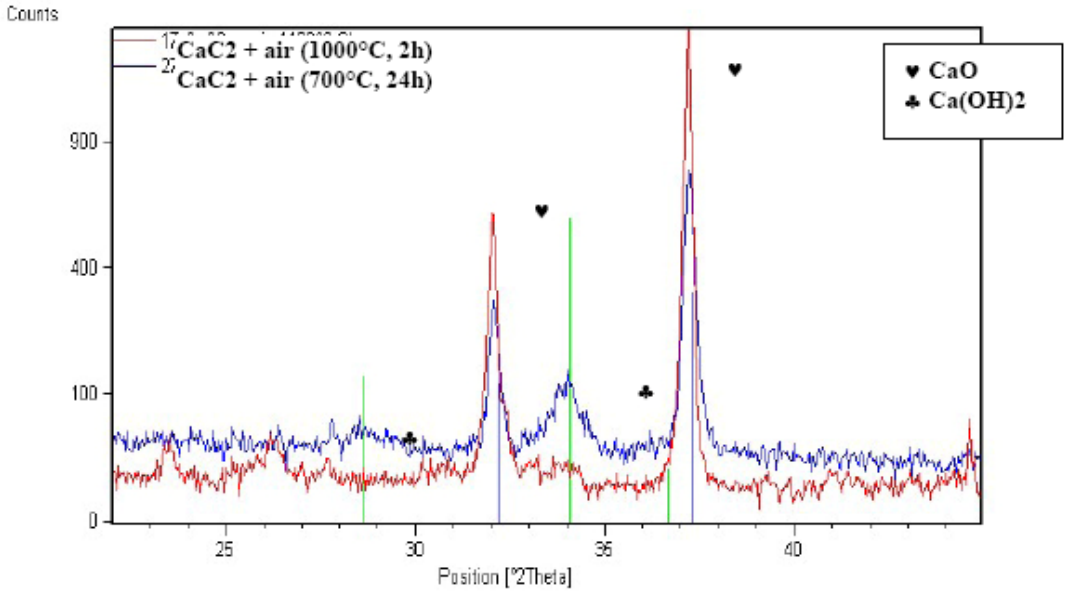

Figure 5.14. Comparison between XRD analyses of two different thermal cycles to obtain CaO.

The oxidation process, applied on porous calcium carbide pieces, yielded porous calcium oxide materials, retaining the original structure of the carbon preform (Fig. 5.15).

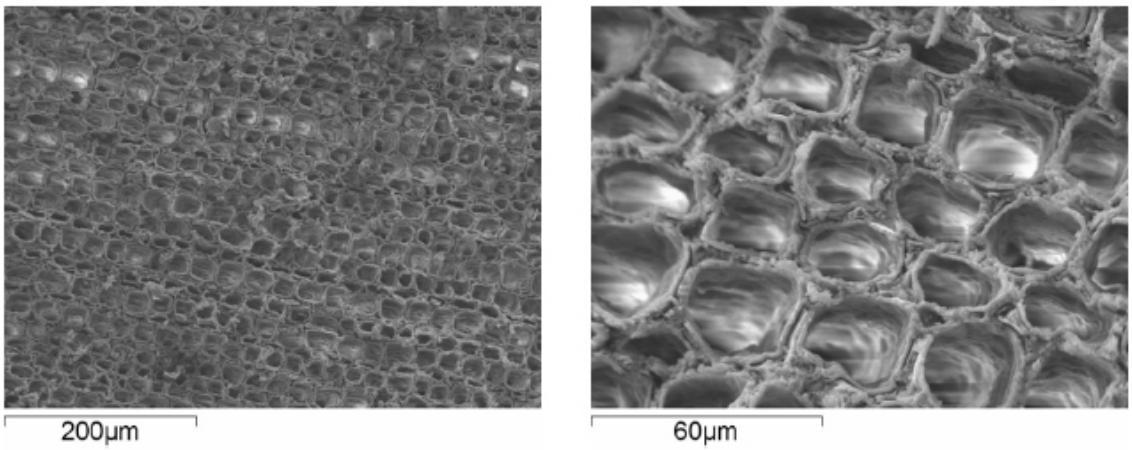

Figure 5.15. SEM micrographs of calcium oxide porous template.

Carbonation

XRD analysis (Fig. 5.16) identified $CaCO_3$ as the main phase under all the operated different working conditions. Anyway, XRD reflections belonging to residual $Ca(OH)_2$ were also found.

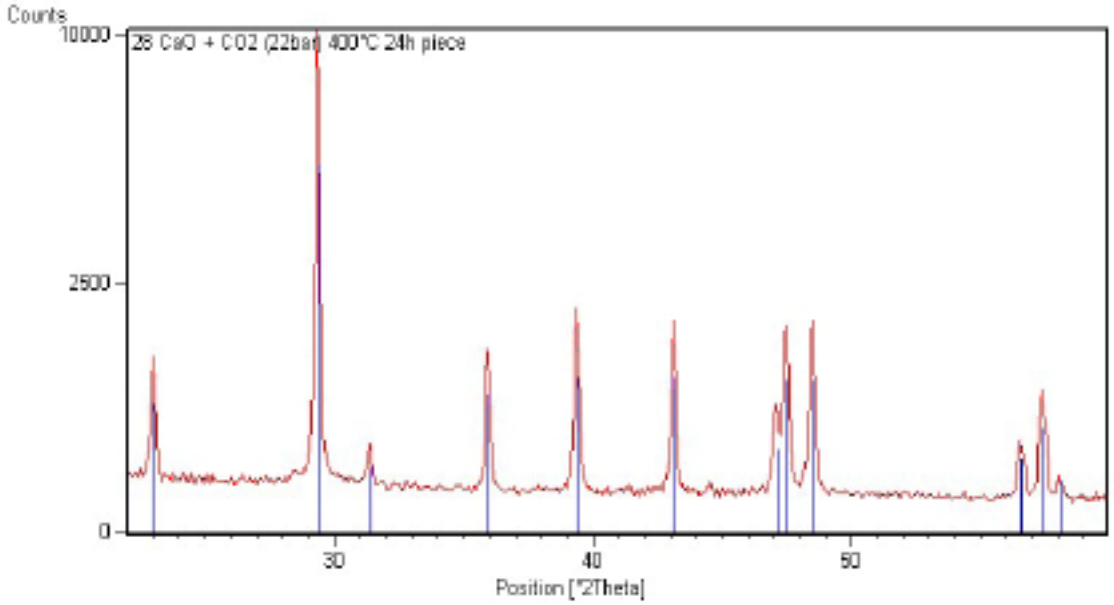

Figure 5.16. XRD analysis after carbonation process by autoclave (400°C, 22bar P_{CO2}, 24 hours).

Thus, the carbonation of the calcium oxide porous bodies did not proceed up to the complete conversion in $CaCO_3$: a maximum of about 90 vol% was achieved after 24 hours (Fig. 5.17).

The gas–solid CO_2–CaO reaction was supposed to proceed through two rate-controlling regimes: at the initial stage the reaction rapidly occurred by a heterogeneous surface reaction kinetic. Following this initial stage, as a compact layer of $CaCO_3$ is formed on the surface of CaO, the rate of reaction decreased due to the diffusion limitation of CO_2 through the $CaCO_3$ layer.

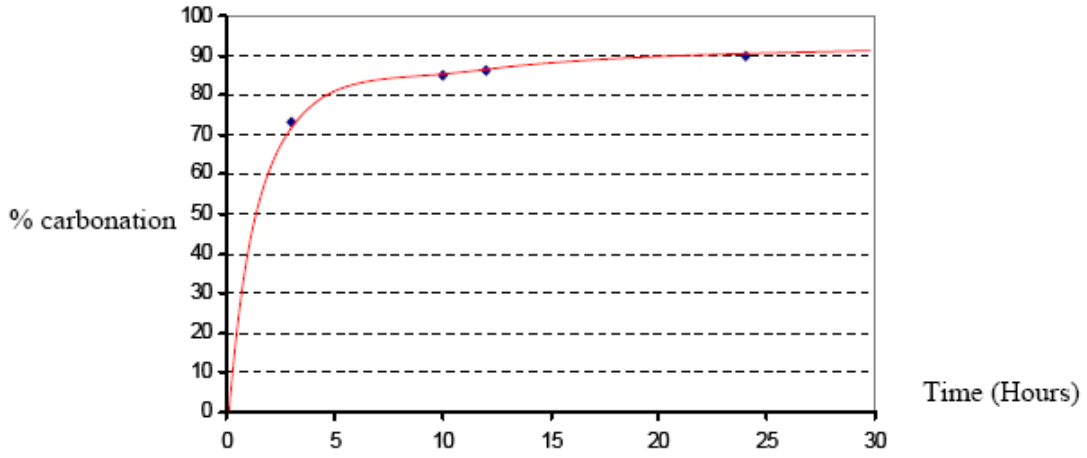

Figure 5.17. Carbonation percentage vs time of reaction in kiln (700°C).

In fact, as the reaction proceeded, the deposition of newly formed $CaCO_3$ layer reduced the permeability and this fact had an impact on the diffusion of CO_2. Thus, the complete conversion of CaO-template into porous $CaCO_3$ should depend not only on the temperature employed but also on the gas pressure in the autoclave, to allow the full reaction of CO_2 with the inner part of CaO template.

Anyway, the process of CaO conversion in $CaCO_3$ did not alter the morphology of porous samples obtained by pyrolysis-carburization-oxidation path. The original morphology and porosity of the carbon preform was retained and no further cracking of the struts was observed, compared to carburized and oxidised pieces (Fig. 5.18).

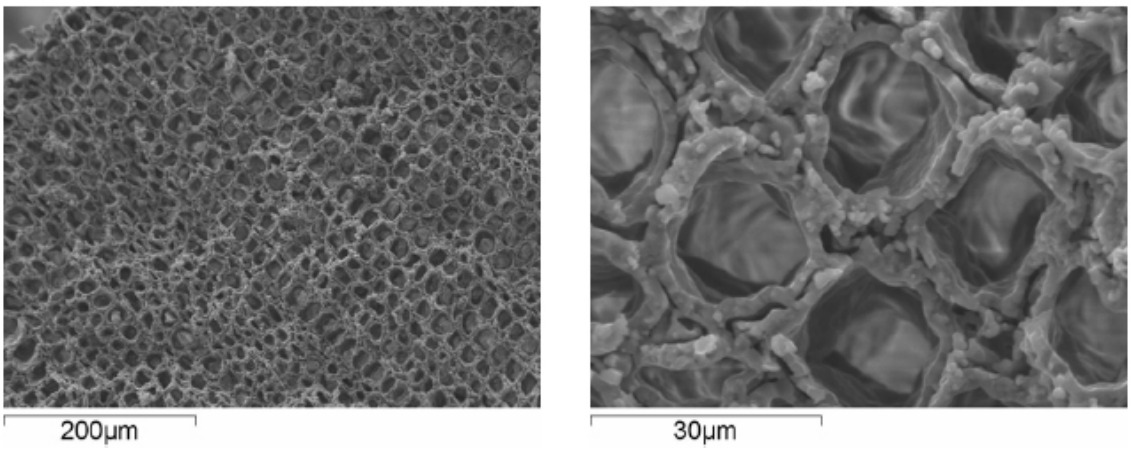

Figure 5.18. SEM micrograph calcium carbonate structure.

Phosphation

Both $CaCO_3$ commercial powder and porous pieces transformed in hydroxyapatite, after the treatment of phosphation in autoclave, as confirmed by the XRD spectrum in Fig. 5.19.

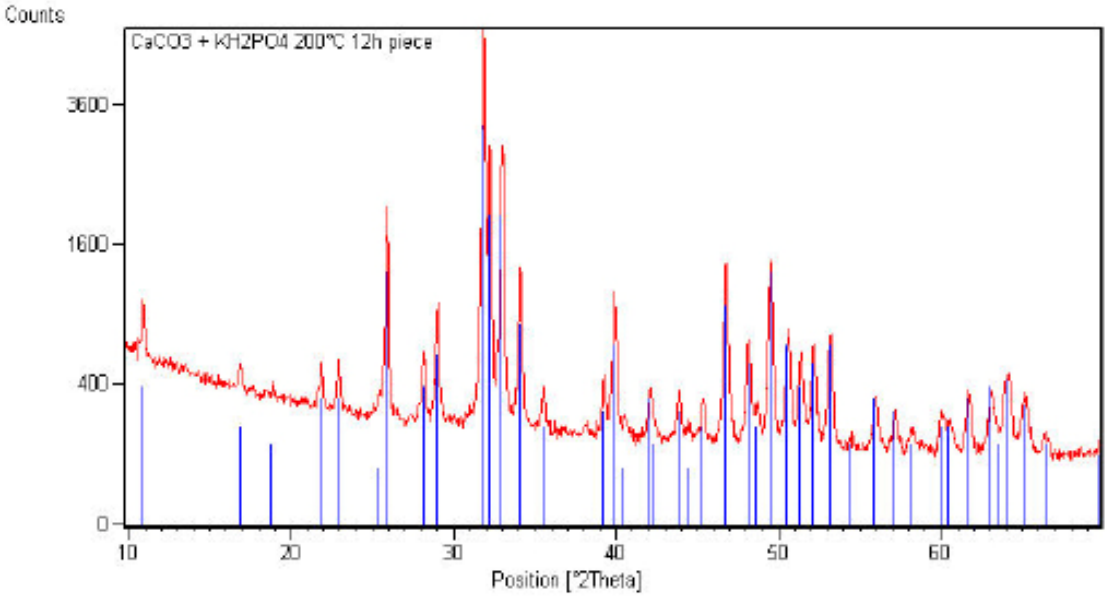

Figure 5.19. XRD analysis after hydrothermal treatment of calcium carbonate in phosphate-saturated atmosphere.

The final piece retained its original porosity and microstructure, so that the reaction path devoted to transform porous vegetable structure in porous HA bodies was successful.

Further characterization should be performed on HA pieces obtained following this route, in particular devoted to a deep morphological investigations and mechanical characterization, in order to assess whether the hierarchic arrangement of the final HA body is able to yield increased mechanical strength compared to porous HA bodies obtained by conventional manufacturing methods.

Since the porous HA was obtained by reaction of transformation, the mechanical strength can result affected by the presence of cracks and flaws occurred into the struts; anyway, the strength of these materials can be increased by suitable sintering treatments to improve the densification of the consolidated parts.

5.6 Conclusions

Ceramisation process to obtain HA porous ceramics starting from wood templates was successfully performed following five different steps of chemical-physical transformations.

The different steps were set up and optimized to maintain the original wood morphology; anyway, the whole process can require adjustments on the basis of the microstructure of

the selected wood. In fact, woods characterized by more open porosity (like rattan for example) can also exhibit an increased strut weakness, so to be damaged during the transformation processes.

The feasibility of the process has been anyway demonstrated, so that the future activity shall be devoted to the selection of opportune wood structures, on the basis of the bone portion to be substituted. In fact, there exists a huge variety of woods, characterized by different density, pore size and pore orientation, yielding different potential mechanical strengths, so to be employed as substitutes of cortical and trabecular bone. Pore size and interconnection must be carefully considered in order to be adequate for an efficient osteoconduction, especially considering the reduction in size following the treatment of ceramization.

Finally, since the ceramization process was successful, the set up of the process parameters can drive to the achievement of bone substitutes which are biomimetic from a morphological point of view, with potentially improved biomechanical performances, so to pave the way for the development of substitutes for long and load-bearing bone portion.

References

1. Wegst UGK, Ashby MF. The mechanical efficiency of natural materials. Philos Mag 2004; 84: 2167-2181.

2. Fratzl P, Weinkamer R. Nature' s hierarchical materials. Prog Mater Sci 2007; 52: 1263-1334.

3. Fengel D, Wegener G. Wood: chemistry, ultrastructure, reactions. Berlin: de Gruyter, 1989.

4. Greil P, Lifka T, Kaindl A. Biomorphic Cellular Silicon Carbide Ceramics from Wood, Part I. Processing and Microstructure. J. Eur Ceram Soc 1998; 18: 1961-1973.

5. Greil P, Lifka T, Kaindl A. Biomorphic Cellular Silicon Carbide Ceramics from Wood, Part II. Mechanical Properties. J. Eur Ceram Soc 1998; 18: 1975-1983.

6. Sieber H, Hoffmann C, Kaindl A, Greil P. Biomorphic Cellular Ceramics. Adv Eng Mat 2000; 2: 105-109.

7. Sieber H, Vogli E, Müller F, Greil P, Popovska N, Gerhard H, Emig G. CVI-R gas phase processing of porous, biomorphic SiC ceramics. Key Eng Mater 2002; 206-213: 2013-2016.

8. Greil P. Biomorphous ceramics from lignocellulosics. J. Eur. Ceram Soc 2001; 21: 105-118.

9. Esposito L, Sciti D, Piancastelli A, Bellosi A. Microstructure and properties of porous β-SiC templated from soft woods. J Eur Ceram Soc. 2004; 24: 533-540.

10. Parfen'eva LS, Orlova TS, Kartenko NF, Sharenkova NV, Smirnov BI, Smirnov IA, Misiorek H, Jezowski A, Varela-Feria FM, Martinez-Fernandez J, de Arellano-Lopez AR. Thermal conductivity of the SiC/Si biomorphic composite, a new cellular ecoceramic. Phys Sol St 2005; 47 (7): 1216-1220.

11. Kardashev BK, Burenkov YA, Smirnov BI, de Arellano-Lopez AR, Martinez-Fernandez J, Varela-Feria FM. Internal friction and Young's modulus of a carbon matrix for biomorphic silicon carbide ceramics. Phys Sol St 2005; 47 (5): 886-890.

12. Gonzalez P, Borrajo JP, Serra J, Liste S, Chiussi S, Leon B, Semmelmann K, de Carlos A, Varela-Feria FM, Martinez-Fernandez J, de Arellano-Lopez AR. Extensive studies on biomorphic SiC ceramics properties for medical applications. Bioceramics 2004; 16: 1029-1032.

FINAL CONCLUSIONS AND FUTURE PERSPECTIVES

In the present work, the achievement of biomimetic bone substitutes has been pursued under three different perspectives.

In a biochemical perspective, methodologies were set up and optimized, to obtain biomimetic HA powders characterized by multiple atomic substitutions, involving the most relevant ions present in the biological environment (carbonate, magnesium, silicon) in adequate amounts for the stimulation of the natural processes of bone regeneration. Particular care has been devoted to the effect of silicon on the physical-chemical properties and solubility behaviour of the Si-doped HA powders.

In view of structural applications, consolidation techniques have been developed and applied on mixtures of hydroxyapatite and bioactive calcium silicates, with the purpose of obtaining bioactive materials characterized by improved mechanical resistance, for the development of bioactive load-bearing scaffolds. The presence of silicon in these materials was kept in consideration also to improve the biomimetism of the whole composite. There was evidence of possible ion migration in HA, during the thermal treatments of consolidation of bulk materials; if confirmed, this effect might be exploited on a large variety of calcium silicates also containing magnesium and characterized by different mechanical properties and reactivity with HA, still largely unexplored.

Finally, the problem of the morphological biomimetism has been faced, by taking Nature as starting point to develop synthetic structures characterized by hierarchically organized morphologies. In the present work, new methodologies have been explored and applied to different wood structures to obtain porous hydroxyapatite ceramics maintaining the same morphology of the native woods. The results are novel, as the experimented techniques involved very complex transformations, in five different steps;

in the past, similar procedures have been applied on woods for transformation in silicon carbide, which involved only a single-step process after pyrolysis.

The results obtained in the present work were positive in all the three different areas of investigation. The conclusions that can be drawn is that only at the convergence of the three different fields it is possible to find out the best solutions to develop the *ideal* bone-like scaffold. Thus, the future activity should be devoted to solve the problems at the borderline between the different research lines, which hamper this convergence; in particular:

- as hydroxyapatite becomes more biomimetic, it also becomes more chemically unstable when heated at high temperatures, so that the development of composites with a controlled phase composition becomes more challenging. In this case, the employment of bioactive reinforcing phases containing ions influent for the HA biomimetism can help to solve this problem, as already demonstrated in this work.

- from a morphological / structural point of view, the achievement of porous structures obtained by the transformation of native woods is promising for the development of scaffolds exhibiting an increased biomimetism. In this case, the problem is still widely open, as many different woods should be selected and tested on the basis of the desired structure and also the effective increase of mechanical performances and osteoconductive properties is still to be assessed. Following, a further increase of the chemical biomimetism of these porous materials can be needed, so that specific methodologies for incorporating ions like magnesium and silicon in the wood-derived structures should be developed.

ACKNOWLEDGEMENTS

I wish to acknowledge my colleagues of ISTEC-CNR institute who supported me in collecting and discussing the experimental data of the whole research, In particular:

I wish to acknowledge Dott.ssa Anna Tampieri for the continuous coordination of the whole research work and fruitful discussion on the different faced topics, which contributed to improve the focusing and efficiency of the research activity.

I also wish to acknowledge Dott.ssa Elena Landi for the relevant discussions and suggestions concerning the development of the multi-substituted hydroxyapatite powders.

Moreover, I acknowledge Dott. Giancarlo Celotti for interpretation and deep discussion of X ray diffraction data; Dott.ssa Monica Sandri for performing ICP analyses and Dott.ssa Selanna Martorana for electroacoustic measurements.

I particularly acknowledge Dott. Andrea Ruffini for the set up of the different steps of ceramization process on natural wood structures.

Finally, I want to acknowledge Mr. Daniele Dalle Fabbriche for the carrying out of the Fast Hot Pressing experiments, Mr. Cesare Melandri for flexural strength and nanoindentation tests and Dott. Stefano Guicciardi for the fruitful discussion on the mechanical properties of ceramics. Also, Ms. Andreana Piancastelli for specific surface area analysis and Ms. Guia Guarini for the measurement of powder density and particle size distribution.